U.S. DEPARTMENT OF ENERGY

PNNL-22553

Prepared for the
U.S. Nuclear Regulatory Commission
under a Related Services Agreement
with the U.S. Department of Energy
Contract DE-AC05-76RL01830

Final Assessment of Manual Ultrasonic Examinations Applied to Detect Flaws in Primary System Dissimilar Metal Welds at North Anna Power Station

MT Anderson
AA Diaz
AD Cinson
SL Crawford
M Prowant
SR Doctor

March 2014

Pacific Northwest
NATIONAL LABORATORY

Proudly Operated by Battelle *Since 1965*

DISCLAIMER

PACIFIC NORTHWEST NATIONAL LABORATORY
operated by
BATTELLE
for the
UNITED STATES DEPARTMENT OF ENERGY
under Contract DE-AC05-76RL01830

Printed in the United States of America

Available to DOE and DOE contractors from the
Office of Scientific and Technical Information,
P.O. Box 62, Oak Ridge, TN 37831-0062;
ph: (865) 576-8401
fax: (865) 576-5728
email: reports@adonis.osti.gov

Available to the public from the National Technical Information Service,
U.S. Department of Commerce, 5285 Port Royal Rd., Springfield, VA 22161
ph: (800) 553-6847
fax: (703) 605-6900
email: orders@ntis.fedworld.gov
online ordering: http://www.ntis.gov/ordering.htm

This document was printed on recycled paper.
(9/2003)

PNNL-22553

Final Assessment of Manual Ultrasonic Examinations Applied to Detect Flaws in Primary System Dissimilar Metal Welds at North Anna Power Station

MT Anderson
AA Diaz
AD Cinson
SL Crawford
M Prowant
SR Doctor

March 2014

Prepared for
U.S. Nuclear Regulatory Commission
under a Related Services Agreement
with the U.S. Department of Energy
Contract DE-AC05-76RL01830

Pacific Northwest National Laboratory
Richland, Washington 99352

Executive Summary

Beginning in spring 2012, Pacific Northwest National Laboratory (PNNL) conducted a technical assessment in support of a request from the U.S. Nuclear Regulatory Commission (NRC) Office of Research (RES) of the nondestructive examination (NDE) issues and protocols that led to missed detections of several axially oriented flaws in a steam generator primary inlet dissimilar metal weld at North Anna Power Station, Unit 1 (NAPS-1). This particular component design exhibits a significant outside-diameter (OD) taper that is not included as a blind performance demonstration mock-up within the industry's Performance Demonstration Initiative (PDI), administered by the Electric Power Research Institute (EPRI). The service-induced flaws at NAPS-1 were eventually detected as a result of OD surface machining in preparation for a full structural weld overlay. The machining operation uncovered the existence of two through-wall flaws, based on the observance of primary water leaking from the dissimilar metal weld (DMW). Further ultrasonic tests were then performed, and a total of five axially oriented flaws, classified as primary water stress corrosion cracking (PWSCC), were detected in varied locations around the weld circumference.

The field volumetric examination that was conducted at NAPS-1 was a non-encoded, manual conventional ultrasonic examination. PNNL conducted both an initial assessment, and subsequently, a more rigorous technical evaluation (reported here), which has identified an array of NDE issues that may have led to the subject missed detections. These evaluations were performed through technical reviews and discussions with NRC staff, EPRI NDE Center personnel, industry and ISI vendor personnel, and ultrasonic transducer manufacturers, and included laboratory tests, to better understand the underlying issues at North Anna.

PNNL's technical evaluation included a site visit to NAPS-1 to evaluate the actual probe and ultrasonic testing (UT) responses produced from the site-specific DMW flaw mock-ups. In addition, PNNL conducted a review and assessment of the technical justification (TJ), developed by EPRI, for qualification acceptance of the non-encoded, manual conventional ultrasonic technique applied at NAPS-1. Initial acoustic modeling and simulation activities were also employed to identify key variables associated with the conventional UT probes used at NAPS-1, and to assess their potential to detect inside-diameter (ID) surface-connected, axially oriented flaws, given predicted sound field characteristics. The actual probes and mock-ups were sent to PNNL, and UT analyses were performed to obtain confirmatory data for validating the modeling results. This technical letter report provides the relevant data for comparing and contrasting the use of the encoded, phased-array ultrasonic examination techniques performed by PNNL alongside results from both the manual conventional ultrasonic examination protocol implemented at NAPS-1, and encoded results acquired in the laboratory (PNNL) using the actual tandem probes on the mock-ups. PNNL also conducted an evaluation of fabricated flaws in the mock-ups, including UT responses from artifacts other than the targeted flaws, or that were welding related in origin, to determine if their presence could impact detection of the intended flaws.

Further probe modeling and acoustic beam simulations were conducted to help quantify actual sound field densities and beam propagation characteristics, while empirical data from sound field mapping and characterization activities shed further light on performance, indicating critical issues associated with the design and operations of the NAPS-1 tandem probes. Results indicated the tandem probe configuration, as fabricated, would produce maximum longitudinal mode ultrasonic energy at a refracted angle of approximately 30 degrees with adequate sound field intensity located at only a shallow distance within

the component (along the metal path) as compared to that required for an effective inspection of ID-connected flaws. An empirical assessment of the acoustic beam produced by the tandem probe was performed via benchmarking of sound field maps. This provided insights into critical attributes that determine probe performance as a function of beam characteristics (spot size, signal strength, frequency content, etc.), spatial coherence, excitation function (voltage, modality), probe design specifications, and sensitivity. Results of the beam mapping study, using four different pulser excitation scenarios, indicated that a lower voltage (200V rather than 450V as employed in the field) square-wave excitation function produced the most symmetric sound beam. Further, the better sound beam emanated from the rear (back) element, rather than the front element (which was used for transmission at NAPS-1). As the excitation voltage is increased, the amount of scatter and loss of spatial coherence of the sound field increases. This reduces sensitivity and may have contributed to a reduced detection capability. These results indicate that underlying issues exist regarding how the probe was deployed, and that it is highly likely the tandem probes were being overdriven at NAPS-1. Thus, based on their design and field operation, the tandem probes would not be expected to adequately insonify the volume of examination with effective ultrasonic energy. Additionally, it was observed that although the tandem probes were identical in design, they exhibited significant differences in sensitivity. It could not be determined from information provided by the licensee what may have occurred to cause this difference in sensitivity, or when it may have occurred. What is problematic is the fact that the licensee's equipment verification checks prior to performance of the examination, if performed, did not identify this critical issue. Finally, the probes were not distinctively labeled and could easily be used in the reverse orientation (backwards, or directing the sound away from the area of interest) during an examination.

In cooperation with EPRI and Dominion Generation personnel, an evaluation of ultrasonic signal responses from NAPS-1 field DMWs to those obtained from the site-specific mock-ups was also conducted. The effort focused on identifying UT response differences between materials, welding fabrication flaws, and geometric features of the mock-ups and the actual field welds to determine how representative these site-specific mock-ups were, with respect to actual field welds/conditions. Based on general UT background noise, attenuation, and the population and location of welding fabrication flaws detected in the mock-ups and the actual field welds, the welds and adjacent parent materials for cold legs, hot legs, and site-specific mock-ups appear to be ultrasonically similar. Nevertheless, circumferential flaws were implanted during the welding process (fit up/assembly of the mock-up), and if fabricated carefully and properly placed, these should not produce significant implantation artifacts, as were discovered during this evaluation. PNNL data acquisition scans in the circumferential direction (looking for axially oriented flaws) resulted in detection of flaw artifacts in four of the five circumferentially oriented flaws. These are most likely associated with implantation or excavation processes during fabrication. Naturally occurring service-induced planar flaws do not possess similar implantation features nor offer such ultrasonic responses. Further, circumferential scans conducted to detect axial flaws would not ordinarily be able to exhibit circumferentially oriented flaw responses as readily as the data on the NAPS-1 mock-ups show. Equally detrimental to a performance demonstration process is the case where a flaw implantation response highlights the existence of a targeted crack, as occurs for several of the circumferential flaws on the mock-ups. This leads PNNL to conclude that, from the standpoint of implantation quality, and flaw integrity and placement, the mock-ups were poorly fabricated. Site-specific mock-ups are not addressed by Section XI, Appendix VIII. To provide guidance for the fabrication of site-specific mock-ups when component configurations are not included in the Performance Demonstration Initiative (PDI) Supplement 10 or Supplement 11 procedure qualification, industry developed a guidance document entitled, "Mock-Up Criteria for Dissimilar Metal Welds and Weld

Overlays." Revision B of this document, dated 6/27/2011, was in effect at the time of the inspections conducted at NAPS-1.

Following is a summary of the primary findings of the PNNL technical assessment:

- In accordance with PDI-UT-10 (EPRI 2010), the optimum range of ID impingement angles for detecting axial primary water stress corrosion cracking (PWSCC) in dissimilar metal welds is 55-60 degrees. A transmitted refracted angle at 40 degrees theoretically produces an inner diameter (ID) impingement angle of about 58 degrees at the flaw. Theoretical simulations validated by empirical assessments showed that the tandem probes produced energy at a nominal 30-degree refracted longitudinal wave which results in a theoretical ID impingement angle of approximately 41 degrees.
- Sound field simulations showing the acoustic beam density generated by the tandem probe, as modeled using the CIVA 10.1 software suite, shows a drop of 12 dB from the maximum sound intensity that is theoretically reaching the ID. Therefore, only about 25% of the maximum beam intensity is predicted at the ID surface, which is optimistic given the anisotropic nature of weld microstructures. This reduced sound field intensity also predicts a poor signal-to-noise level for detection of ID surface-connected flaws via corner-trapped responses. The simulation results indicate the tandem probes may have been able to detect specular or tip responses from flaws in the outer 60% of the material (which has only been modeled as a simple isotropic media), but would be extremely limited for detection of ID-connected flaws in this DMW weld configuration when non-encoded manual techniques are employed.
- The data acquired on the mock-ups show, in some cases, that weld fabrication and flaw implantation signal responses are higher in amplitude than nearby implanted target flaws. The relative proximity of axial and circumferential flaws, and the presence of significant implantation artifacts, results in spurious reflectors. In addition, screen persistence (a measure of signal detection capability) for axial flaws in the mock-ups was observed to be extremely short-lived, especially if a typical manual scan rate of 2-inches per second is applied. These conditions render assessments (detections) of flaw signal responses in the presence of such ambient noise highly improbable when using a manual non-encoded UT technique.
- Based on site observations and laboratory measurements of UT responses from the flaws and other artifacts during examinations conducted by PNNL on the mock-ups, one would not expect the manual, non-encoded technique employed to consistently detect axial flaws (with low numbers of false calls) without examiners having prior knowledge of where these flaws are located.
- The PNNL assessment of the EPRI NDE Center-developed TJ supporting the manual ultrasonic examination demonstration at NAPS-1 shows that essential variables were changed, which contradict the requirements of Appendix VIII.
- The work conducted here in assessing non-encoded and encoded examination techniques on the mock-ups indicates that encoded scans not only provide enhanced detection rates, but also allow for post-analysis and diagnosis of issues as well as appropriate oversight of examination records.
- PNNL findings suggest that employment of a site-specific approach for an examination must have a solid technical basis to support the methodolgy, and this basis would need to be rigorously and systematically developed in order to meet the intent of Appendix VIII.

Acronyms and Abbreviations

ASME	American Society of Mechanical Engineers
BW	bandwidth
CAD	computer-aided drafting
CCW	counterclockwise
CFR	Code of Federal Regulations
CMTR	certified material test report
CS	carbon steel
CW	clockwise
dB	decibel(s)
DMW	dissimilar metal weld
EPRI	Electric Power Research Institute
HAZ	heat-affected zone
HiP	hot iso-statically pressed
HP	half path
ID	inside diameter
ISI	inservice inspection
LMT	Lambert-MacGill-Thomas Inc.
MHz	megahertz
NAPS-1	North Anna Power Station, Unit 1
NDE	nondestructive examination
NIFG	Nondestructive Examination Improvement Focus Group
NPS	nuclear power station
NRC	U.S. Nuclear Regulatory Commission
OD	outside diameter
PA	phased array
PDI	Performance Demonstration Initiative
PNNL	Pacific Northwest National Laboratory
PWSCC	primary water stress corrosion cracks
RES	Office of Research (U.S. Nuclear Regulatory Commission)
rf	radio frequency
RMS	root-mean-square
SDH	side-drilled hole
SNR	signal-to-noise ratio
SS	stainless steel
TD	true depth
TJ	technical justification

TLR	technical letter report
TRL	transmit-receive longitudinal
UT	ultrasonic testing
V	volts

Contents

Figures

Tables

1.0 Introduction

During an inservice inspection (ISI) of a dissimilar metal weld (DMW) in an inlet (hot leg) steam generator nozzle at North Anna Power Station, Unit 1 (NAPS-1), several axially oriented flaws went undetected by the licensee's manual conventional ultrasonic testing (UT) technique. The flaws were subsequently detected as a result of outside-diameter (OD) surface machining in preparation for a full structural weld overlay. The machining operation uncovered the existence of two through-wall flaws, based on the observance of primary coolant water leaking from the DMW. Further ultrasonic tests were then performed, and a total of five axially oriented flaws, classified as primary water stress corrosion cracking (PWSCC), were detected in varied locations around the weld circumference.

The NAPS-1 hot leg safe end-to-nozzle weld configuration has an approximate 11-degree OD taper from the thinner austenitic piping side, up to the thicker carbon steel nozzle, and is typical of a DMW created during steam generator replacement at Westinghouse-designed nuclear power plants. However, the level of OD taper exhibited by this particular design is not included as a blind performance demonstration mock-up used by the industry's Performance Demonstration Initiative (PDI), which is administered by the Electric Power Research Institute (EPRI). For this reason, the licensee engaged EPRI to assist in the development of a technical justification (TJ) IR-2009-358 (EPRI 2009), to support the basis for a site-specific qualification.

In May 2012, Pacific Northwest National Laboratory (PNNL) conducted a preliminary assessment of the manual conventional ultrasonic examinations applied at NAPS-1. A technical letter report (TLR) was generated (Anderson et al. 2012) based on information provided from a number of sources, and was intended as an initial high-level assessment aimed at identifying pertinent questions and technical issues that required further evaluation. The intent of the current TLR is to summarize the initial information and address remaining technical questions and issues that were raised during the first evaluation process.

The focus of this TLR is to assess failure of the licensee's applied UT technique to detect multiple flaws, describe subsequent studies conducted, and to provide final results and conclusions. The effort was conducted by PNNL in support of a request by the United States Nuclear Regulatory Commission (NRC), Office of Nuclear Reactor Regulation (NRR). The work was sponsored by the NRC Office of Nuclear Regulatory Research (RES) under Job Code Number V6323. Information was gathered from NRC staff, EPRI Nondestructive Examination (NDE) Center and Dominion Generation (the licensee) personnel, and other nuclear industry experts to support this technical assessment. As a result of these interactions and discussions, efforts were directed to better understand applied ultrasonic instrumentation and probes, their design specifications, and performance characteristics, as well as the ISI technique and procedures that were implemented at the site. In addition, assessments of TJ IR-2009-358 and the site-specific mock-ups were performed, including the design, materials, welds, and implanted flaws contained within these mock-ups that were used to demonstrate detection capability of examination procedures implemented at NAPS-1. The work described herein is founded on the acquisition of both theoretical results derived from advanced modeling and simulation activities, as well as empirical laboratory-based validation studies and confirmatory research activities.

This TLR provides a summary of this effort, and in Section 2.0, the objectives and scope of the work are provided. Section 3.0 describes the design specifications of the North Anna DMW mock-ups. Section 4.0 provides a summary of observations obtained during a site visit to NAPS-1, where PNNL and

NRC RES staff conducted a set of initial ultrasonic measurements on the mock-ups. It also presents PNNL's assessment of EPRI TJ IR-2009-358 for ultrasonic examination of the steam generator nozzle DMWs. Section 5.0 describes the tandem probes, their sound fields as modeled and measured, as well as encoded data acquired by PNNL on the mock-ups. Section 6.0 provides an assessment of the mock-ups based on PNNL's ultrasonic phased-array probe evaluation and a comparison of mock-up responses to field responses. Lastly, Section 7.0 provides the findings and discusses the conclusions from this work. References cited in this report are listed in Section 8.0. Appendix A presents an overview of the various ultrasonic data displays used throughout this report. Appendices B through F contain relevant supporting information.

2.0 Scope and Objectives of Technical Evaluation

The NRC asked PNNL to assess the manual conventional UT technique that was applied at North Anna, and evaluate potential causes for the failure of the examination to detect these significant flaws. It cannot be definitively determined that certain factors contributed to the UT detection failure because of mitigating issues, such as (1) the lack of data for review due to the manual non-encoded conventional (real-time) UT examinations that were conducted; one cannot judge whether the data quality was insufficient or if the flaw responses were present, but simply missed during initial examinations; (2) pre-overlay OD machining operations eliminated much of the OD taper changing the configuration and reducing the metal path to improve UT that was subsequently applied; and (3) the machining may have changed residual stresses resulting in altered UT flaw responses (possibly making the flaws more detectable). However, certain definitive technical conclusions are still possible.

PNNL was asked to perform the following activities with respect to the assessment:

- Model the acoustic variables of the manual UT probes used at North Anna to analyze their potential to detect inside-diameter (ID) surface-connected, axially oriented flaws, given predicted sound field characteristics;
- Visit NAPS-1 to evaluate the actual probe and UT responses produced from the site-specific DMW flaw mock-ups;
- Assess Technical Justification IR-2009-358, developed by EPRI, for acceptance of the manual technique that was applied;
- Work with industry experts, ISI vendor personnel, transducer manufacturers, and EPRI NDE Center staff to better understand the issues at North Anna and the potential regulatory ramifications of industry-wide implementation of site-specific mock-ups, modifications to essential variables, and manual ultrasonic examinations;
- Use the tandem probes and mock-ups to conduct laboratory-based NDE assessments at PNNL, and obtain confirmatory data for validation of modeling and simulation results;
- Visit Dominion Generation headquarters to evaluate mock-up and actual field data to assess if the parent material/welds of the site-specific mock-ups used at NAPS-1 were representative of actual field welds/conditions or if substantial differences existed; and
- Compare, contrast, and evaluate the use of encoded, phased-array ultrasonic examination techniques with the manual ultrasonic examination protocol implemented at North Anna.

These activities will be reported in the remaining sections of this report, followed by the conclusions. This final TLR describes work that was conducted to augment initial information reported in Anderson et al. (2012) aimed at supporting resolution of NRC Regional findings for NAPS-1.

3.0 North Anna DMW Mock-ups

The North Anna steam generator nozzle DMW configuration consists of an 11-degree OD-tapered wrought stainless steel safe end with a nominal through-wall thickness from 83.12 mm (3.28 in.) to 121.16 mm (4.77 in.) at the weld toe. The Alloy 82/182 weld and butter regions continue to follow the 11-degree OD taper into the 508 Class 2 steel nozzle forging, as shown in Figure 3.1. A three-dimensional computer-aided drafting (CAD) drawing of this configuration was rendered for modeling purposes.

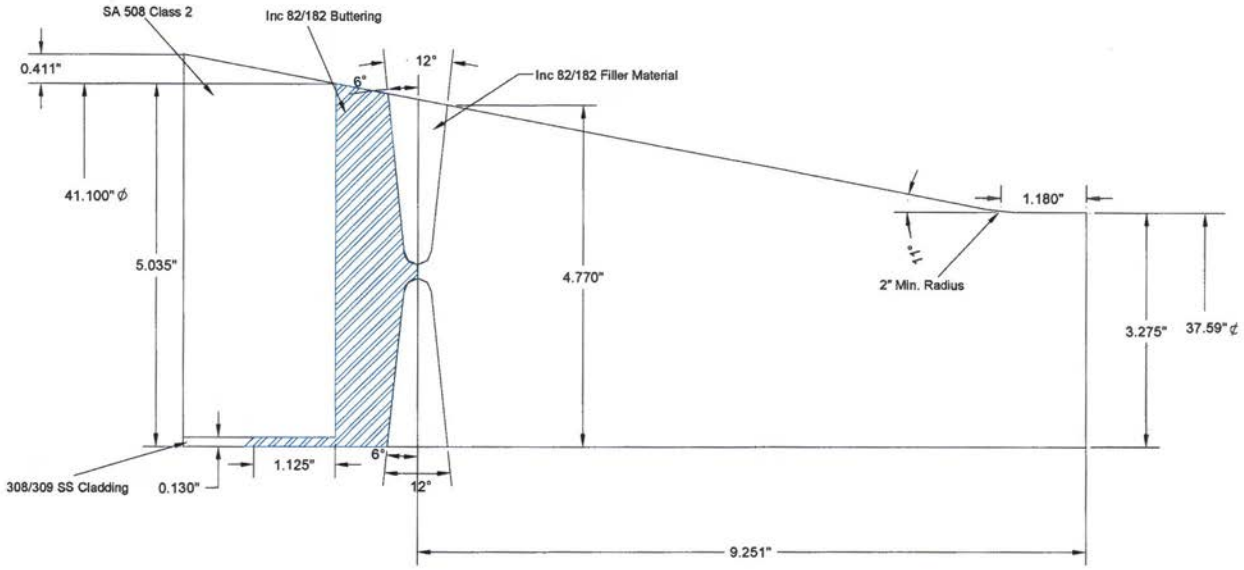

Figure 3.1. Profile of the NAPS-1 Steam Generator DMW (EPRI 2009)

The licensee fabricated steam generator nozzle mock-up specimens for use in a site-specific qualification because the 11 degree taper was outside of the range that had been demonstrated through PDI; these mock-ups were ultrasonically examined at PNNL. Details and flaw specifications for mock-up PQ-31-DM-05 are provided in Figure 3.2 and Table 3.1, while similar information for mock-up PQ-31-DM-10 is shown in Figure 3.3 and Table 3.2, respectively. The parent and weld materials in the mock-ups that simulate the steam generator nozzle DMW tapered configuration include a SA 508 carbon steel (CS) nozzle, Alloy 82/182 weld and butter, and a stainless steel (SS) safe-end. On the carbon steel side, the OD thickness dimension is 106.4 cm (41.9 in.) and on the safe-end side, the OD thickness dimension is 95.48 cm (37.59 in.) as a result of the 11° OD taper. These mock-ups are referred to as DM-05 and DM-10 throughout the body of this TLR.

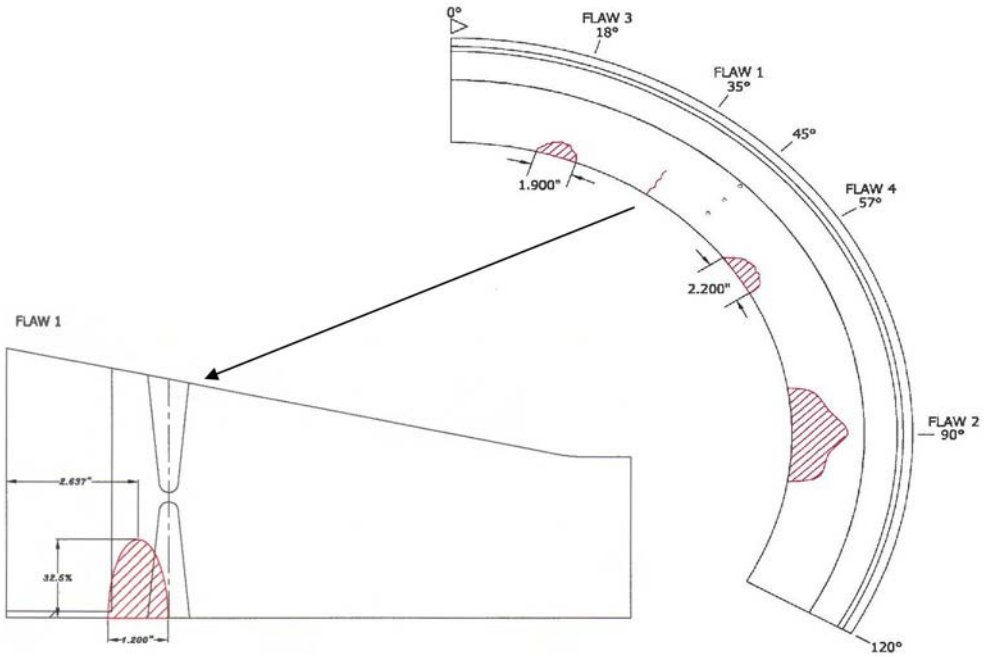

Figure 3.2. NAPS-1 Steam Generator Nozzle Mock-up PQ-31-DM-05 (EPRI 2009)

Table 3.1. Flaw Information for PQ-31-DM-05 (EPRI 2009)

Units: mm

Flaw No.	Flaw					End Ref. to			Location		OD to ID Thickness (T)
	Type	Orient.	Length	Depth Height	Depth % of T	Flaw CL	Flaw Tip	Flaw Base	Circ.	Deg.	
1	Crack	Axial	30.5	40.6	32.5%	67.0	N/A	N/A	291.5	35°	125.0
2	Crack	Circ	127.3	62.0	49.6%	N/A	64.7	61.4	749.5	90°	125.0
3	Crack	Circ	48.3	20.8	15%	N/A	63.1	61.2	167.3	18°	138.3
4	Crack	Circ	55.9	23.7	17%	N/A	63.8	63.1	529.9	57°	138.3

Units: inches

Flaw No.	Flaw					End Ref. to			Location		OD to ID Thickness (T)
	Type	Orient.	Length	Depth Height	Depth % of T	Flaw CL	Flaw Tip	Flaw Base	Circ.	Deg.	
1	Crack	Axial	1.20	1.60	32.5%	2.64	N/A	N/A	11.48	35°	4.92
2	Crack	Circ	5.01	2.44	49.6%	N/A	2.55	2.42	29.51	90°	4.92
3	Crack	Circ	1.90	0.82	15%	N/A	2.49	2.41	6.59	18°	5.44
4	Crack	Circ	2.20	0.93	17%	N/A	2.51	2.49	20.86	57°	5.44

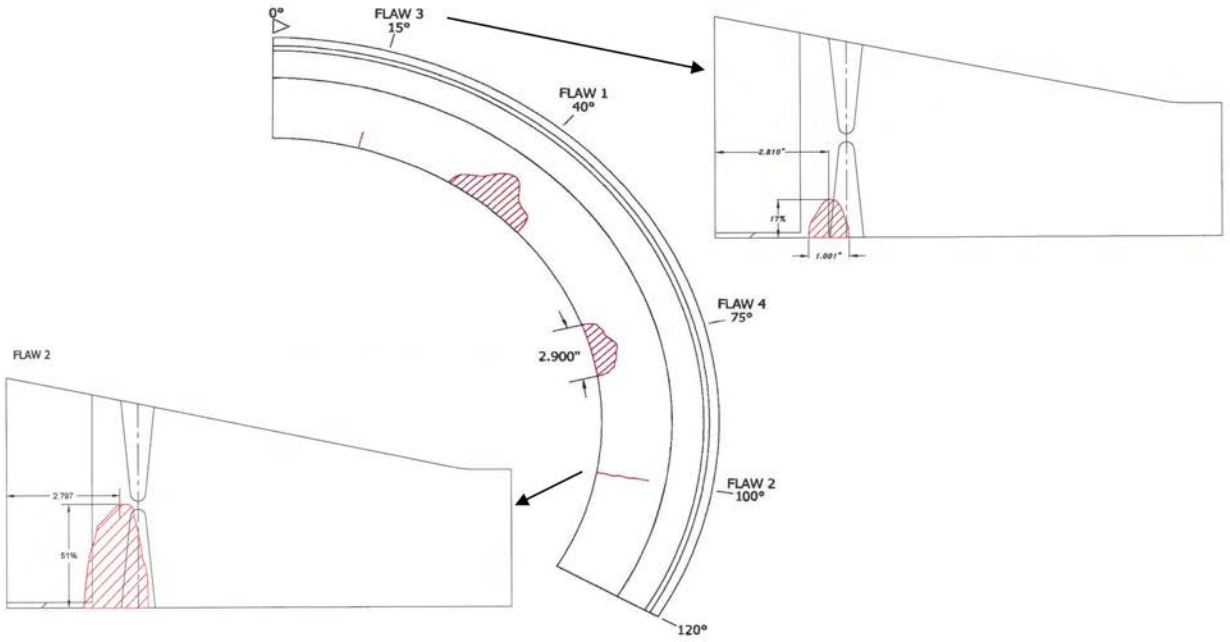

Figure 3.3. NAPS-1 Steam Generator Nozzle Mock-up PQ-31-DM-10 (EPRI 2009)

Table 3.2. Flaw Information for PQ-31-DM-10 (EPRI 2009)

Units: mm

Flaw No.	Flaw					End Ref. to			Location		OD to ID Thickness (T)
	Type	Orient.	Length	Depth Height	Depth % of T	Flaw CL	Flaw Tip	Flaw Base	Circ.	Deg.	
1	Crack	Circ	108.0	53.0	42%	N/A	69.9	62.2	365.7	40°	125.0
2	Crack	Axial	35.0	63.1	51%	71.0	N/A	N/A	910.5	100°	125.0
3	Crack	Axial	25.4	23.9	17%	71.4	N/A	N/A	139.4	15°	139.4
4	Crack	Circ	73.7	32.1	23%	N/A	66.8	66.9	697.2	75°	138.6

Units: inches

Flaw No.	Flaw					End Ref. to			Location		OD to ID Thickness (T)
	Type	Orient.	Length	Depth Height	Depth % of T	Flaw CL	Flaw Tip	Flaw Base	Circ.	Deg.	
1	Crack	Circ	4.25	2.09	42%	N/A	2.75	2.45	14.40	40°	4.92
2	Crack	Axial	1.38	2.49	51%	2.80	N/A	N/A	35.85	100°	4.92
3	Crack	Axial	1.00	0.94	17%	2.81	N/A	N/A	5.49	15°	5.49
4	Crack	Circ	2.90	1.26	23%	N/A	2.63	2.63	27.45	75°	5.46

4.0 Initial Technical Review and Plant Visit Summary

4.1 Observations from North Anna NPS Visit

On May 2, 2012, two PNNL personnel accompanied a representative from the NRC RES on a site visit to NAPS-1. Collectively, this team represented over 75 years of ultrasonic testing experience in relation to complex weld materials and geometries. The purpose of the visit was to obtain first-hand information, using the licensee's tandem UT probes, cables, and ultrasonic instrument, on simulated flaws in the licensee DMW mock-ups used to qualify the manual conventional, non-encoded technique. This equipment included a GE-IT USN60SW, a portable, digitally controlled UT instrument typical of those employed by industry for manual examinations, and coaxial-type cabling that was a standard 2 m (~6 ft) in length. The probes are described in Section 5.0.

The licensee's mock-ups were fabricated with implanted thermal fatigue cracks simulating PWSCC, as opposed to hot iso-statically pressed (HiP) notches, as stated in TJ IR-2009-358. Each mock-up represents an approximate 120-degree segment of DMW matching the configuration of the North Anna steam generator inlet pipe-to-nozzle weld, including the 11-degree OD taper on the safe end, DMW, and carbon steel nozzle. Figure 4.1 shows a photograph of one of the NAPS-1 mock-ups (Section 3.0 of this report contains a detailed listing of flaws and geometries for the mock-ups).

Figure 4.1. NAPS-1 DMW Mock-up

4.1.1 UT Observations for Mock-up DM-05

This mock-up has one axial flaw that is reported to be approximately 32% in through-wall depth. The flaw was ultrasonically located in near proximity to the side-drilled holes (SDHs) with the "LR" probe at a 2:1 signal-to-noise ratio (SNR). This flaw was also detected in the opposite scan direction with the "RR" probe, but with much less than a 2:1 SNR. Several other mid-to-upper wall ultrasonic responses were observed along the weld length; these are potentially welding fabrication or, based on the location detected, implantation artifacts from circumferentially oriented flaws in the mock-up. The presence of these "spurious indications" in near vicinity to axial flaws is somewhat unusual for a demonstration mock-up and makes manual UT detection more challenging, even when the locations of the targeted axial flaws are known. Figure 4.2 provides an example of the A-scan results showing typical mid-wall indications. Figures 4.3 through 4.6 provide additional pictorial support of the discussion in this section.

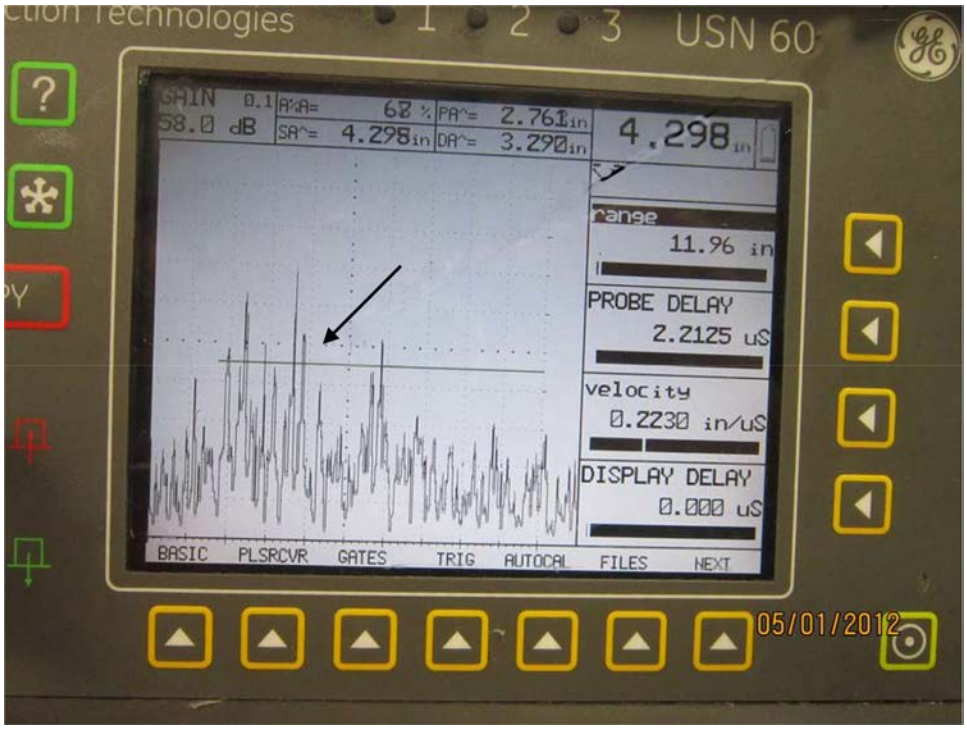

Figure 4.2. Mid-wall Fabrication Flaws or Implantation Artifacts Detected in NAPS-1 Mock-ups (as indicated by the arrow)

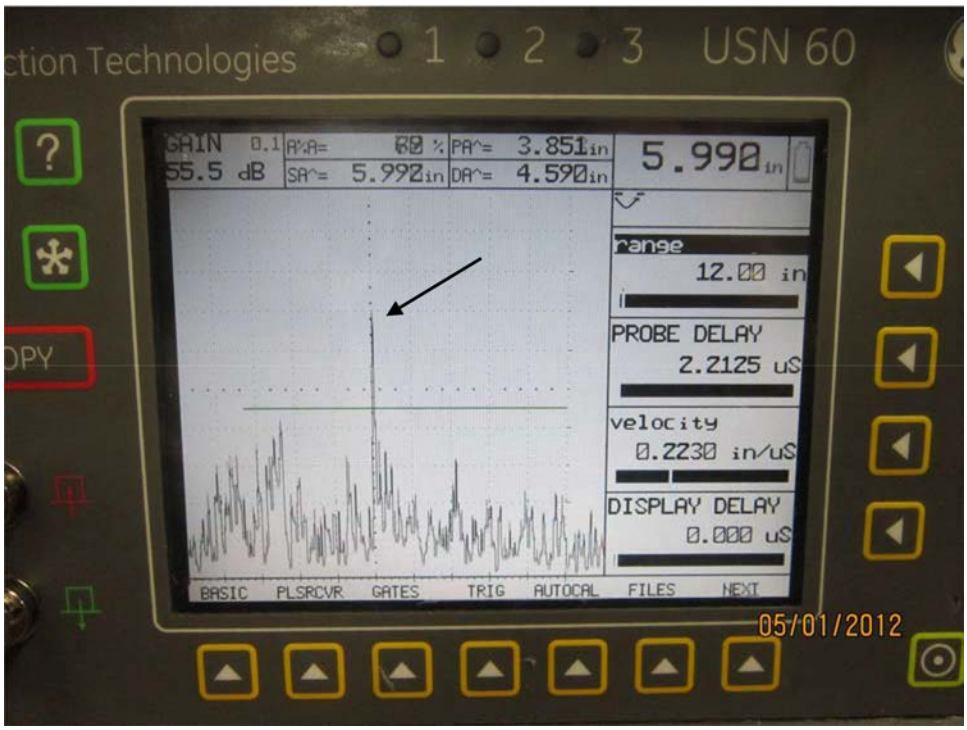

Figure 4.3. DM-05 32% Through-Wall Axial Flaw with LR Probe

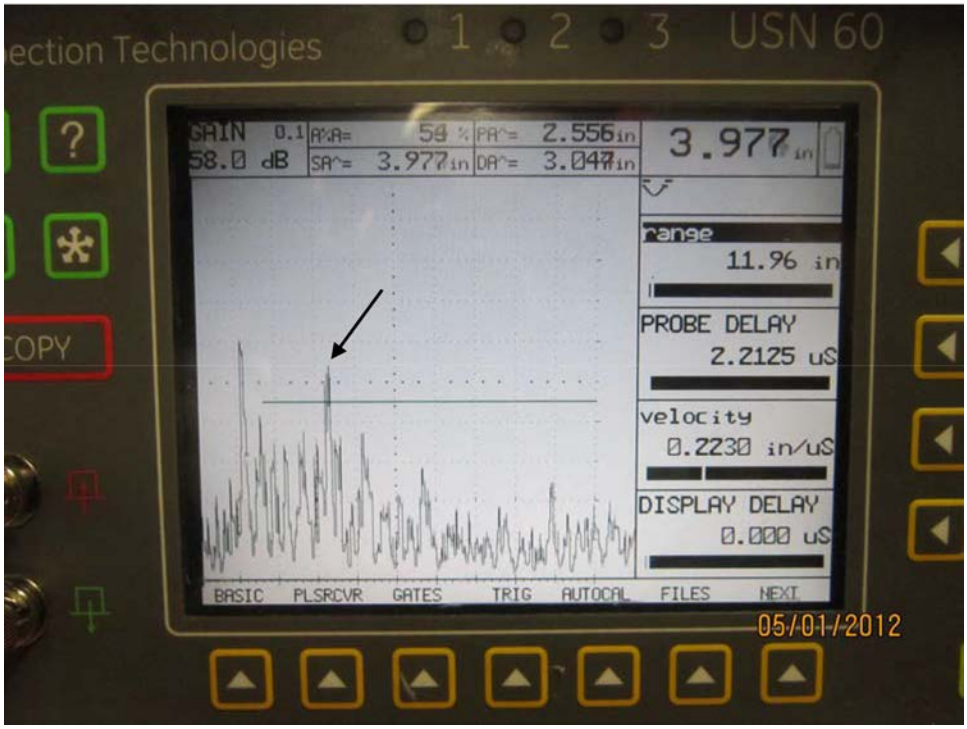

Figure 4.4. DM-05 Fabrication/Implantation Flaws

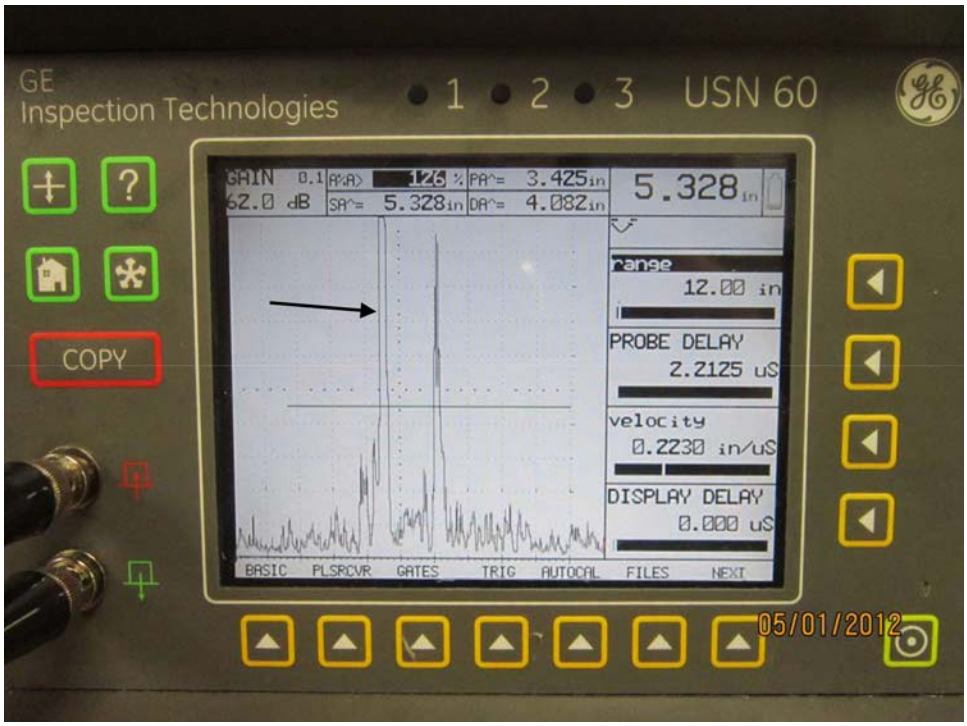

Figure 4.5. DM-05 End-of-Block through Safe End

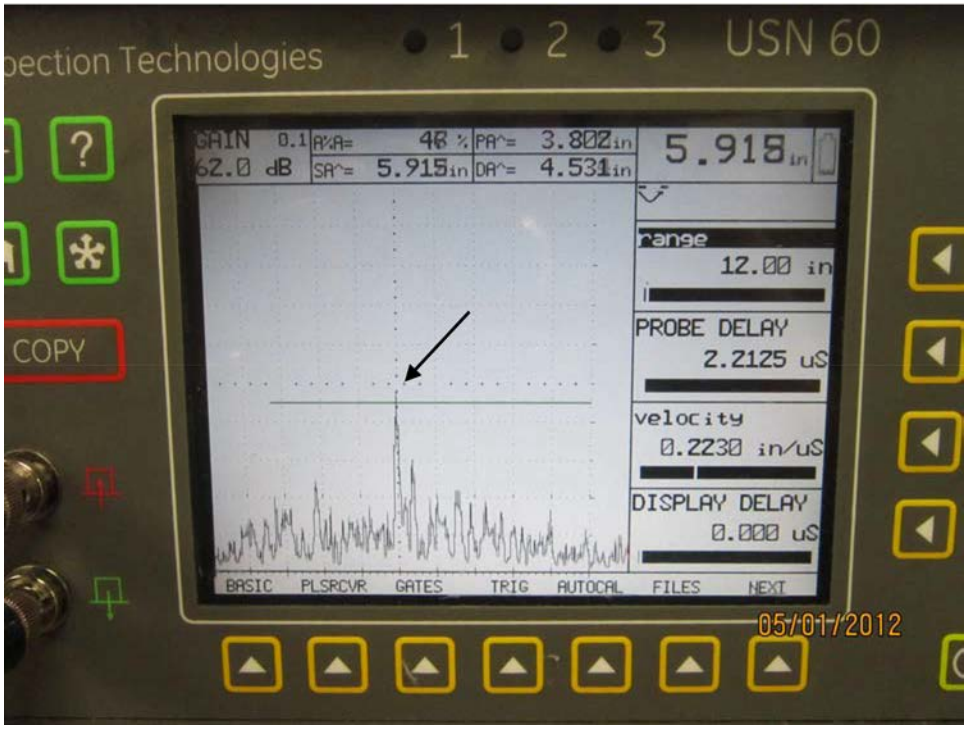

Figure 4.6. DM-05 End-of-Block through Weld

The end-of-block response from the mock-up, which represents a 100% through-wall smooth reflecting surface, was very easy to detect when scanning from the wrought safe end, but exhibited a significantly lower response when scanning through the weld material. In addition, the UT response from the end-of-block appeared to be slightly shifted out in time, indicating that the weld microstructure may be re-directing the primary sound beam "upward" or at a higher inspection angle. There was a noticeable difference in sensitivity between the LR and RR tandem probes—this was on the order of 4 to 6 dB—and each set of probes exhibited a high-pitched "whining" sound. It should be noted that this repetitive "whining" noise occurred while exciting the probes with the USN60 in the "High" square-wave mode setting (while at North Anna and during assessments at PNNL). The USN60 contains two square wave mode pulser voltage settings – high and low. The USN60 low voltage setting was not applied, as this evaluation was aimed at assessing the field operation at NAPS-1. However, when lower voltage settings were subsequently applied to the tandem probes using instrumentation at PNNL, no audible "whine" was observed.

4.1.2 UT Observations for Mock-up DM-10

Two axial flaws were detectable with the LR probe (less so with RR), and the SNRs were poor. Each pair of tandem probes required careful manipulation (skewing) to approach a SNR of 2:1. Many larger fabrication/ implantation artifact responses were observed in DM-10 in contrast to those observed in DM-05; these were also found in the near vicinity of the axial flaw locations. The end-of-block response appeared somewhat higher in amplitude through the weld, which could indicate that the weld microstructure varies between DM-05 and DM-10. Figures 4.7 through 4.9 provide additional pictorial support of the discussion in this section.

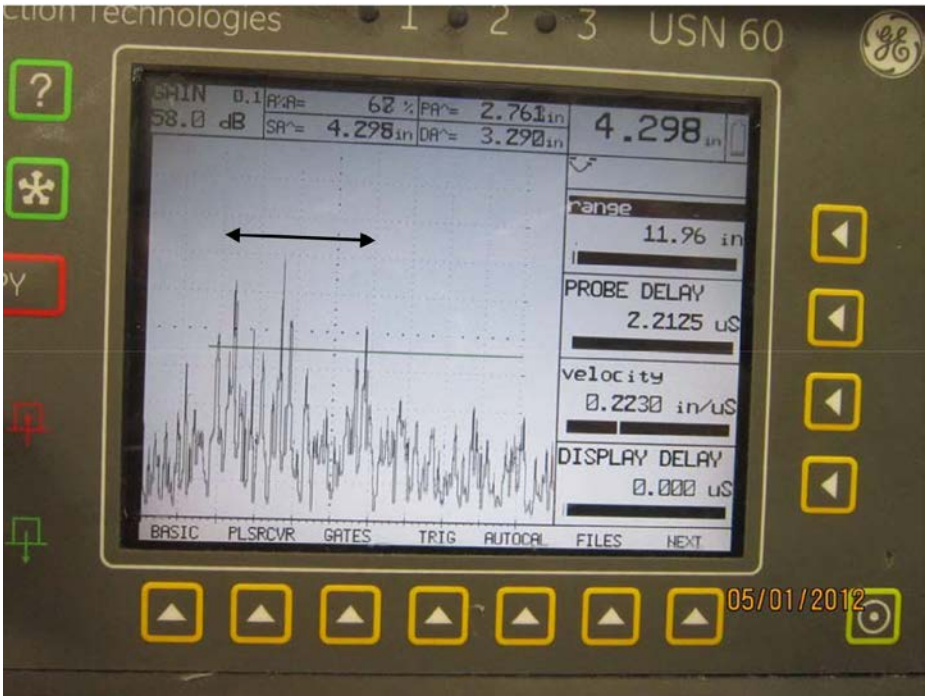

Figure 4.7. Assumed DM-10 Fabrication/Implantation Flaws (shown within time base depicted by arrows)

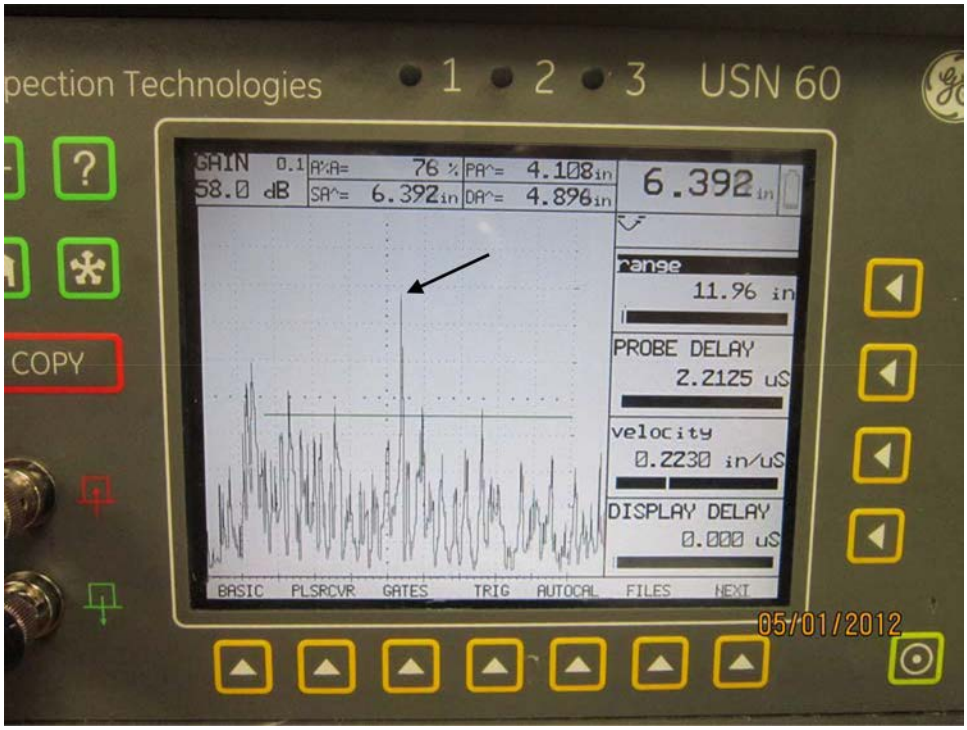

Figure 4.8. Assumed DM-10 17% Through-Wall Axial Flaw with LR Probe

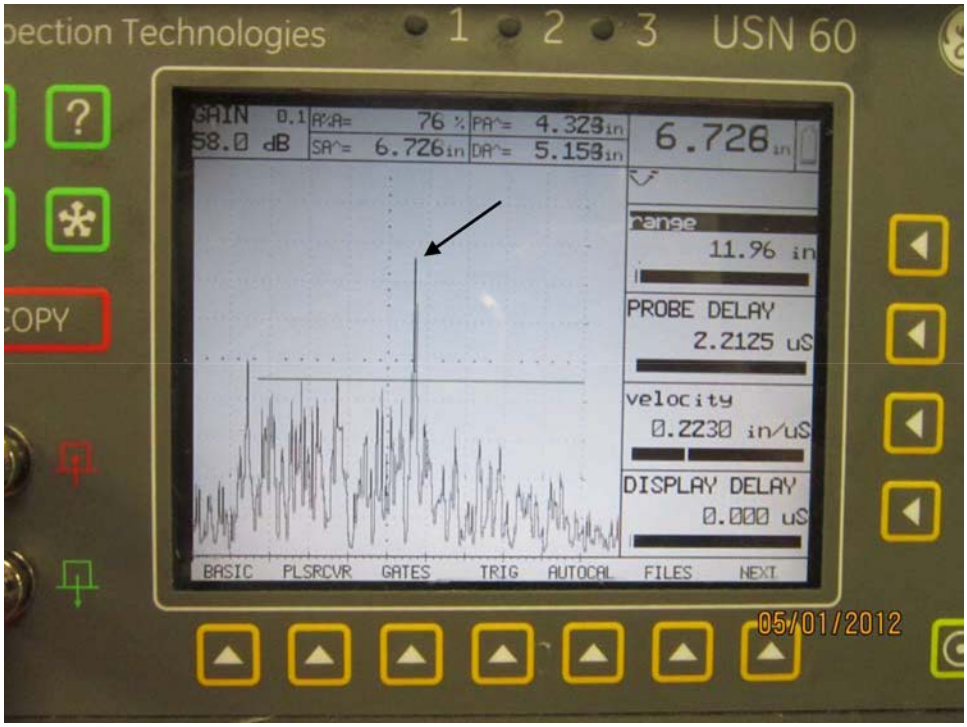

Figure 4.9. Assumed DM-10 51% Through-Wall Axial Flaw with LR Probe

As a general observation, one would expect fewer inadvertent fabrication flaw, or implantation artifact, signal responses to be present. The UT responses from these imperfections impede detection and characterization of the axial flaws as cracks. Based on the site observations using the tandem probe configurations, there are many transient indications detected on the NAPS-1 mock-ups that interfere with targeted flaws; this makes it especially difficult for one to unequivocally determine the effectiveness of the inspection system to detect cracks. The placement of the axial flaws, in relative proximity to the locations of the circumferential flaws in these mock-ups results in challenging detection conditions because of implantation or fabrication artifacts.

Section XI, Appendix VIII, of the ASME Code, does not address site-specific mock-ups. The industry position on the use of a site-specific process is that the procedure and techniques have been previously qualified through PDI, and that the site-specific process is merely a transfer of the procedure to a site-specific configuration. Further, the site-specific process is used to address configuration variations, search unit, and/or scan parameters that need to be modified in order to provide the best examination process for the unique conditions. The licensee determines the quantity of flaws needed in a mock-up. Guidance is provided in a PDI document entitled, "Mock-Up Criteria for Dissimilar Metal Welds and Weld Overlays." Revision B of this document, dated June 27, 2011, was in effect at the time that the subject NAPS-1 examinations were performed. The ability of these mock-ups to adequately represent field conditions, materials, weldments, and geometrical/metallurgical features from the standpoint of ultrasonic signal responses is the focus of Section 6.0 of this report.

4.2 Assessment of EPRI Technical Justification

A review was performed on several documents that are related to the inspection of the NAPS-1 steam generator nozzle dissimilar metal weld configuration. The documents reviewed included *Technical Justification for the Acceptance of Ultrasonic Examination Demonstration Results on North Anna Steam Generator Nozzle Dissimilar Metal Weld Configurations with PDI-UT-10, Rev. C* (IR-2009-358) (EPRI 2009) and *Rev. E* (EPRI 2010); *Generic Procedure for the Ultrasonic Examination of Dissimilar Metal Welds, Rev. C* (EPRI 2006); and *Performance Demonstration Initiative (PDI) - Dissimilar Metal Weld Mock-up Criteria Rev. A* (EPRI 2004).

ASME Section XI, Appendix VIII, paragraph VIII-3140, states "When a change in an examination procedure causes an essential variable to exceed a qualified range, the examination procedure shall be re-qualified for the revised range." Furthermore, ASME Section XI, Appendix VIII, Supplement 10, Paragraph 4.0(d), requires that in order to qualify new essential variables, at least one personnel performance demonstration set is needed. The abstract and introduction of TJ IR-2009-358 (EPRI 2009) stated that site-specific mock-ups are used to *optimize* certain inspection variables and to demonstrate the effectiveness of the examination for the site-specific geometry. With regard to the review of the 2009 TJ as implemented at NAPS-1, it was established that the guidance did not prohibit the following essential variables to be revised, or modified:

- Alternative search unit angles
- Element size, focal depths, and contours of the search units
- Selection of compound angles to accommodate unique configurations (tapered inspection surfaces)
- Adjustment to scan patterns to compensate for limited access

- Other essential inspection variables as required.

On March 18, 2013, the Chairman of the industry's NDE Integration Committee, made a presentation at a public meeting of the NRC and the industry NDE Improvement Focus Group (NIFG), indicating that the guidance had been revised, and the use of site-specific process to change a previously qualified essential variable was not allowed. This was addressed through Revision C, dated December 12, 2012, of the PDI guidance document entitled, "Site Specific Configuration Mockup Requirements for Dissimilar Metal Welds."

In Sections 4, 5, and 6 of TJ IR-2009-358, it is stated several times that changes in refracted angles were used to compensate for the NAPS-1, 11-degree OD taper, but no modeling results or other calculations were included to support the position that ID impingement angles remain the same as those demonstrated during the original PDI qualification process. In addition, it would seem prudent to address the transducer aperture (overall size) at the frequency used so that one could confidently state that sufficient sound field energies would be present in the component to adequately insonify and detect flaws. This is a critical point and modeling results for the sound fields that were originally demonstrated along with those for the substituted transducers need to be presented in order to begin to build a case that ensures inspection performance has not been reduced or compromised. Yet, this type of basic acoustic information was not described in TJ IR-2009-358.

In Section 7 of TJ IR-2009-358, Table 7-1 and criteria paragraph 4.7.7, it was stated, "This mock-up was not commercially dedicated." The meaning of this statement is unclear. Perhaps it is a reference to paragraph 4.2.7 in Revision B of the PDI mock-up criteria document which states that mock-ups shall be manufactured in accordance with Quality Assurance programs that meet certain attributes. In the TJ IR-2009-358, Section 8, it was stated, "For circumferential scans, the examinations can be performed from both nozzle and safe-end sides including the attachment weld area." However, use of the tandem probe configuration at NAPS-1 made this problematic. This is because of the number of relevant flaws (axial) in the mock-ups for conducting the non-blind demonstration. TJ IR-2009-358 stated that two of the three axial flaws that exist in the NAPS-1 mock-ups are "out of range" as specified in PDI Dissimilar Metal Weld Mock-up Criteria, Rev. A and are for "information only." This implies that only one axial mock-up flaw could be used to assess inspection technique validity, because two of the three axial flaws are essentially "out-of-compliance" with the mock-up criteria; this could significantly impact the rigor of the demonstration for axial flaw detection.

In Section 9 of TJ IR-2009-358, it was stated under the heading of Ultrasonic Hardware, Cabling and Transducers, that no previous transducer and ultrasonic equipment combination exist. However, one would think that some combination of these items had been demonstrated at PDI for initially meeting Supplement 10 and now an equipment substitution is being proposed to compensate for the 11-degree taper configuration. The statement in TJ IR-2009-358 is not understood and needs further explanation.

Finally, Section 11 of TJ IR-2009-358 stated that, "The parameters for the design and fabrication of these site-specific mock-ups are consistent with ASME Appendix VIII requirements." This statement is misleading, in that the NAPS-1 mock-ups (as a set) do not actually conform to the requirements listed in ASME Code, Appendix VIII, Supplement 10. For instance, there are only eight flaws in the NAPS-1 set as compared to the minimum ten flaws required by Supplement 10. In another example, Supplement 10, Paragraph 2.1(b) stated "Specimens shall have sufficient volume to minimize spurious indications that may interfere with the interpretation process." This is not the case, as is described in the previous section

of this report describing observations made during the North Anna site visit. Also, Section 11 of TJ IR-2009-358 reported that all implanted flaws were successfully detected with a 2:1 SNR or better during the on-site open demonstration. The 2:1 SNR value is highly questionable, based on physical measurements conducted on-site by PNNL and NRC staff on the actual NAPS-1 mock-ups, probes, and inspection system. This issue is further explored in the next section of this report.

5.0 Description and Performance Evaluation of the Tandem Probes

A description of the tandem probes used in the NAPS-1 ISI is described in Section 5.1 followed by a discussion on the modeled sound field in Section 5.2. The effects of two square wave pulsers used to excite the tandem probes were investigated by mapping the sound fields produced and evaluating responses from a standard notch reflector. These results are presented in Sections 5.3 and 5.4, respectively. Lastly, the tandem probes' responses from the mock-ups are assessed from laboratory-acquired encoded data via both image and A-scan analyses so that the data may be compared to manual non-encoded data. These mock-up data were acquired with a single pulser with results discussed in Section 5.5.

5.1 Tandem Probe Configuration

As outlined in TJ IR-2009-358, the manual UT method included the use of a 1.0-MHz pitch-catch tandem (front-rear configuration) set of probes, applied during circumferential scanning for detection of axial flaws located in/near the weld region. The probes, manufactured by Sigma Transducers (Kennewick, Washington), were fabricated with the intent to generate an initial refracted longitudinal sound wave at a 30-degree angle into the specimen. The effective *refracted angle* produced by the probe is not to be interchanged with the *ID impingement angle* of the sound field. When attempting to detect axially oriented, ID surfacing-breaking planar flaws, there is a theoretical optimum angle of ID impingement that should be used to ensure effective corner-trapped flaw responses. The desired ID impingement should be within a critical range of angles [below which (too steep) the sound beam would simply reflect off the ID surface, not impacting the surface corner-breaking region of the flaw, and above which (too shallow) sound would not impact the ID surface but simply continue to travel farther around the circumference of the pipe]. An optimum angular value can be determined by the following relationship:

$$\sin(\alpha) = \frac{\mathrm{OD}}{\mathrm{ID}} \sin(\beta) \tag{5.1}$$

where: α is the ID impingement angle,
β is the initial refracted angle from the probe on the OD surface, and
OD/ID is the ratio of the outside-to-inside pipe diameters.

A graphical depiction of this relationship is shown in Figure 5.1. According to the industry's Performance Demonstration Initiative (PDI) generic DMW ultrasonic procedure 10 (PDI-UT-10), the optimum ID impingement angle (α) for detecting PWSCC on the subject welds is within the range of 55-60 degrees (this range attempts to account for nominal diameter deviations). The transmitted refracted angle (β) at 30 degrees theoretically produces an ID impingement angle of 41 degrees at the flaw, which is not in agreement with DMW PDI-UT-10 for recommended optimum ID impingement angles (i.e., a transmitted refracted angle at 40 degrees would theoretically produce an ID impingement angle of 58 degrees at the flaw, in accordance with PDI-UT-10). For clarity in the remainder of this report, the transmitted refracted angle and associated ID impingement angle for circumferential scans to detect axial

flaws will be listed with the following convention: refracted angle (impingement angle); for example, 30(41) degrees.

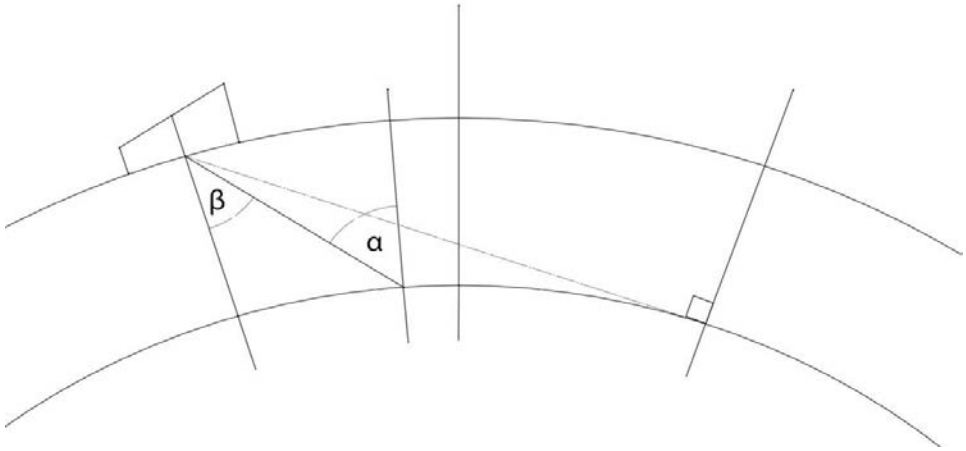

Figure 5.1. Representation of Solution for ID Impingement Angle

The probe sets have wedges with roof angles of 4.66-degrees to re-direct the sound beams laterally (in the axial direction on the pipe) to accommodate the 11-degree OD taper on the weld. The probe sets are designated as "LR" and "RR" relating to the scan direction; LR for left, or counterclockwise (CCW), if facing the nozzle from the pipe side, and RR for right, or clockwise (CW) as viewed from the pipe side. Sigma Transducers was contacted, and they provided details of the integral probe/wedge configurations, which can be found in Table 5.1. The information shown in Table 5.1 is for the LR tandem probe (serial number 2887-07001), and only this direction has been modeled; it is assumed the RR probe set (serial number 2886-07001 would produce a mirror image if simulated.

The tandem pitch-catch probes shown in Figure 5.2 were designed to inspect steam generator nozzle DMW welds with 11-degree OD tapers as found at NAPS-1. The two elements in these probes are placed in a front/back arrangement with a roof angle to account for the 11-degree specimen taper. The integral wedge and probe configuration are shown in Figure 5.3 for the LR (or CCW) probe. The beam angle is specified as being 30(41) degrees, and sound field modeling of the tandem probes confirmed these values (refer to the next section). As previously stated, the 41-degree impingement angle falls outside of the optimum range of 55 to 60 degrees that is listed in PDI-UT-10.

Table 5.1. Tandem Probe Description

Design	2007 Integral Probe/Wedge
Manufacturer	Sigma Transducers
Frequency	1.0 MHz
Bandwidth	52% at −6 dB
Damping material	Backed, **not** inductively tuned
Angle/mode	40-degree L
Examination type	Circumferential scan
Element size	2× (25×25) mm [2× (1.0×1.0) in.]
Pulser-receiver	Front-transmit; rear-receive
Wedge material	Low 10
Wedge velocity	2449 m/s (0.964 in/μs)
Separation	0.76-mm (30-mil) cork material
Contour	533.4-mm (21-in.) radius
Front Wedge	
Length	25.65 mm (1.01 in.)
Width	25.4 mm (1.0 in.)
Height	4.72-mm (0.186-in.) low point
Incident angle	9.0 degrees
Roof angle	4.66 degrees
Back Wedge	
Length	27.84 mm (1.096 in.)
Width	25.4 mm (1.0 in.)
Height	4.55-mm (0.179-in.) low point
Incident angle	13.707 degrees
Roof angle	4.66 degrees

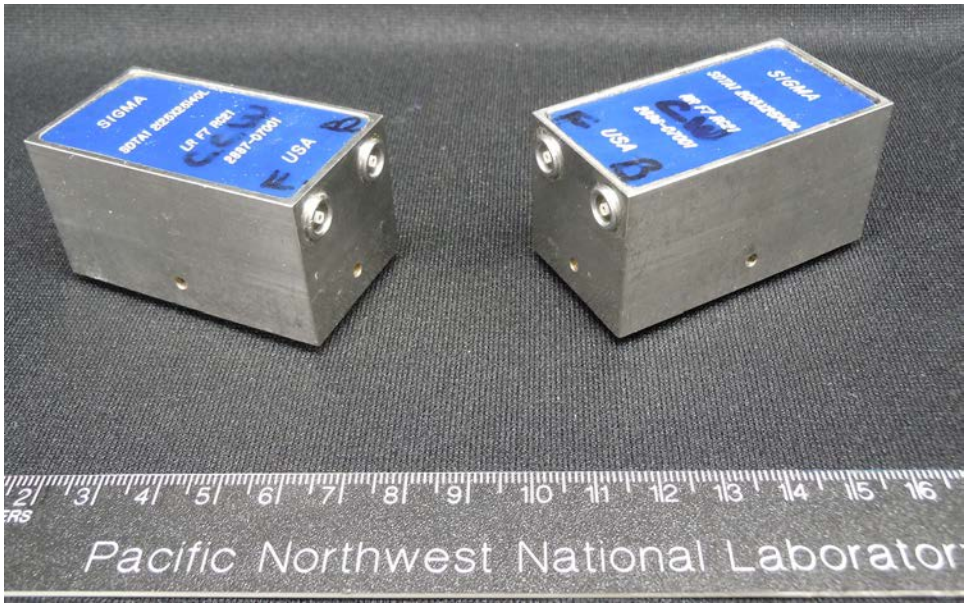

Figure 5.2. The LR and RR Tandem Probes Used for Inspection of the North Anna Mock-ups

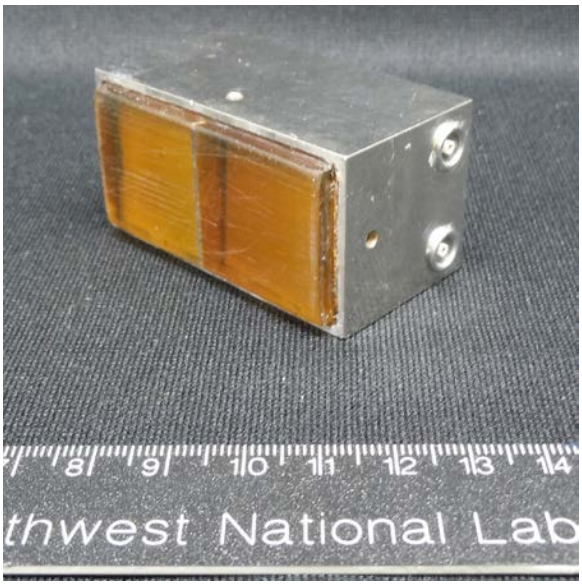

Figure 5.3. A View of the Integral Wedge on the LR Tandem Probe

5.2 Sound Field Simulations for the Tandem Probes

The tandem probe, shown in a circumferential scanning orientation for the detection of axial flaws, is illustrated in Figure 5.4. The integral tandem probe is mounted on the CAD specimen near the weld location with the right image depicting the front and back beams (crossover) intersecting in the specimen through-wall dimension.

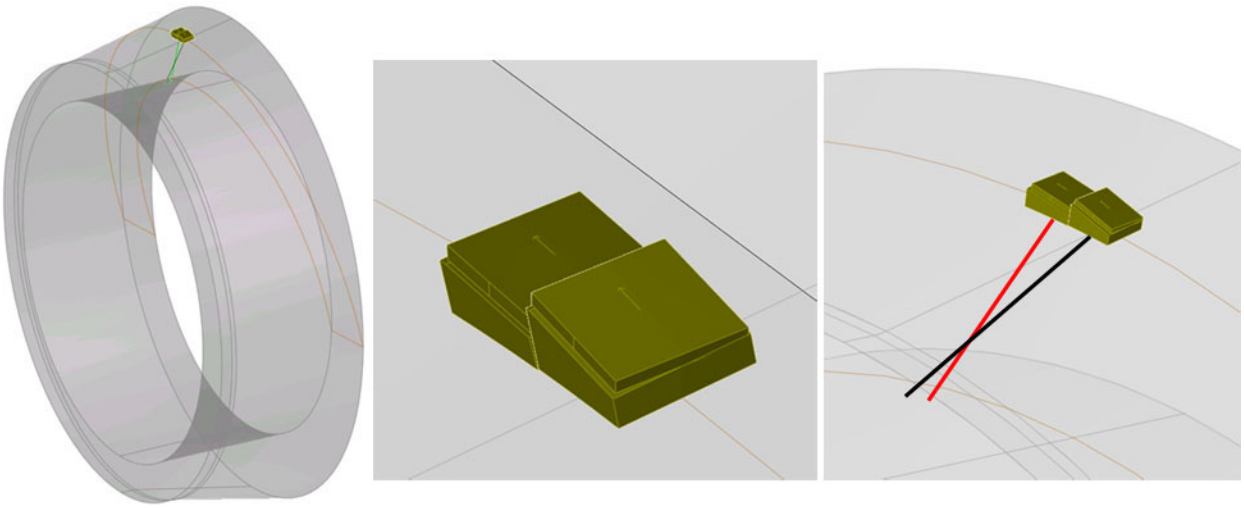

Figure 5.4. CAD Drawing of Tandem Probe Setup on DMW Specimen

Sound field simulations showing the acoustic beam density generated by the tandem probe as modeled with the CIVA 10.1 software suite are displayed in Figure 5.5. CIVA was chosen for these simulations as this software platform supports a tandem probe configuration whereas UltraVision 3 [the software chosen to depict theoretical PA transmit-receive (TR) probe sound fields] does not as yet have this capability (see Section 6.0 of this report). As depicted, simulated sound field energy increases from blue to red. The left image shows an unfiltered sound beam in the specimen; OD and ID surface locations are indicated. The middle image has a −6 dB filter (50% amplitude threshold) applied that highlights a −6 dB focal zone. The right-most image in Figure 5.5 has the same −6 dB filter applied, but without the full computational zone visible, emphasizing the insufficient extent of the −6 dB focal zone (or high intensity sound field expected to produce 2:1 signal-to-noise ratios) to reach the desired specimen ID surface region. The model indicates that this probe configuration produces refracted longitudinal mode ultrasonic energy at a transmitted angle of 30(41) degrees, with the maximum value of sound field intensity located at 44 mm (1.73 in.) from the OD along the metal path. The −6 dB focal zone length along the metal path is 83 mm (3.27 in.) or only 56% of the entire through-wall metal path. The required metal path at 30(41) degrees to reach the ID is approximately 148 mm (5.83 in.).

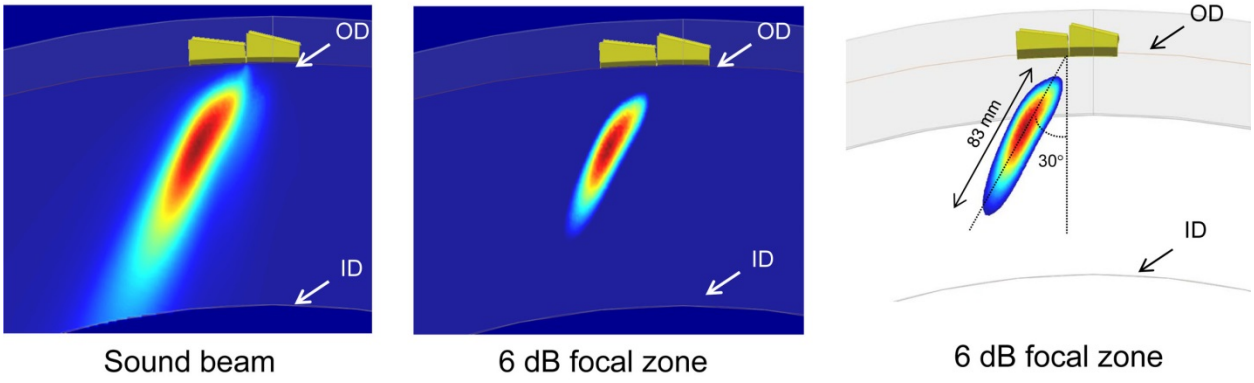

Figure 5.5. Sound Field Simulations and −6 dB Filter

By applying a −12 dB filter, the simulated sound field was projected to the specimen ID, and indicates the sound field energy to be substantially diminished in strength. A drop of 12 dB from the maximum sound intensity is a ratio of approximately 4:1. Therefore, only about 25% of the maximum beam intensity is predicted at the ID surface; this is optimistic, given the anisotropic nature of the weld microstructure. This reduced field intensity also predicts a poor signal-to-noise level for detection of ID surface-connected flaws via corner-trapped responses. These results suggest the tandem probe may potentially be suited for detection of specular or tip responses from flaws in the outer 60% of the material (which has only been modeled as a simple isotropic media), but is extremely limited for detection of ID-connected flaws in this specimen configuration.

5.3 Sound Field Mapping of the Tandem Probes

To empirically assess beam forming capability, the “RR” (or CW) and “LR” (or CCW) tandem probes were evaluated in an aluminum pipe section as two different excitation pulses were separately applied. Aluminum is a very fine-grained, homogeneous, and isotropic material in relation to these

wavelengths, so a minimally distorted sound field could be generated in the specimen, allowing one to evaluate probe and pulser effects without significant material influences being observed. The tandem probe was fixed on the OD of an approximately 82-mm (3.2-in.) thick specimen and a pinducer was raster scanned over the ID surface in an immersion setup, to collect a sound field image at the ID region. Figure 5.6 shows the assembly with the tandem probe acting as transmitter on the OD of the pipe section and the pinducer receiving probe extending from a search tube mounted on the scanner in a position under the specimen. An ID view of the pinducer is displayed in Figure 5.7 on the left side (noted by the red arrow) with the right side illustrating the pinducer holder.

The pulsers used in the inspections of the DMW in the hot and cold legs of the steam generator nozzles at NAPS-1 used USN60SW flaw detectors with the tandem probes (for axial flaw detection) and ZETEC phased-array instruments/probes for circumferentially oriented flaw scans. A USN60SW instrument was loaned to PNNL by an ISI vendor (Lambert-MacGill-Thomas Inc. – LMT), allowing a laboratory assessment of typical equipment that had been qualified through PDI and employed at NAPS-1 for the actual examinations. This loaned instrument allows square wave pulse widths in the 50- to 1000-nsec range with 10-nsec increments; thus, it can accommodate probes with center frequencies in the 10- to 0.5-MHz range. As a reference benchmark, a 1.0-MHz transducer requires a pulse-duration of 500 nsec for optimum excitation performance. As was stated in Section 4.0, during the NAPS-1 visit the probes emitted an audible high-pitched sound when pulsed; one possible cause is that the probes were being over driven in the field. The USN60SW has only two pulser drive voltage settings—low and high, with the high setting emitting excitation energy at 450 volts. The same high-pitched audible sound was noted during PNNL laboratory work when using this high setting. Although the licensee did not apply the “low” voltage setting in the field, PNNL explored the use of lower voltages on the operability of the tandem probes. In order to compare the operation of these probes in the laboratory, and for ease of data collection, PNNL elected to use a ZETEC DYNARAY Lite (DYNARAY) system for probe excitation. The DYNARAY is a standard “off-the-shelf” instrument and is being commonly used at both nuclear and non-nuclear facilities. Of particular note, when using the DYNARAY, a matched square wave at 200 volts was applied to the probes with no audible high-pitched sound being observed. For the laboratory comparative analyses, a Ritec BR-640 receiver and Gage CS-82G digitizer were employed for data acquisition; thus, only the effects of different pulsers and voltages are compared. Responses from pulsing the front element (designed to act as the transmitter) and separately pulsing the back element (designed to act as the receiver) were recorded. The data images are shown in Figure 5.8 for the CW probe and in Figure 5.9 for the CCW probe. Each image is normalized to the peak response so that a comparison of the sound field shape, size, and coherence can be visually assessed. Extremes of the color scale are red for maximum amplitude and blue for minimum amplitude. The upper images represent the back element while lower images represent the front element. Left-side images show the DYNARAY 200-volt responses and the right-side images show the USN60SW 450-volt responses.

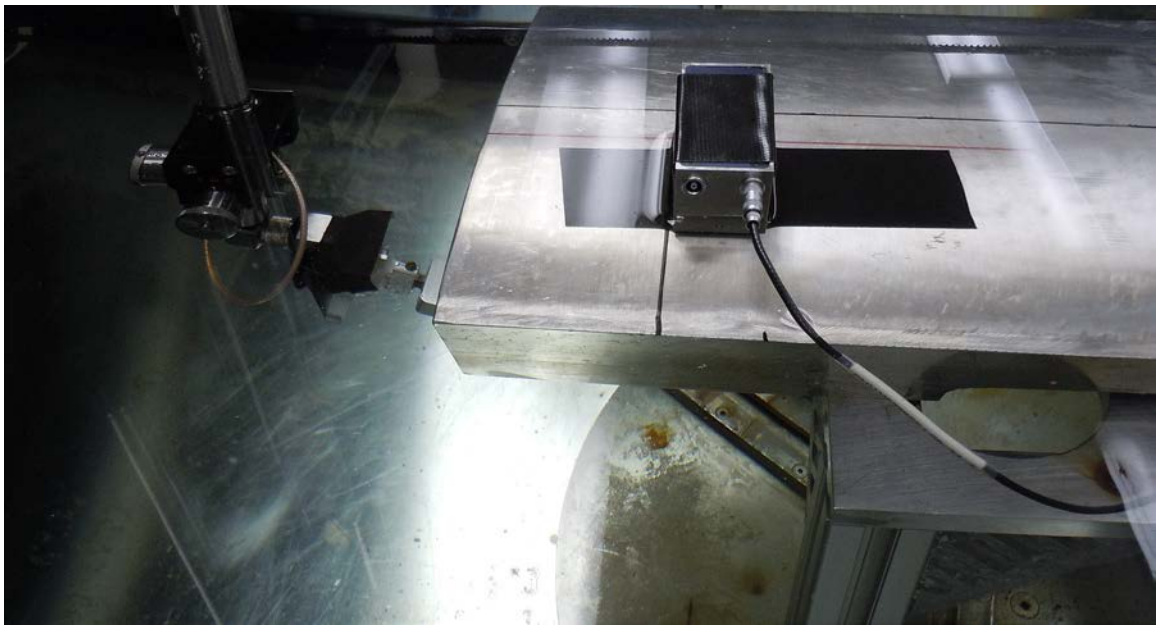

Figure 5.6. Tandem Probe Sound Field Mapping Setup in an Aluminum Pipe Section

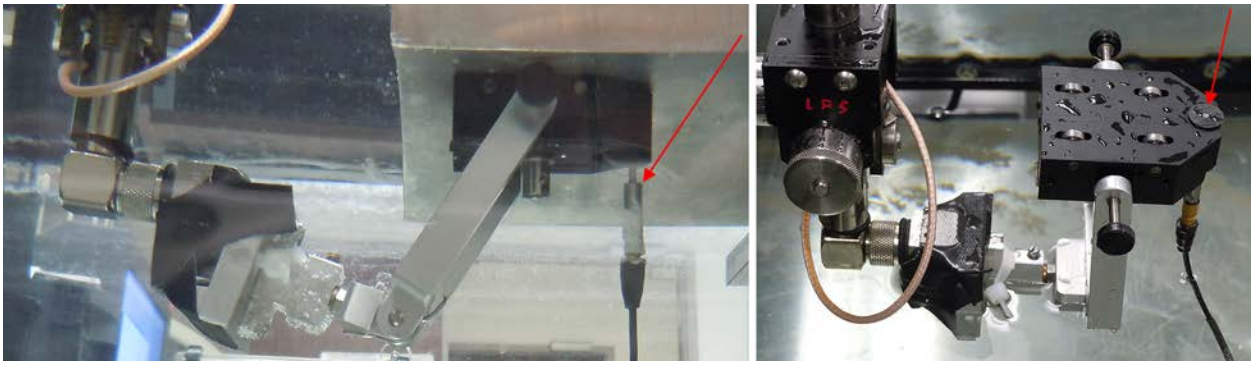

Figure 5.7. Bottom or ID View of Setup and the Receiver Pinducer on the Left and Pinducer in Holding Fixture on the Right. Red arrows point to the pinducer in each image.

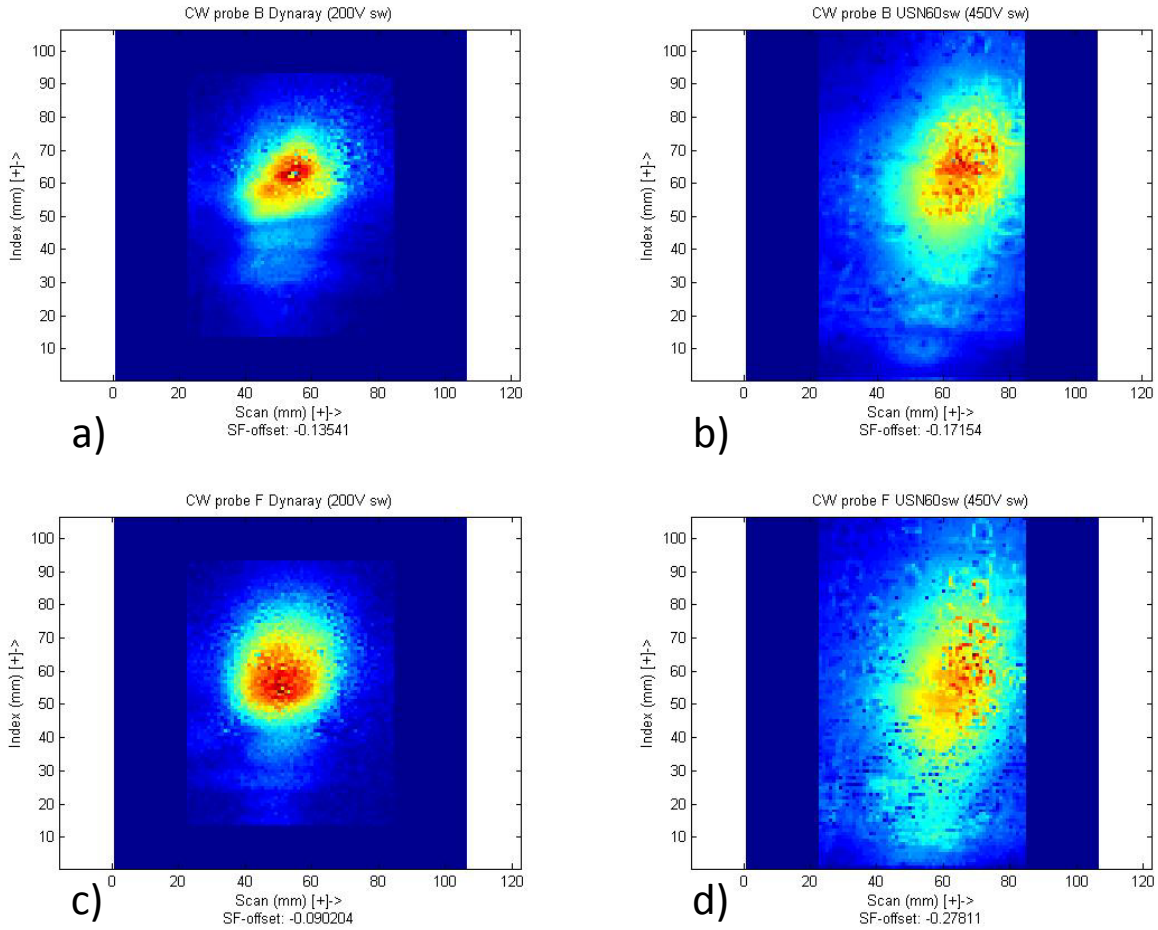

Figure 5.8. Sound Field (MatLab) Images from the CW Tandem Probe: a) back element DYNARAY square wave pulser at 200V; b) back element USN60SW square wave pulse at 450V; c) front element DYNARAY square wave pulser at 200V; d) front element USN60SW square wave pulse at 450V

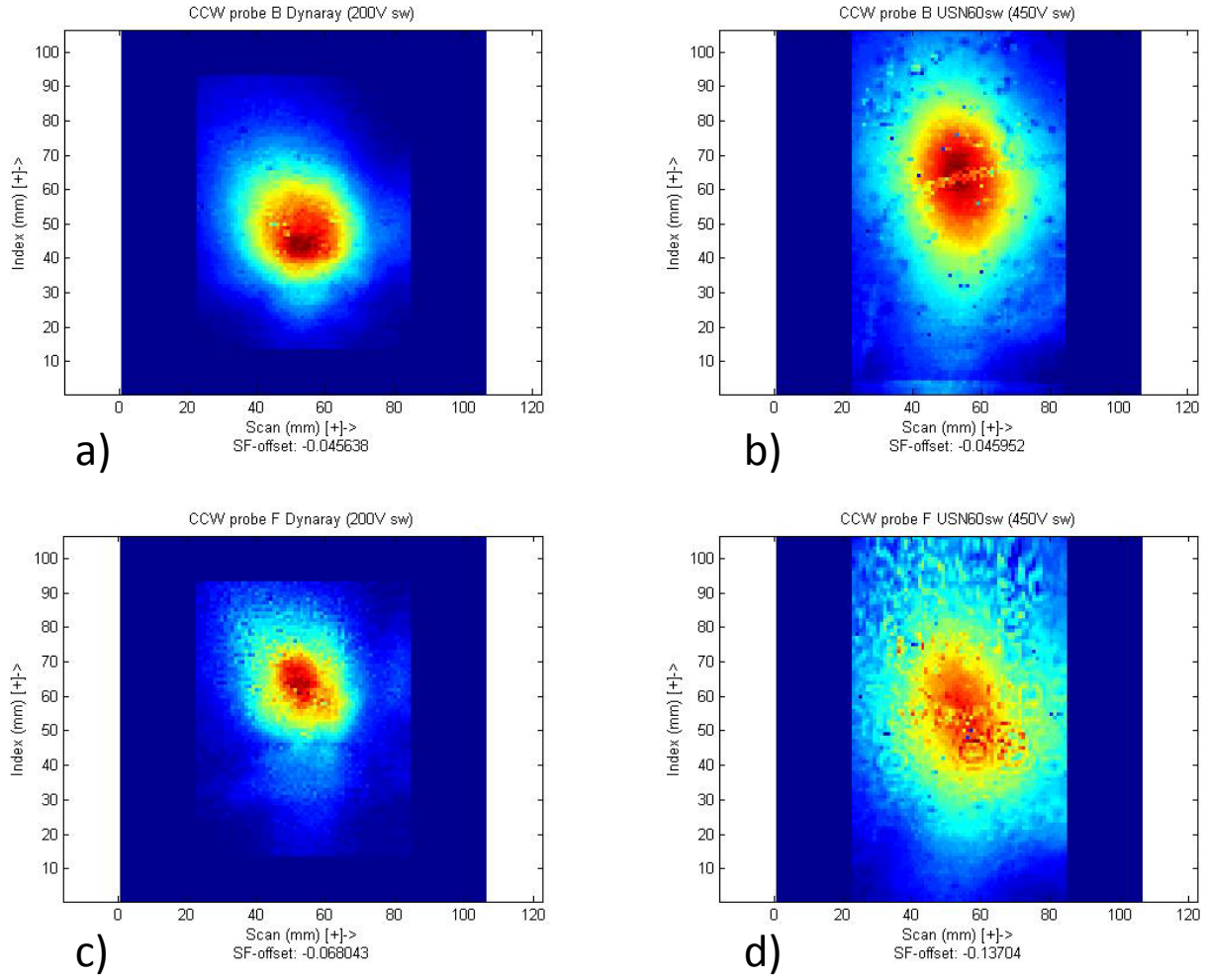

Figure 5.9. Sound Field (MatLab) Images from the CCW Tandem Probe: a) back element DYNARAY square wave pulser at 200V; b) back element USN60SW square wave pulse at 450V; c) front element DYNARAY square wave pulse at 200V; d) front element USN60SW square wave pulse at 450V

To assess the images in a quantitative sense, the beam sizes at the −6 dB level were measured using the sound field data in Figures 5.8 and 5.9. The DYNARAY and the USN60SW square waves were tuned to the same pulse duration so that the voltages of 200 and 450 could be compared. The results are listed in Table 5.2. Also listed are the ratios of the beam sizes in the scan (image horizontal) direction relative to the beam in the index (image vertical) direction. The DYNARAY pulser produces a more focused and symmetric beam in all scenarios. Symmetry variations in the DYNARAY system are as much as 17% from an ideal (ratio of 1); whereas, the USN60SW shows a deviation of up to 38%. The USN60SW beam size is approximately 20% to 2 times larger in the scan direction (horizontal) and 2 to 2.5 times greater in the index direction (vertical) than the DYNARAY beam. A metric to measure scatter is discussed in the following paragraph.

Table 5.2. Beam Spot Size at the −6 dB Level for the CW Tandem Probe in Aluminum

				Front Element			Back Element		
Probe	**Pulser**	**Voltage**	**Pulse Type**	**Scan (mm) (in.)**	**Index (mm) (in.)**	**Ratio**	**Scan (mm) (in.)**	**Index (mm) (in.)**	**Ratio**
CW	DYNARAY	200	SqWv	30.5 (1.20)	30.5 (1.20)	1.00	27.4 (1.08)	23.4 (0.92)	1.17
CW	USN60SW	450	SqWv	37.6 (1.48)	61.0 (2.40)	0.62	33.5 (1.32)	43.8 (1.72)	0.76
CCW	DYNARAY	200	SqWv	27.4 (1.08)	29.5 (1.16)	0.93	29.5 (1.16)	30.5 (1.20)	0.97
CCW	USN60SW	450	SqWv	52.8 (2.08)	77.2 (3.04)	0.68	41.7 (1.64)	63.0 (2.48)	0.66

A metric to measure scatter, or lack of spatial coherence in images from the UT beam, was applied that had previously been developed (in MatLab) for a sound field mapping study conducted on cast austenitic stainless steel material. The measure of scatter is based on the points above a user-selected threshold (70%) and calculates the difference between the current pixel value and the pixel values of all points at a selected distance away (2 pixels). These difference perimeter values for a specific pixel were averaged to give a mean difference value for the center pixel, and then all such calculated values were averaged to give one value for the entire image. For an image with low scatter, such a difference value would be small, indicating similar responses in a neighboring area. An image with a higher amount of scatter would have a large difference value, indicating many transitions in a localized area. Because a two-dimensional Gaussian image was assumed to represent an ideal sound field, the scatter difference was also calculated on an ideal Gaussian data image for comparison. The final measure of scatter for an experimental image was then determined as the difference between the ideal Gaussian image value and the experimental image value. The resulting negative values, listed in Table 5.3 for the tandem probe data, indicate more variation (scatter) than the ideal Gaussian case. Clearly, from both the images and the scatter measurements, the 200-volt square wave DYNARAY pulser produces the least amount of scatter, or conversely, the most coherent beam. On average, the scatter measurement from the four 200-volt images is −0.085 while the average for the four 450-volt images is −0.158, approximately two times greater. One possible explanation is that the 450-volt excitation is over driving the piezoelectric element in the probes. Given the poor performance of the probes, use of the less tightly formed and asymmetrical beam produced by the 450-volt square wave, rather than at 200-volts, would have served to further decrease the reliability and effectiveness of the examinations conducted at NAPS-1.

Table 5.3. Scatter Measurements for the CW Tandem Probe in Aluminum

Probe	Pulser	Excitation (volts)	Pulse Type	Front Element	Back Element
CW	DYNARAY	200	SqWv	−0.090	−0.135
CW	USN60SW	450	SqWv	−0.278	−0.172
CCW	DYNARAY	200	SqWv	−0.068	−0.046
CCW	USN60SW	450	SqWv	−0.137	−0.046

In summary, a beam mapping study on the CW tandem probe with two pulser excitations has shown:

- The 200-volt square wave DYNARAY excitation produced the most symmetric beam, given the operating parameters of the tandem probes.
- The 450-volt square wave USN60SW excitation produced a beam with a larger spot size as measured at the −6 dB points, by 20% to 2 times as great in the scan direction and 2 to 2.5 times as great in the index direction.
- A 450-volt square wave USN60SW excitation produced, on average, two times more scatter (reduced spatial coherence) in the beam.
- Efficiencies in the DYNARAY electronics allow pulsing the probe at 200 volts, and data suggest the 450-volt USN60SW pulse may by over driving the probe

5.4 DYNARAY Square Wave and USN60SW Square Wave Pulser Comparisons on a Reference Reflector

After the initial beam modeling and sound field mapping, the USN60SW unit (on loan from LMT) with square wave excitation capability was again employed to assess backscatter from a reference reflector using high and low voltage settings with the tandem probes. The study was conducted by recording the tandem CW probe response from a 20% through-wall electro-discharge machined (EDM) notch in a stainless steel (304/304L) pipe section having a 63.5-mm (2.5-in.) wall thickness. The complexities due to the taper of the mock-up and material changes in propagating from the safe-end through the weld and butter region were avoided in this simple pipe/notch reflector configuration. The same two pulser excitation scenarios were evaluated as were applied in the sound field mapping exercise; these included:

- DYNARAY square wave (200V)
- USN60SW square wave (450V)

All of the notch responses were received and recorded with the DYNARAY system. The A-scan waveforms from the notch are displayed in Figure 5.10 with the response from the DYNARAY on the left and USN60SW on the right. The peak responses were measured as 0.033 and 0.045 volts for the DYNARAY and USN60SW pulsers, respectively (an increase of 36%).

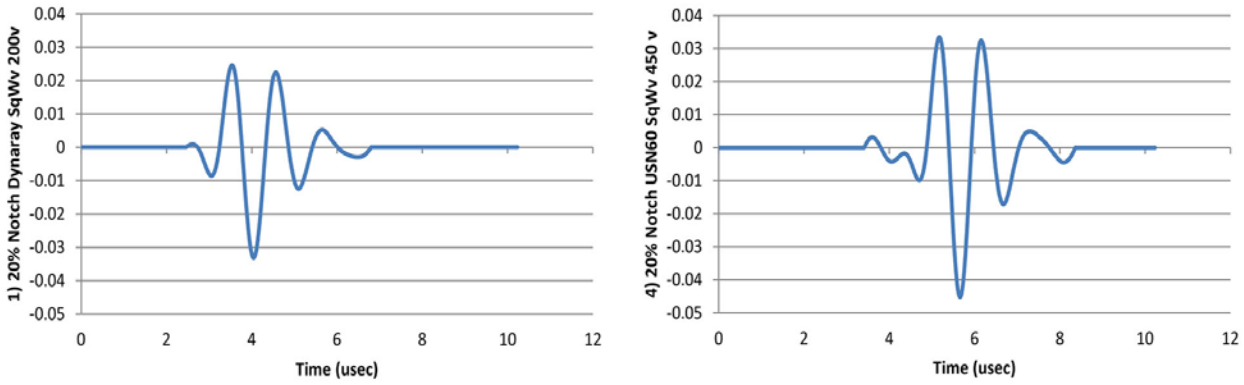

Figure 5.10. Ultrasonic Responses from a 20% Through-wall Deep Notch: DYNARAY square wave pulser at 200V on the left; USN60SW square wave pulser at 450V on the right

The frequency content of these waveforms was obtained through spectral analyses, with the results shown in Figure 5.11. As expected, the 200-volt DYNARAY response has less energy than the 450-volt USN60SW pulse. Center frequencies are similar for either pulser at 0.92 MHz for the DYNARAY system and 0.96 MHz for the USN60SW system. The bandwidth of the USN60SW pulse response was slightly greater (by 14%) at 65% as compared to the 57% bandwidth of the DYNARAY pulse response. Finally, the SNRs from the reflected notch waveforms were calculated at 22.4 and 24.2 dB for the DYNARAY and USN60SW pulsers, showing minimal to no variation. These SNRs were calculated from the A-scans and represent a peak signal to mean noise value. Peak signal to peak noise values were 8.7 and 9.6 dB for the DYNARAY and USN60SW pulsers.

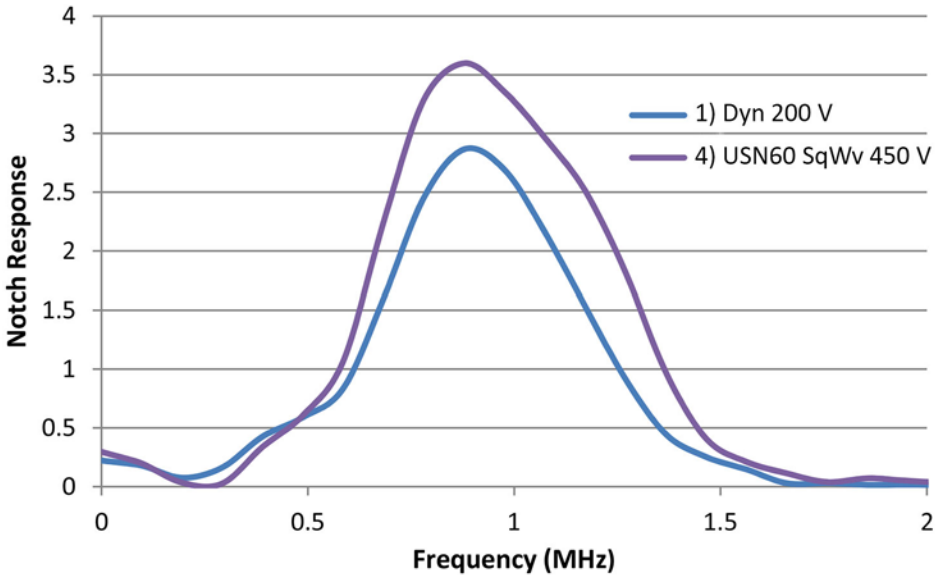

Figure 5.11. Frequency Content of the Notch Response Waveforms Obtained with Two Pulse Excitation Scenarios

In summary, the square wave pulse excitation function from the DYNARAY at 200 volts and USN60SW at 450 volts were each evaluated on the response from a 20% through-wall deep reference notch in stainless steel. This evaluation used the DYNARAY system as receiver for both pulsers, so this was not a completely independent evaluation of the pulsers, as was done with the sound field mapping exercise. The amplitude response from the USN60SW was approximately 35% greater than the DYNARAY response, but SNRs as measured by both peak response-to-peak noise in the A-scan and peak response-to-mean noise in the A-scan were similar. Frequency responses showed similar center frequencies in the reflected echoes and approximately 15% greater bandwidth in the USN60SW response. It appears that both pulsers produce strong responses from the notch in this stainless steel material. The notch signal from either pulser has a good SNR and both show similar frequency responses; that is, the frequency content of the notch response waveforms obtained with the two pulse excitation scenarios are similar.

5.5 Mock-up Responses with the Tandem Probes

PNNL acquired encoded radio frequency (rf) data with the CW and CCW tandem probes on the two site-specific mock-ups, DM-05 and DM-10. Acquiring encoded data allows off-line image analyses to be performed and potential review of the data by independent analysts. An image may be gated, or filtered, in any of three orthogonal axes (scan, index, and through-wall depth) and viewed as a composite of the gated region; or one may incrementally view the data image one volumetric slice at a time in the three orthogonal planes (B-scan side view, D-scan end view, and C-scan top view). This assists in filtering out geometrical reflectors and fabrication (or other) flaw responses that interfere with the signal of interest. Soft (digital) gain may be added to enhance features of the targeted flaws. When data are acquired in un-rectified forms (as rf waveforms), frequency analyses through fast Fourier transforms (FFT) of signal responses may also be conducted. These and other techniques are applied to enhance the detection of flaws in a component. All three of the axial flaws included in these specimens were detected during PNNL image analyses. The raw A-scan (amplitude and time) data were also evaluated, but these evaluations were led by the imaging methods. Without initial feedback from imaged data, the A-scan analyses alone would have made discrete flaw detection especially challenging. It is doubtful that conventional ultrasonic testing using real-time analyses of transient A-scan signals would provide meaningful information, without foreknowledge of flaw locations in these mock-ups.

Site-specific mock-ups DM-05 and DM-10 were evaluated with both CW and CCW Sigma tandem probes. Data were acquired with the DYNARAY system using a 200V square wave pulse. Figure 5.12 displays the data acquired from axial flaw 1 and the end-drilled holes in DM-05 with the axial flaw indications circled in red. (A brief overview of the ultrasonic data view(s) used in this report is presented as Appendix A.) The C-scan top view is shown in the upper left, the rectified A-scan in the top right, the B-scan side view in the bottom left and the D-scan end view in the bottom right. The A-scan was acquired along the slanted red measurement line displayed in the B-scan side view. At this position the peak flaw response is well above the noise. During image analyses, SNR is normally calculated as a measure of the peak flaw response relative to the mean noise in the image at the same part path or through-wall depth. The imaged SNR for flaw 1 from Figure 5.12 was calculated as 9.9 dB. This same technique does not apply to an A-scan analysis. For example, Figure 5.13 shows the A-scan from the flaw with the average noise level represented by the red line. The dashed red lines represent +1 and +2 standard deviations (σ). A peak signal response and mean noise level SNR from the A-scan results in a SNR of 15.5 dB. If, however, peak signal response and peak noise level are used, the SNR is 7.4 dB. For

comparison, the peak response compared to the noise as defined by the mean+2σ, for a 95% confidence interval, results in a SNR of 10.2 dB.

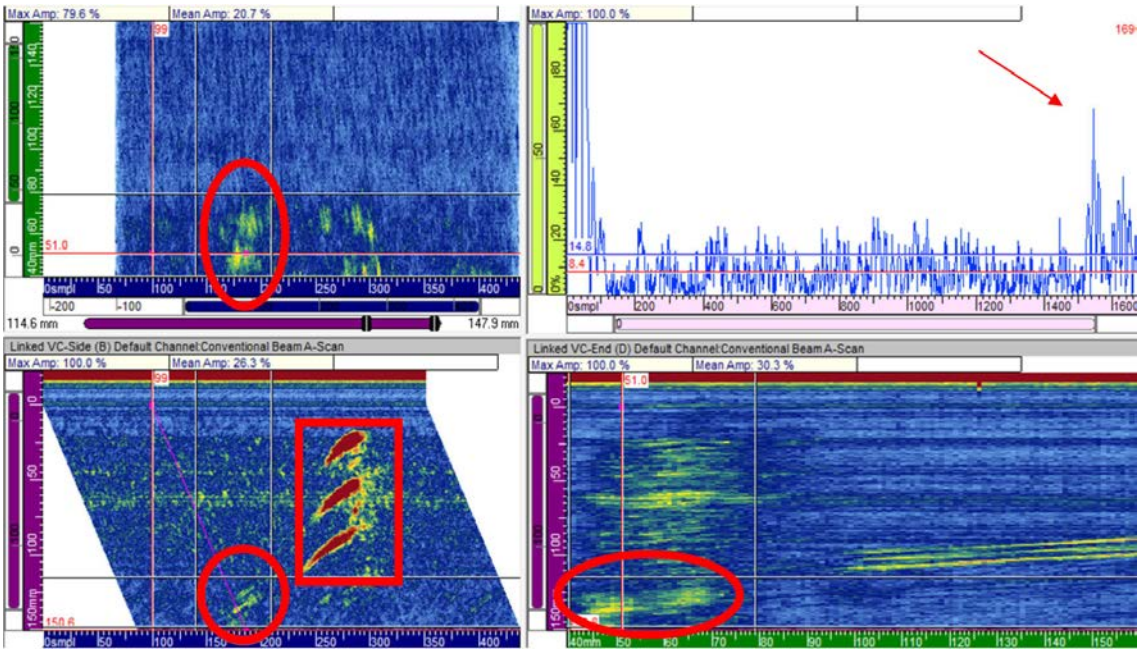

Figure 5.12. DM-05 CW Tandem Probe, Axial Flaw 1 (circled in red and noted by arrow in A-scan) and End-Drilled Hole Responses (boxed in red)

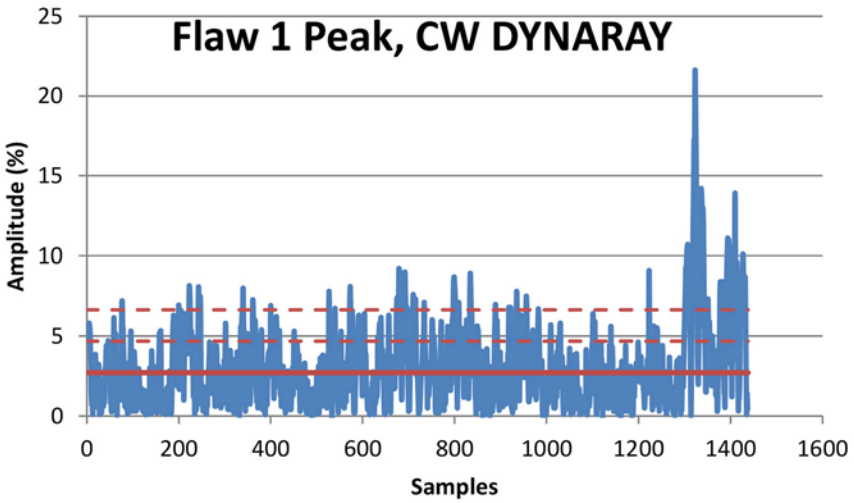

Figure 5.13. DM-05 Axial Flaw 1 Peak Response with the Tandem CW Probe. The average noise level is noted by the solid red line and the average +1σ and average +2σ noise levels are noted by the dashed lines.

In a manual non-encoded examination, the operator observes the UT instrument screen and, in real time, assesses transient reflections while assuring the transducer is being properly manipulated; thus, a peaked reflector response may not be observed during successive manual scan paths. There can also be significant changes in the A-scans over small changes in probe position. For example, Figure 5.14 shows the data from flaw 1 at a scan position that was incremented by two samples [or 2 mm (0.08 in.)]. This response has a peak-to-mean SNR of 15.5 dB and a peak-to-peak SNR of only 2.1 dB. This response was more typical of the manual data presented in Section 4.0 where SNRs were reported to be at best 2:1 or 6 dB. Figure 5.15 shows the A-scan data with added horizontal lines for the mean, mean +1σ and +2σ. The SNR at the mean +2σ level was 3.3 dB.

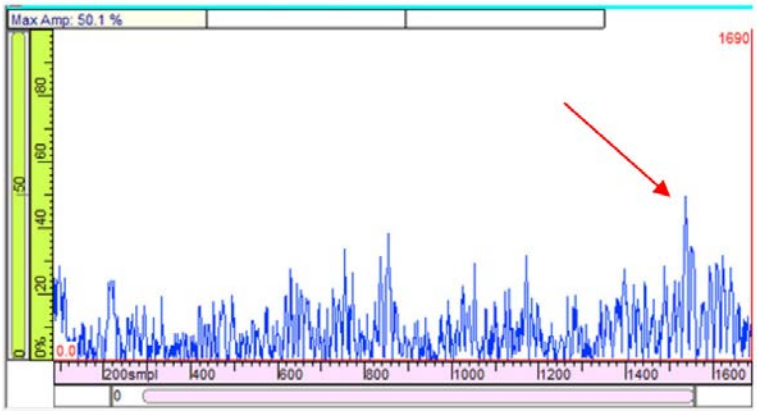

Figure 5.14. DM-05 CW Tandem Probe, Axial Flaw 1 Response at a Scan Position 2 mm (0.08 in.) from the Image Peak Response. The arrow marks the flaw response in the A-scan.

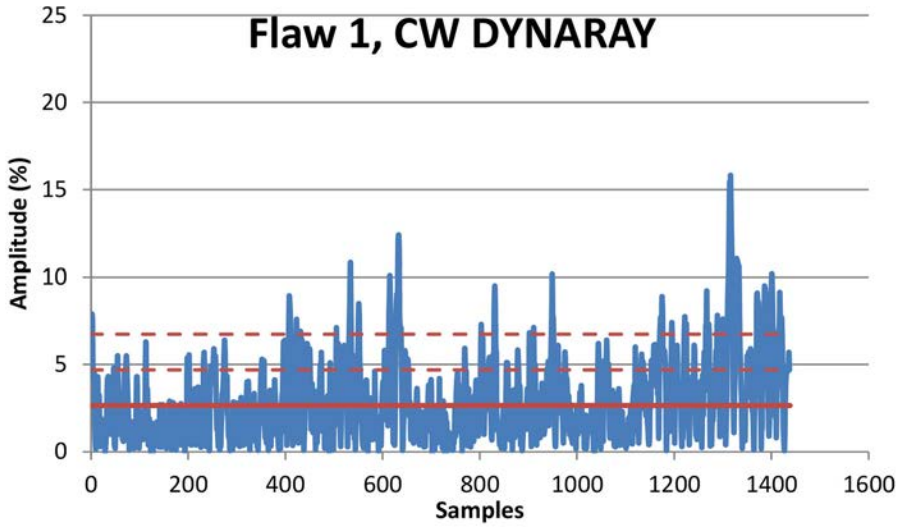

Figure 5.15. DM-05 Axial Flaw 1 Response with the Tandem CW Probe at a Scan Position 2 mm (0.08 in.) from the Image Peak Response. The average noise level is noted by the solid red line and the average +1σ and average +2σ noise levels are noted by the dashed lines.

All three axial flaws were detected in the encoded data from the CW and CCW directions (data images are displayed in Appendix B). Table 5.4 lists the SNRs for the axial flaws based on a peak flaw response relative to: 1) mean noise, 2) mean noise +2σ, and 3) peak noise. The two entries for flaw DM-05-1 at +2 mm and +1 mm (0.08 and 0.04 in.) represent A-scan data at scan positions 2 and 1 mm (0.08 and 0.04 in.) away from the peak A-scan position. These give some indication of the variation in the flaw response as scan position varies. All other data entries represent the peak flaw response based on the imaged data. The data show similar SNRs from both CW and CCW probes, unlike the manual data that showed a lower SNR from the CW (RR) probe.

Table 5.4. Axial Flaw SNRs as Determined from A-scans Using Encoded Data

Flaw	Probe	SNR P-Mean (dB)	SNR P-Mean+2σ (dB)	SNR P-P (dB)
DM-05-1	CW	18.0	10.2	7.4
+2 mm (+0.08 in.)	CW	15.5	3.3	2.1
	CCW	18.1	9.6	3.7
+1 mm (+0.04 in.)	CCW	15.2	7.0	2.9
DM-10-2	CW	17.8	9.3	4.6
	CCW	19.1	10.8	5.9
DM-10-3	CW	18.4	10.0	5.4
	CCW	20.7	11.8	6.6

For completeness, the encoded axial flaw data were also analyzed for flaw length and SNR as determined using an image analysis approach, a standard procedure for analyzing encoded phased-array data. In the image analyses of the USN60SW and DYNARAY data, the flaw signal of interest was isolated by using electronic gates. The isolated flaw signal was then amplified by adding soft gain and the flaw length was measured at the −6 dB amplitude level. The background noise level was large enough that the length of the flaw could not be measured to the loss-of-signal level (approximately 25% or −12 dB of the peak response). The SNR was calculated for each flaw; this was based on the peak flaw signal response and the mean noise response at a similar part path. These results are displayed in Table 5.5. No flaw tips or upper specular (mid-wall) reflections were observed; thus, time-of-flight depth information was not obtained.

Table 5.5. Axial Flaw Measurements of SNR and Length

		SNR (dB)		Length, mm (in.)		
Specimen	Flaw	CW	CCW	True	CW	CCW
DM-5	1	9.9	11.1	30.5 (1.20)	36.0 (1.42)	31.0 (1.22)
DM-10	2	9.7	12.7	35.0 (1.38)	35.0 (1.38)	19.0 (0.75)
DM-10[(a)]	3	13.0	15.3 11.9	25.4 (1.00)	18.0 (0.71)	23.0 (0.91) 29.0 (1.24)

(a) Flaw 3, CCW provided both an upper and lower response.

As a point of reference for this report, a commonly held standard for reliable ultrasonic detection of volumetric and planar flaws has been that the signal response should, at a minimum, be twice the amplitude of ambient noise. Thus, the signal-to-noise ratio (SNR) is two-to-one (2:1), or 6 dB. Noise can be defined in various ways and is typically represented as either a peak or average value, which may result in significantly different SNRs. The NDT Resource Center website (ISU 2012) states that a SNR of three-to-one (3:1) (or 9.5 dB) is often required as a minimum value for reliable UT. Neumann (1989), on inspection of austenitic welds, requires a recording level for the signal to be at least 6 dB above the peak noise level. Further, from Schuster et al. (1998), echoes with 6 dB or greater SNR correlated well with actual flaw positions. Also Schuster et al. (2013) stated that round robin testing results were unreliable when the SNR was less than 6 dB. In this case, noise was determined as a root mean square value.

Several ASTM standards suggest greater than 6 dB SNR. ASTM E213-09 (2009), *Standard Practice for Ultrasonic Testing of Metal Pipe and Tubing*, states that "a S/N value of at least three-to-one [3:1] is usually considered to be minimum" and that a higher minimum value is desirable and may be specified by the contracting agency (Section 9.2 of the Standard). ASTM E273-10 (2010), *Standard Practice for Ultrasonic Testing of the Weld Zone of Welded Pipe and Tubing*, requires that peak noise signal amplitudes observed on the reference standard shall not exceed 40% of the minimum amplitude from the reference indicators (Section 9.2 of the Standard); this is equivalent to 8.0 dB. Finally, ASTM E2192-13 (2013), *Standard Guide for Planar Flaw Height Sizing by Ultrasonics*, (Section 8.4.4.7 of the Standard) discusses dual-element focused longitudinal or shear probe system standardization and the need for the detection of calibration notches or holes with a SNR of at least 3.

Another important issue was discovered when assessing axial flaw responses using encoded tandem probe data. A fundamental variable when applying manual ultrasonic evaluations is flaw persistence, or the amount of time an examiner has to observe a transient flaw response that is visible above ambient background noise. This persistence is affected by not only the overall signal-to-noise response, but also by scan speed and examiner skill. In order to determine the maximum persistence of a typical axial flaw in the mock-up when using the tandem probe configuration, PNNL employed encoded data. The peak flaw response from Axial Flaw 1, as detected with the CW tandem probe, occurred at an index position of 51 mm (2.0 in.) and a scan position of 249 mm (9.80 in.). The response was noted to peak at 61.0% full screen height (FSH) with 29 dB of total gain (20.0 dB of hardware gain and 9.0 dB of soft gain) being applied. The system gain level was based on an end-of-block edge response. This edge was set at a high enough gain to stay just below saturation.

In order to measure persistence, the scan position was moved forward (toward the flaw) until the signal dropped to a 50% amplitude level (−6 dB, or about 30% FSH) and then backward (away from the flaw) to a 50% amplitude level. This full scan distance between −6 dB points was measured to be approximately 26.0 mm (1.02 in.), which represents the flaw persistence while scanning. The A-scan data are displayed in Figure 5.16 for the peak response at the 249-mm scan position. Figure 5.17 shows the two positions where the signal drops to the 50% level at 243 and 269 mm in the scan axis. The flaw signals at this 50% (−6 dB) level are comparable to ambient peak noise responses in the A-scan; thus, at these points, the flaw is essentially undetectable.

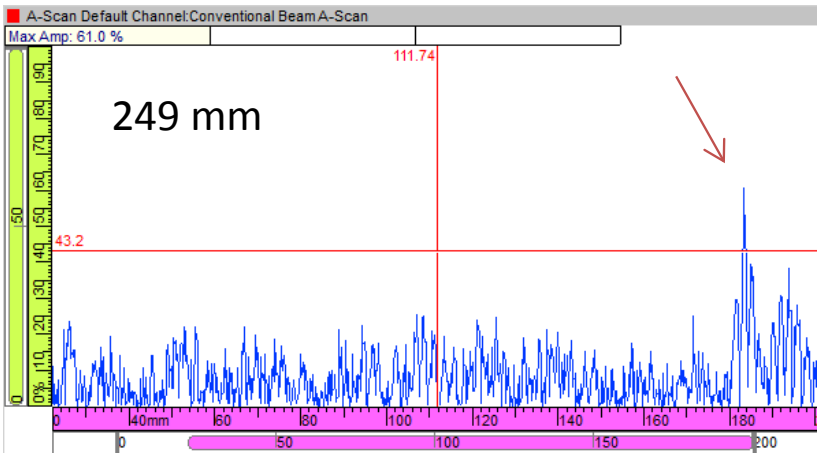

Figure 5.16. Peak Response from Axial Flaw 1

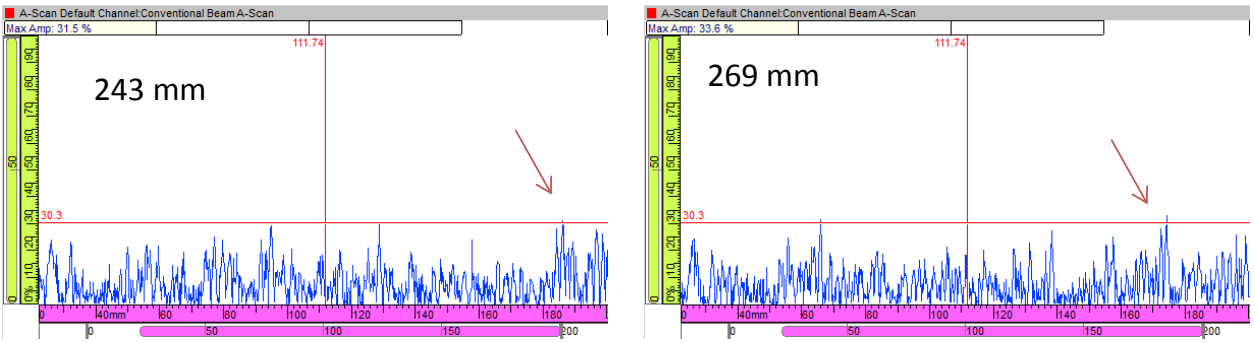

Figure 5.17. Responses at 50% Amplitude Level (−6 dB)

If the signal persistence is instead measured at a relatively higher amplitude level [−3 dB, or about 70% (43% FSH) of the peak flaw response] as displayed in Figure 5.18, the flaw end points are 247 and 251 mm (9.72 and 9.88 in.) for a 4-mm (0.16-in.) scan persistence. At this level, the flaw signal is detectable above the peak noise. However, at this persistence value, the flaw response is highly transient. Regardless of the amplitude one chooses for assessing flaw detection, at any value above the 50% (−6 dB) points, the flaw persistence, as measured in scanning time, is noted to be only a fraction of a second. As shown by laboratory measurements, and assuming a typical manual scan rate of 50.8 mm/sec (2.0 in./sec), flaw persistence for Axial Flaw 1 only equates to approximately 0.51 or 0.08 seconds, based on a 50% or 70% amplitude threshold level, respectively. This extremely short time window (persistence) for a flaw response to be observed during a manual scanning operation would not be expected to afford adequate or reliable detection.

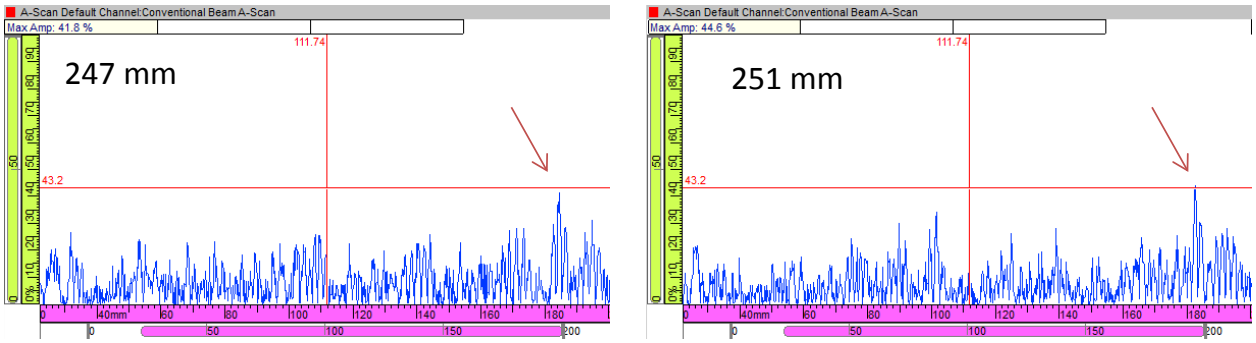

Figure 5.18. Responses at 71% Amplitude Level (−3 dB)

In summary, data using the tandem probes on the mock-ups show the importance of correctly operating the probes and acquiring encoded data. As a result of using spatial encoding and applying a tuned 200-volt square wave pulse, all axial flaws could be clearly identified in resulting data images. Encoded image analyses allow for an off-line review of the data, detection of the peak flaw response, and filtering of unwanted signals (fabrication flaws, implantation artifacts, etc.) with electronic gating. The SNRs of imaged data were in the 10 to 15 dB range (peak flaw response to average noise), while an A-scan analysis showed large variations in SNR depending on probe position and the method used to determine the noise level. As a point of reference, the manual non-encoded data SNR was reported at 6 dB at best (Section 4.0). Without initial feedback from imaged data, the A-scan analyses alone would have made discrete flaw detection especially challenging, and potentially not possible in certain scans. A-scan analyses of the encoded data approximated the poor performance of the manual data when the SNR was calculated as the peak response relative to the peak noise value. Under this scenario, the flaw SNRs were on average 5.6 dB. With a peak signal and mean +2σ noise level, the SNRs average 10 dB. Probe position is critical as was seen by a SNR drop of 7 dB with a 2-mm (0.08-in.) probe position change. Flaw length sizing was possible, but as no tip or upper specular reflections were detected, no depth sizing could be performed. Therefore, based on the information summarized above, it is believed that, had the licensee applied encoding and operated the tandem probes within proper parameters, the axial flaws in the mock-ups would have been more readily detected. However, because of surface irregularities, potential coupling issues, typical scanning speeds, and other field examination parameters that may have been experienced at NAPS-1, it cannot objectively be determined whether improved probe operation (200-volt excitation) in conjunction with encoded data would have made the PWSCC easier to detect.

6.0 Mock-up Assessment

The NAPS-1 site-specific mock-ups' design, manual data acquired with the tandem probes during a site visit, and laboratory data acquired with the tandem probes, including a comparison of encoded and non-encoded data, were discussed in previous areas of this report. This section further evaluates the two mock-ups in terms of advanced phased-array (PA) probe responses to the implanted flaws, fabrication flaws, and implantation artifacts to assess whether the artifacts and fabrication flaws potentially interfere with UT examinations of the targeted implanted flaws. Additionally, a comparison of acoustic responses is made to determine if the mock-ups adequately represent actual field components in terms of material, weld fabrication flaws, and target flaw responses.

6.1 Phased-Array Probes Employed for Laboratory Work

The mock-ups were evaluated with three phased-array (PA) probes at design center frequencies of 0.5, 1.0, and 2.0 MHz to provide flaw responses over a range of frequencies. PNNL PA probes have been designed to be highly adaptable to most component geometries and allow the application of varied focal styles, ranges of focal depths, and refracted and skewed angles, in order to insonify regions of interest with well-focused beams. The probes are described in detail, along with beam modeling results, and examples of data from the mock-ups are provided in the following sections.

6.1.1 Description of Phased-Array Probes

The three PNNL PA probes used to examine North Anna mock-ups are side-by-side transmit–receive matrix-arrays with 10 elements in the active (primary) direction and 5 elements in the passive (secondary) direction for each of the transmitting and receiving sides of the probes. Three frequencies were selected to assess flaw detection, and characterize the mock-up in terms of material noise, weld fabrication flaw content, and overall representativeness of the mock-ups. The first frequency selected was 1.0 MHz to match the center frequency of the tandem conventional probes. The second frequency was 0.5 MHz to provide better penetration, and less sound beam attenuation and scatter. A 2.0 MHz frequency probe was selected as the third to better characterize implantation or fabrication artifacts in the outer 30 to 50% of the wall thickness. It was realized that 2.0 MHz probe would not work well for axial flaws, but the use of multiple frequencies provides important information. The PA probes are displayed in Figures 6.1–6.3, and their design characteristics are listed in Table 6.1. Refracted angles, as listed, were used in circumferential scanning for the detection of axial flaws. Focal laws for scanning in the circumferential direction to detect axial flaws were developed for each probe to accommodate refracted angles in the 20(27) to 53 (no ID impingement)-degree range with skew angles of 0 and ±11 degrees. The refracted angle range was selected to extend sufficiently above and below the 30-degree refracted angle of the tandem probes. The skew angles were selected to compensate for the specimen taper such as was done with the skewed wedge in the tandem probe configuration. With the proper skew angle, a 0-degree insonification at the ID in the passive direction (axial piping direction) is produced. Due to the 11-degree taper of the mock-up specimens, circumferentially scanned PA probes with a 0-degree skew effectively form a beam that impinges on the plane of the flaw at 11 degrees in the passive direction. Similarly, the 11-degree skew was used to produce an effective 0-degree, or normal insonification of the flaw plane in the passive direction.

The 0.5-MHz PA probe was designed for evaluation of thick-section large-grain components as this lower frequency provides better penetration and less sound beam attenuation and scatter in austenitic welds. It consists of a 2 × (10 × 5) element configuration for optimized focusing and skewing capabilities in the primary and secondary axes. The transmit/receive arrays are identical and consist of an active area of 65 × 35 mm (2.56 × 1.38 in.) and greater than or equal to 50% bandwidth at −6 dB. Individual elements have pitch dimensions of 6.5 × 7.0 mm (2.6 × 2.7 in.) in the active and passive axes, respectively. The non-integral probes are mounted on customized Rexolite wedges side-by-side to operate in a pitch-catch mode. The effective wedge dimensions are 80 × 83 mm (3.15 × 3.27 in.). The actual wedge has a total width of 102 mm (4.01 in.) to accommodate the water ports used for ultrasonic coupling. A wedge angle of 15 degrees and no roof angle results in a natural refracted angle of 40 degrees in the material with no natural crossover depth of the transmit and receive trajectories for this wedge. This refracted angle yields a theoretical ID impingement angle of approximately 58 degrees when scanning circumferentially (for detection of axial flaws), not accounting for beam re-direction caused by weld structures. A 58-degree impingement angle is within the PDI-UT-10 prescribed impingement angle range of 55 to 60 degrees. The probe's wavelength in stainless steel is approximately 11.7 mm (0.46 in.).

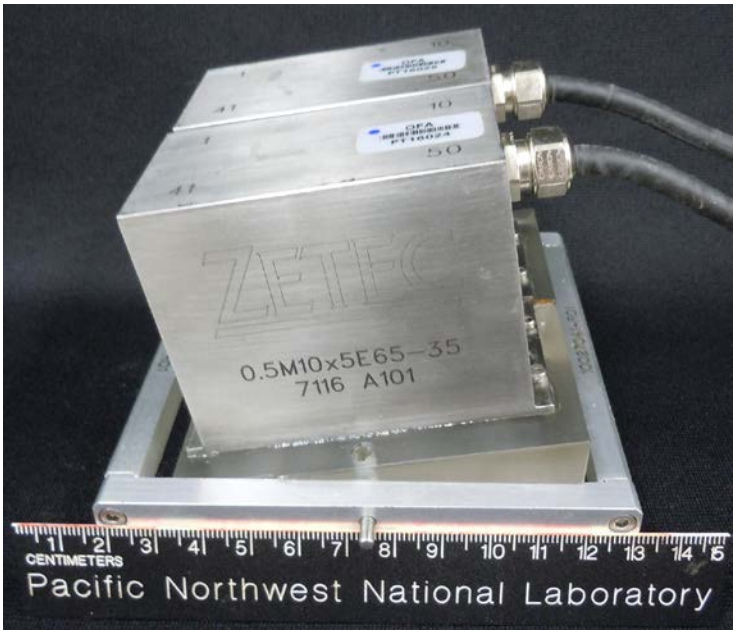

Figure 6.1. 0.5-MHz TRL PA Probe

The 1.0-MHz transmit-receive longitudinal (TRL) array was originally designed for evaluating inspection effectiveness of PA methods on components with inlays, onlays, and overlays. It consists of two 5-element by 10-element matrix arrays. One array is used for transmitting, the other for receiving ultrasonic signals. This probe has a 58% bandwidth (BW) at −6 dB and an approximately 50-mm^2 (1.97-in.^{2}) footprint with a customized wedge for data collection in tight geometrical configurations. The 1.0-MHz probe was used with a removable Rexolite wedge assembly with a wedge angle of 15 degrees. The probe's nominal wavelength in stainless steel is 5.31 mm (0.21 in.) at its average center frequency of 1.1 MHz. Skew angles of ±20 degrees were possible with this array.

Figure 6.2. 1.0-MHz TRL PA Probe

The 2.0-MHz TRL array was also originally designed for evaluating inspection effectiveness of PA methods on components with inlays, onlays, and overlays. This frequency was selected to characterize implantation or fabrication artifacts in the outer 30−50% of the wall thickness. This probe consists of two, 5-element by 10-element matrix arrays where one array is used for transmitting and the other for receiving ultrasonic signals. This probe has a 62% BW at −6 dB and an approximately 30-mm^2 (1.2-in.^{2}) footprint with a customized wedge for data collection in tight geometrical configurations. The 2.0-MHz probe was used with a removable Rexolite wedge assembly with a wedge angle of 15 degrees. The probe's nominal wavelength in stainless steel is 2.92 mm (0.12 in.) at its average center frequency of 2.0 MHz. Skew angles of ±20 degrees were possible with this array.

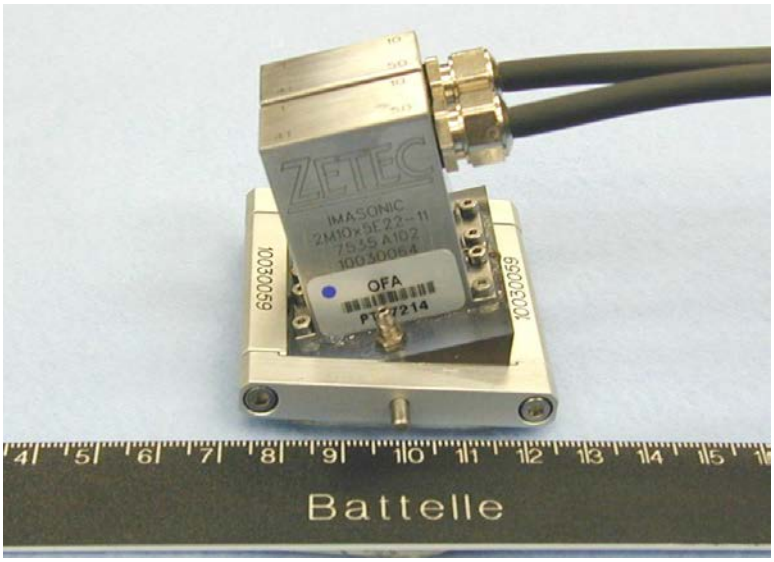

Figure 6.3. 2.0-MHz TRL PA Probe

Table 6.1. Design Specifications of the PA-Probes

	0.5 MHz TRL PA-Probe	**1.0 MHz TRL PA-Probe**	**2.0 MHz TRL PA-Probe**
Bandwidth (−6 dB)	51%	57%	62%
Refracted angles used/mode	20-53°/L	20-53°/L	20-53°/L
Active aperture (mm, inch)	64, 2.52	39.5,1.56	21.75, 0.86
Passive aperture (mm, inch)	34, 1.34	19.5, 0.77	10.75, 0.42
Configuration (# of elements)	2 × (10 × 5)	2 × (10 × 5)	2 × (10 × 5)
Element size (active × passive) (mm, inch)	5.5 × 6.0, 0.22 × 0.24	3.5 × 3.5, 0.14 × 0.14	2.0 × 2.0, 0.08 × 0.08
Wedge angle	15 degrees	15 degrees	15 degrees

6.1.2 Focal Law Development

Prior to performing phased-array examinations, a set of focal laws were developed to control the firing of individual elements. The focal laws are inputs to the UltraVision control software, which determines specific elements to excite at appropriate times to allow for proper beam-forming in the material to be examined. In order to work properly, the focal laws must also contain details about the angles being generated, the focal point of the sound field, the delays associated with the wedge and electronics, and the orientation of the probe. PNNL uses a software package known as the "ZETEC Advanced Focal Law Calculator" contained in the UltraVision 3.3R4 software program, for producing focal laws. This software package performs two functions: (1) focal law generation and (2) simulation of the ultrasonic field produced by the probe when using the generated laws. The software beam simulation produces a simple image of the probe on the wedge, ray-tracing to show the focal depth and steering desired, and density mapping to enable the viewer to see how well the sound field is formed for a particular angle. Grating lobes (unwanted energy formed off-axis from the design angle), if present, would also be mapped. Figure 6.4 shows an example of the ray tracing for a probe on the left with the sound field density mapping on the right. It should be noted that this simulation is generated by assuming an isotropic material; that is, the acoustic velocity in the material is constant for any angle for a particular wave mode. This ideal case does not produce an exact representation of sound fields in real components such as DMWs. However, this simulation provides a useful first-approximation for sound beam modeling and enables the user to estimate sound field parameters and transducer performance for optimal array design and focal law development.

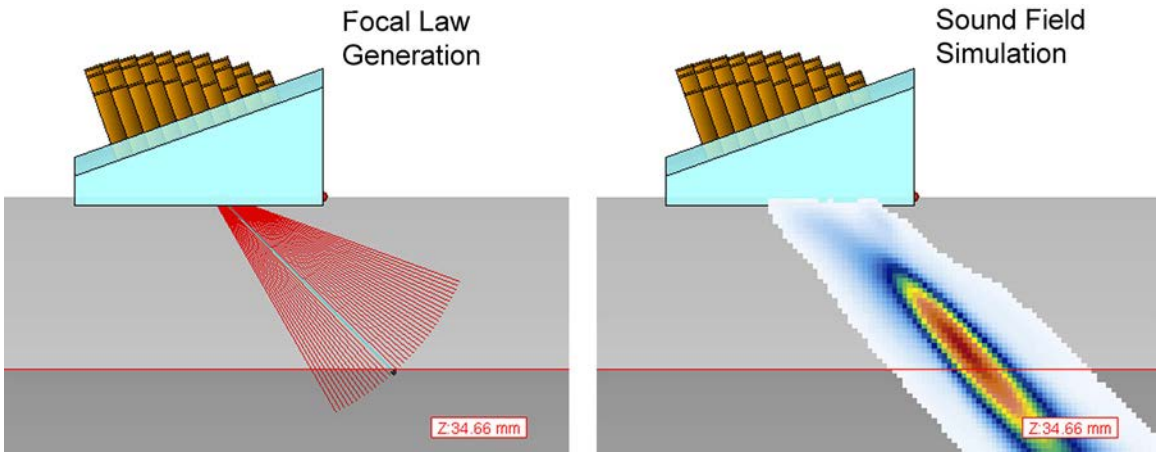

Figure 6.4. The ZETEC Advanced Phased-Array Calculator is Useful for Generating Focal Laws (left) and Simulating the Sound Field for the Focal Law (right) to Determine Idealized Beam Characteristics

Focal laws were generated to optimize examination of the mock-ups for axial flaws based on the location of the weld, butter, and flaws, noting that the thicknesses of the mock-ups change with respect to the axial position. The nominal thickness in the region of the weld and butter (implanted flaw location) was used to determine beam focusing. Both true-depth (TD) and half-path (HP) focusing techniques were employed on separate channels during the data acquisition process. The TD focusing was set to a fixed focal depth of 125 mm (4.92 in.), just above the ID nominal thickness of the butter region (127.9 mm or 5.04 in.) for all angles insonified. A constant focus at the ID region of the specimens was of interest for the detection of ID-connected flaws. The HP focusing channel was set at a 140 mm (5.51 in.) constant metal path to achieve a more volumetric insonification of the upper region of the specimens. For angles above 30 degrees, the HP focusing technique adequately insonified additional weld region volume for assessment of the through-wall extent of the flaw(s).

Focal laws for scanning in the circumferential direction to detect axial flaws were developed for each probe to accommodate refracted angles in the 20(27) to 53 (no ID impingement)-degree range with skew angles of 0 and ±11 degrees. The refracted angle range was selected to extend sufficiently above and below the 30-degree refracted angle of the tandem probes. The skew angles were selected to compensate for the specimen taper such as was done with the skewed wedge in the tandem probe configuration. With the proper skew angle, a 0-degree insonification at the ID in the passive direction (axial piping direction) is produced. Due to the 11-degree taper of the mock-up specimens, circumferentially scanned PA probes with a 0-degree skew effectively form a beam that impinges on the plane of the flaw at 11 degrees in the passive direction. Similarly, the 11-degree skew was used to produce an effective 0-degree, or normal insonification of the flaw plane in the passive direction.

The specimen was also scanned axially for detection and characterization of the implanted circumferential flaws using the same three PA probes; however, different wedges contoured for the pipe OD geometry in an axial scan direction were employed. The limited axial dimension of the mock-up specimens allowed for only an examination of the weld region from the safe end. This direction adds an 11-degree increase to the angle of the wedge because of the taper of the specimen. Therefore, angles were generated at 15-45 degrees on the outer surface to actually inspect at an angle range of

26-56 degrees with respect to the inner surface of the specimens. On an ideal flat plate, or for scanning in the axial direction on a pipe, the refracted and ID impinged angles are essentially identical. Focusing used for the axial scans was similar to that used for circumferential scans, HP at 140 mm (5.5 in.) and TD at 125 mm (4.9 in.), to nominally focus on the ID at the weld centerline. Skew angles of both positive and negative 10 degrees were collected along with a skew of 0 degrees for a comparison of flaw response and sizing.

6.1.3 Modeling/Simulation

Each PA probe was modeled in UltraVision 3.3R4 as if scanning circumferentially (to detect axial flaws) for 30(41) and 40(58) degree refracted angles, an electronic skew angle of 11 degrees to compensate for the specimen 11-degree taper, and with an assumed 15-degree wedge angle to produce a refracted angle of 40(58) in the part. A refracted angle of 30(41) degrees was chosen as this was the actual angle produced from the Sigma tandem probe, based on PNNL simulation results and the encoded data images. The additional refracted angle of 40(58) degrees was based on the original design angle for the tandem probes and the need to produce a 58-degree ID impingement angle, which is in the recommended range from PDI-UT-10. Beam simulations are displayed in Figure 6.5 for the 0.5-MHz data with the 30(41)-degree data on the left and the 40(58)-degree data on the right. Idealized weld cross sections have been added to the figures. The data have been filtered to the −6 dB or half-amplitude level. Similarly the 1-MHz data are displayed in Figure 6.6 and the 2.0-MHz data in Figure 6.7, with the 30(41)-degree refracted data on the left and the 40(58)-degree refracted data on the right, for each figure. The red and gold bars on top of the wedge graphically represent the elemental time delays necessary to create the prescribed focus and steering in the component; however, these bars do not add to the actual beam simulation and are only an artifact of the UltraVison software. Similarly, the small red dots are an artifact of the simulation image. Note that the 0.5-MHz probe theoretically produces a beam that reaches slightly beyond the specimen ID surface at the −6 dB level. The 1.0-MHz probe however falls short of transmitting sound at the −6 dB level to the ID surface by nominally 15 and 25 mm (0.6 and 1.0 in.) at refracted angles of 30(41) and 40(58) degrees, respectively. This equates to an approximate shortfall of 10 and 15% of the through-wall part path as compared to a 44% shortfall with the tandem probe. As would be expected, the 2.0-MHz modeled sound field at the −6 dB level also does not extend to the ID surface of the mock-up. At the 30(41)- and 40(58)-degree refracted angles, the sound beams are short of the ID by approximately 45 and 50 mm (1.8 and 2.0 in.). This corresponds to a shortfall of nominally one-third of the part path. However, at the −12 dB level, the sound beams just reach the ID surface.

All three PA probes show an improvement over the tandem probe in terms of generating a focused sound field with higher energy at the ID surface. The modeling results indicate that either the 0.5 MHz or 1.0-MHz probe should perform well in examinations of the mock-up specimens for ID-connected flaws based on the modeled beam coverage. As previously indicated, the 2.0-MHz frequency was chosen to better characterize implantation and fabrication artifacts. While probes of higher frequency have been used under certain circumstances for examinations, for this application the probe coverage is not sufficient, and frequency too high to provide an effective inspection through the coarse grains of the weld material. This was anticipated, with the 2.0-MHz probe being used primarily for evaluating artifacts and fabrication flaws in the mock-ups, as the higher frequency provides better resolution for these types of reflectors.

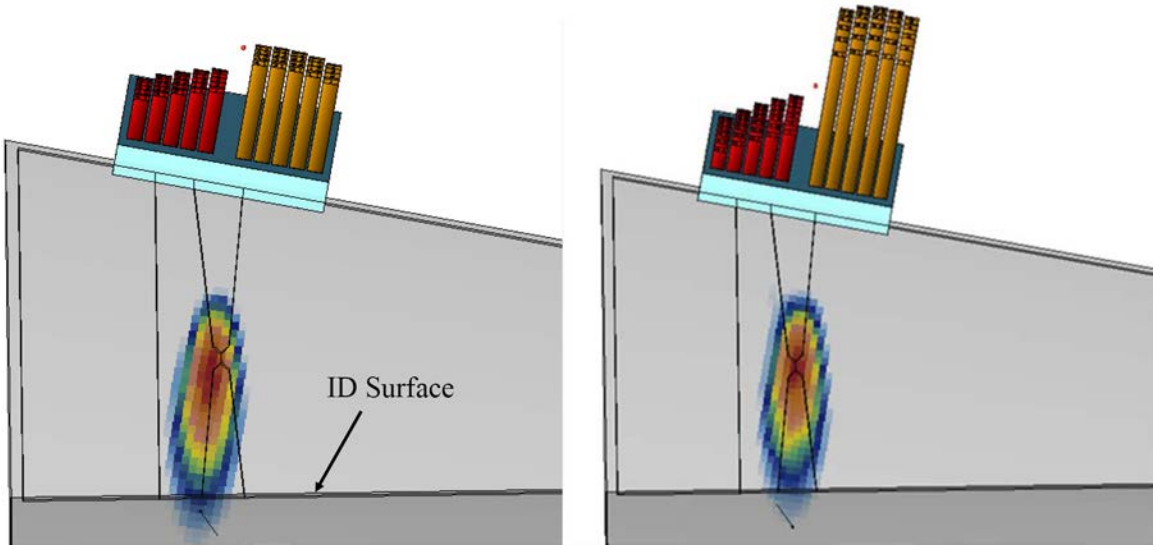

Figure 6.5. Probe Simulations for the 0.5-MHz PA Probe with Refracted Angles of 30(41) Degrees (left) and 40(58) Degrees (right) for the NAPS-1 DMW Configuration. A −6 dB filter was applied.

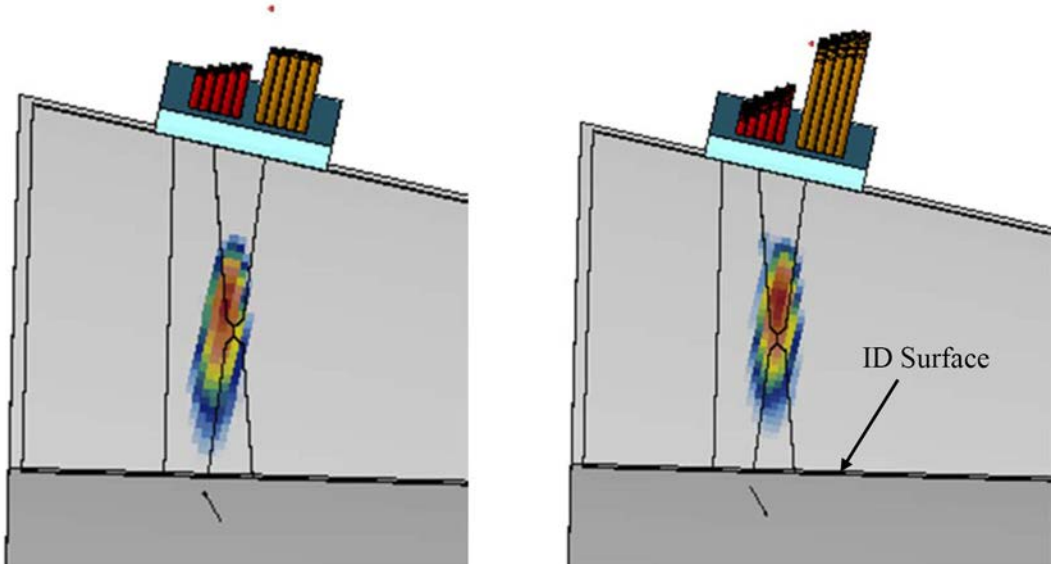

Figure 6.6. Probe Simulations for the 1-MHz PA Probe with Refracted Angles of 30(41) Degrees (left) and 40(58) Degrees (right). A −6 dB filter was applied.

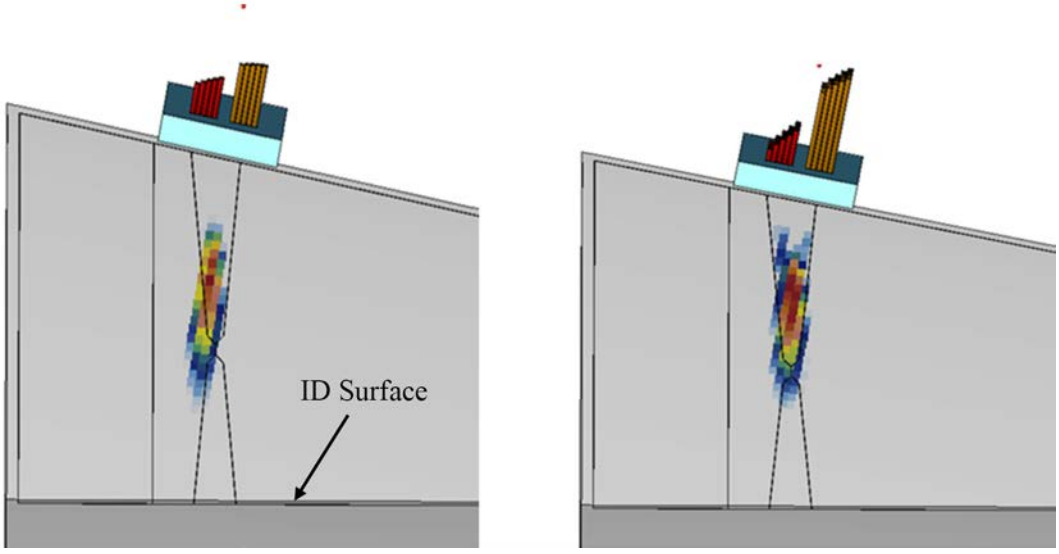

Figure 6.7. Probe Simulations for the 2-MHz PA Probe with Refracted Angles of 30(41) Degrees (left) and 40(58) Degrees (right). A −6 dB filter was applied.

6.2 Phased-Array Data on the Mock-ups

Data were acquired while scanning circumferentially for detection of axial flaws as well as scanning axially for the detection of circumferential flaws with the three PA probes. The data were analyzed for detection and characterization of the implanted flaws and for fabrication flaws and implantation artifacts. Sections 6.2.1, 6.2.2, and 6.2.3 discuss the 0.5, 1.0, and 2.0 MHz PA data, respectively.

6.2.1 PA-UT Mock-up Data—0.5 MHz

Data were acquired on the NAPS-1 site-specific mock-ups at PNNL with a 0.5-MHz PA probe for the detection of axial and circumferential flaws. The primary assessment of the mock-ups was performed at this frequency as it provides improved depth of penetration of the sound field in thick austenitic specimens, as well as exhibiting reduced attenuation (mainly scattering) and beam redirection through the coarse grains of the dissimilar metal weld. At 0.5-MHz, the probe would be less sensitive to small fabrication flaws, but produces better imaging of ID-connected flaws and geometrical reflectors that provide a benchmark, or reference response, in the data. The data were initially reviewed for flaw detection and characterization, which included a measurement of flaw length, depth, and SNR. SNR values were determined by the peak flaw response and mean noise at a similar part path (or depth in the material). Initial axial flaw data analyses are presented in Section 6.2.1.1. Subsequent analyses included a limited noise and implantation artifact detection assessment, and these results are discussed in Section 6.2.1.2. The circumferential flaw results are presented in Section 6.2.1.3.

6.2.1.1 Results from Axial Flaw Evaluation

Both DMW mock-ups, DM-05 and DM-10, were evaluated with the PNNL 0.5-MHz PA probe. Circumferential scanning with indexing in the axial direction to detect axial flaws and artifacts was

conducted over nearly the full (approximately 120-degree) circumferential length of the mock-ups. The data were acquired in overlapping files with five files per mock-up and each file covering approximately 200 mm (7.9 in.) or 22 degrees in the circumferential direction. A 50-mm (2.0-in.) or 5.5-degree overlap was used. Data were acquired with the probe scanning in the CW and CCW directions, also known as looking positive and looking negative, respectively, in the PNNL nomenclature for laboratory scanning. Full rf A-scan data (not rectified) were recorded with a 25-MHz digitization rate and spatial resolution of 1 mm (0.039 in.) in both the scan and index directions. The equivalent angular resolution in the scan direction is 0.11 degrees. The pulser voltage was set to 200V with a square wave pulse width of 1000 nsec to match the 0.5 MHz probe center frequency. Two focal styles were used: half-path focus (sound focused along a constant arc) at 140 mm (5.51 in.) and a true-depth focus (focus at a constant depth) at 125 mm (4.92 in.) with refracted angles of 20 to 53 degrees. Finally, skew angles of 0 and ±11 degrees (depending on CW or CCW scan direction) were implemented. The 0-degree skew effectively produces a beam that impinges on the plane of the flaw at an 11-degree angle from vertical due to the taper of the component while the 11-degree skew produces a normal (0-degree) beam to the flaw.

After initial reviews of a portion of the data, the half-path focusing was found to produce images with similar or slightly better (1 dB) SNRs. Figures 6.8 and 6.9 show the true-depth and half-path images from axial flaw 1 and three SDHs in DM-05. This presentation of data will be the standard format for the 0.5-MHz PA data in this report. The sector scan is displayed in the upper left, the C-scan top view in the upper right, the B-scan side view in the lower left, and the D-scan end view in the lower right. Electronic gating is accomplished with the black horizontal and vertical lines. Because the half-path focusing produced similar or marginally better SNRs, only the half-path data were analyzed to expedite the data review.

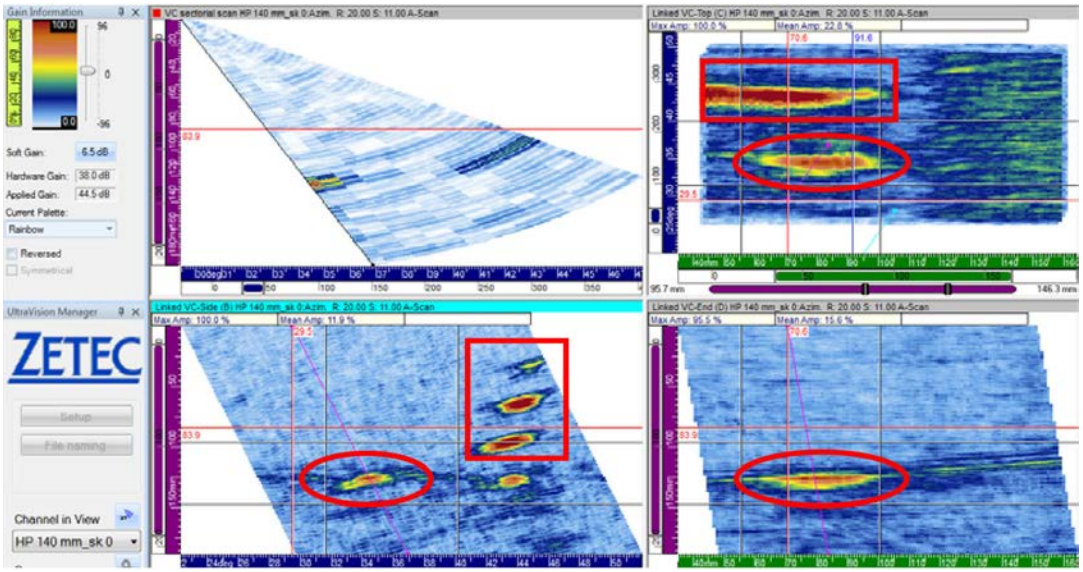

Figure 6.8. Mock-up DM-05 Axial Flaw 1 (circled) and Three SDHs (boxed) with a True-Depth Focus at 125 mm (4.92 in.). The scan is in the CW direction with a 0-degree skew.

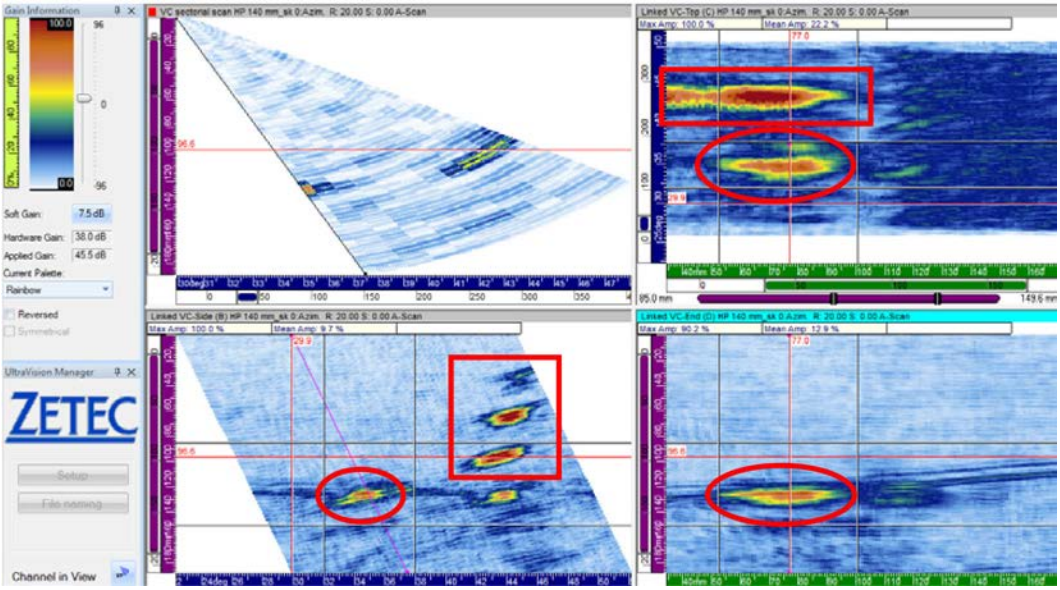

Figure 6.9. Mock-up DM-05 Axial Flaw 1 (circled) and Three SDHs (boxed) with a Half-path Focus at 140 mm (5.51 in.). The scan is in the CW direction with a 0-degree skew.

Summary measurement values for flaw length, depth, and SNR are listed in Table 6.2 for both mock-ups. A complete set of DM-05 and DM-10 data images collected are contained in Appendix C.

All of the axial flaws were detected in both scan directions and both skew angles by the presence of a strong ID corner trap signal. SNR values were strong with the lowest value at approximately 14 dB. Typically, a minimum SNR value of 6–8 dB is needed for reliable flaw detection. Although based upon a small sampling, the combined length sizing error as measured by a root mean square error (RMSE) value was 11.75 mm (0.46 in.), well within the 19-mm ASME Code, Section XI, length sizing requirement. No tip-diffracted or upper (mid-wall) specular signals were seen in axial flaw 1 data from DM-05, so no depth information was obtained. The axial flaw 2 data from DM-10 contained tip-diffracted signals. In the CCW, skew 0 file, the upper extent of the tip signal did not exceed the noise level, but a tip response from a shallower portion of the flaw was detected leading to an under sizing of the flaw depth. Flaw 3 in DM-10 did not have an upper extent response for depth sizing in the CW direction; however, the CCW data showed a strong specular reflection from the upper part of the flaw. This flaw could merely have a preferential side for detection, or it is possible that the strong response is due to the implantation process.

Table 6.2. Results of 0.5-MHz Data Analyses of Axial Flaws

		Measured Length, mm (in.)			
		CW		CCW	
Flaw	True Length	Sk0	Sk11	Sk0	Sk-11
DM-05-1	30.5 (1.20)	39.0 (1.54)	38.1 (1.50)	40.0 (1.57)	43.1 (1.70)
DM-10-2	35.0 (1.38)	43.0 (1.69)	48.1 (1.89)	28.0 (1.10)	41.1 (1.62)
DM-10-3	25.4 (1.00)	41.0 (1.61)	47.1 (1.85)	33.0 (1.30)	39.0 (1.54)
		Measured Depth, mm (in.)			
		CW		CCW	
Flaw	True Depth	Sk0	Sk11	Sk0	Sk-11
DM-05-1	40.6 (1.60)	--	--	--	--
DM-10-2	63.3 (2.49)	49.0 (1.93)	52.5 (2.07)	18.1 (0.71)	66.3 (2.61)
DM-10-3	23.9 (0.94)	--	--	19.8 (0.78)	19.5 (0.77)
		SNR (dB)			
		CW		CCW	
Flaw		Sk0	Sk11	Sk0	Sk-11
DM-05-1		14.1	13.9	15.2	16.6
DM-10-2		18.5	15.6	14.5	16.9
DM-10-3		18.3	16.7	19.2	17.2

-- No Measurement

6.2.1.2 Responses from Other Artifacts Detected During Circumferential Scanning of Mock-ups

Measurements were made on B-scan side views of the 0.5-MHz PA data to evaluate other responses (UT reflections) in the near vicinity of targeted axial flaws. These UT reflections could potentially be caused by flaw implantation artifacts or welding fabrication flaws observed in the data acquired during circumferential scans for detection of axial flaws. In theory, the implanted circumferential flaws should only present a "knife-edge" planar profile to the ultrasonic beam and thus not be detected during these scans. PNNL performed a brief parametric study to determine if circumferential flaws implanted in DMW mock-ups would typically be expected to present similar artifact responses. A total of ten circumferentially flawed areas in two DMW mockups were examined. Eight of ten of these flaws did not exhibit any responses above baseline noise when scanned parallel to the flaw major axis (scan direction to detect axially-oriented flaws); the two flaws that were detected possessed considerable tilts away from the radial plane, making portions of their morphologies available for reflection. It is concluded that flaw implantation artifacts are atypical, thus would not reasonably be manifested in a mock-up fabricated under strict quality control measures. The full parametric investigation is described in more detail in Appendix F.

The 0.5-MHz data set is the only PNNL data that fully captures the entire 120-degree circumference of the mock-ups. Other data sets included only the scan regions of the flaws and adjacent material

because access time to the mock-ups at PNNL facilities was limited. Baseline noise levels were established in the 0.5-MHz data at the ID and mid-wall regions in terms of through-wall depth. Flaw and artifact responses were measured in these two depth regions and compared to their respective baseline noise levels. A discussion of the procedure and results follow. The data were compared at a 41.0 dB total gain level to keep all responses within 100% of full scale amplitude.

DM-05 CW Skew 0- and 11-Degree Data on Axial Flaws

Baseline noise levels were established for the ID region where a flaw corner response would occur. This region represents approximately 105 to 150 mm (4.1 to 5.9 in.) in depth. Baseline noise levels were also established for a region representing an upper flaw response (mid-wall) and correspond to approximately 55 to 105 mm (2.2 to 4.1 in.) in depth. The data image from the 540 to 740 mm (21.3 to 29.1 in.), or 55.5 to 77.8 degree, circumferential location is displayed in Figure 6.10 from DM-05, when scanning in the CW direction with a skew angle of 0 degrees. The B-scan side view in the lower left quadrant represents approximately 56 to 78 degrees in the scan direction (horizontal axis) and 0 to 188 mm (0 to 7.4 in.) in depth (vertical axis). Noise and signal measurements were made from the B-scan side views of the data. The ID corner region is outlined by the red and blue lines in Figure 6.10, and the mid-wall region is outlined in Figure 6.11. Red arrows point to the two corners of the boxed regions. Mean and peak noise levels were measured over these regions and at several other circumferential locations between implanted axial and circumferential flaws. These values were averaged and resulted in an ID mean noise level of 9.2% and peak level of 27.1% at a gain setting of 41.0 dB. The upper or mid-wall region's average mean and peak noise levels are 6.4 and 14.1%, respectively. For comparison the axial flaw in mock-up DM-05 has a peak response of 53.7% at the ID.

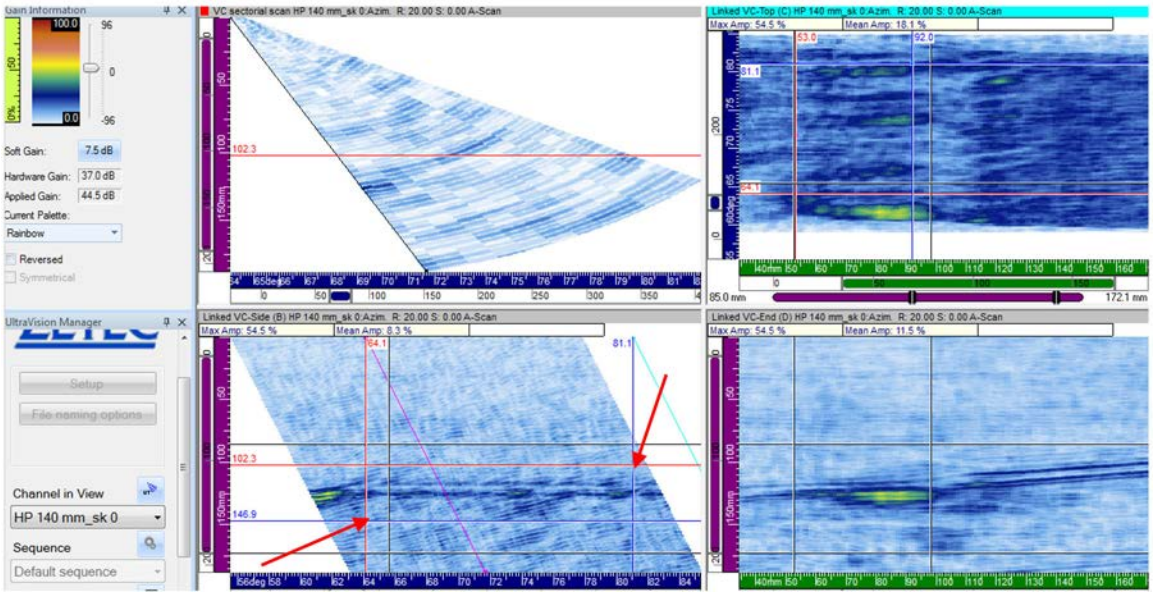

Figure 6.10. B-scan Side View (bottom left) Outlines a Region for ID Noise Measurements with the Red and Blue Lines, DM-05. Red arrows point to corners of the subject region.

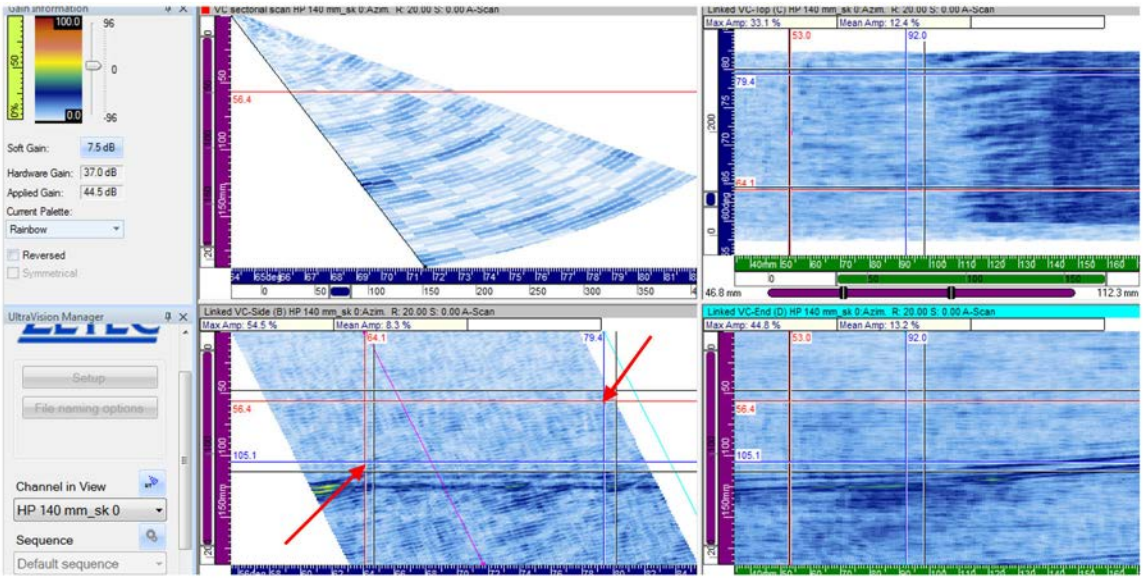

Figure 6.11. B-scan Side View (bottom left) Outlines a Region for Mid-wall Noise Measurements with the Red and Blue Lines, DM-05. Red arrows point to corners of the subject region.

With the baseline noise levels established, the data was screened for signals above this threshold. Data from the ID region containing circumferential flaw 3 is shown in Figure 6.12. The region boxed with the red and blue lines (corners marked with red arrows) represents the 15- to 21-degree region where the flaw is located. The mean noise in this area is 8.5% with a peak response of 27.8%. These values are similar to the baseline noise levels established for the mock-up, implying that the region containing circumferential flaw 3 has no detectable artifacts from the implantation process when scanning for axial flaws.

An artifact, however, was detected at approximately 62 degrees and is shown within the red circle in Figure 6.13. The peak response from this signal is 32.5%, which is approximately 20% above the baseline noise level and the signal also displays a broader response (in depth or time; i.e., more cycles in the reflected A-scan) than the noise seen in Figure 6.12. Circumferential flaw 4 is located at 54 to 60 degrees so this artifact is only 19 mm outside of the reported flaw region which is less than 1% circumferentially. While the characterization of this artifact is unclear using the 0.5-MHz data, the closer proximity of implantation artifact-to-flaw distances seen around other flaws would indicate that this may be a coincident welding fabrication flaw, but is more likely an unintended flaw from the circumferential flaw implantation process.

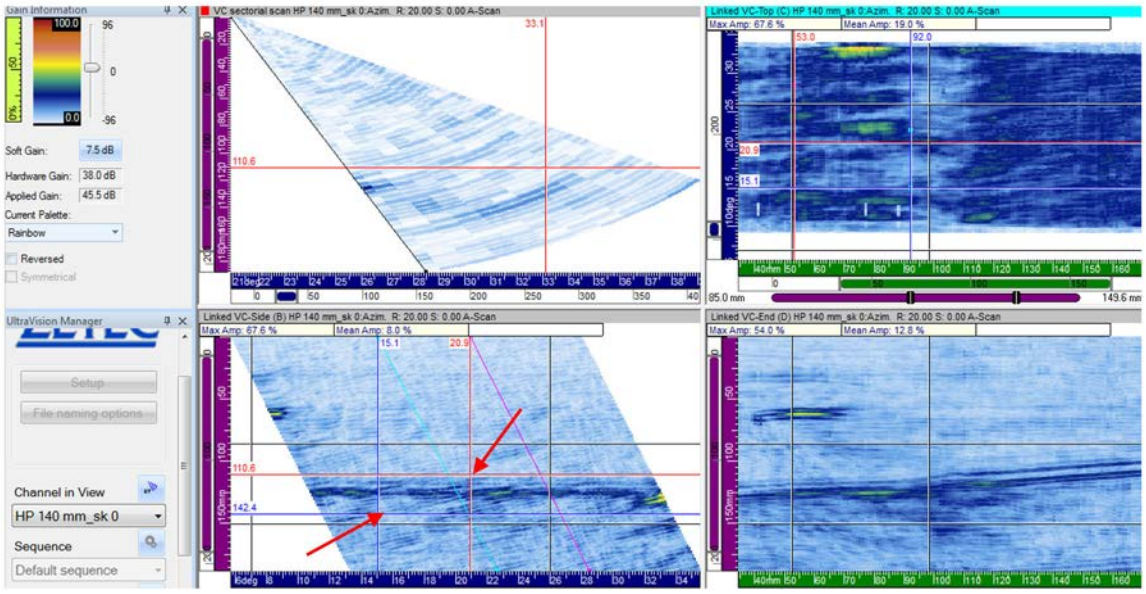

Figure 6.12. DM-05 B-scan Side View (bottom left) Outlines a Region for Circumferential Flaw 3. The response levels in this region are comparable to the baseline noise levels indicating no observed artifacts from the flaw implantation. Red arrows point to corners of the subject region.

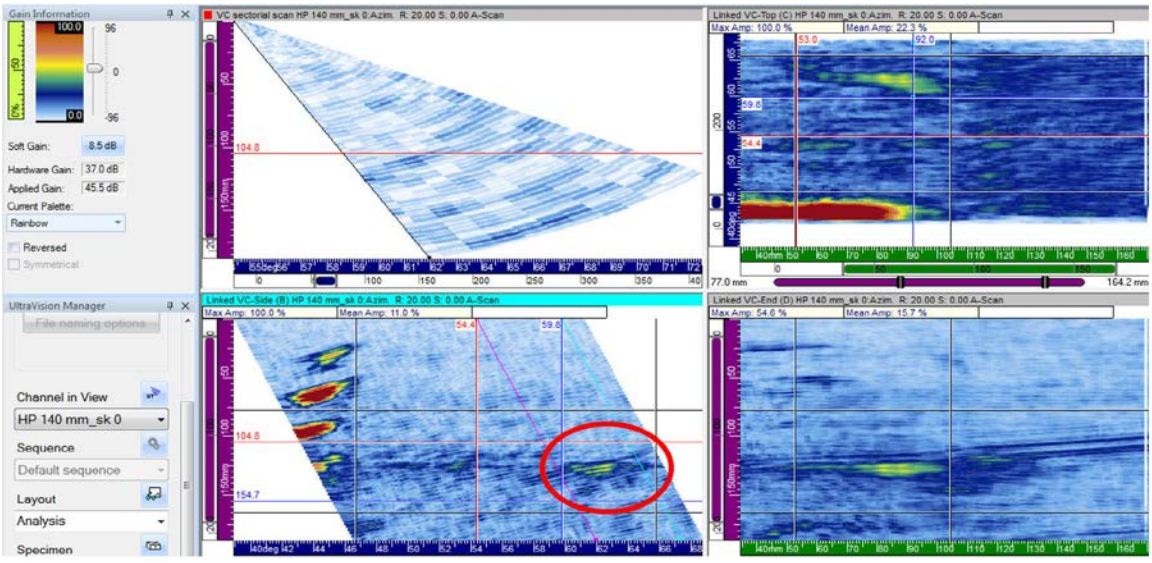

Figure 6.13. DM-05 B-scan Side View (bottom left) Displays an Artifact (circled) at Approximately 62 Degrees, Circumferential Flaw 4

Implantation artifacts are evident in the region of circumferential flaw 2 as shown in Figure 6.14, also circled in red. This flaw is reported at the circumferential region between 83 and 97 degrees. While a strong ID corner response is not visible, except possibly to the right at 94 to 98 degrees (in the red boxed region) with a peak response of 28.7%, there is a noticeable upper flaw signal response. This upper signal

has a peak response of 29.0%, well over the mid-wall peak and average baseline noise levels determined earlier. The flaw depth is measured at 50.5 mm (2.00 in.) while the true depth is reported at 62.0 mm (2.44 in.). This nearly 50% through-wall deep circumferential flaw is thus detected by a mid-wall response outlining the upper part of the flaw and by possible stronger ID signal responses at the extremities of the flaw.

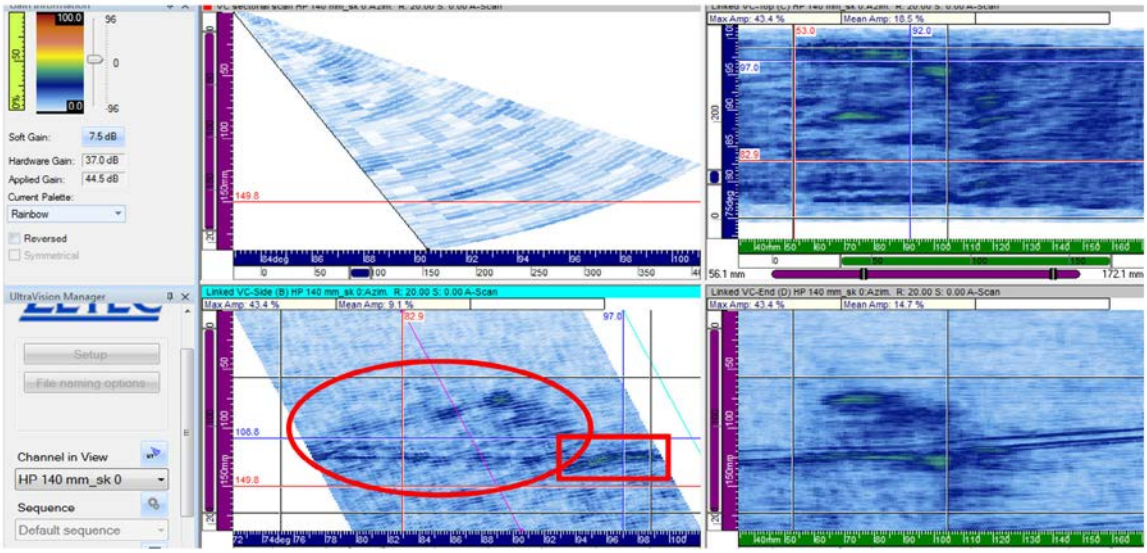

Figure 6.14. DM-05 B-scan Side View (bottom left) Depicts an Implantation Artifact from Circumferential Flaw 2 (circled) and ID Corner Response (boxed)

A summary plot of the CW data responses obtained with a skew angle of 0 degrees is shown in Figure 6.15. The mean and peak ID noise values are represented by the solid and dashed orange horizontal lines, respectively. The noise from the mid-wall region as measured by the mean and peak values is represented by the blue solid and dashed lines, respectively. In general the color orange denotes ID signals and blue denotes mid-wall signals. Further, the axial flaw response (A1) is plotted as a filled diamond symbol. These signals, noise and axial flaw responses, establish a baseline to which all unknown signals may be compared. Based on the comparison, it is believed that all of the artifact responses can be attributed to circumferential flaw implantation and are plotted with hollow markers (except for circumferential flaw 2 in the DM-05 mock-up which shows an artifact at 10 degrees, which is not a documented flaw implantation site). The horizontal axis represents the circumferential position of the peak response. Indication length and proximity of indications will be presented later. The peak ID artifact or circumferential flaw 4 (C4) signal observed at 62 degrees is plotted as well as the circumferential flaw 2 (C2) artifact peak responses from the ID and mid-wall regions. Clearly the peak mid-wall response from circumferential flaw 2 is much greater than the peak noise value in the mid-wall region of the mock-up as was seen in the data image. The ID response of circumferential flaw 2 is not noticeably larger than the peak ID response in the mock-up but is well above the mean ID noise. This flaw might not be detected based solely on its ID response amplitude, but the ID signal was wider (in time or depth) than the baseline noise and the large mid-wall indications clearly show the presence of an implantation artifact in this location.

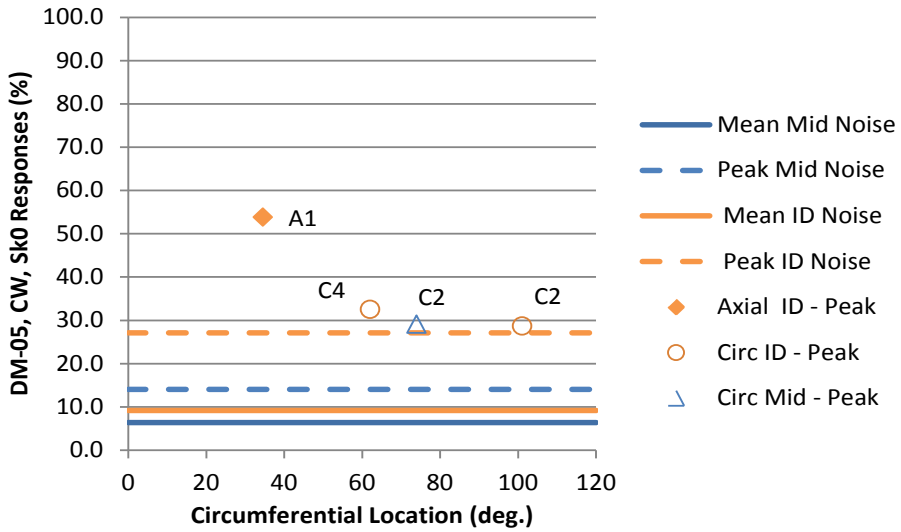

Figure 6.15. Summary of Noise and Signal Responses for DM-05 Scanning CW with a Skew Angle of 0 Degrees. The normalized gain setting is 41 dB.

The DM-05, CW data with a skew angle of 11 degrees were similarly analyzed for noise, known signals, and artifact responses. A summary of these results is plotted in Figure 6.16 and is comparable to the skew 0-degree data in Figure 6.15. Within measurement error, the true state location is the same as what is plotted. The axial flaw response is well above the noise levels and the mid-wall signal from the circumferential flaw 2 stands out along with the artifact or circumferential flaw 4 signal observed at the ID (at 62 degrees). Artifacts from circumferential flaw 3 implantation were not detected in either of the CW data sets.

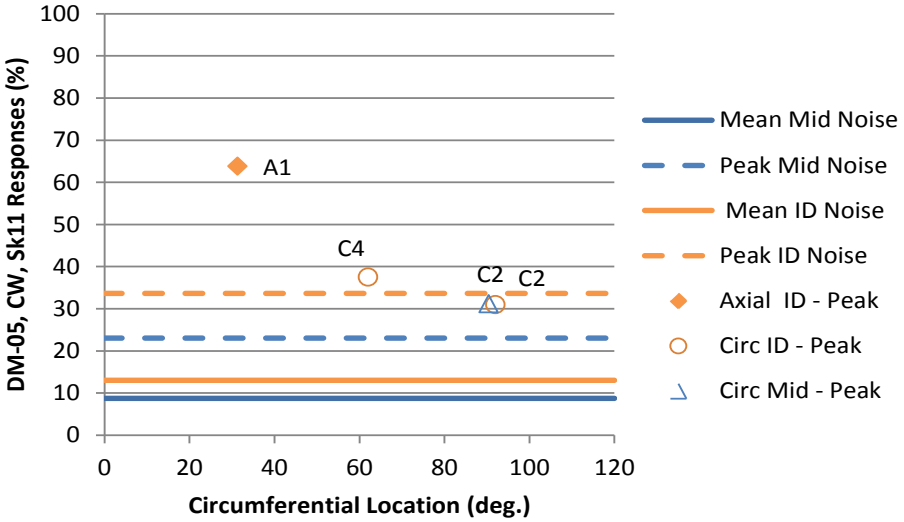

Figure 6.16. Summary of Noise and Signal Responses for DM-05 Scanning CW with a Skew Angle of 11 Degrees. The normalized gain setting is 41 dB.

DM-05 CCW Skew 0 and −11 Degree Data on Axial Flaws

The DM-05, scanning CCW with skew angles of 0 and −11 degree data were analyzed as well. Noise levels were measured for the ID and mid-wall regions. The artifact from circumferential flaw 4 implantation, seen in the CW data at 62 degrees, was not observed in the CCW data; however, an artifact at approximately 10 degrees was noted and is attributed to circumferential flaw 3. Data images at a skew angle of 0 degrees are shown in Figure 6.17 and show the 10-degree circumferential flaw 3 artifact signals in the bottom two images, circled in red. The B-scan side view is displayed on the bottom left and the D-scan end view on the bottom right. Summary plots of the response levels including noise, axial flaw, circumferential flaw artifact, and mid-wall artifact levels are displayed in Figures 6.18 and 6.19 for the skew 0 and −11 degree data, respectively. Clearly the ID axial flaw responses (A1) are well above the mean and peak noise levels in all the data sets. Also evident are the mid-wall responses in the locations of circumferential flaw 2 and the 10-degree circumferential flaw 3 artifact. In both data sets, these responses are well above the mean and peak mid-wall noise levels. Possible ID responses are noted at the ends of circumferential flaw 2 as was seen in the CW data. While the axial flaw responses are 2–3 dB greater in the CCW data than the CW data, the noise levels between CW and CCW data also show 1–3 dB variation.

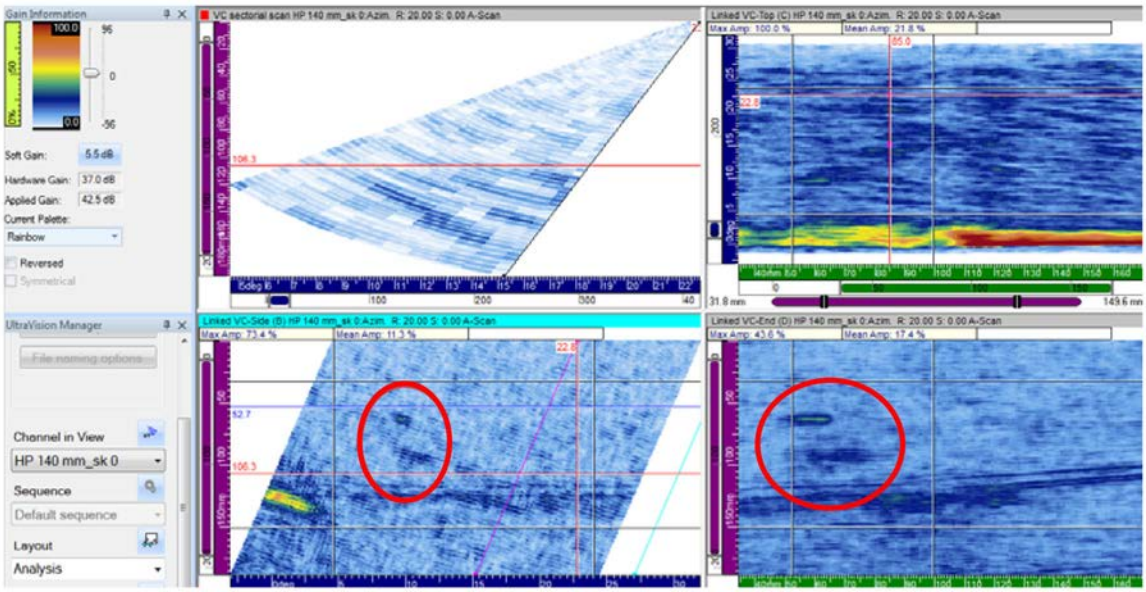

Figure 6.17. DM-05 CCW B-scan Side View (bottom left) and D-scan End View (bottom right) Show an Implantation Artifact at 10 Degrees (circled), Likely from Circumferential Flaw 3

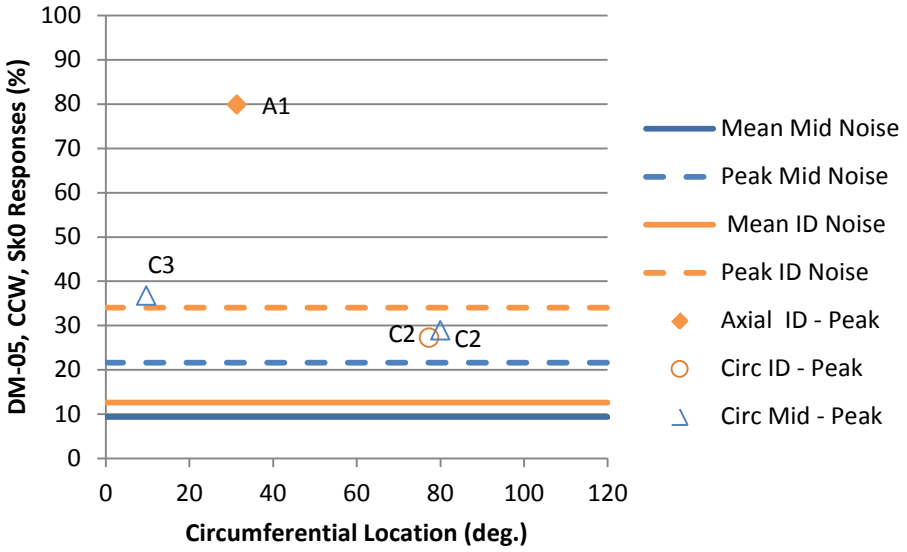

Figure 6.18. Summary of Noise and Signal Responses for DM-05 Scanning CCW with a Skew Angle of 0 Degrees. The normalized gain setting is 41 dB.

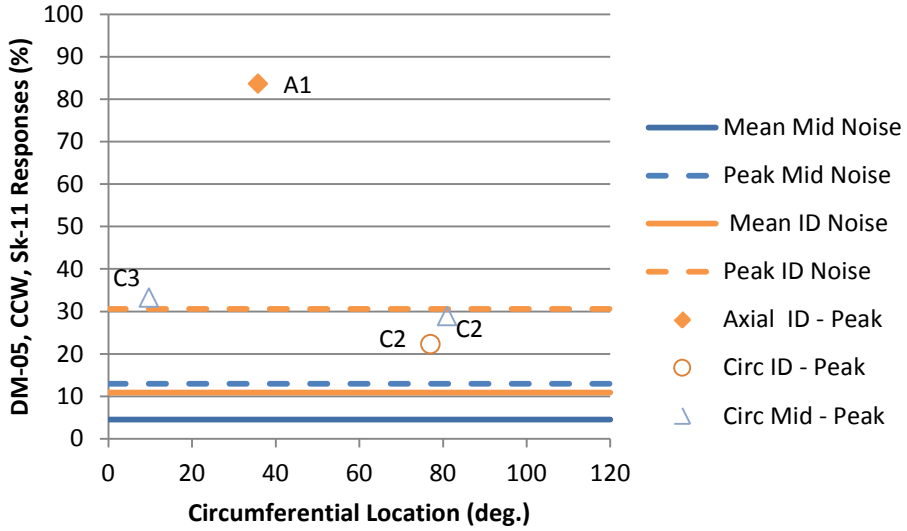

Figure 6.19. Summary of Noise and Signal Responses for DM-05 Scanning CCW with a Skew Angle of −11 Degrees. The normalized gain setting is 41 dB.

In summary, DM-05 mock-up CW axial flaw data scans show artifacts from circumferential flaws 2 and 4. The CCW axial flaw data scans show implantation artifacts from circumferential flaw 2 and an artifact at 10 degrees, which is not a documented flaw implantation site. Artifacts from circumferential flaw 3 were not detected. This is interesting as circumferential flaws 3 and 4 are nearly identical, 1.9-inches long and 15% through-wall and 2.2-inches long and 17% through-wall, respectively. This is probably just a coincidence of the implantation process.

DM-10 Data on Axial Flaws

The data summaries in graphical form for the DM-10 mock-up are displayed in Figures 6.20 through 6.23. Figures 6.20 and 6.21 capture the CW scan data with skew angles of 0 and 11 degrees, respectively, while Figure 6.22 and 6.23 capture the CCW scan data with skew angles of 0 and −11 degrees, respectively. The two axial flaw responses (orange diamonds A2 and A3) from the ID are well above the noise levels. A smaller mid-wall response is evident in axial flaw 2 (blue diamond A2) in all data sets; however, a large mid-wall response is seen from axial flaw 3 (blue diamond A3) when scanning in the CCW direction. This response is nearly as bright as the ID corner response and is indicative of a specular reflection from the flaw as opposed to a tip signal. It could also be an effect of the implantation and not a direct flaw response. Implantation artifacts are evident from circumferential flaws 1 and 4 in all data sets with the 42% through-wall deep circumferential flaw 1 more noticeable than the 23% through-wall deep flaw 4. The PA data images are presented in Appendix C.

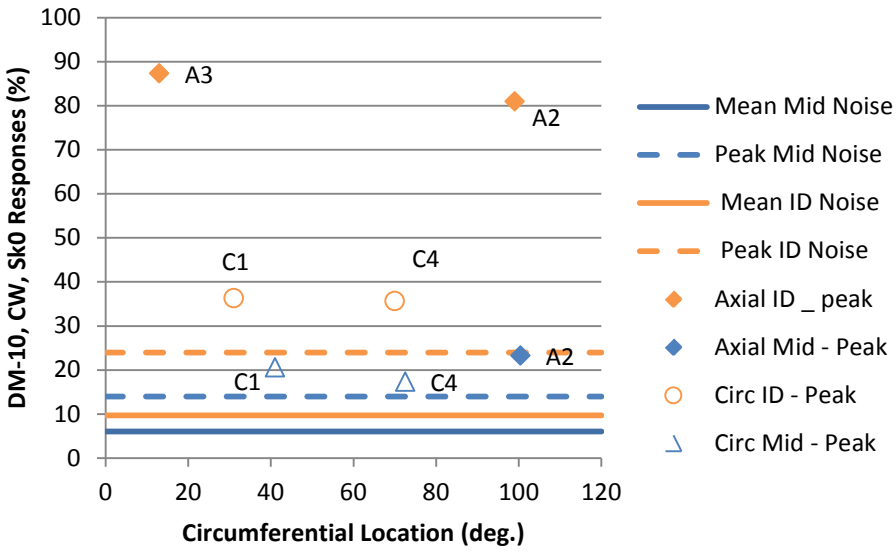

Figure 6.20. Summary of Noise and Signal Responses for DM-10 Scanning CW with a Skew Angle of 0 Degrees. The normalized gain setting is 41 dB.

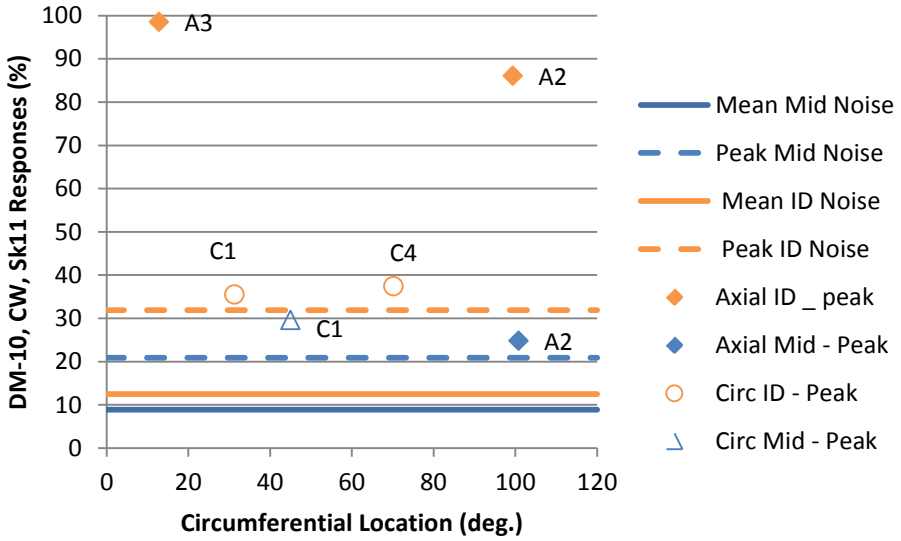

Figure 6.21. Summary of Noise and Signal Responses for DM-10 Scanning CW with a Skew Angle of 11 Degrees. The normalized gain setting is 41 dB.

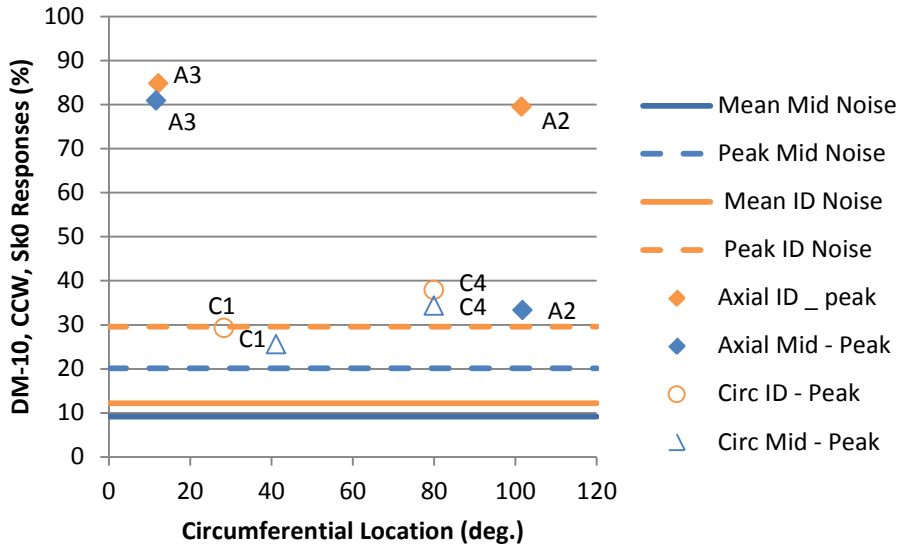

Figure 6.22. Summary of Noise and Signal Responses for DM-10 Scanning CCW with a Skew Angle of 0 Degrees. The normalized gain setting is 41 dB.

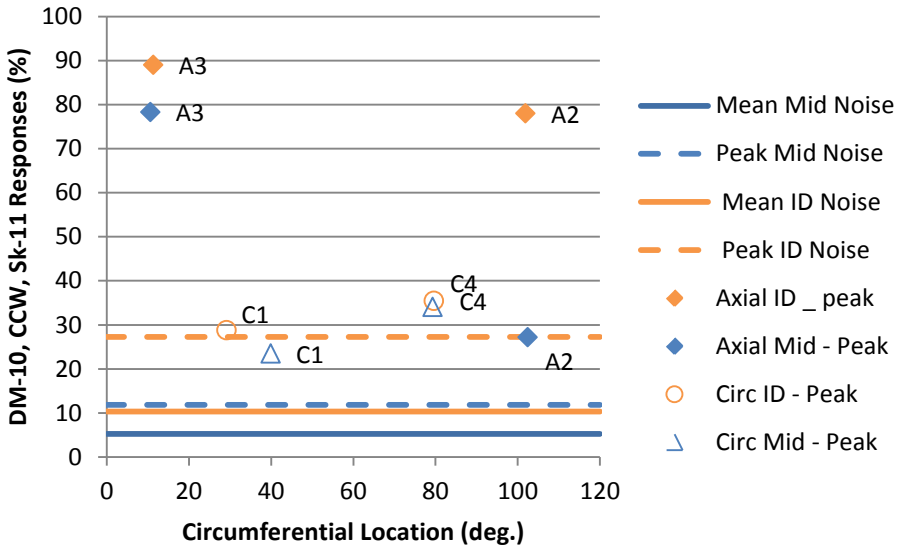

Figure 6.23. Summary of Noise and Signal Responses for DM-10 Scanning CCW with a Skew Angle of −11 Degrees. The normalized gain setting is 41 dB.

In summary, circumferential scan data (to detect axial flaws) were acquired in multiple scans covering the weld volume in the mock-ups. All of the axial flaws were detected. Data analyses also reveal that all of the five implanted circumferential flaws were found. As previously stated, these flaws were not expected to be detected in this orientation as they present a knife-edge profile to the ultrasonic beam. It is therefore assumed that these flaws were detected as a result of implantation artifacts. These findings indicate that the mock-ups as evaluated using 0.5-MHz PA encoded data exhibit multiple artifacts that could be identified as potential axial flaw indications if blind manual non-encoded examinations were to be performed on these welds. A summary of the detected implantation artifacts from the circumferential artifacts is listed in Table 6.3.

Table 6.3. Circumferential Flaw Artifacts Detected When Scanning for Axial Flaws

	CW		CCW	
Flaw/Artifact	**Skew 0**	**Skew 11**	**Skew 0**	**Skew 11**
DM-05				
C2	yes	yes	yes	yes
C3	no	no	yes	yes
C4	yes	yes	no	no
DM-10				
C1	yes	yes	yes	yes
C4	yes	yes	yes	yes

Proximity

The responses from circumferential scans to detect axial flaws were mapped to circumferential locations with the results summarized in Figures 6.24 and 6.25. These figures show the reported or true axial flaw locations as black dots and the circumferential flaw locations as black lines. The beginning and ending positions of the flaw response in the circumferential extent as measured at the approximately −6 dB level are plotted along the horizontal axis. The vertical axis has no units and is merely a means of displaying the responses from the CW scan direction at skew 0 and 11 degrees and CCW scan direction at skew 0 and −11 degrees all on the same plot. From Figure 6.24, the axial flaw was detected at all four probe scanning combinations as were implantation artifacts from circumferential flaw 2 at 90 degrees. Circumferential flaw 3 artifacts at 18 degrees were only detected using the CCW data and circumferential flaw 4 at 57 degrees was only detected in the CW data. The two axial and two circumferential flaws in DM-10, Figure 6.25, were detected in all four scan configurations. Based on using the PNNL 0.5-MHz PA probes and the ability to use imaging analyses from encoded data, adequate separation between the targeted axial flaws and circumferential flaw implantation artifacts is observed; thus, the artifacts do not negatively influence axial flaw sizing. However, axial flaw detection and/or sizing using a manual non-encoded method would not be expected to resolve the responses this easily.

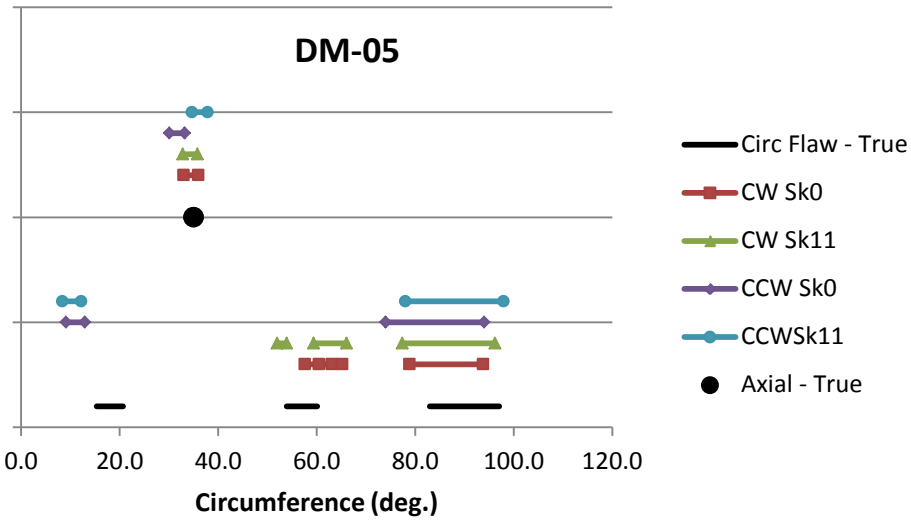

Figure 6.24. Circumferential Location of Flaws and Responses in Mock-up DM-05

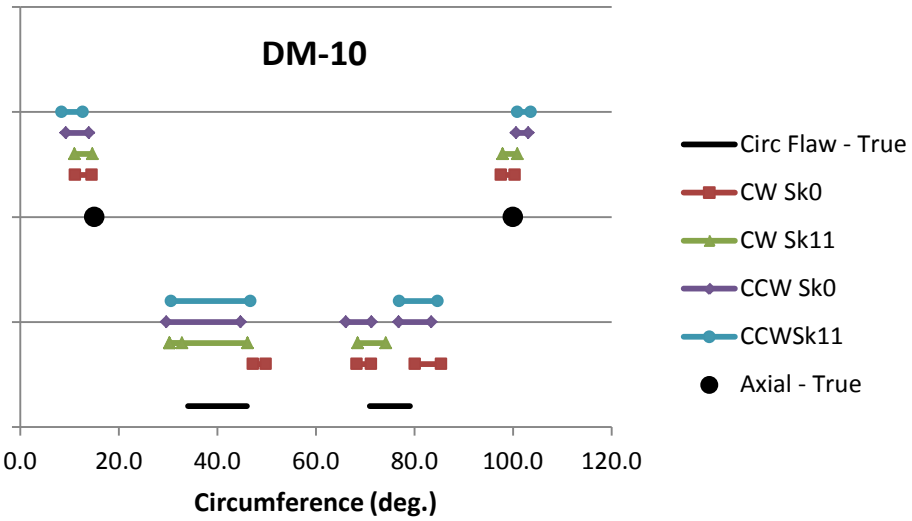

Figure 6.25. Circumferential Location of Flaws and Responses in Mock-up DM-10

6.2.1.3 Results from Circumferential Flaw Evaluation

The mock-ups were also scanned in the axial direction to validate detection and characterization of the five implanted circumferential flaws. Flaw characterization results are listed in Table 6.4 and include the measured flaw length, depth, and SNR. All of the flaws were detected; however, it was often difficult to separate out the flaw's ID corner response from weld geometrical signals. The upper portion of a flaw could be isolated and was used for some of the measurements as noted in the table. In particular, the SNRs as measured at the ID, when possible, were nominally 11 dB; whereas, the values were 11 to 21 dB when measured at mid-wall flaw responses. These mid-wall indications were in an acoustically less noisy part of the mock-up, away from the large geometrical reflectors at the ID. The data images are presented in Appendix C. No artifacts were detected but the scanned regions only extended on the order of 20 to 60 mm (0.8 to 2.4 in.) beyond the flaws' circumferential extents.

Table 6.4. Results of 0.5-MHz PA Data Analyses of Circumferential Flaws

Flaw	Measured Length, mm (in.)	True Length, mm (in.)	Measured Depth mm (in.)	True Depth, mm (in.)	SNR (dB)
DM-05-2	156 (6.1)	127.3 (5.01)	55.3 (2.2)	62.0 (2.44)	21.3[(a)]
DM-05-3	89 (3.5)[(a)]	48.3 (1.90)	17.4 (0.7)	20.8 (0.82)	11.0[(a)]
DM-05-4	117 (4.6)	55.9 (2.20)	14.4 (0.6)	23.7 (0.93)	11.2
DM-10-1	91 (3.6)[(a)]	108.0(4.25)	40.9 (1.6)	53.0 (2.09)	20.4[(a)]
DM-10-4	80 (3.2)[(a)]	73.7 (2.90)	14.6 (0.6)	32.1 (1.26)	14.9[(a)]

(a) Measured on mid-wall response.

0.5-MHz Summary

Based on initial beam modeling, and results from the empirical data obtained in the laboratory, the 0.5-MHz PA probe provided good penetration of the DMW and fully insonified the examination volume, including the ID surface of the mock-ups. Both mock-ups were scanned for nearly the full 120-degree circumference of the pipe segment. The three axial flaws were detected with good SNRs (14–19 dB). Length-sizing error of the axial flaws was within ASME requirements. Depth-sizing data was limited with only tip-diffracted data being observed from one of the three flaws; a strong specular reflection from the mid-wall region was also observed from another of the three flaws. Based on an amplitude analysis where artifact responses were compared to noise levels, significant implantation artifacts were detected from all of the circumferential flaws at the ID surface, mid-wall, or both. The purpose of a site-specific mock-up is to familiarize a qualified examiner with the peculiarities of a particular geometry, and expected responses should flaws be present in the actual configuration. The responses from the artifacts in the mock-ups could be easily misinterpreted as flaws using manual non-encoded techniques, and degrades the suitability of the mock-ups for such training purposes. However, using encoded data at the 0.5-MHz range, the circumferential flaw artifacts were easily separated from the axial flaw responses and would not be included in axial flaw sizing based on their relative proximity. All of the artifacts detected with the 0.5-MHz probe were associated with the circumferential flaws. The five circumferential flaws were also easily detected and characterized using axial scan data.

6.2.2 PA-UT Mock-up Data—1 MHz

Data were acquired on the North Anna mock-ups with a 1.0-MHz PA probe to assess the axial and circumferential flaws at this frequency, which is the same as the tandem probes. The data were initially reviewed for flaw detection and characterization, including measurements of flaw length, depth, and SNR. Axial flaw data analyses are presented in Section 6.2.2.1. Subsequent analyses included a limited noise or artifact detection assessment, and these results are discussed in Sections 6.2.2.2 and 6.2.2.3. The circumferential flaw results are presented in Section 6.2.2.4.

6.2.2.1 Axial Flaw Evaluation

Dissimilar metal weld mock-ups DM-05 and DM-10 were evaluated with a PNNL-designed 1.0-MHz PA probe (see Section 6.1 for a description of this probe). Circumferential scans with indexing direction parallel to the weld to detect axially oriented flaws and artifacts were conducted over the areas of implanted flaws in the mock-ups. Scanning protocols described in Section 6.2.1.1 (for the 0.5-MHz probe) were applied except that only the flaw regions and nearby material were evaluated; not the entire mock-up circumference. As was determined with the 0.5-MHz data, half-path focusing produced images with similar or better SNRs than true-depth focusing; therefore, only these data were analyzed. Figure 6.26 shows the image from axial flaw 1, the three SDHs, and an artifact in DM-05. The uncorrected sector scan is displayed in the upper left and used for angle selection; beside the sector view (to the right) is the A-scan along the selected angle. The C-scan top-view is depicted in the upper right, the B-scan side-view in the lower left, and the D-scan end-view in the lower right. Axial flaw 1 is circled in red and is clearly lower in amplitude than the artifact which is circled in orange. This artifact appears at the same scan (circumferential) location as the flaw, but also extends into the safe end material. It appears to be flaw related, perhaps from the implantation process. The artifact response is more coherent than the flaw response and is 1.6 dB higher in amplitude. This adds confusion to detection of the axial

flaw in the weld and butter region. Preliminary PNNL assessments identified the artifact as the axial flaw since the exact locations of the butter region, weld and safe end material, with respect to the end of the mockup, were not known. Summary measurement values for flaw length, depth, and SNR are listed in Table 6.5 for both mock-ups. Complete displays of DM-05 and DM-10 data images are contained in Appendix D.

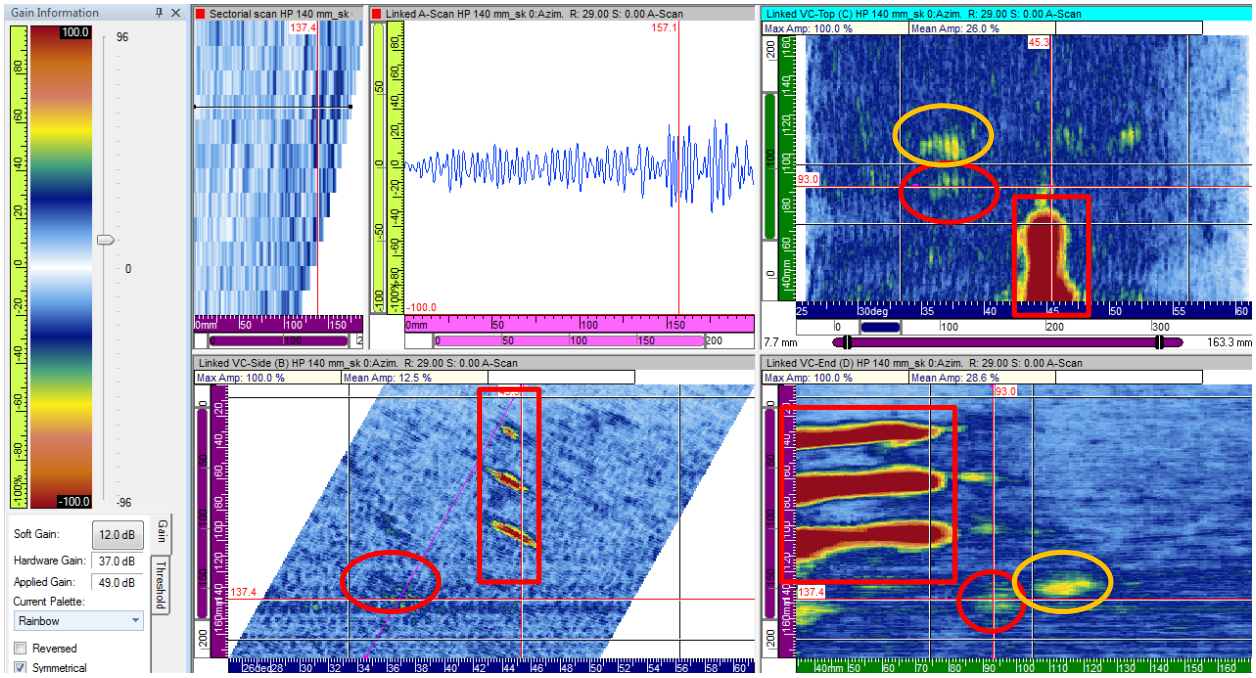

Figure 6.26. Mock-up DM-05 Axial Flaw 1 (circled in red), Three SDHs (boxed), and Artifact (circled in orange) that Extends into the Safe End Region. The scan is in the CCW direction with a 0-degree skew and half-path focusing at 140 mm (5.51 in.).

The two axial flaws in DM-10 were detected in both scan directions and respective skew angles by the presence of a strong ID corner trap signal. The average SNR values DM-10 flaw 2 and 3 were 16.0 and 14.2, respectively. Axial flaw 1 in DM-05 had a weaker corner response and was shadowed by a stronger artifact that extends into the safe end region. Flaw 1 was detected in both scan directions and respective skew angles, but only had an average SNR of 8.0 dB. A minimum SNR value of 6–8 dB is needed for reliable flaw detection. Tip-diffracted or upper (mid-wall) specular signals were seen in axial flaw 1 data from DM-05 in 0 skew CCW inspection direction and both skews in the CW direction. Axial flaw 2 data from DM-10 had tip-diffracted or top of flaw specular reflection signals in both scan directions and skew angles. The implantation artifact extending into the safe end provides a tip response signal that sizes close to the reported flaw depth; this appears to provide further indication that the artifact is clearly flaw related. Flaw 3 in DM-10 did not produce an upper extent response for depth sizing in the CW direction at skew 0; however, the CCW data showed a strong specular reflection from the upper part of the flaw. This flaw could merely have a preferential side for detection, or it is possible that the strong response was due to the implantation process.

Table 6.5. Results of 1.0-MHz PA Data Analyses of Axial Flaws

		Measured Length, mm (in.)			
		CW		CCW	
Flaw	True Length	Sk0	Sk11	Sk0	Sk-11
DM-05-1	30.5 (1.20)	13.0 (0.51)	79.0 (3.11)	19.0 (0.75)	55.0 (2.17)
DM-10-2	35.0 (1.38)	30.0 (1.18)	32.0 (1.26)	63.0 (2.48)	62.0 (2.44)
DM-10-3	25.4 (1.00)	29.0 (1.14)	31.1 (1.22)	42.0 (1.65)	47.2 (1.86)
		Measured Depth, mm (in.)			
		CW		CCW	
Flaw	True Depth	Sk0	Sk11	Sk0	Sk-11
DM-05-1	40.6 (1.60)	34.1 (1.34)	30.5 (1.20)	49.0 (1.93)	--
DM-10-2	63.1 (2.49)	65.0 (2.56)	61.0 (2.40)	42.7 (1.68)	30.4 (1.20)
DM-10-3	23.9 (0.94)	--	17.1 (0.67)	24.3 (0.96)	24.6 (0.97)
		SNR (dB)			
		CW		CCW	
Flaw		Sk0	Sk11	Sk0	Sk-11
DM-05-1		7.9	9.2	6.9	8.0
DM-10-2		19	13.3	18	13.6
DM-10-3		13.7	12.3	15.4	15.5

-- No Measurement

6.2.2.2 Responses from Other Artifacts Detected During Circumferential Scanning of Mock-ups

Analysis of circumferential scan data included an assessment of other artifacts detected that were neither intentional flaws nor geometric responses. Unlike the 0.5-MHz data set that fully captures the entire 120-degree circumference of the mock-ups with baseline noise levels established at the ID and mid-wall regions, the 1.0-MHz scans were focused only on the intentional flaws and adjacent material; therefore, representative baseline values were not possible. These restrictions were dictated by the short stay of the mock-ups at PNNL. However, observations were made on the 1.0-MHz PA data to determine the presence of circumferential flaw implantation artifacts or welding fabrication flaws in the limited data acquired during circumferential scans. Again, unless designed for a tilt away from the radial plane, circumferential flaws should only present a knife-edge profile to the ultrasonic sound field and, thus, should not be detected.

In addition to DM-05 axial flaw 1 shown in Figure 6.27 as indicated by the arrows, a similar amplitude response exists emanating from the ID region of the specimen in line with the weld region (similar index position as flaw 1) as circled in the C-scan view. The location of this indication is circumferentially positioned at 53.5 degrees and corresponds to the start location of circumferential flaw 4 that is centered at 57 degrees (52- to 60.5-degree range). This response is most likely an implantation artifact associated with the installation of flaw 4 in the specimen.

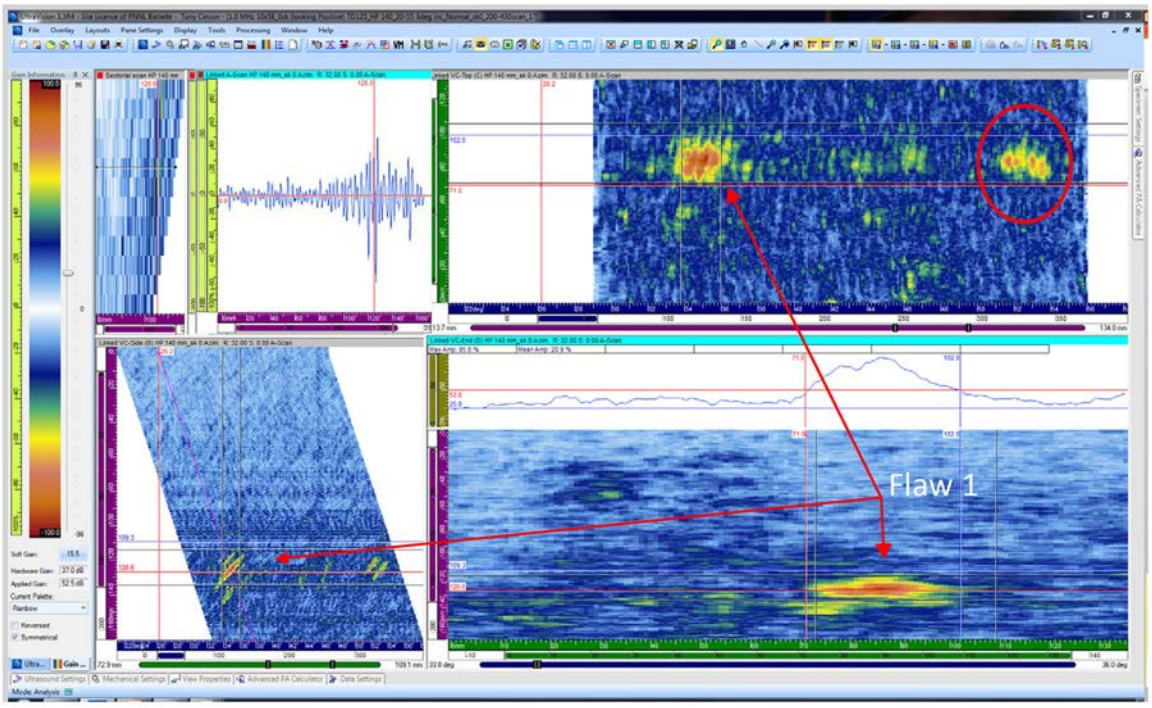

Figure 6.27. DM-05 CW Skew 0 View of Axial Flaw 1 Region with Implantation Artifact from Circumferential Flaw 4 Circled in Red

An example of a welding fabrication flaw or ID geometrical response can be seen in specimen DM-10 in Figure 6.28 where the scan region for axial flaw 3 includes detection of a strong ID response at 25 degrees in the circumferential (scan) direction. This location is outside of the circumferential flaw 1 region (scan positions between 34 and 47 degrees), or near any of the possible implantation artifacts associated with flaw 1. Figure 6.28 shows a CW skew 0 view of the region with the extra indication circled in red in the C-scan view. For reference, axial flaw 3 is indicated by the arrows in the figure.

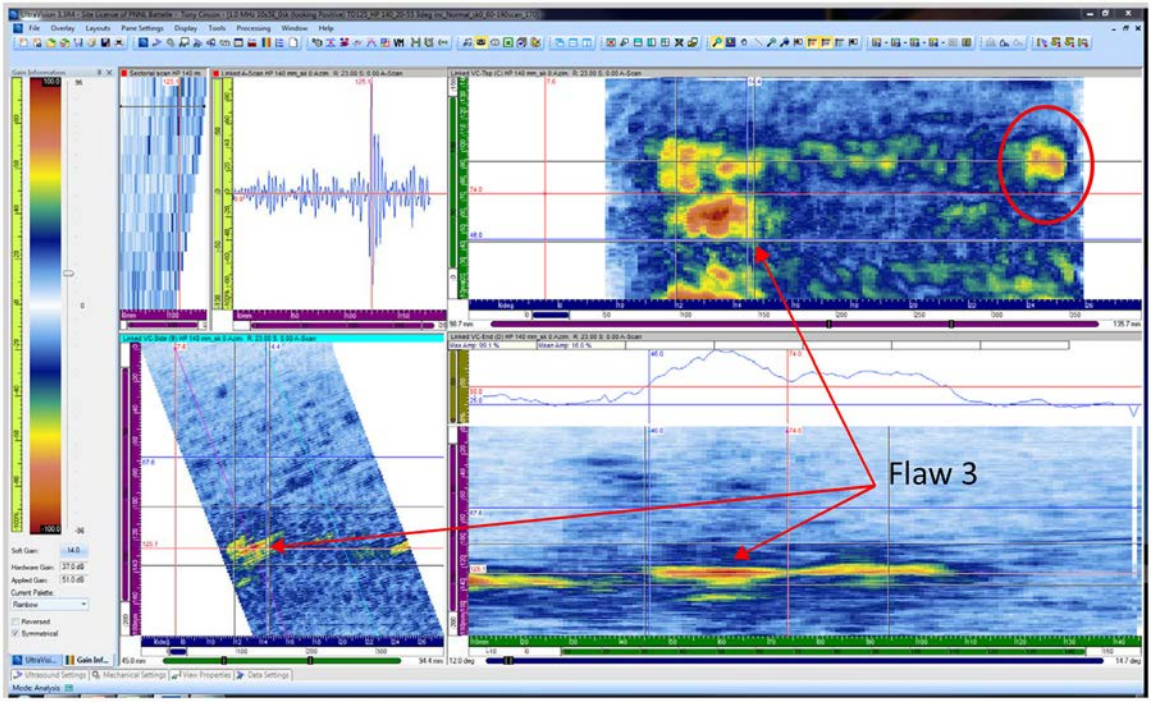

Figure 6.28. DM-10 CW Skew 0 View of Axial Flaw 3 Region with Bonus Indication Circled in Red

Other responses associated with axially oriented flaws have also been observed during imaging of axial flaw 3 in DM-10, when inspected from the CCW direction and with a 0 skew. Illustrated in Figure 6.29, an artifact circled in red is located adjacent to axial flaw 3 and could have formed as a result of the welding process or flaw implantation. Indications such as these can lead to flaw over-sizing.

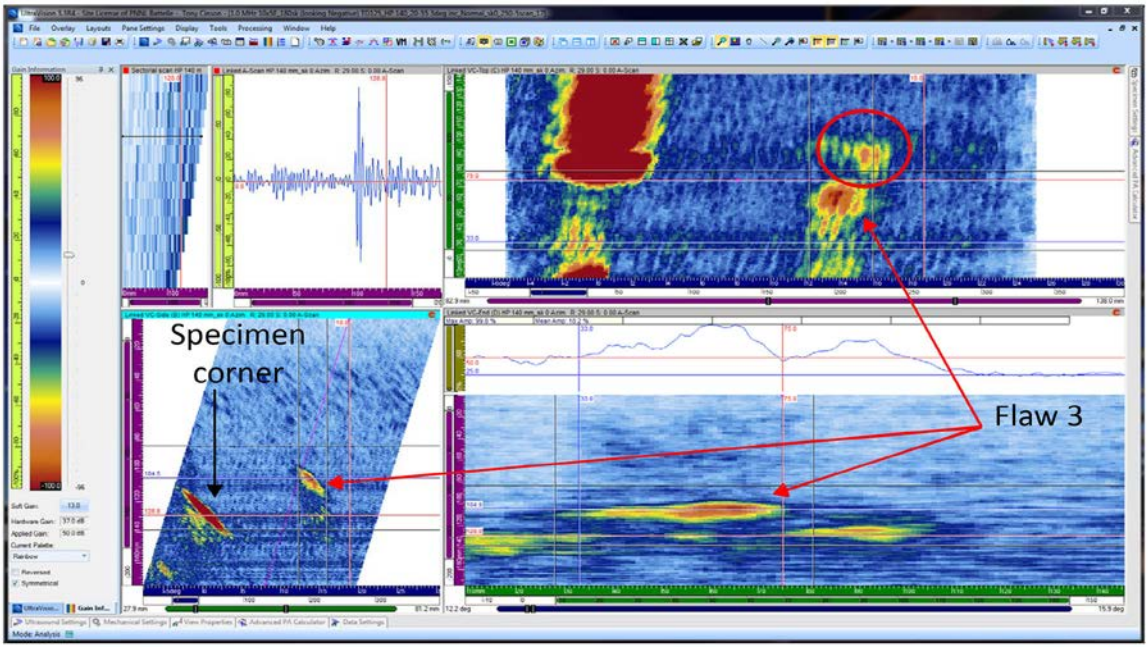

Figure 6.29. DM-10 CCW Skew 0 View of Axial Flaw 3 with Artifact Circled in Red

In summary, limited 1.0-MHz circumferential data (to detect axial flaws) were acquired in axial flaw locations on the mock-ups. All of the axial flaws were detected. Data analyses also reveal that (as similarly seen in the 0.5-MHz data) responses from implanted circumferential flaws were detected (see previous parametric study discussion and Appendix F). It is therefore assumed that these flaws were detected as a result of implantation artifacts. Additionally, artifacts were found adjacent to two of the three axial flaws which could lead to miss-characterizing the targeted flaw, or over-sizing the length of the targeted flaw. The two artifacts were located in the safe end material which should not have been disturbed during the flaw implantation process. These findings indicate that the mock-ups as evaluated with a nominal 1.0-MHz PA probe show multiple artifacts that could be misidentified as flaw indications.

6.2.2.3 Welding Fabrication Flaws Detected During Axial Scanning of Mock-ups

Axial scanning was conducted on the mock-up specimens in the regions of the circumferential flaws and limited surrounding material. With access to only the safe-end side of the weld because of the short nozzle section, all five of the circumferential flaws were detected and characterized. This section focuses on additional fabrication features that are not intended flaws as identified in the true-state descriptions of the mock-up specimens, i.e., circumferentially-oriented flaws resulting from the typical welding process and direction.

Figure 6.30 shows the CW view of circumferential flaw 3 region in DM-05. The data gates have been applied to isolate the region immediately above the ID surface and do not include the intentionally placed target flaw. The C-scan view shows several indications in the weld region (circled in red) that are likely a result of the welding process. The B-scan view shows the depth variation of the indications. Similarly, Figure 6.31 shows the CW view of circumferential flaw 4 with similar strings of indications found at the mid-wall depth.

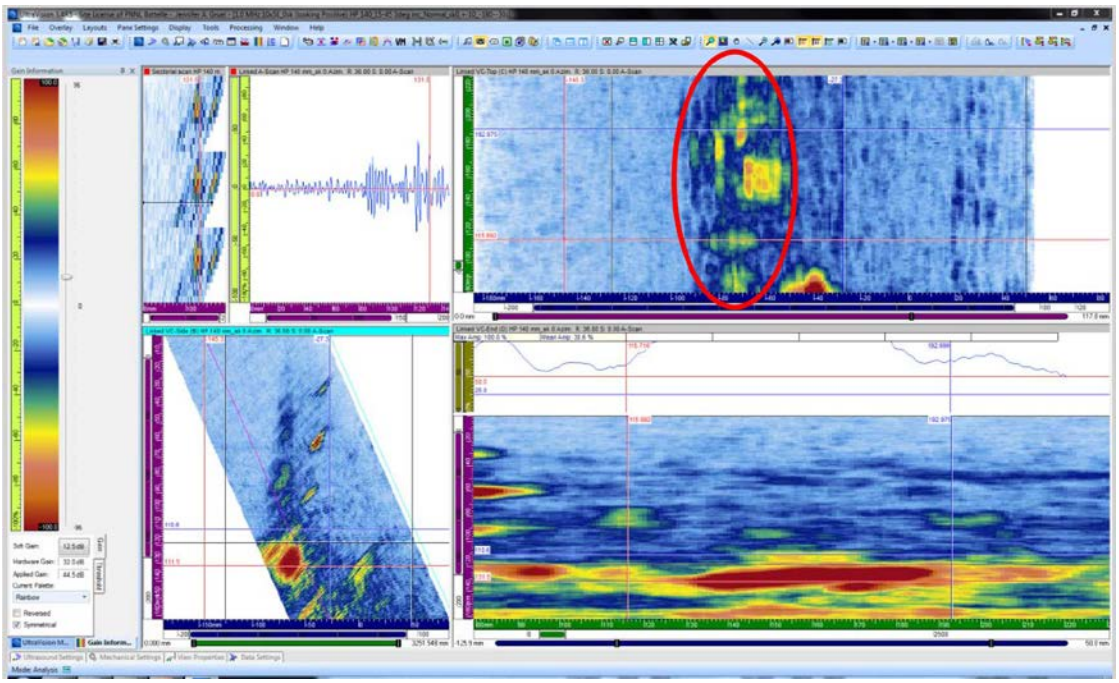

Figure 6.30. Skew 0 View of DM-05Weld Region Indications Adjacent to Circumferential Flaw 3 (all circled in red)

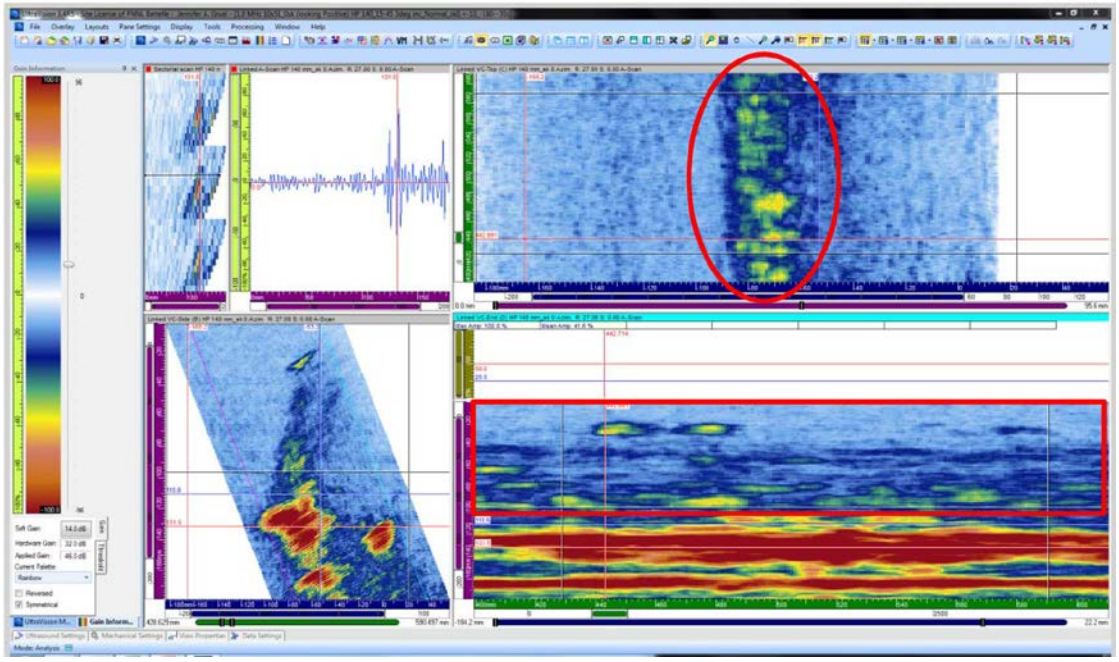

Figure 6.31. Skew 0 View of DM-05 Weld Region Indications Adjacent to Circumferential Flaw 4 (all circled/boxed in red)

Specimen DM-10 also presented a range of fabrication flaws present in the weld region of the specimen. The circumferential flaw 4 region depicted in Figure 6.32 highlights some of the stronger, more detectable strings of fabrication indications present. Here, the fabrication flaws circled in red actually provide a stronger signal response than the intentionally placed flaw (marked by a red arrow) in this region.

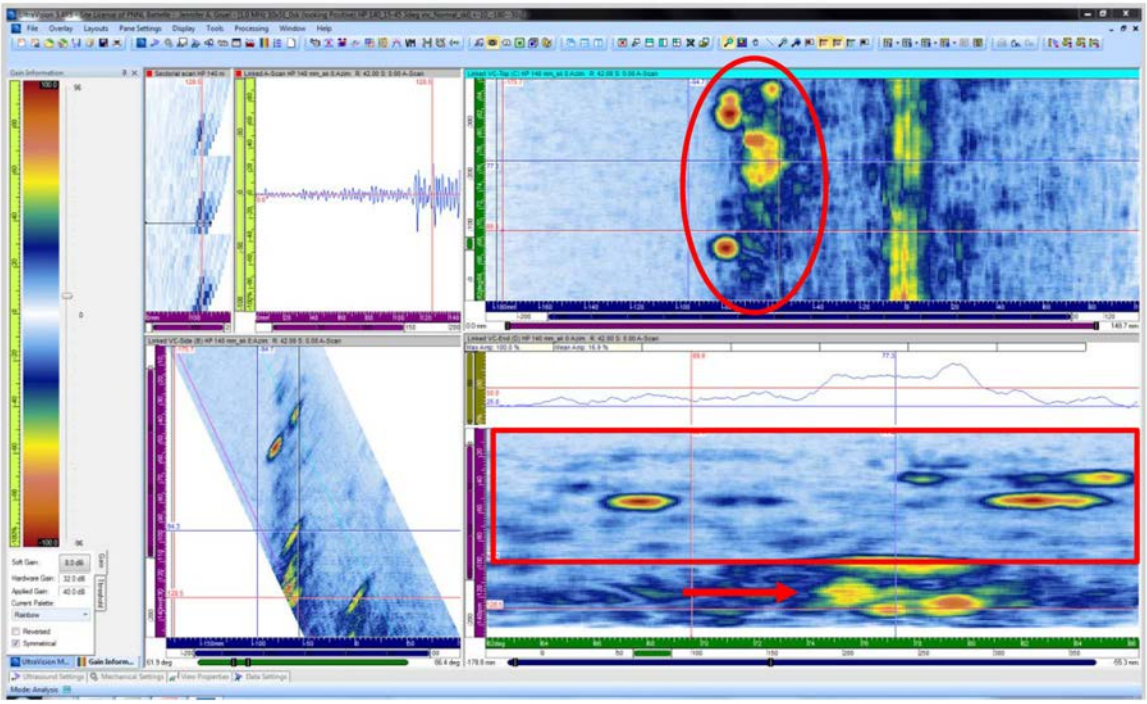

Figure 6.32. Skew 0 View of Axial Flaw 4 DM-10 (red arrow) with Weld Region Indications Circled/Boxed in Red

The presence of the fabrication flaws can have a significant influence on the detection and/or characterization of service degradation present in field welds. It is for this reason that performance demonstration mock-up specimens are expected to have a population and variety of fabrication flaws similar to those that would exist in typical field component welds. An assessment of acoustic features between the NAPS-1 mock-ups and actual DMWs is discussed in more detail in Section 6.2.5.

6.2.2.4 Results from Circumferential Flaw Evaluation

The mock-ups were scanned in the axial direction to assess and validate detection of the five implanted circumferential flaws. All of the circumferential flaws were detected. Results of the data analyses are listed in Table 6.6 and include the measured flaw length, depth, and SNR. Figure 6.33 shows circumferential flaw 2 from DM-05 examined at the refracted angle of 33 degrees. The flaw response is circled in the figure. This flaw has strong specular reflections from multiple locations along its through-wall extent that facilitate characterization. Occasionally it was difficult to separate flaw ID corner responses from weld geometrical signals; however, the upper portion of a flaw could be isolated in most

cases. The SNRs as measured at the ID were between 13.5 and 16.1 dB. The full set of data images are presented in Appendix D.

Table 6.6. Results of 1.0-MHz PA Data Analyses of Circumferential Flaws

Flaw	Measured Length, mm (in.)	True Length, mm (in.)	Measured Depth, mm (in.)	True Depth, mm (in.)	SNR (dB)
DM-05-2	120.3 (4.74)	127.3 (5.01)	67.5 (2.66)	62.0 (2.44)	15.1
DM-05-3	56.0 (2.20)	48.3 (1.90)	20.9 (0.82)	20.8 (0.82)	15.1
DM-05-4	75.0 (2.95)	55.9 (2.20)	22.1 (0.87)	23.7 (0.93)	16.1
DM-10-1	113.0 (4.45)	108.0 (4.25)	58.3 (2.30)	53.0 (2.09)	14.8
DM-10-4	72.0 (2.83)	73.7 (2.90)	34.2 (1.35)	32.1 (1.26)	13.5

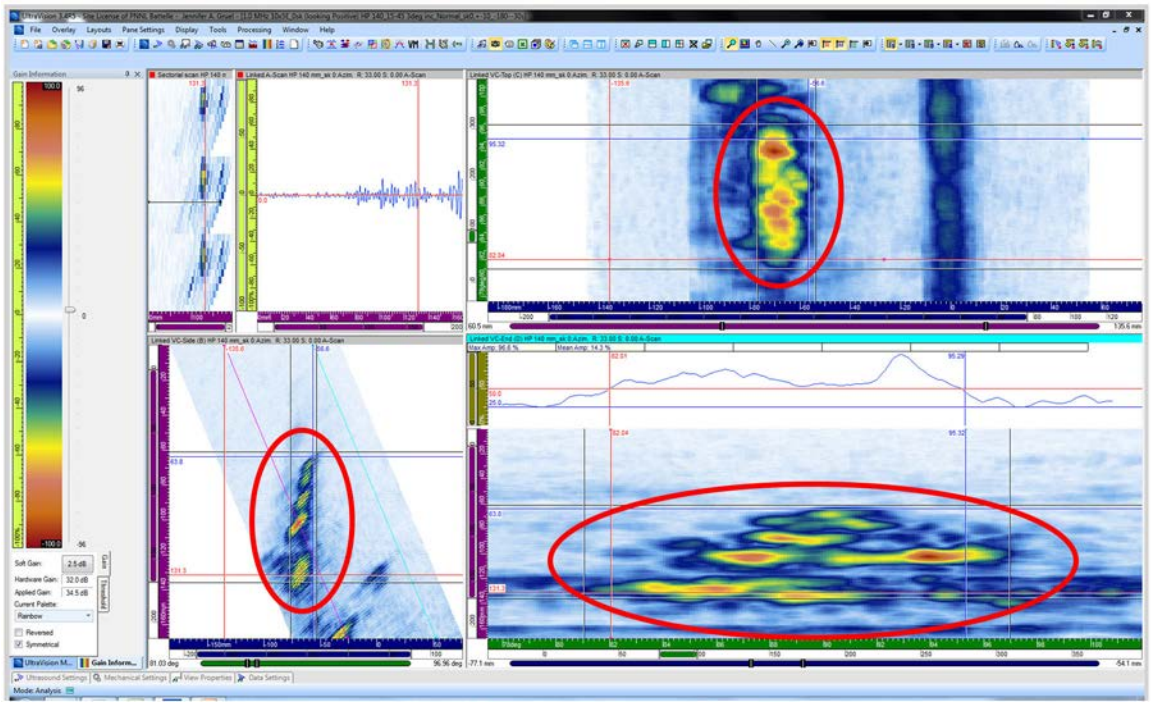

Figure 6.33. 1.0-MHz Axial Scan, Circumferential Flaw 2 in DM-05 Circled in Red

1.0 MHz Summary

All of the axial flaws were detected and characterized using circumferential scan data. However, an artifact adjacent to, or associated with, flaw 1 in DM-05 was initially identified as the target flaw because the artifact had a stronger response than the flaw. After further review the artifact was determined to be in the safe end material and a response in the weld/butter material was detected and characterized as the intended flaw. The SNR of flaw 1 was low with an average value of 8.0 dB as compared to SNRs of 16.0 and 14.2 dB for flaws 2 and 3, respectively, in DM-10. An artifact extending into the safe end region at

flaw 3 in DM-10 was also found. While the artifact amplitude was lower than the flaw 3 response, its proximity to the flaw could lead to an over-sizing of flaw length. Length-sizing RMSE for these three flaws was approximately 19.8 mm (0.78 in.), which is slightly greater than the ASME requirement of 19.0 mm (0.75 in.). Tip-diffracted and upper (mid-wall) specular reflectors were seen in some of the data, more frequently than in the 0.5-MHz data; this was expected due to the shorter wavelength resulting in slightly better resolution at 1.0-MHz. Circumferential flaw implantation artifacts were also observed in axial flaw scans. As observed with the 0.5-MHz encoded data and using image analysis techniques, the circumferential flaw artifacts can be spatially resolved and did not interfere with detection or sizing of the axial flaw indications.

In the axial scan data for detection of circumferential flaws, numerous mid-wall fabrication flaws were evident. These mid-wall indications were detected with the 1.0-MHz probe and not the 0.5-MHz probe, most likely due to the improved resolution (smaller wavelength) of the 1.0-MHz probe, but responses were also influenced by the shorter primary focal zone of the 1.0-MHz probe. The five circumferential flaws were detected and characterized with SNRs in the 14–16 dB range.

6.2.3 PA-UT Mock-up Data—2 MHz

Additional data were acquired on the North Anna mock-ups with a 2.0-MHz PA probe to assess detection of both axial and circumferential flaws. The data were reviewed for flaw detection and characterization, which included a measurement of flaw length, depth, and SNR. Initial axial flaw data analyzes are presented in Section 6.2.3.1. Subsequent analyses included a limited noise or artifact detection assessment, and these results are discussed in Sections 6.2.3.2 and 6.2.3.3. The circumferential flaw results are presented in Section 6.2.3.4.

6.2.3.1 Results from Axial Flaw Evaluation

North Anna mock-ups DM-05 and DM-10 were evaluated at 2.0 MHz with scanning protocols similar to those used for the 1.0-MHz data set. The pulser voltage was set to 200V with a square wave pulse width of 250 nsec to match the 2.0-MHz probe center frequency. Figure 6.34 illustrates the HP focused image from the axial flaw 1 region and the three SDHs in DM-05. A complete display of the DM-05 and DM-10 data images is contained in Appendix E.

At 2.0 MHz, none of the implanted axial flaws were detected using the varied scan directions and skew angles. Only the SDHs are visible in the flaw 1 segment scan. In all of the data views, the weld area is identifiable by a diminished response (or clean) region, as seen in the center of the D-scans, boxed in red on Figure 6.34. The implanted axial flaws are located in this region, but a lack of any specular reflections from the flaws in these regions of interest, leads to a ‘no detection’ result. Typically, ‘no detection’ assessments are made when the material under evaluation is acoustically “noisy” and convolutes the image data with many spurious signals that either mask a targeted flaw, or reduce a flaw response below ambient material noise. However, in this situation, the lack of response from the ID flaw region when propagating a 2.0-MHz sound field through the weld volume, as seen in the entire data set, indicates the austenitic weld material has a significantly deleterious effect on beam propagation. The beam is severely scattered and/or attenuated at this inspection frequency, preventing adequate flaw responses from being observed. PNNL simulations corroborate this assessment by indicating that, at 2.0 MHz, sufficient sound field intensities are not likely to extend to the ID surface in this component.

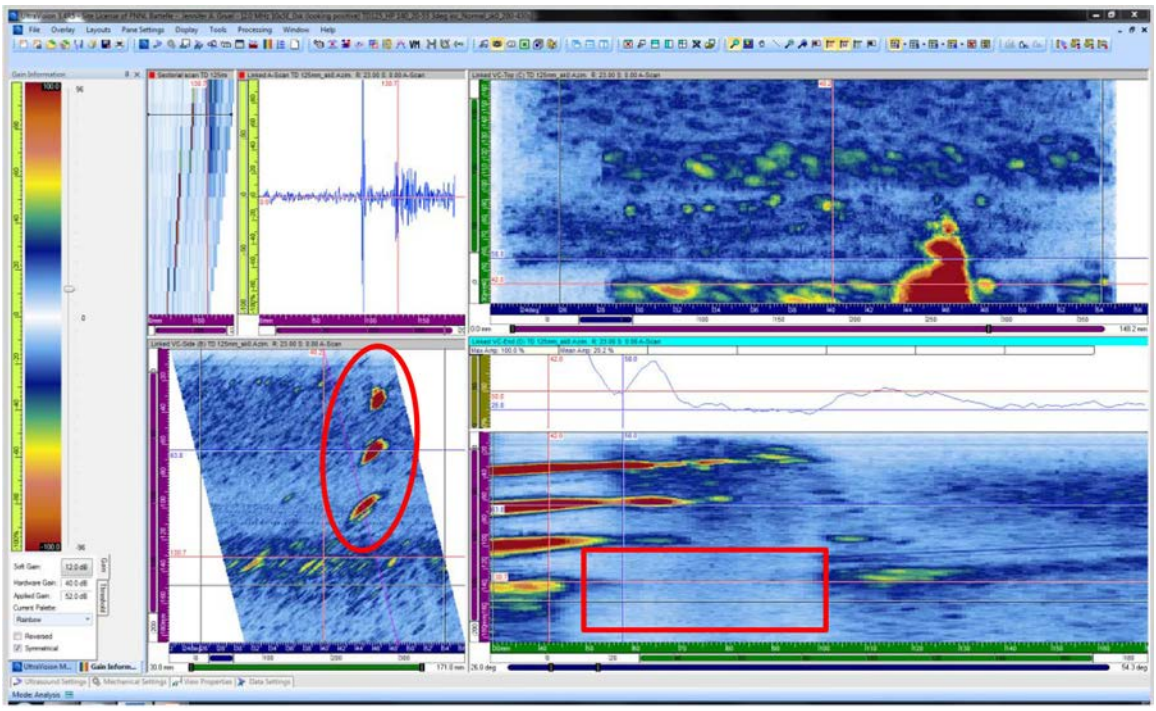

Figure 6.34. Mock-up DM-05 Axial Flaw 1 Region (flaw not detected) and Three SDHs Circled in Red with a TD Focus at 125 mm (4.92 in.). The scan is in the CW direction with a 0-degree skew. ID weld region is boxed in red.

6.2.3.2 Welding Fabrication Flaws Detected During Circumferential Scanning of Mock-ups

Analysis of 2.0-MHz circumferential scan data included an assessment of artifacts previously seen that were neither intentional flaws nor geometric responses. As with the 1.0-MHz data, the 2.0-MHz data scans only covered regions containing the implanted flaws and not the full 120-degree circumference of the mock-ups. Unlike the 0.5 MHz and 1.0-MHz data that displayed several ID response artifacts in regions of, or adjacent to, the intentional flaws, the 2.0-MHz data exhibit a lack of signal response at the ID flaw/weld region, but the presence of a significant number of weld fabrication flaws that begin in mid-wall and extend to the OD were observed. Figure 6.35 shows a cluster of weld fabrication flaws circled in red in the C-scan, B-scan, and D-scan views from the CCW data in the flaw 2 region of DM-10. The fabrication flaws are located directly in the weld region of the component with volumetric-like responses indicative of slag or porosity as a result of the welding process.

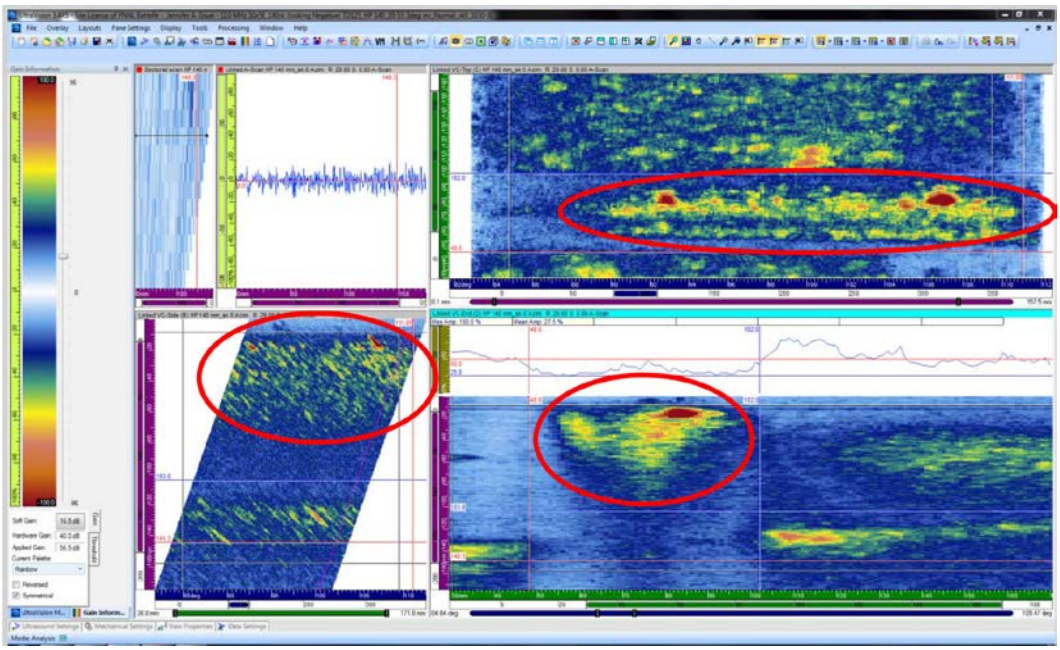

Figure 6.35. DM-10 CCW Skew 0 View of Axial Flaw 2 Region (flaw not detected) with Weld Fabrication Flaws Circled in Red

Data from the axial flaw 3 region of DM-10 also has a significant population of fabrication flaws in the weld region as circled in red on Figure 6.36. The responses again appear volumetric.

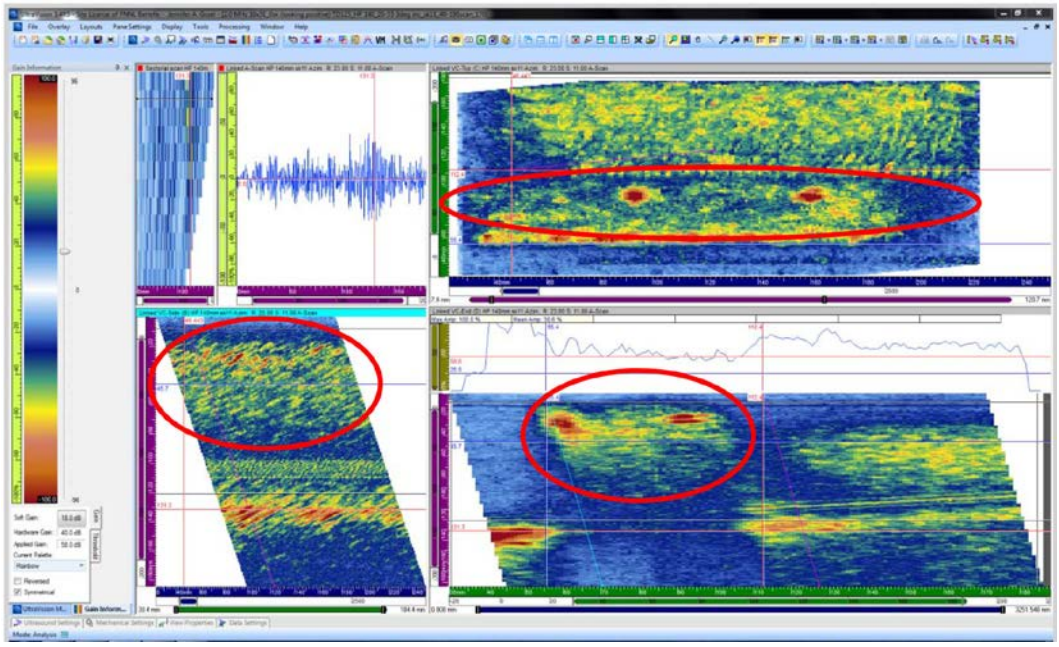

Figure 6.36. DM-10 CW Skew 10 View of Axial Flaw 3 Region (flaw not detected) with Weld Fabrication Flaws Circled in Red

In summary, circumferential data (to detect axial flaws) were acquired in axial flaw locations in the mock-ups. Data analyses revealed that, while the implanted axial flaws could not be detected, many fabrication flaws were revealed in the mid- to upper-weld region. However, circumferential scan data as analyzed here are not ideal for detection or characterization of fabrication flaws, as the scan direction is in the same plane as the weld pass (weld bead). The following Section 6.2.3.3 describes data analyzed for detection of circumferential flaws where the scan direction is orthogonal to the weld pass.

6.2.3.3 Welding Fabrication Flaws Detected During Axial Scanning of Mock-ups

Axial scanning was conducted on the mock-up specimens in the regions of the circumferential flaws and limited surrounding material. Even with limited access to only the safe-end side of the weld due to the short length of the nozzle side, all five of the circumferential flaws were detected and characterized. This section focuses on the additional features that are not prescribed flaws as identified in the true-state descriptions of the mock-up specimens. Likely, the indications shown in this section are a result of welding fabrication flaws residing in these mock-ups.

Figure 6.37 shows the CW view of the circumferential flaw 3 region in DM-05. The data gates have been applied to isolate the region above the ID region. The C-scan view shows the many indications in the weld region (circled in red) that are likely a result of the welding process. The B-scan view shows the depth variation of the indications. Similarly, Figure 6.38 shows the CW view of circumferential flaw 4 with similar strings of indications found mid-wall.

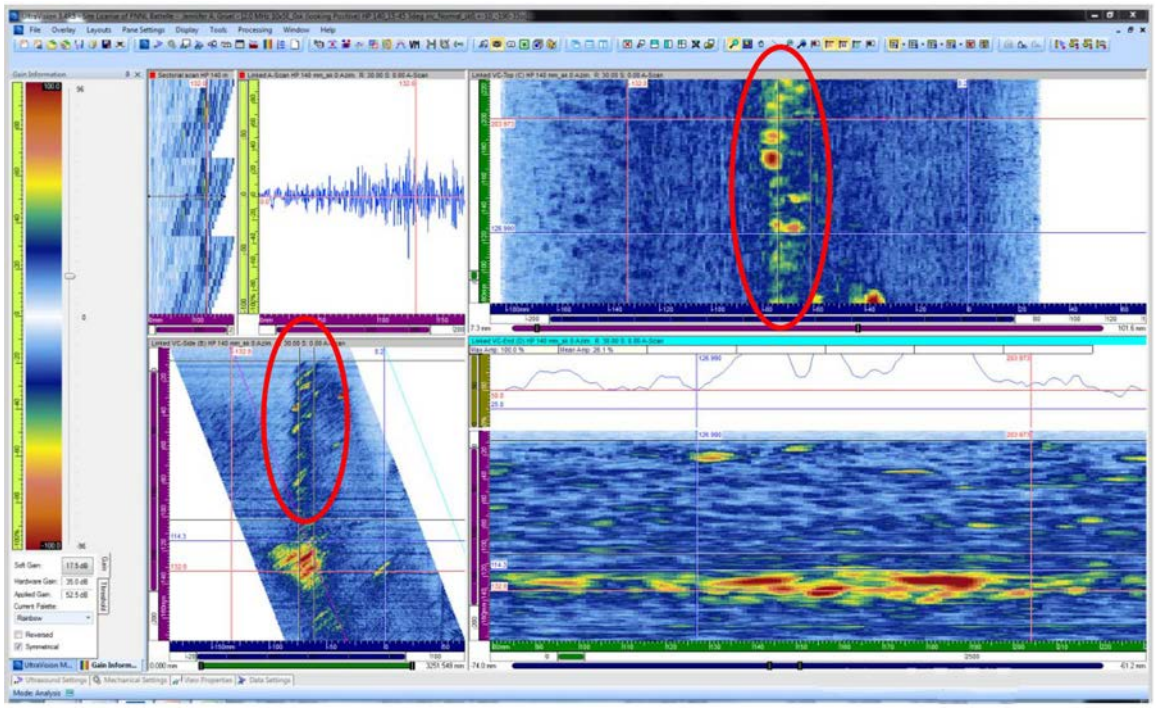

Figure 6.37. Looking Positive Skew 0 View of Circumferential Flaw 3 DM-05 (indicated by red arrow) with Weld Fabrication Flaws Circled in Red

Specimen DM-10 also presented a range of fabrication flaws present in the weld region of the specimen. The circumferential flaw 4 region depicted in Figure 6.39 highlights some of the stronger, more detectable strings of fabrication indications present. Here, the fabrication flaws (circled and boxed) are actually stronger than the intentional flaw of the region, marked by the red arrow.

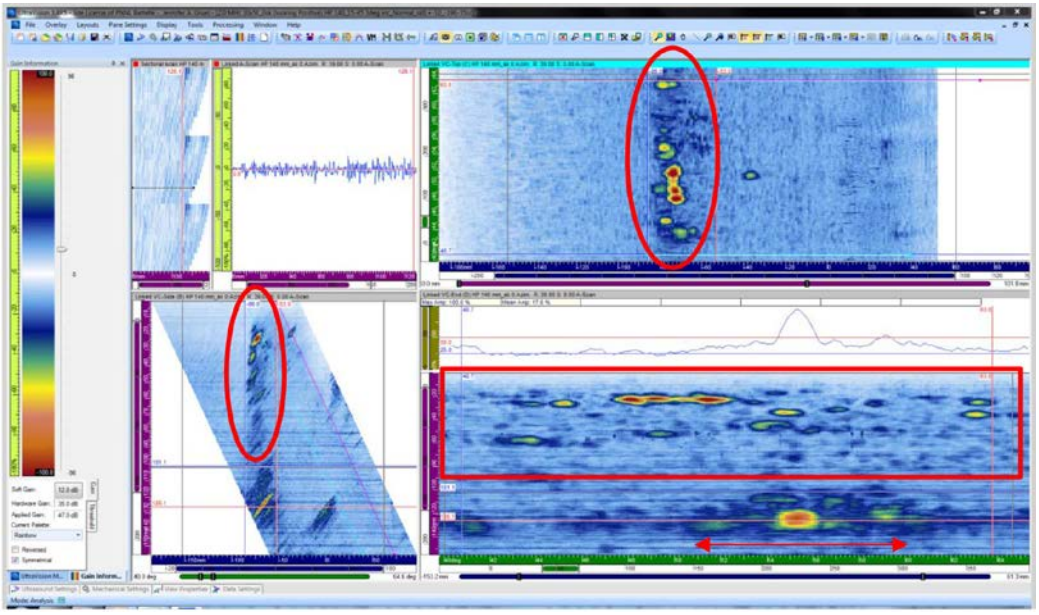

Figure 6.38. Looking Positive Skew 0 View of Circumferential Flaw 4 (indicated by red arrow) DM-05 with Weld Fabrication Flaws Circled and Boxed in Red

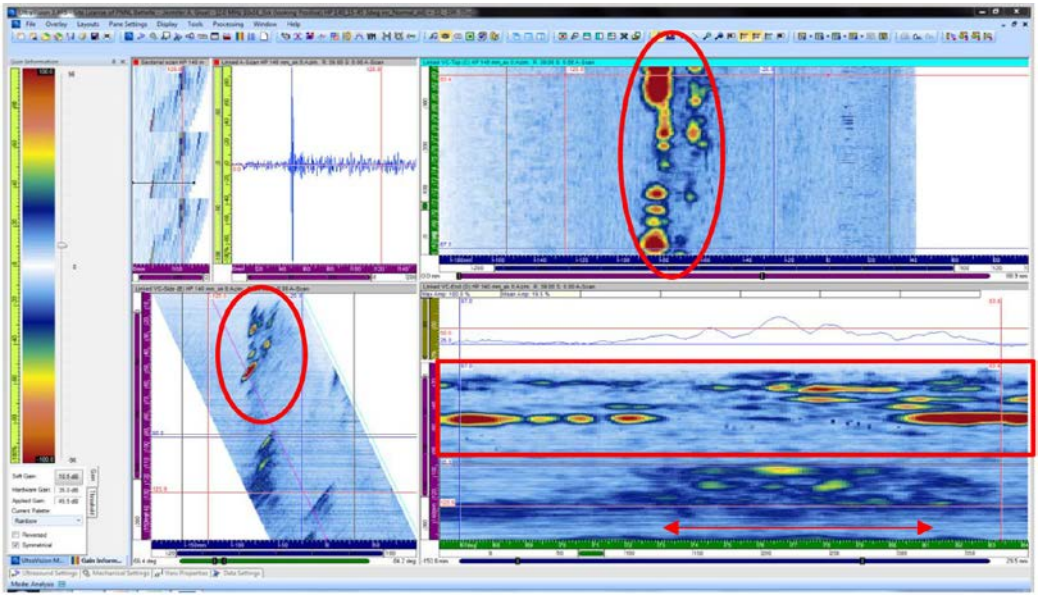

Figure 6.39. Looking Positive Skew 0 View of Circumferential Flaw 4 (indicated by red arrow) DM-10 with Weld Fabrication Flaws Circled and Boxed in Red

6.2.3.4 Results from Circumferential Flaw Evaluation

The mock-ups were scanned in the axial direction for the detection of the five implanted circumferential flaws. Results of the data analyses are listed in Table 6.7 and include the measured flaw length, depth, and SNR. Figure 6.40 shows circumferential flaw 1 (circled) from DM-10 examined at the refracted angle of 36 degrees. This flaw also has strong specular reflections from multiple locations along its through-wall extent that facilitate characterization. All of the circumferential flaws were detected; however, occasionally it was difficult to separate flaw ID corner responses from weld geometrical signals. The SNRs as measured at the ID were between 13.6 and 18.6 dB. The full set of data images are presented in Appendix E.

Table 6.7. Results of 2.0-MHz PA Data Analyses of Circumferential Flaws

Flaw	Measured Length, mm (in.)	True Length, mm (in.)	Measured Depth, mm (in.)	True Depth, mm (in.)	SNR (dB)
DM-05-2	101.0 (3.98)	127.3 (5.01)	62.9 (2.48)	62.0 (2.44)	15.6
DM-05-3	62.0 (2.44)	48.3 (1.90)	18.2 (0.72)	20.8 (0.82)	13.6
DM-05-4	16.0 (0.63)	55.9 (2.20)	25.0 (0.98)	23.7 (0.93)	16.7
DM-10-1	114.9 (4.52)	108.0 (4.25)	28.5 (1.12)	53.0 (2.09)	17.4
DM-10-4	55.0 (2.17)	73.7 (2.90)	34.2 (1.35)	32.1 (1.26)	18.6

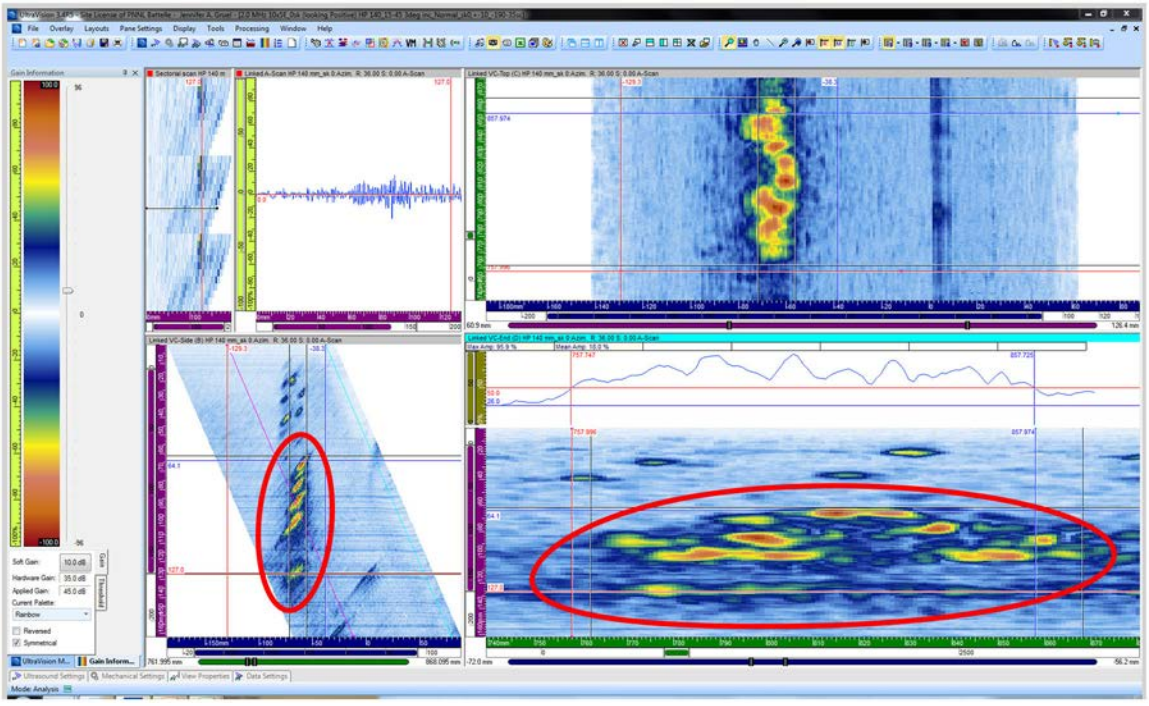

Figure 6.40. 2.0-MHz Axial Scan, Circumferential Flaw 1 (circled in red) in DM-10

6.2.4 Summary of Phased-Array Examinations on NAPS-1 Mock-ups

North Anna mock-up specimens DM-05 and DM-10 contain several axially and circumferentially oriented ID-connected thermal fatigue cracks that were detected and characterized when examined with PNNL phased arrays at frequencies of 0.5- and 1.0-MHz. Image analyses were completed on the targeted flaws in the spatially encoded phased-array data, resulting in combined (both axial and circumferential flaws) average SNR values of 16.2 dB and 14.1 dB, for the 0.5- and 1.0-MHz data, respectively. The strong signal-to-noise values indicate that these frequencies are well matched for non-destructive examinations of DMW components of similar composition and size to those of the subject NAPS-1 mock-ups.

Data was also acquired at 2.0 MHz; a relatively high frequency for evaluating a thick component such as the NAPS-1 DMW mock-ups. As previously indicated, multiple frequencies were used to determine if other reflections are observed, and their potential impact on the use of the mock-ups for their intended purpose. The 2.0 MHz frequency provides an evaluation of the mock-ups for welding fabrication flaws and possible artifacts at a greater resolution than previous data sets. As the probe was unable to adequately insonify the ID surface through the weld material when scanning circumferentially, none of the axial flaws could be detected. However, all circumferential flaws were detected and sized at this frequency. Numerous mid- and upper-wall fabrication flaw responses were observed in the weld region.

Welding fabrication flaws were detected in the North Anna DMW mock-ups when examined at frequencies of 1.0- and 2.0-MHz. In certain cases, strings of these embedded flaws extend from the ID region of the specimen up through the weld volume. The presence of welding fabrication flaws is representative of actual field weld conditions. The use of the mock-ups for training is further discussed in Section 6.2.5.

The work presented here indicates that the presence of implantation artifacts and fabrication flaws in these mock-ups does not preclude lower frequency (1.0 MHz or below) encoded PA-UT from detecting and discriminating the targeted flaws. However, based on the assessment conducted here, the artifacts and fabrication flaws in the NAPS-1 mock-ups present a significant degradation in signal fidelity, and would impact detection and discrimination capabilities when employing non-encoded, manual, real-time examination methods. With such markers, the mock-ups would not be representative of flaws in the field which raises questions with respect to the effectiveness of the training that an examiner would have received.

6.2.5 Signal Response Comparison of Mock-ups to Field Components

On December 11 and 12, 2012, two PNNL personnel accompanied a representative from NRC Office of Research on a site visit to Dominion Generation Headquarters in Richmond, Virginia, to meet with the licensee's UT Level III and an EPRI NDE Center representative to discuss the mock-ups. The objective of this visit was to evaluate the ultrasonic signal responses from weld material in the actual component welds versus the NAPS-1 site-specific mock-ups to determine if the site-specific mock-ups are truly representative/realistic or if substantial differences exist between material properties, fabrication flaws, and geometric features of the mock-ups and the actual field welds.

UT vendor PA data acquired by LMT (in 2009 and 2012) on both the hot and cold leg welds at 1.5 MHz were compared to UT data acquired by the EPRI NDE Center on the mock-ups (again at

1.5 MHz) along with PNNL-acquired data (at both 1.0 and 2.0 MHz) on the mock-ups. The EPRI data were acquired with identical probes to LMT's field data and employed similar scan procedures. Both axial- and circumferential-oriented scans were evaluated. The analysis focused on weld material, interfaces, and heat-affected zone (HAZ) areas. UT responses from weld geometry and any fabrication flaws observed were assessed. No actual field data were provided to PNNL; however, screen shots of the field data were provided for subsequent review. PNNL was allowed to take these screen captures offsite. Analysts from EPRI, Dominion, and PNNL operated side-by-side laptops to simultaneously evaluate field- and laboratory-acquired data. The team isolated data "slices" in the same regions of the welds in order to conduct relevant assessments. The results provided a qualitative comparison between data sets. Data files were reviewed by weld (six different welds), inspection angle (25° and 35° angles were chosen), skew (0°, ±10°, ±25°, and ±35° skews were chosen), direction (CW versus CCW), and scan orientation (axial versus circumferential). Figure 6.41 depicts examples of the refracted angles and skews chosen for comparison in the circumferential scan orientation. The component's true 11-degree OD taper is not shown in Figure 6.41 for simplicity to show skew angles.

One cold leg weld was fully evaluated while individual quadrants of the remaining two cold leg welds were selected to assess trends seen in the primary weld that was initially examined. In addition, data from hot leg welds were provided by Dominion and a review and screen capture exercise was conducted on those components as well. Figures 6.42 and 6.43 show example data containing fabrication flaws and general weld 'noise' from the field welds.

The field data (acquired by LMT) and the EPRI mock-up data were captured with 12 mm × 1.9 mm (0.47 in. × 0.07 in.) resolution (index increment × scan step increment) and PNNL data were acquired with 1 mm × 1 mm (0.04 in. × 0.04 in.) resolution. The course index field data and EPRI mock-up data covered the necessary weld volume by electronically skewing the PA beam into the weld zone. Data were acquired with skews ±35 degrees in 2.5-degree increments. The comparative evaluation was challenging to configure properly between data sets; however, a suitable process was developed enabling the analysts the ability to establish similar views of the data. It was determined that a comparison of LMT field data and the EPRI mock-up data would provide an alternative assessment where frequency, incremental step size, and scan resolution are the same. It should be noted that PNNL chooses to acquire PA data at smaller index and scan increments than typically used by EPRI and field vendors. The smaller increments provide greater resolution and richer imaging capabilities, but the data file size becomes significantly larger. This can be a problem for field vendors with limited capabilities to handle such files. Additionally, it has been suggested that when acquiring data with finer increments, more time is needed for scans to be completed. However, PNNL has not seen a dramatic increase in scan time as a result of finer index and scan increments; therefore, it is believed that coarser scans typically performed in the field are the product of economic considerations.

It was noted that the EPRI-acquired data were taken with a DYNARAY PA-UT instrument and an 8 × 4 element probe using the full number of elements (no splitter cable used). The field-acquired data were taken with an Omniscan PA-UT instrument and an 8 × 4 element probe, but they linked two elements together (using a splitter cable). This particular configuration was used in the field so that the PDI-qualified procedure could be met. The PDI-qualified procedure specifies the use of a 16-element PA probe. To maintain the full aperture of the 8 × 4 (32 total) element array, individual elements were paired to achieve a 4 × 4 (16 total) element array. This difference could have implications to the directivity and focusing (delay laws) between the two different data sets. In addition, the pulser settings were slightly

different. The Ominscan pulser voltage was 90 V with a 333-ns pulse duration, while the DYNARAY pulser voltage was 200 V and 330-ns pulse duration.

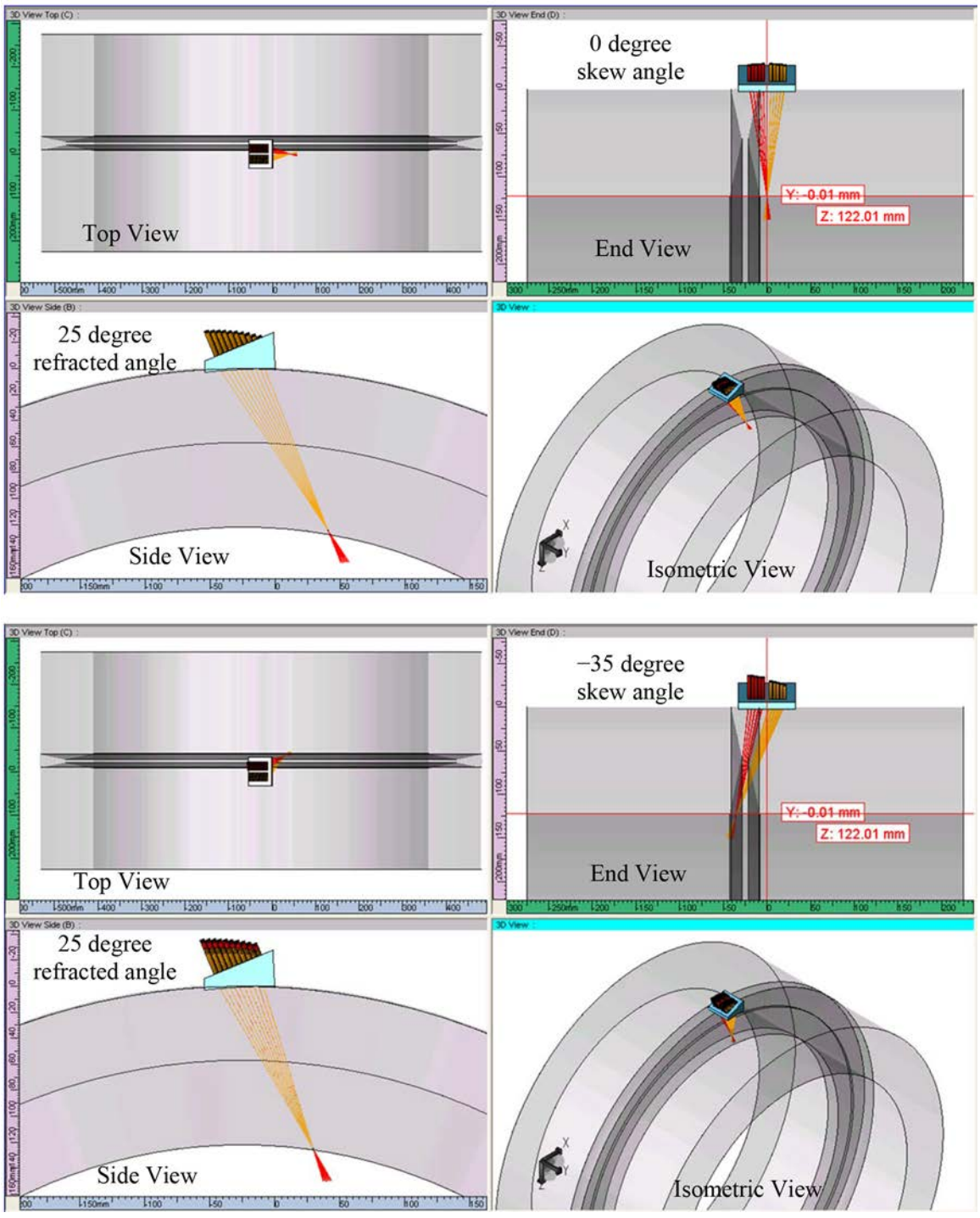

Figure 6.41. Examples of Refracted Angles and Skews Chosen for Comparison in Axial Flaw Detection Scans. Focal law calculator representation of 25-degree refracted angle at 0-degree skew (top) and −35 degree skew (bottom).

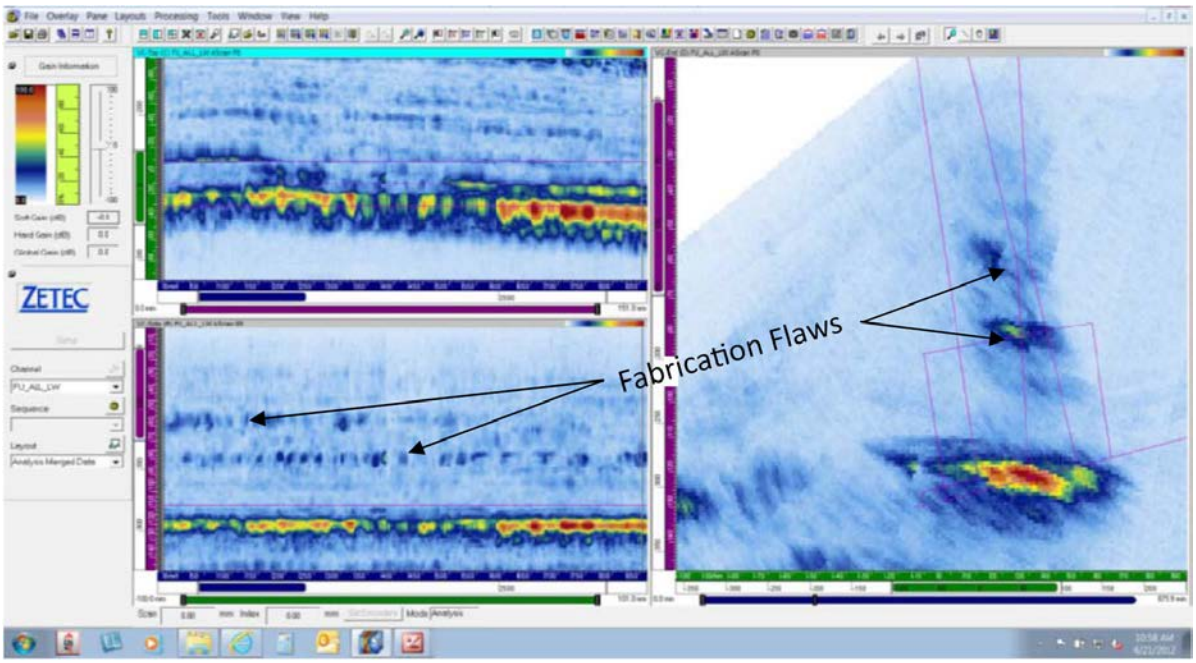

Figure 6.42. Axial Scan Data from a Field Weld

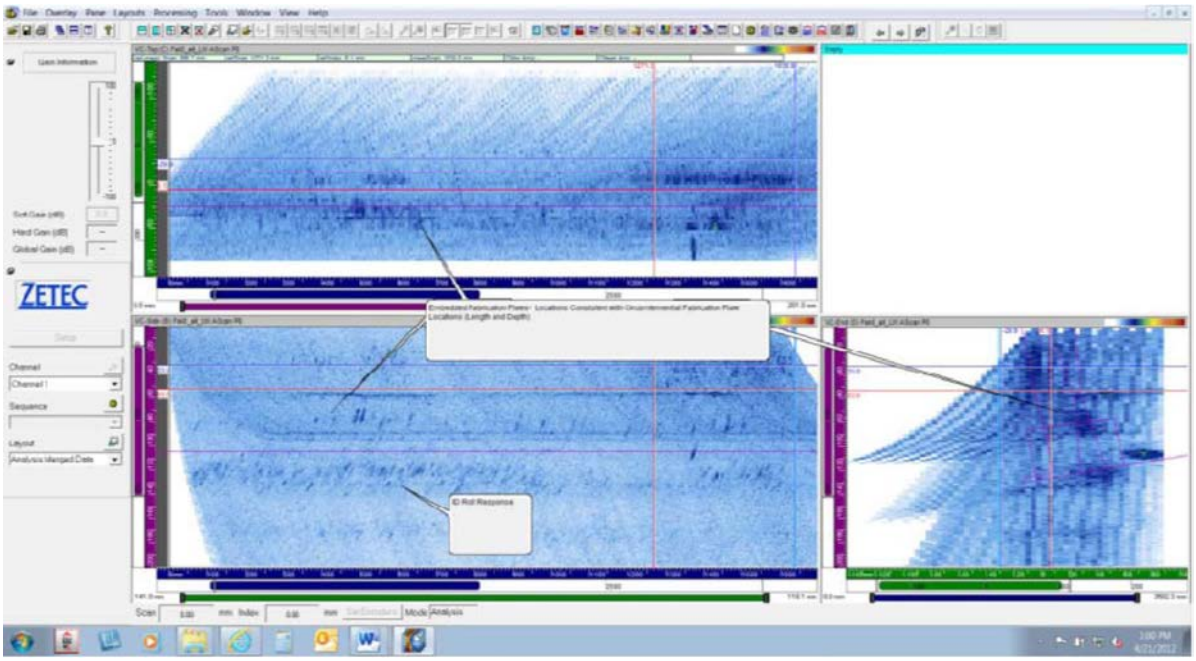

Figure 6.43. Circumferential Scan Data from a Field Weld – "Weld Noise" Noted

A comparative data analysis "process" was developed among the analysts to isolate similar volumes with similar gains and dynamic ranges, and then these volumes were captured via a screen capture. These screen captures were used to obtain a qualitative comparison between material noise in the welds of both the mock-ups and the field welds. Dominion personnel stated that the field welds were shop-fabricated

welds, made in a similar fashion to the way the mock-up welds were fabricated. The licensee stated that circumferential flaws were introduced into the mock-ups during the weld fabrication, while the axial flaws were implanted after initial weld fabrication. Additional screen captures with gated weld volumes (eliminating the ID signal response) were captured at 25-degree and 35-degree skews showing full weld coverage in the circumferential scanning mode.

In a preliminary look at the vendor-acquired circumferentially scanned data (looking for axial indications), a comparison of CW and CCW data over the same field weld volumes, frequencies, and skews indicates that the CCW data are generally 10% more noisy than the CW data across the board. Perhaps this is attributed to the direction of welding, but this trend is also evident in base material so this may be due to some other source. The variation in general background noise across CW scans over the various volumes evaluated was of the order of only about 1%.

A trend was noted with regard to the fabrication flaw locations in the field weld data. A tendency was observed for linear fabrication flaws to be located in the mid to lower 1/3 weld volume (closer to the ID) in the field weld data, but similar linear fabrication flaws were observed in the mid to upper (closer to the OD) region of the mock-up data. It is anticipated that this same pattern (linear propensity of fabrication flaws along a specific weld bead) would be evident in the PNNL data; but the PNNL scans were taken in a segmented fashion; that is, PNNL did not acquire full 180-degree segments of data, but rather focused on areas where the flaws were located.

From a review of the data, it was concluded that all materials used in the welds and parent materials for cold legs, hot legs, and mock-ups appeared to be have similar ultrasonic properties. While no certified material test reports (CMTRs) were reviewed by PNNL staff, the licensee stated that the materials came from the same lots of materials, but some were fabricated from different heats. There was no reason to believe that any substantial physical property differences in materials between field components and mock-ups existed that would impact the propagation of ultrasonic energy to any measurable degree. The team of analysts was able to acquire screen captures of vendor-obtained data from both the hot and cold legs. PNNL evaluated the background noise and clutter (fabrication flaws) from the weld and material volumes across a wide spectrum of field and mock-up data from both axial and circumferential scans. A varied distribution of fabrication flaws was evident at different areas throughout the volumes of these components, and the evaluation indicated that the mock-ups and field welds were all within a reasonable range with regard to localization, distribution, and number of fabrication flaws in similar volumes. The sizes of the fabrication flaws were all very small and were very similar to those found in the mock-ups. There were no appreciable or significant differences between the parent materials and welds in the mock-ups versus the same volumes in the field welds. A document package of screen captures was generated and saved for further review and analysis at PNNL. The amount of data reviewed, a combined total of six field hot- and cold-leg welds scanned both axially and circumferentially, was substantial [approximately 19,900 mm (783.5 in.) of circumferential weld length] and more than enough to provide a firm basis for determining the nature and representativeness of the materials and welds contained in the mock-ups.

7.0 Discussion and Conclusions

In support of a request from the U.S. Nuclear Regulatory Commission (NRC) Office of Research (RES), PNNL conducted a technical assessment of the NDE issues and protocols that may have led to missed detections of multiple flaws in a steam generator primary inlet dissimilar metal weld at North Anna Power Station, Unit 1. Throughout the effort, PNNL participated in technical reviews and discussions with NRC staff, EPRI NDE Center personnel, industry and ISI vendor personnel, and ultrasonic transducer manufacturers, to better understand the issues at North Anna.

PNNL's technical assessment was initiated by participating in a site visit to NAPS-1 to evaluate the actual probes and UT responses produced from the manual UT technique, as applied to site-specific DMW flaw mock-ups. In addition, the team conducted a review and assessment of the Technical Justification, developed by EPRI, for acceptance of the manual technique used at NAPS-1. The technical evaluation employed modeling and simulation activities to identify key acoustic variables associated with the manual UT probes used at NAPS-1, and to assess their potential to detect ID surface-connected, axially oriented flaws, given predicted sound field characteristics. Upon receipt of the actual probes and mock-ups at PNNL, laboratory-based UT analyses were performed to obtain confirmatory data for validating the modeling and simulation results. From the data provided here, the reader can compare and contrast the use of encoded, phased-array ultrasonic examination techniques alongside results from both the manual ultrasonic examination protocol implemented at NAPS-1, and encoded results acquired in the laboratory using the actual tandem probes on the mock-ups. Finally, an evaluation of the mock-ups was also conducted, including a comparison of mock-up UT characteristics with actual field data to assess if the parent material/welds of the site-specific mock-ups used at NAPS-1 were representative of actual field welds/conditions. In addition, UT responses from artifacts other than the targeted flaws or geometrical in origin were assessed to determine if their presence could impact detection of the intended flaws.

Axial flaw detection and characterization were the main emphasis of the technical evaluation on the NAPS-1 mock-ups; however, circumferential flaw data have been presented for completeness. PA-UT data were acquired at two different focusing styles over a range of angles. A true-depth focus, where all angles were focused at a constant depth from the OD of the component, and a half-path focus, where the angles were focused at a constant metal path, were used to examine the two DMW mock-ups in the laboratory. The true-depth and half-path data yielded similar responses from both types of flaws.

The probe model developed was validated by the performance of the tandem probe under laboratory conditions. The results of probe modeling and beam simulation were critical in providing a theoretical basis for understanding the performance of the transducers to inform confirmatory work in quantifying actual sound field densities and beam propagation characteristics. Empirical data from sound field mapping and characterization studies shed further light on performance and critical issues associated with the design and operation of the NAPS-1 tandem probes became readily apparent. Initial modeling results indicated the tandem probe configuration, as fabricated, would produce maximum longitudinal mode ultrasonic energy at a refracted angle of approximately 30 degrees. The optimum ID impingement angle in accordance with PDI-UT-10 for detecting axial PWSCC in dissimilar metal welds is between 55-60 degrees. Theoretical simulations validated by empirical assessments showed that the probes produced an ID impingement angle of about 41 degrees. Additionally, based on the small overall probe aperture, adequate sound field intensities appear to be located at only a shallow distance within the component (along the metal path) which would significantly decrease the effectiveness of inspection for

the detection of ID-connected flaws. To better understand performance issues associated with the tandem probes, an empirical assessment of the tandem probe's beam forming capability was performed by creating sound field maps on a fine-grained specimen. This provided insights into certain critical probe attributes that may affect the performance as a function of beam characteristics (spot size, signal strength, frequency content, etc.), spatial coherence, excitation function (voltage, modality), probe design specifications, and sensitivity. The results of this beam mapping study indicated that a lower voltage (200V rather than 450V as employed in the field) square wave excitation function produced the most symmetrical sound beam. Further, the best sound beam emanated from the rear (back) element of the tandem probe, rather than the front element (which was the methodology used for transmission in the field at NAPS-1). As the excitation voltage is increased, the amount of scatter and loss of spatial coherence of the sound field increases. This in turn reduces sensitivity and may lead to a reduced detection capability. Overall results indicate that underlying issues exist with regard to how the probe was deployed, and that it is highly likely the tandem probes were being overdriven at NAPS-1.

In discussions with the licensee, it was determined that circumferential flaws were implanted during the welding process (fit up/assembly of the full mock-up) and if fabricated carefully and placed properly, should not produce significant implantation artifacts, as were discovered during this evaluation. PNNL data acquisition while scanning in the circumferential direction (looking for axial flaws) resulted in the detection of flaw artifacts in four of the five circumferential flaws. These are most likely associated with implantation or excavation processes during fabrication. Real service-induced planar flaws do not typically offer such responses and an inspector conducting a circumferential scan aimed at detecting axial flaws should not ordinarily be able to detect these circumferential flaw responses as readily as the data show. This is especially true at the lower frequency of 0.5 MHz, as the signal response from essentially a knife-edge circumferential reflector that is oriented parallel to the sound beam should provide a nearly non-detectable (very low amplitude, if any) response. The data also show the existence of an axial flaw "artifact" that was evident in the 1.0-MHz PA-UT data, but not observed in the 0.5-MHz PA-UT data.

The assessment also focused on detection performance of conventional manual and encoded techniques with data obtained using the tandem probes on the mock-ups, and phased-array encoded data acquired primarily from the 0.5-MHz and 1.0-MHz PNNL probes (although some PA data at 2.0 MHz was obtained to assess frequency limitations). The performance of the tandem probe on the mock-ups was assessed by contrasting signal responses and SNR values obtained from manual real-time examination data versus results from encoded tandem probe examination data discussed previously, and further illustrated in Appendix B. Using the tandem probes in manual inspection mode with 450V square-wave excitation results in a quite challenging examination where typical SNRs are in the range of 4–6 dB. As previously discussed, the lower 200V square-wave excitation function produced a more symmetric sound beam. Encoded scanning with the tandem probes using an optimal excitation function that does not overdrive the probes provided an opportunity to more effectively detect and characterize the axial flaws in the mock-ups, as the SNRs are in the range of 9–16 dB. The encoded PA-UT results at 0.5- and 1.0-MHz show the capability to detect all targeted flaws in the mock-ups with SNRs up to nearly 20 dB, with off-line (post-) data imaging and analytical capabilities enabling flaws to be reliably discriminated from geometrical reflectors and fabrication artifacts.

The 2.0-MHz PA probe was primarily used to determine the upper limit frequency threshold for inspections of this nature and also provide insights into the prevalence, significance, and impact of mid-to-upper through-wall weld fabrication flaws and implantation artifacts that may have affected the probe performance and inspectability of these mock-ups. The PA data set at 2.0 MHz did not result in

detection of any axial flaws in either specimen, and the lack of ID geometrical response at this frequency shows a deleterious affect due to the weld microstructure. As clearly seen in the 2.0-MHz CCW skew 0 data over axial flaw 3, and the specimen corner regions, a complete signal drop-out in the weld area compared to strong corner-of-block responses (noted with arrows) produced in the wrought carbon and stainless steel areas at this frequency (see Figure 7.1). The lack of corner response in the weld region (circled in red) provides further evidence that sound energy at 2.0 MHz is being significantly redirected or attenuated. PNNL results show that ultrasonic inspections with frequencies approaching 2.0 MHz or above are expected to have a low probability of detection and a less accurate characterization capability for ID-connected flaws in similar thick-walled DMW components.

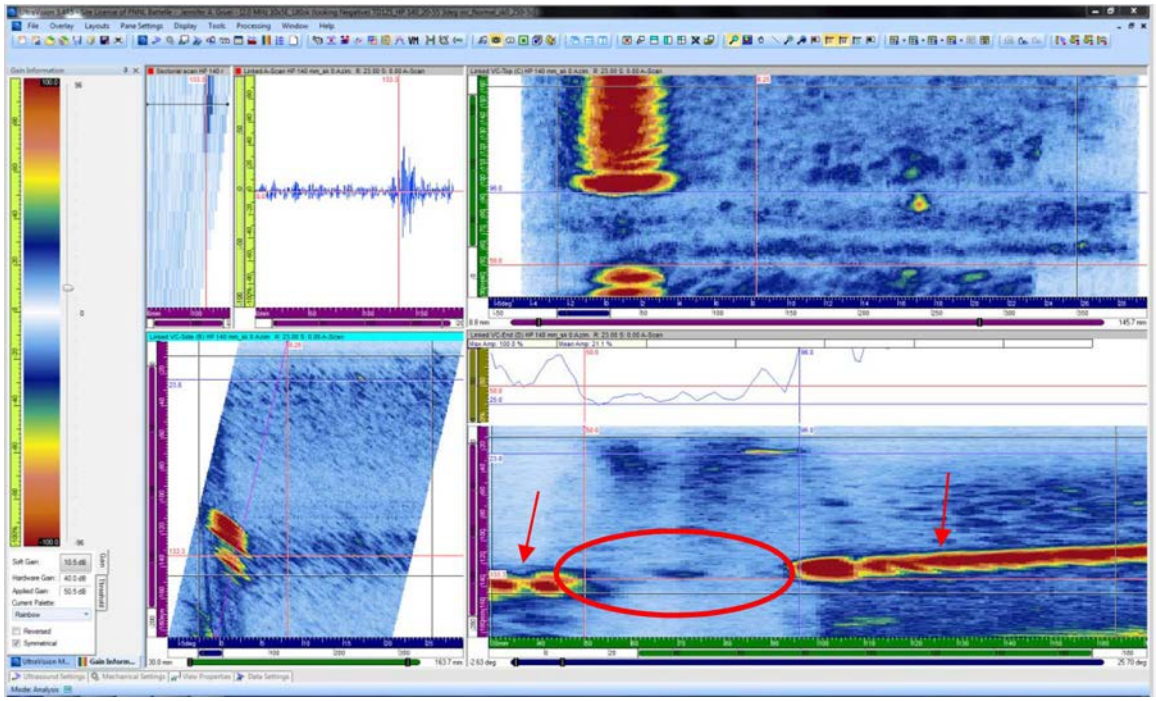

Figure 7.1. DM-10 CCW, Skew 0, Half-path Focus. End-of-specimen is visible in the axial Flaw 3 region and is noted by red arrows. Lack of specimen corner response in the weld is circled in red.

Initial ultrasonic modeling of specific probe parameters for manual, non-encoded examinations employed on the subject DMW configuration indicated that insufficient acoustic energy would be available near the inner surface of the weld to enable robust detection of ID surface-connected axially oriented flaws, especially in light of attending mitigating factors. In addition, these results predict inadequate performance for manual, real-time examinations using the NAPS-1 tandem probes to properly discriminate and characterize surface-connected flaws from other welding or metallurgical features in the inner one-third of the weld volume on these DMWs. This finding is corroborated by site observations and hands-on manual examinations that produced low SNRs and short flaw persistence values for the targeted (axial) mock-up flaws in the presence of spurious indications that interfere with detection and classification of these simulated ID-connected cracks. PNNL's assessment of the design, operational, and

performance characteristics of the tandem probes, coupled with analyses of encoded UT data acquired on the mock-ups with these probes, suggests the following observations and conclusions:

- The tandem probes were poorly designed and ineffectively operated:
    - The acoustic aperture of these probes is too small to adequately insonify the volume of examination with effective ultrasonic energy at the metal paths required for this application.
    - The probes were being over-driven at 450V, producing sound fields that were not optimally formed, and resulting in reduced spatial coherence of the sound fields.
    - Although both the CW and CCW probes were identical in design (essentially mirror images of each other), they exhibited significant differences in sensitivity.
    - It could not be determined from information provided by the licensee what may have occurred to cause this difference in sensitivity, or when it may have occurred. What is problematic is the fact that the licensee's equipment verification checks prior to performance of the examination, if performed, did not identify this critical issue.
    - The probes were not distinctively labeled and could easily be used in the reverse orientation (backwards) during an examination.

The PNNL assessment also included a site visit to Dominion Generation headquarters to evaluate ultrasonic signal responses from NAPS-1 field DMWs versus those obtained from the site-specific mock-ups to ascertain if the mock-ups adequately represent field DMWs. The effort focused on identifying encoded UT response differences between materials, fabrication flaws, and geometric features of the mock-ups and the actual field welds. Based on general UT background noise, attenuation, and the population and location of welding fabrication flaws detected in the mock-ups and the actual field welds, the welds and adjacent parent materials for cold legs, hot legs, and site-specific mock-ups DM-05 and DM-10 appear to be acoustically similar. These results pertain to non-flawed regions of the mock-ups, as fabrication artifacts are very prevalent around the implanted target flaws.

As stated above, PNNL concluded that weld and parent materials used for mock-up fabrication, ID and OD component geometric features, and welding fabrication flaws (distribution, size, population, and location) were similar to those of the field components. However, data indicate that some implantation artifacts provided responses greater than the intended flaws raising questions of flaw realism and validity, even for training purposes. The relative proximity of axial and circumferential flaws, and the presence of significant implantation artifacts, results in spurious reflectors making signal response conditions unnecessarily challenging, especially for non-encoded real-time manual examinations. Site-specific mock-ups should provide realistic UT flaw responses that are consistent, robust, and that easily stand out from spurious indications. As an example, 0.5-MHz circumferentially acquired data (to detect axial flaws) were acquired in multiple scans covering the weld volume in the mock-ups. Data analyses revealed that four out of the five implanted circumferential flaws were found. These flaws were not expected to be detected in this orientation, as theoretically (and confirmed via a parametric study on similar flaws), they present a knife-edge profile to the ultrasonic beam. During analysis, it was apparent that implantation artifacts could easily impact detection decisions. Additionally, an artifact was located at 10 degrees in mock-up DM-05 where no documented flaw exists. The findings raise further questions with respect to the mock-ups representing service-related PWSCC.

Based on site and laboratory observations of UT responses from the flaws and other artifacts during examinations conducted by PNNL on the mock-ups, it is not expected that the manual, non-encoded technique employed would have consistently detected axial flaws (with low numbers of false calls) without examiners having prior knowledge of where these flaws were located.

In addition to evaluating the probes and mock-ups, PNNL was asked to assess the Technical Justification developed for acceptance of the manual ultrasonic examination demonstration using the site-specific mock-ups. This assessment resulted in the identification of key findings and issues of concern associated with the qualification and performance demonstration processes and protocols employed at NAPS-1, the "optimization" or modification of essential inspection variables, and the inability to generate adequate inspection records for post diagnosis or examination oversight. The TJ suggests that one of the primary objectives resulting from the use of site-specific mock-ups is to "aid examination personnel in familiarizing themselves with the ultrasonic responses from unique geometric configurations." Based upon the mock-up assessment conducted at PNNL, the manual UT inspections using the tandem probes described here, on the NAPS-1 mock-ups, do not meet the intent described in the TJ. If an examiner is exposed to ultrasonic responses that are inundated with spurious signals due to implantation or other artifacts, in combination with very low SNRs caused by poorly designed probes, one would not think that effective training with respect to the examination parameters could be suitably achieved.

This assessment further indicates that requirements to control design and construction of site-specific mock-ups are inadequate. The PDI document governing this process is vague; as such, it may allow a wide spectrum of design and fabrication specifications. Site-specific mock-ups will continue to be employed by utilities for challenging inspection scenarios (as PDI cannot feasibly replicate all component configurations); therefore, it is suggested that more rigor be applied to control the design and fabrication process. While it is acknowledged that the PDI program has limited configurations for DMW qualification examinations, this limitation in and of itself cannot provide the foundation for a technical justification that allows inefficient and poorly designed probes or site-specific mock-ups, and ineffective inspection techniques that would apply modifications to essential inspection variables during an open demonstration process.

A number of critical factors may have combined in the failure to detect the axial flaws at NAPS-1. The intent of the site-specific performance demonstration was to apply a modified version of a generic PDI-qualified procedure for the examinations. The NAPS-1 qualification approach, with poorly designed and ineffectively operated tandem probes, mock-up deficiencies, and inherent changes to essential variables within a non-blind demonstration, inevitably played a substantial role in this event. Subsequently, this combination of factors may have resulted in allowing site demonstrations and manual non-encoded field examinations with poorly fabricated flaws (perhaps even implantation artifacts were used as positive detection of flaws) and inadequately functioning probes. The technical justification developed to extend PDI qualifications to NAPS-1 DMWs has been found inadequate to make a reasonable case for using the manual, non-encoded procedure that was employed. The primary issue with TJ IR-2009-358 is associated with allowing essential variables to be changed without providing sufficient technical bases for these changes. For instance, a physics-based technical assessment, either through calculations or modeling, has not been included to support the manual tandem probe design. Other issues associated with the design of mock-ups, and the "open" nature of the site demonstrations, are also questionable. The TJ document leaves many questions unanswered about the effectiveness of changes made to a qualified generic procedure. NIFG industry representatives agree that modification of essential

variables using a site-specific approach is not addressed by ASME Section XI, Appendix VIII, which is reflected in Revision C (December 2012) to the mock-up criteria for dissimilar metal welds.

ASME Appendix VIII is a framework that has been developed to support procedure, personnel, and equipment (UT system) demonstrations through rigorous and statistically based testing protocols by screening out poorly performing systems. TJ IR-2009-358, as written, enabled the licensee to implement changes to essential variables in a successfully demonstrated procedure simply by stating that this change is necessary for implementation at their site.

In summary, this technical assessment provides data and analyses that shed light on certain issues that influenced the licensee's failure to detect multiple PWSCCs in a steam generator primary inlet DMW at North Anna Power Station, Unit 1. If a licensee is going to employ a site-specific approach for an examination, the effort to establish the technical basis for this approach needs to be rigorously and systematically developed. The empirical data obtained by PNNL indicate that had the licensee applied available technology such as spatially encoded UT examinations using appropriately designed phased-array or conventional probes, and a robustly qualified procedure, the axial flaws at NAPS-1 would have been readily detected.

The failure of the licensee's UT technique to detect deep through-wall cracking on the subject DMWs erodes confidence in UT techniques that are being applied for site-specific PWSCC inspections. The probes performance was poor and did not meet the requirements in PDI-UT-10. The mock-ups were questionable even for training purposes. TJ IR-2009-358 stated that two of the three axial flaws that exist in the NAPS-1 mock-ups are "out of range" as specified in PDI Dissimilar Metal Weld Mock-up Criteria, Rev. A and are for "information only." This implies that only one axial mock-up flaw could be used to assess inspection technique validity. The relative proximity of axial and circumferential flaws, and the presence of significant implantation artifacts, results in spurious reflectors. In some instances, the weld fabrication flaw signal response was higher in amplitude than the nearby implanted flaw. The results reported here, based upon a systematic evaluation of the UT techniques, instrumentation, and mock-ups used at NAPS-1, indicate that the licensee did not apply the necessary rigor to implement an effective volumetric inspection of the subject steam generator primary inlet (hot leg), safe end-to-nozzle DMW.

8.0 References

Anderson MT, AA Diaz and SR Doctor. 2012. *Evaluation of Manual Ultrasonic Examinations Applied to Detect Flaws in Primary System Dissimilar Metal Welds at North Anna Power Station*. PNNL-21546, Pacific Northwest National Laboratory, Richland, Washington. ADAMS Accession No. ML12200A216.

ASTM E213-09. 2009. "Standard Practice for Ultrasonic Testing of Metal Pipe and Tubing." ASTM International, West Conshohocken, Pennsylvania. www.astm.org.

ASTM E273-10. 2010. "Standard Practice for Ultrasonic Testing of the Weld Zone of Welded Pipe and Tubing." ASTM International, West Conshohocken, Pennsylvania. www.astm.org.

ASTM E2192-13. 2013. "Standard Practice for Planar Flaw Height Sizing by Ultrasonics." ASTM International, West Conshohocken, Pennsylvania. www.astm.org.

EPRI. 2004. *Performance Demonstration Initiative (PDI) - Dissimilar Metal Weld Mock-Up Criteria, Rev. A*. Electric Power Research Institute, Palo Alto, California.

EPRI. 2006. *Generic Procedure for the Ultrasonic Examination of Dissimilar Metal Welds*. PDI UT-10, Revision C, Electric Power Research Institute, Palo Alto, California.

EPRI. 2009. *Technical Justification for the Acceptance of Ultrasonic Examination Demonstration Results on North Anna Steam Generator Nozzle Dissimilar Metal Weld Configurations with PDI-UT-10, Rev. C*. IR-2009-358, Electric Power Research Institute, Palo Alto, California.

EPRI. 2010. *Performance Demonstration Initiative (PDI) - General Procedure for the Ultrasonic Examination of Dissimilar Metal Welds*. PDI-UT-10, Revision E, Electric Power Research Institute, Palo Alto, California.

ISU. 2012. *Signal-to-Noise Ratio*. NDT Resource Center, Center for NDE, Iowa State University (ISU). Ames, Iowa. Accessed October 31, 2013. Available at http://www.ndt-ed.org/EducationResources/CommunityCollege/Ultrasonics/Physics/signaltonoise.htm.

Neumann AWE. 1989. "On the State of the Art of the Inspection of Austenitic Welds with Ultrasound." *International Journal of Pressure Vessels and Piping* 39:227-246.

Schuster GJ, SL Crawford, AA Diaz, PG Heasler and SR Doctor. 2013. *Reliability of Ultrasonic In-Service Inspection of Welds in Reactor Internals of Boiling Water Reactors*. NUREG/CR-7159, U.S. Nuclear Regulatory Commission, Washington, D.C.

Schuster GJ, SR Doctor and PG Heasler. 1998. *Characterization of Flaws in U.S. Reactor Pressure Vessels: Density and Distribution of Flaw Indications in PVRUF*. NUREG/CR-6471, PNNL-11143, Vol. 1, U.S. Nuclear Regulation Commission, Washington, D.C.

Appendix A

Ultrasonic Imaging and Display Overview – Axial Flaws

Appendix A

Ultrasonic Imaging and Display Overview – Axial Flaws

The tandem and phased-array (PA) probes were scanned circumferentially and indexed in the axial direction for detection and characterization of axial flaws. A diagram of an axial flaw and a probe with scan and index axes noted is displayed in the left of Figure A.1. As scan lines are acquired, a volume of data is collected and stored. After the file is saved, the data can be viewed interactively via electronic gates and cursors. The three orthogonal views (B-, C-, and D-scans) are displayed in the right of Figure A.1. Descriptions for all ultrasonic PA plots are provided below:

- A-scan: Time and amplitude plot at a specific probe position for a specific refracted angle.
- B-scan: Side-view image, time (vertical) and circumferential or scan position (horizontal), showing the side of the axial flaw. This view can be used for depth measurements.
- C-scan: Top or plan view image, scan and index positions represent the horizontal and vertical axes, showing the length and location of the axial flaw.
- D-scan: End-view image, time (vertical) and axial or index position (horizontal), showing the length and possibly depth of the axial flaw.
- Volume-corrected sector view: Also known as an azimuthal scan; corrected for delay and refracted angle, only useful with multiple refracted angles.
- Sector view, uncorrected: Not corrected for refracted angle, rectilinear plot at each skew and refracted angle, useful for selecting a skew and refracted angle of interest for the three orthogonal plots.

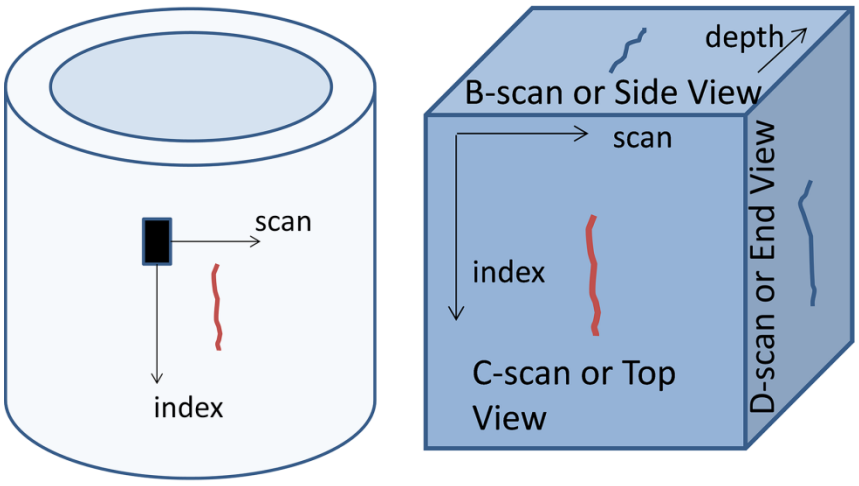

Figure A.1. Scan and Index Directions for Circumferential Scanning of an Axial Flaw (left); Acquired Data Volume with the Three Orthogonal Display Views (right)

Further explanations of the views as typically used in the report are given by the following:

Figure A.2 represents tandem probe data and as such only has one angle of insonification; therefore, the sector views do not apply. The upper left image is the C-scan top view, the upper right is the rectified A-scan view, the lower left image is the B-scan side view, and the lower right image is the D-scan end view. Also note that the axes scales are color-coded. The scan axis is blue; the index axis is green, while the time (or depth into the material) axis is magenta in the side- and end-view images and pink in the A-scan.

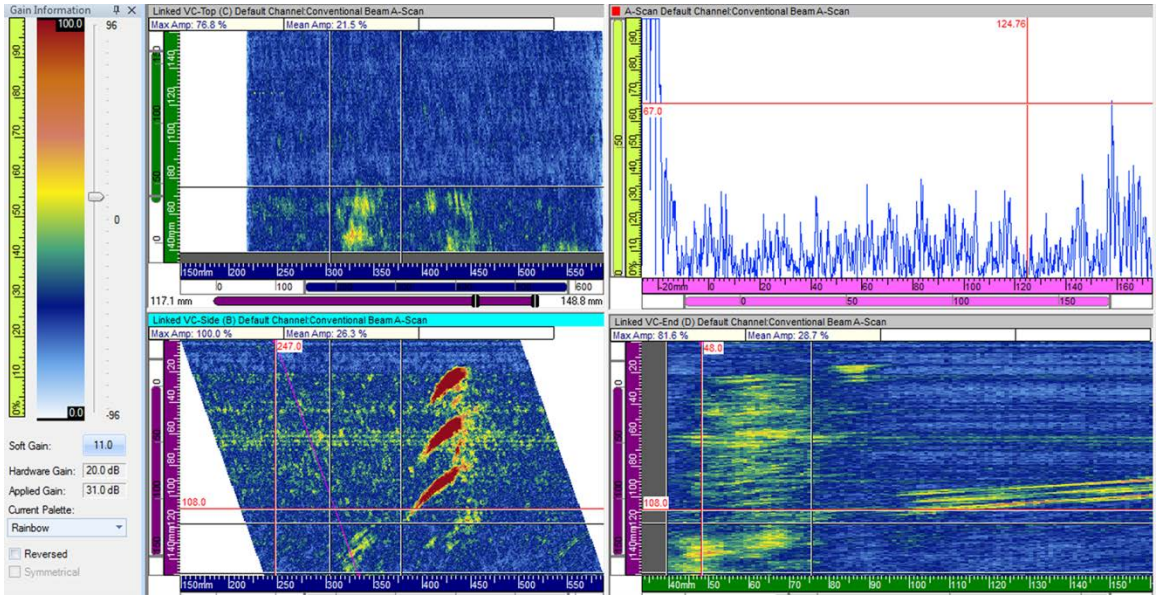

Figure A.2. Tandem Probe Data with Three Orthogonal Views and an A-Scan in the Top Right

Figure A.3 represents PA data acquired over a refracted angle range of 20 to 53 degrees with 3-degree increments at each specified scan and index position. The volume-corrected sectorial view, or sector scan, in the upper left shows data through the range of angles. The position of the black line in the sectorial view (noted by the red arrow) determines the refracted angle used for the data projection of the three orthogonal views. These three orthogonal views are the C-scan in the upper right, B-scan in the lower left, and D-scan in the lower right.

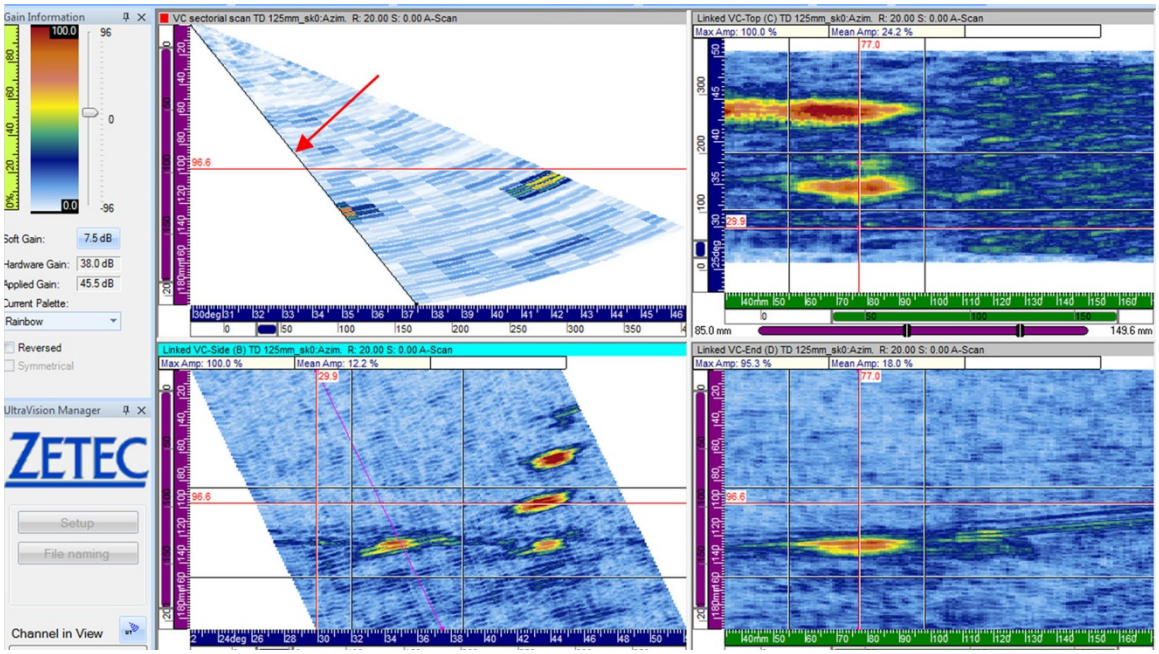

Figure A.3. PA Data with Three Orthogonal Views and a Volume-Corrected Sector Scan Image in the Top Left

Figure A.4 also represents PA data acquired over a given range of refracted angles. The difference in this view as compared to Figure A.3 is that the upper left shows an uncorrected sectorial scan and an A-scan. As in Figure A.3, the black line in the sectorial scan (noted by the red arrow) determines the refracted angle for the data projection of the three orthogonal views.

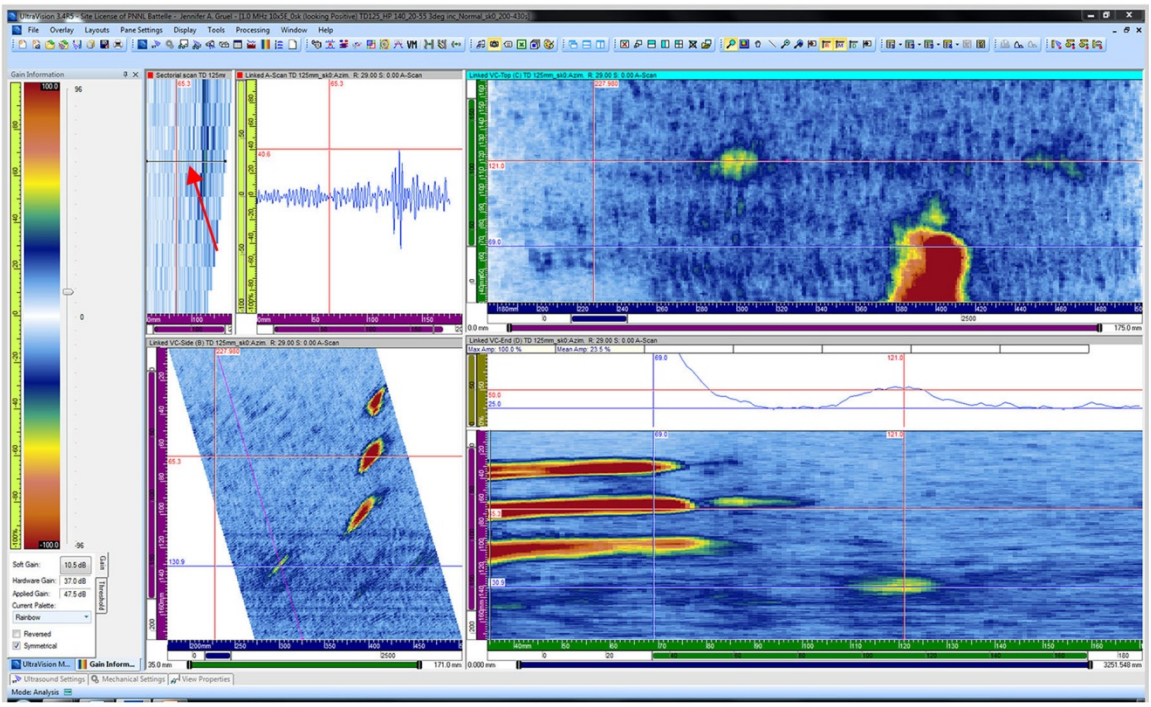

Figure A.4. PA Data with Three Orthogonal Views and an Uncorrected Sector Scan in the Top Left. An A-scan is displayed to the right of the sector scan.

Figure A.5 represents PA data acquired over a given range of refracted and three skew angles. The upper left uncorrected sectorial view shows data, from top to bottom, for skew −11 at all refracted angles, skew 0 at all refracted angles, and skew 11 degrees at all refracted angles. A volume-corrected sectorial view with the multiple refracted and skew angles would present too much overlap of data to be meaningful. The three orthogonal views (C-scan upper right, B-scan lower left, and D-scan lower right) all represent data at a selected skew and refracted angle.

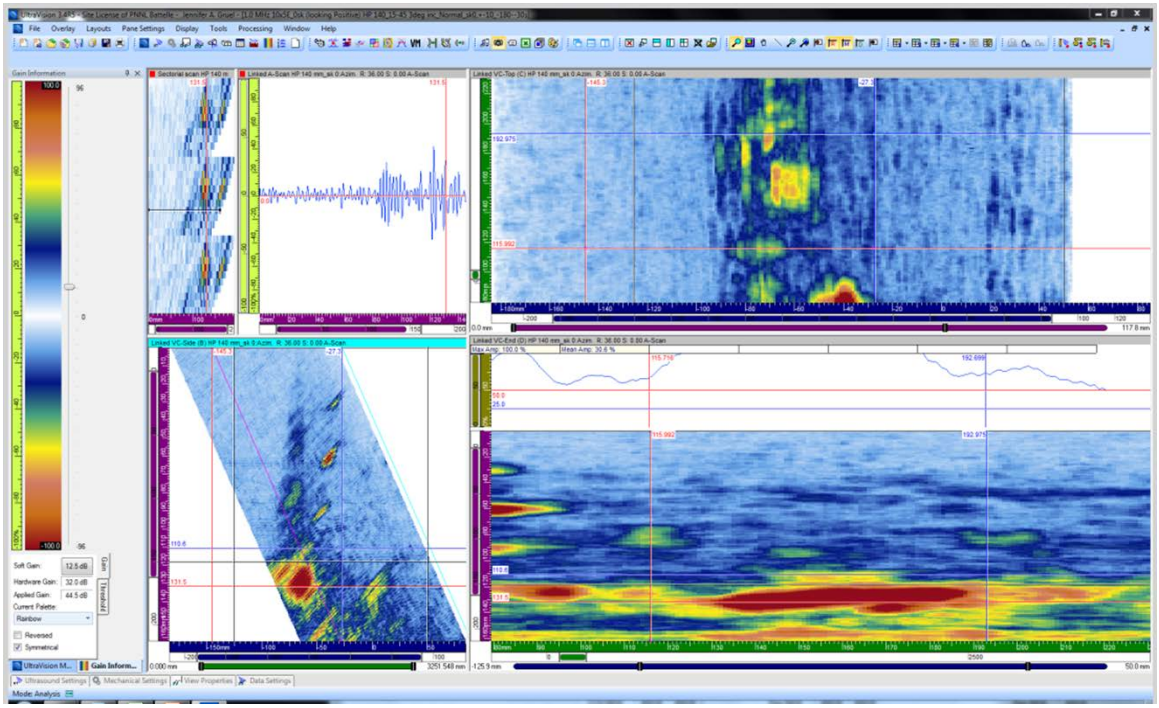

Figure A.5. CW Probe, DM-10 Axial Flaw 2 Circled in Red

Appendix B

1.0-MHz Sigma Tandem Probe Images, Pulsed with DYNARAY – Side-Drilled Holes and Axial Flaws in DM-05 and DM-10

Appendix B

1.0-MHz Sigma Tandem Probe Images, Pulsed with DYNARAY – Side-Drilled Holes and Axial Flaws in DM-05 and DM-10

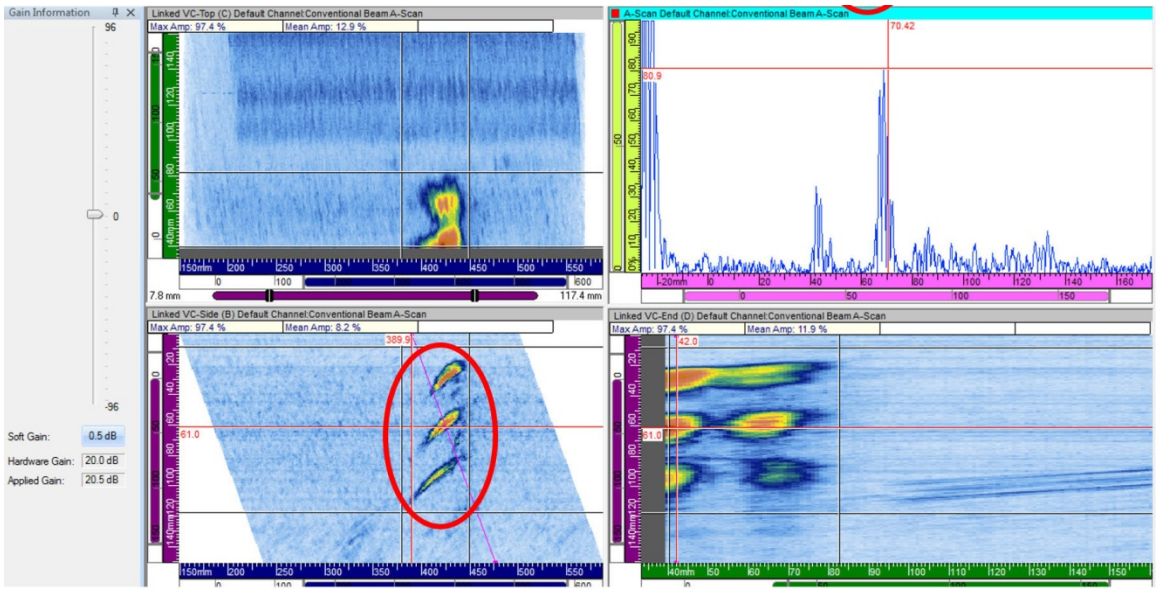

Figure B.1. CW Probe, DM-05 Three Side-drilled Holes Circled in Red

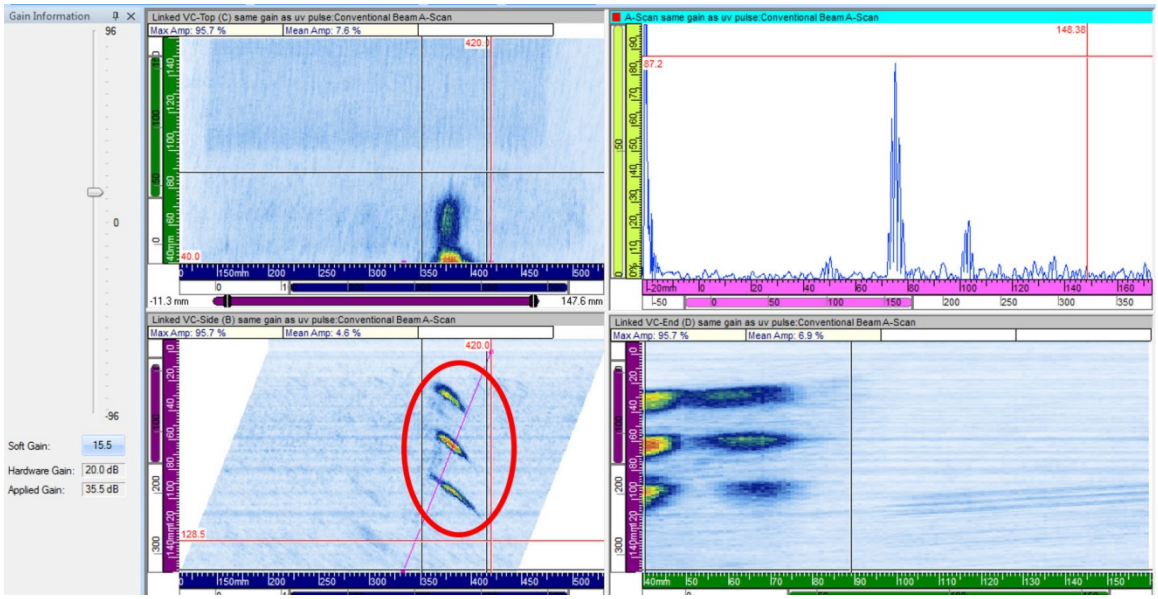

Figure B.2. CCW Probe, DM-05 Three Side-drilled Holes Circled in Red

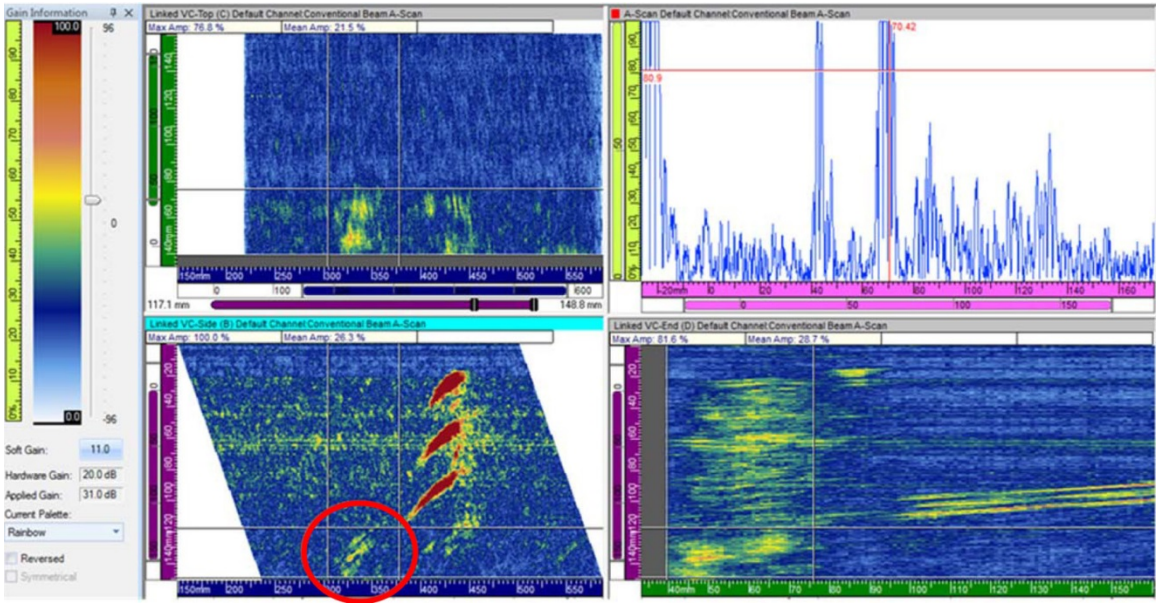

Figure B.3. CW Probe, DM-05 Axial Flaw 1 Circled in Red

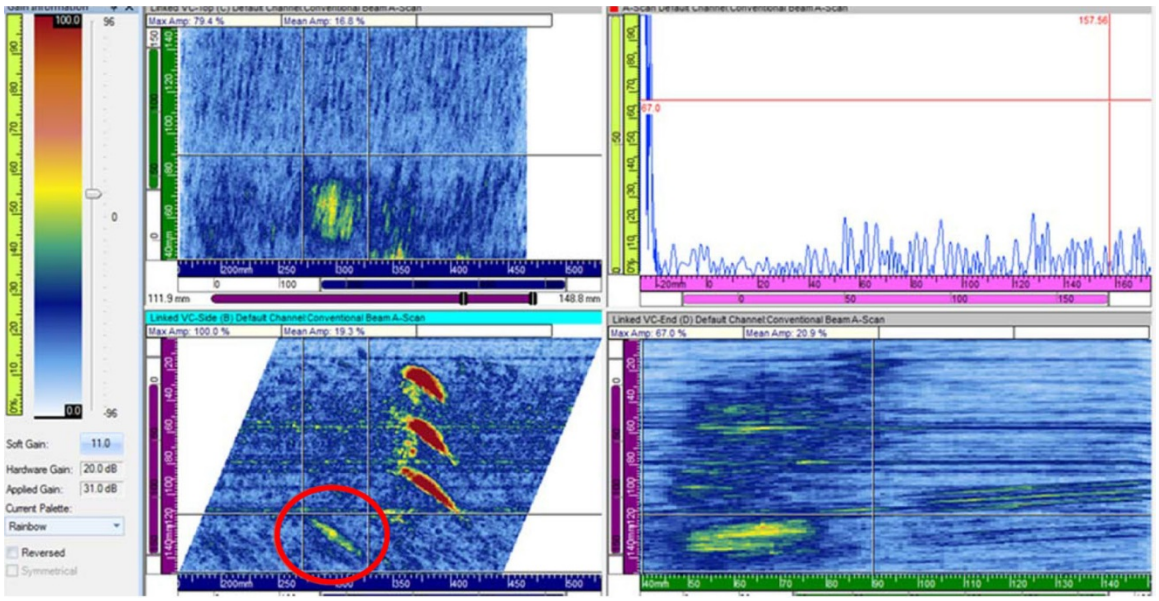

Figure B.4. CCW Probe, DM-05 Axial Flaw 1 Circled in Red

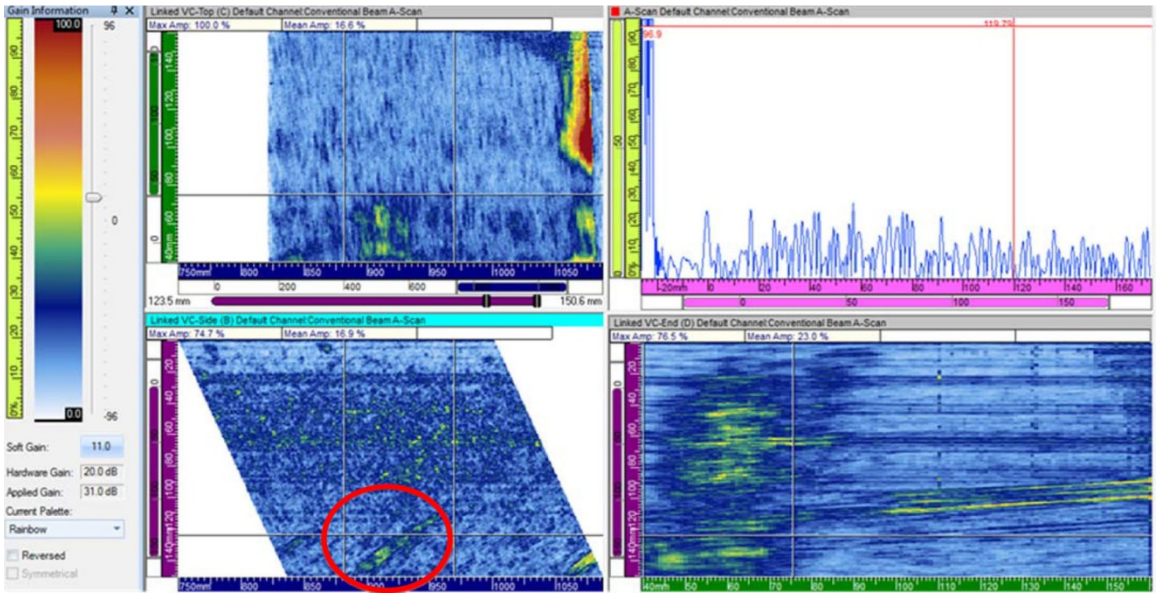

Figure B.5. CW Probe, DM-10 Axial Flaw 2 Circled in Red

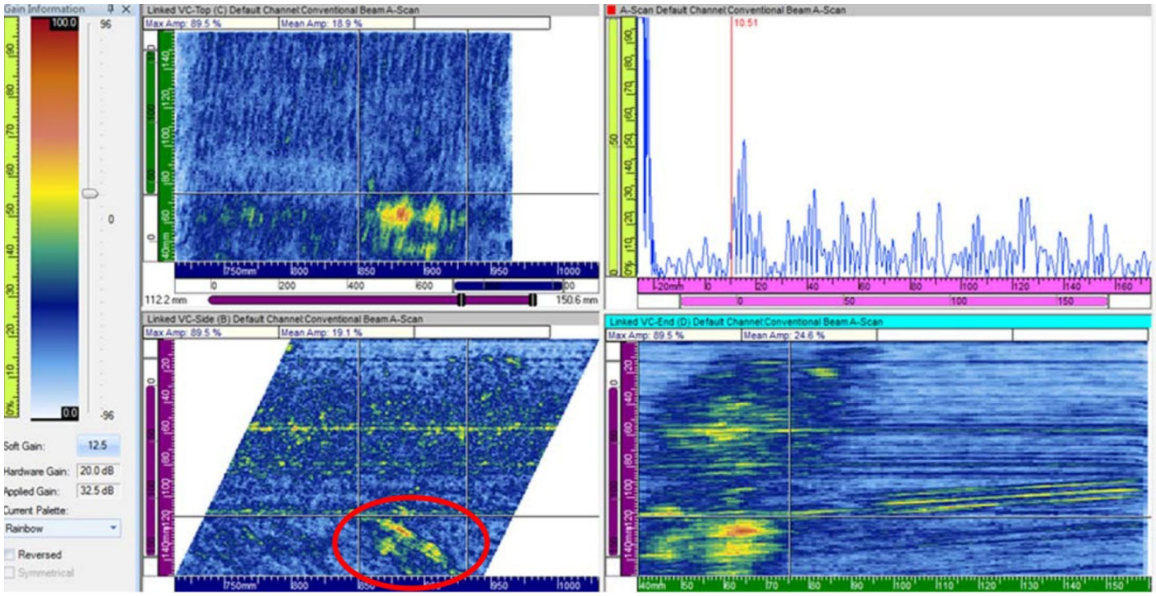

Figure B.6. CCW Probe, DM-10 Axial Flaw 2 Circled in Red

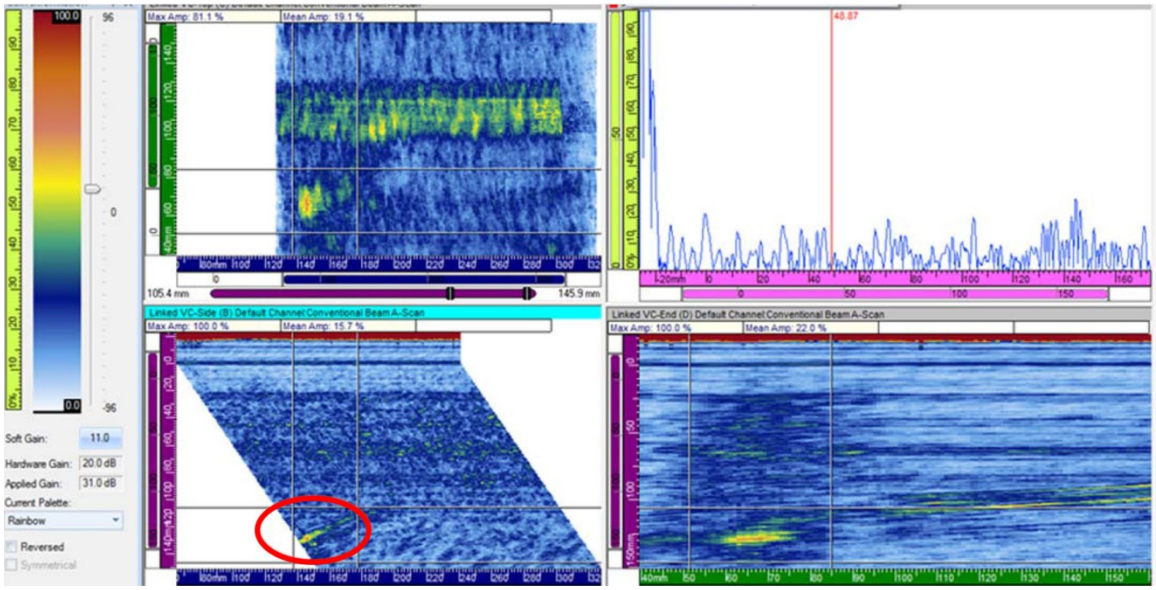

Figure B.7. CW Probe, DM-10 Axial Flaw 3 Circled in Red

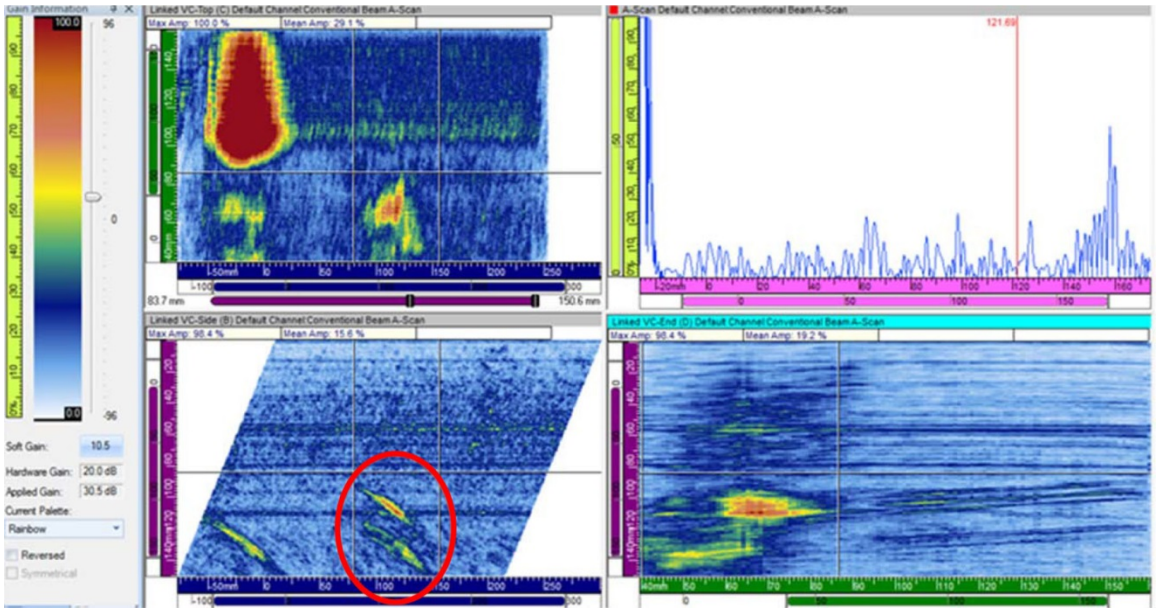

Figure B.8. CCW Probe, DM-10 Axial Flaw 3 Circled in Red

Appendix C

0.5-MHz PA Data Images, Half-Path Focus

Appendix C

0.5-MHz PA Data Images, Half-Path Focus

C.1 DM-05

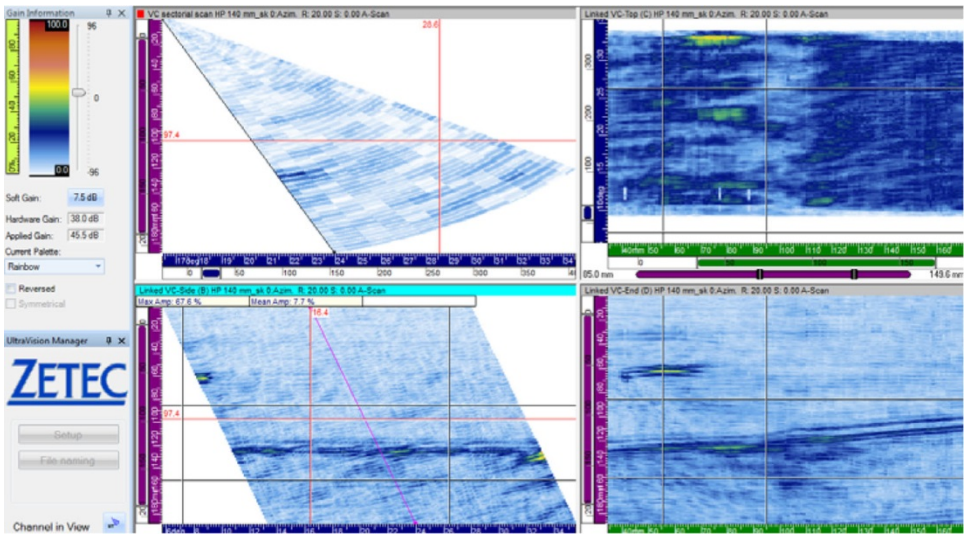

Figure C.1. CW, Skew 0, File 90 to 290 (mm)

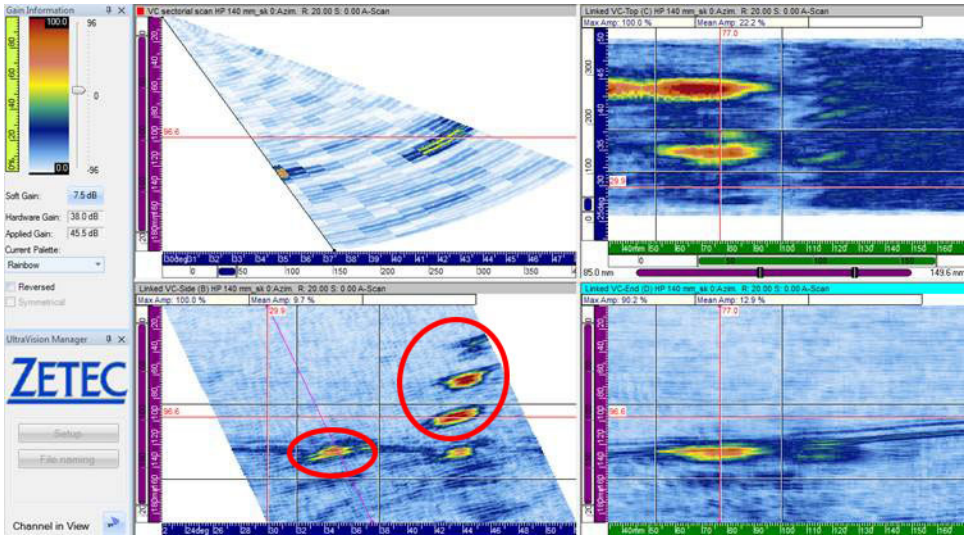

Figure C.2. CW, Skew 0, File 240 to 440 (mm). Axial flaw 1 (left) and three side-drilled holes (right) are circled in red.

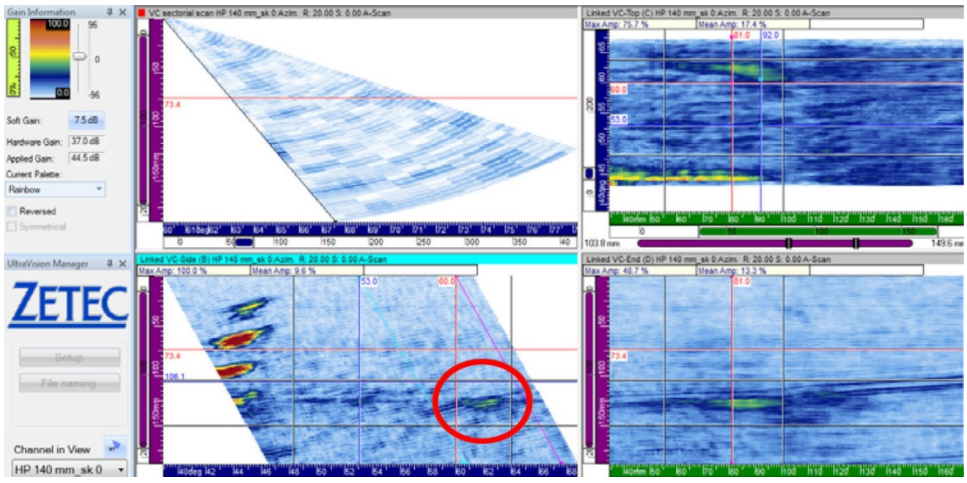

Figure C.3. CW, Skew 0, File 390 to 590 (mm). Artifact is visible at 62 degrees (circumferential flaw 4) and circled in red.

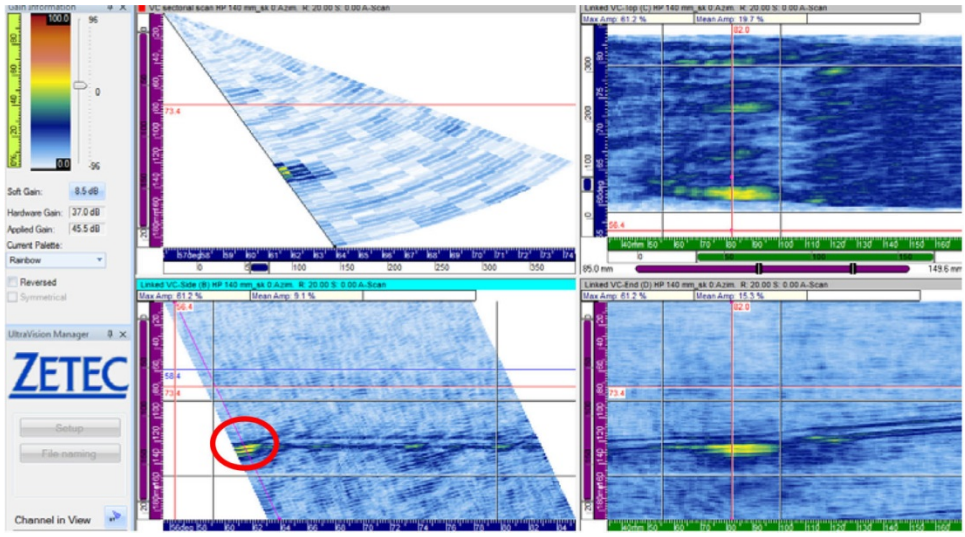

Figure C.4. CW, Skew 0, File 540 to 740 (mm). Artifact is visible at 62 degrees (circumferential flaw 4) and circled in red.

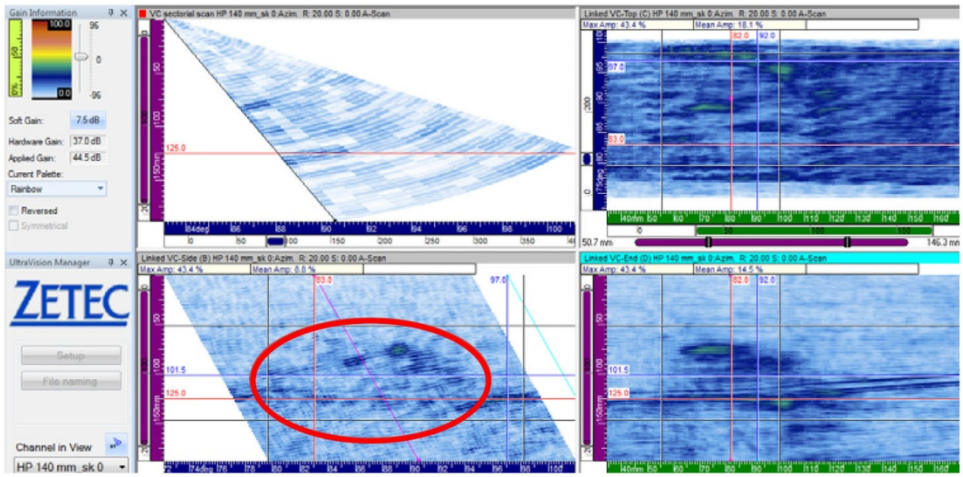

Figure C.5. CW, Skew 0, File 690 to 890 (mm). Circumferential flaw 2 implantation artifact is visible and circled in red.

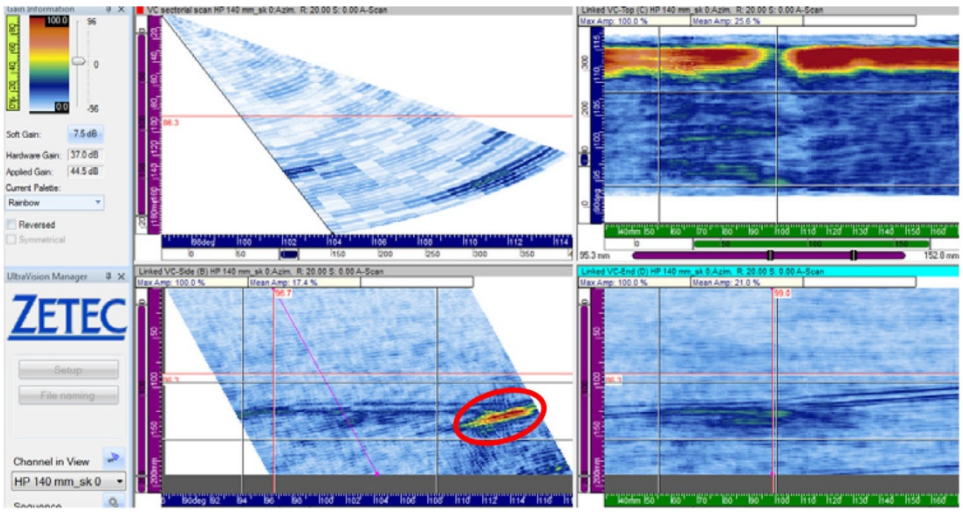

Figure C.6. CW, Skew 0, File 840 to 1040 (mm). Specimen end is visible and circled in red.

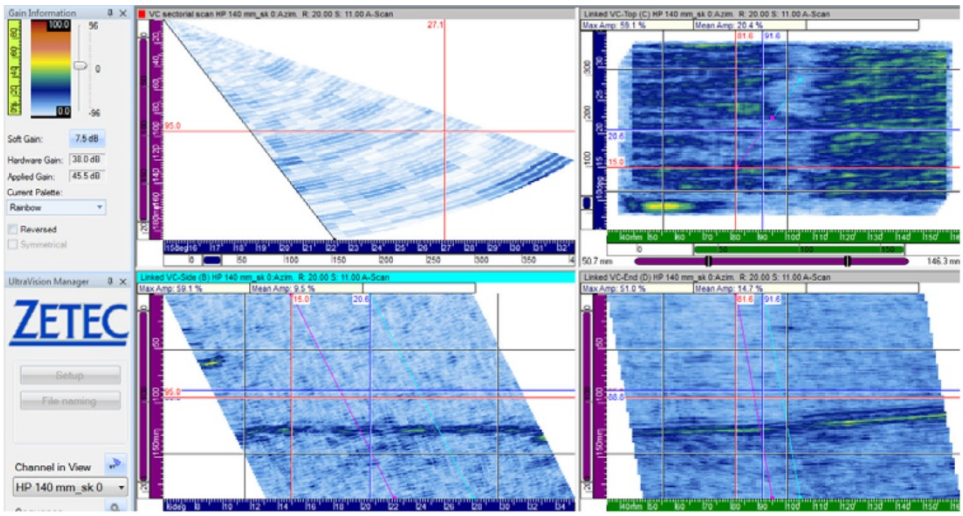

Figure C.7. CW, Skew 11, File 90 to 290 (mm)

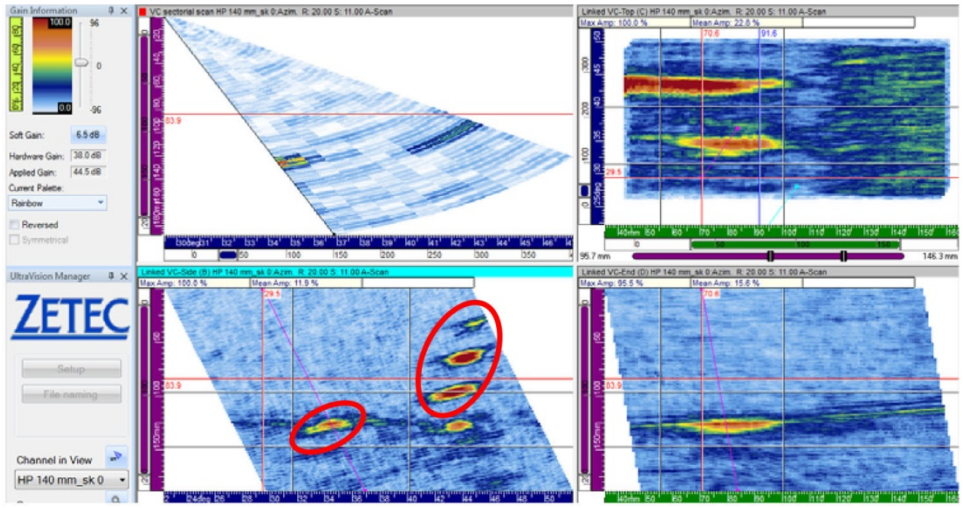

Figure C.8. CW, Skew 11, File 240 to 440 (mm). Axial flaw 1 (left) and the three side-drilled holes (right) are visible and circled in red.

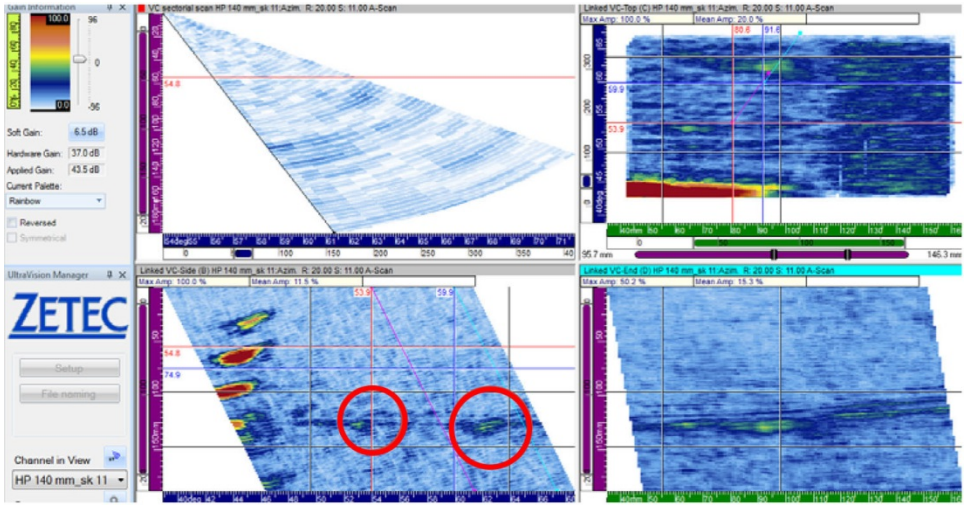

Figure C.9. CW, Skew 11, File 390 to 590 (mm). Possible implantation artifacts at 53 and 62 degrees are visible from circumferential flaw 4 and circled in red.

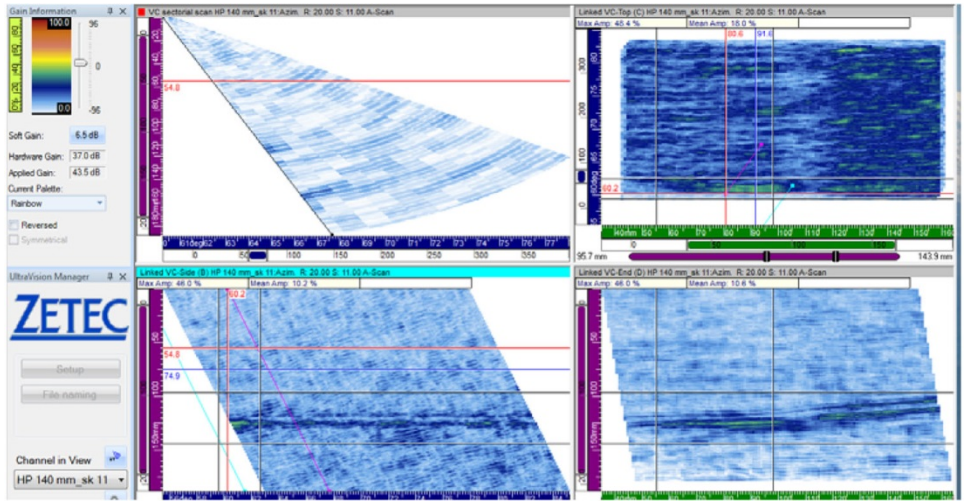

Figure C.10. CW, Skew 11, File 540 to 740 (mm)

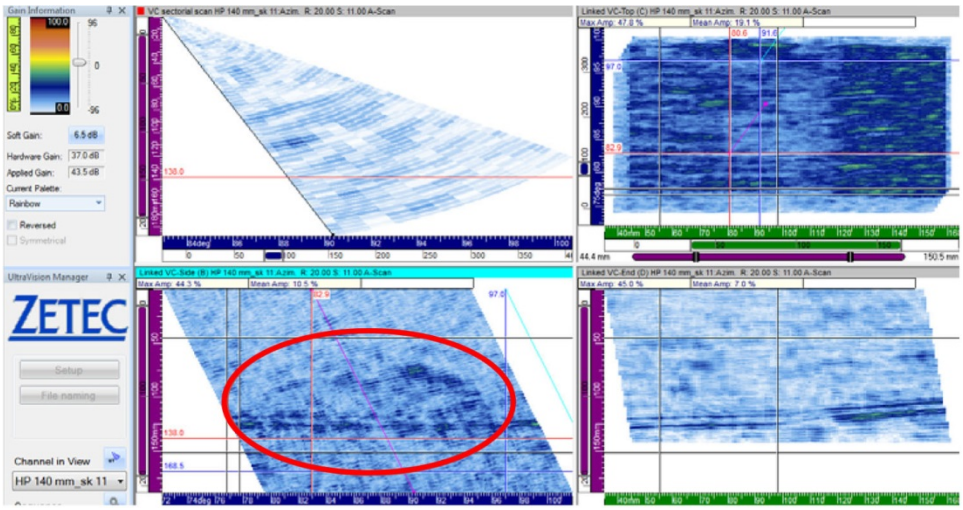

Figure C.11. CW, Skew 11, File 690 to 890 (mm). Possible implantation artifact from circumferential flaw 2 is visible and circled in red.

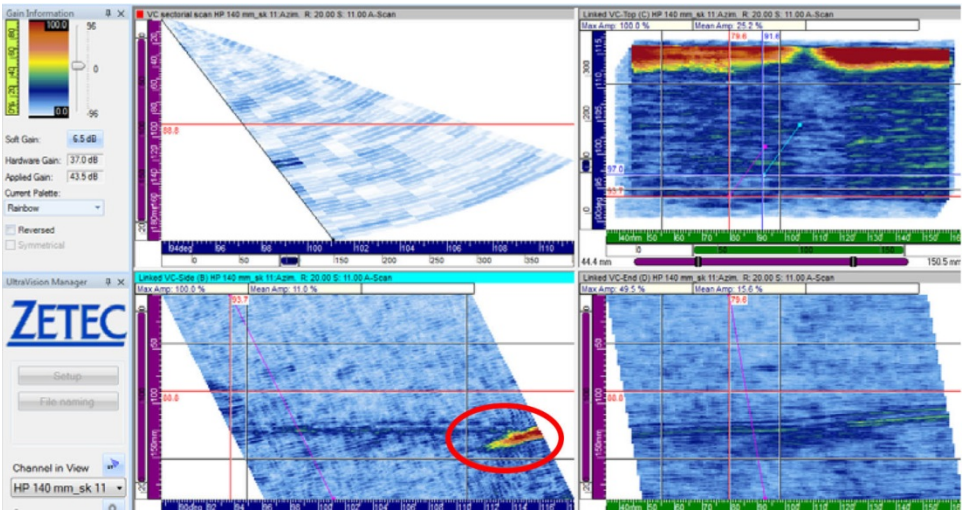

Figure C.12. CW, Skew 11, File 840 to 1040 (mm). The end of the specimen is visible and circled in red.

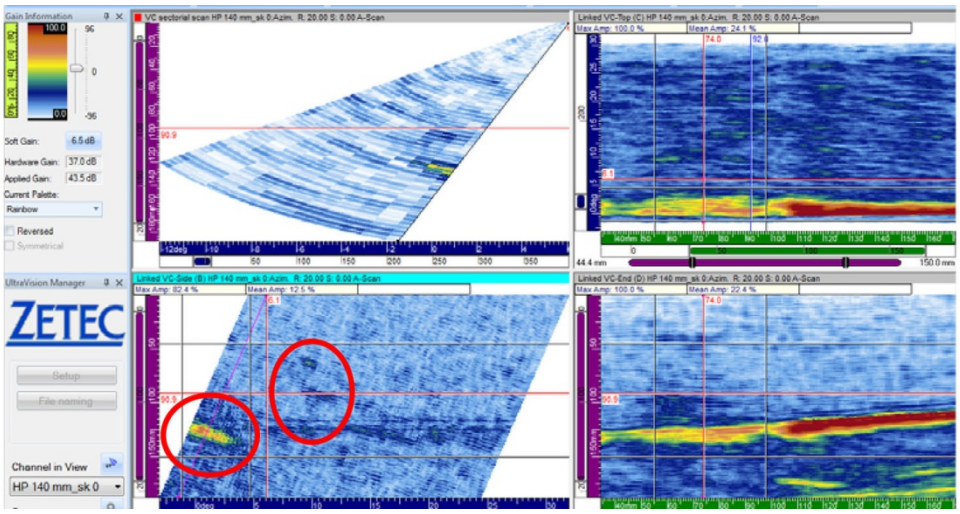

Figure C.13. CCW, Skew 0, File 250 to −3 (mm). The end of the specimen (left) is visible as well as mid-wall circumferential flaw 3 artifacts (right) and circled in red.

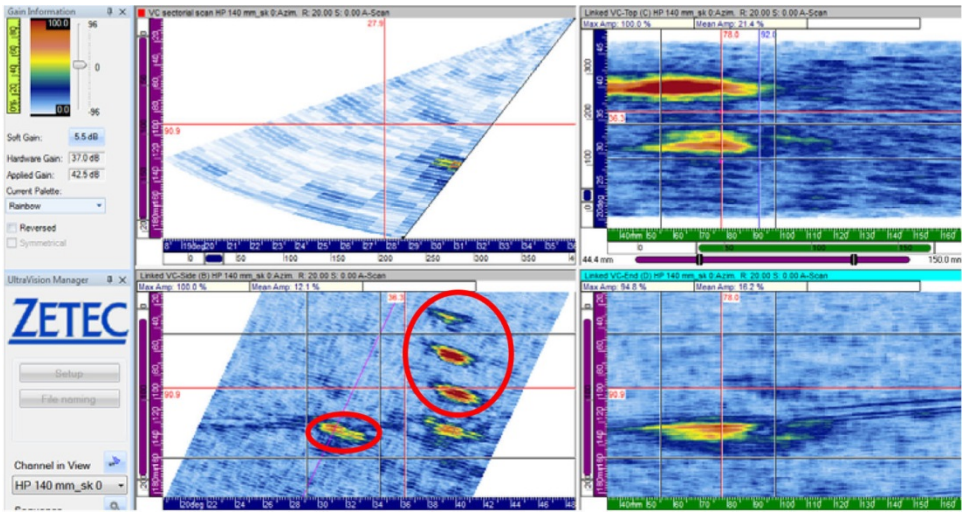

Figure C.14. CCW, Skew 0, File 400 to 200 (mm). Axial flaw 1 (left) and the three side-drilled holes (right) are visible and circled in red.

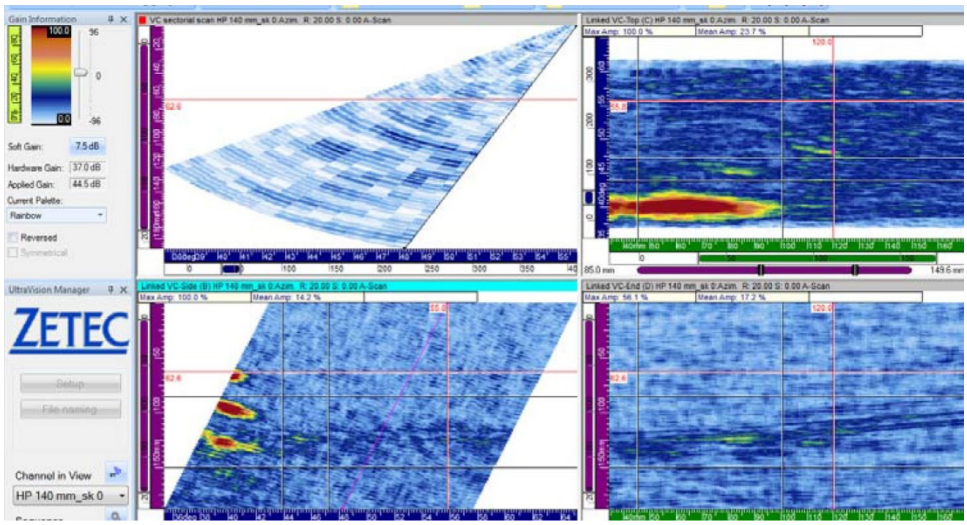

Figure C.15. CCW, Skew 0, File 550 to 350 (mm)

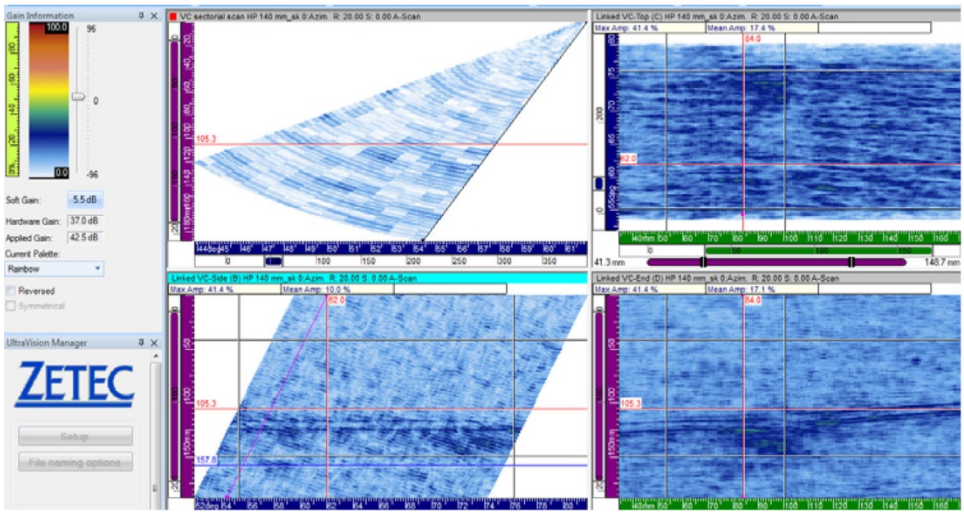

Figure C.16. CCW, Skew 0, File 700 to 500 (mm). No artifact is seen at 62 degrees.

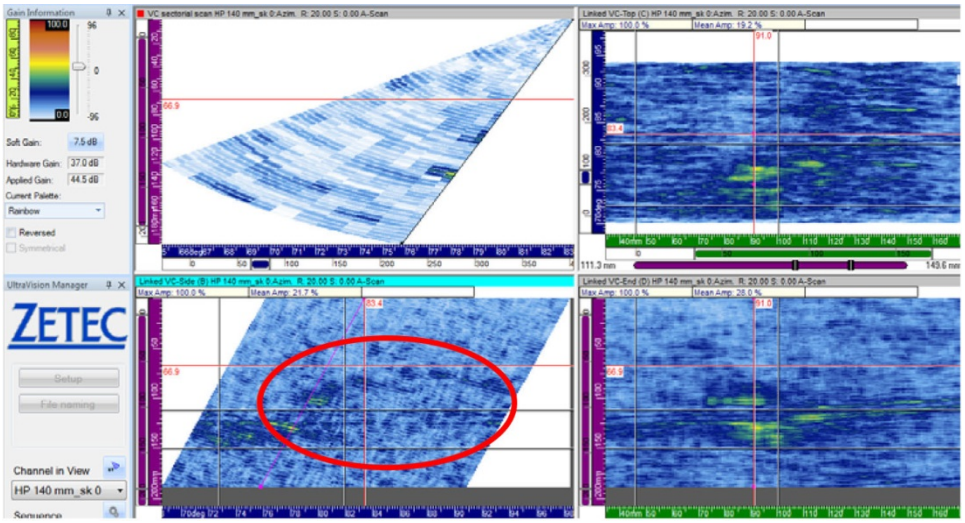

Figure C.17. CCW, Skew 0, File 850 to 650 (mm). Possible artifact from circumferential flaw 2 is visible and circled in red.

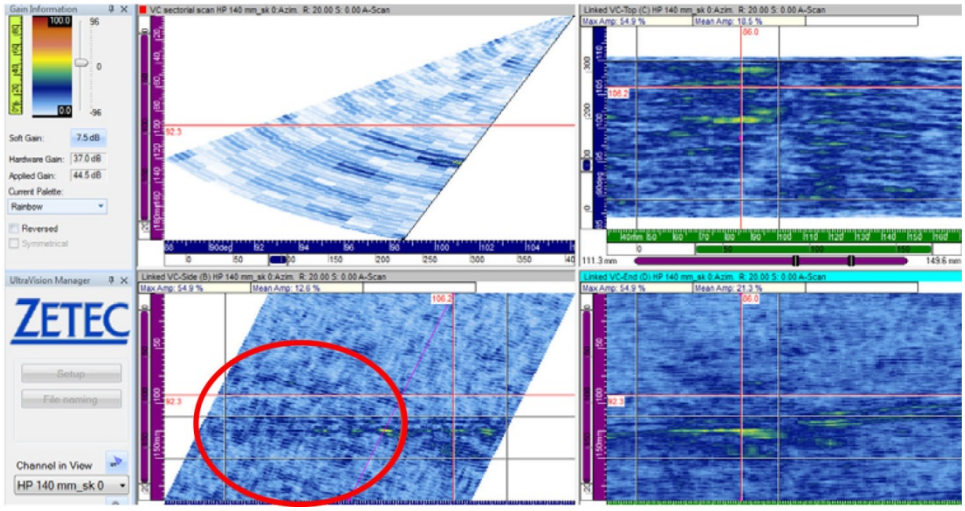

Figure C.18. CCW, Skew 0, File 1000 to 800 (mm). Possible artifact from circumferential flaw 2 is visible and circled in red.

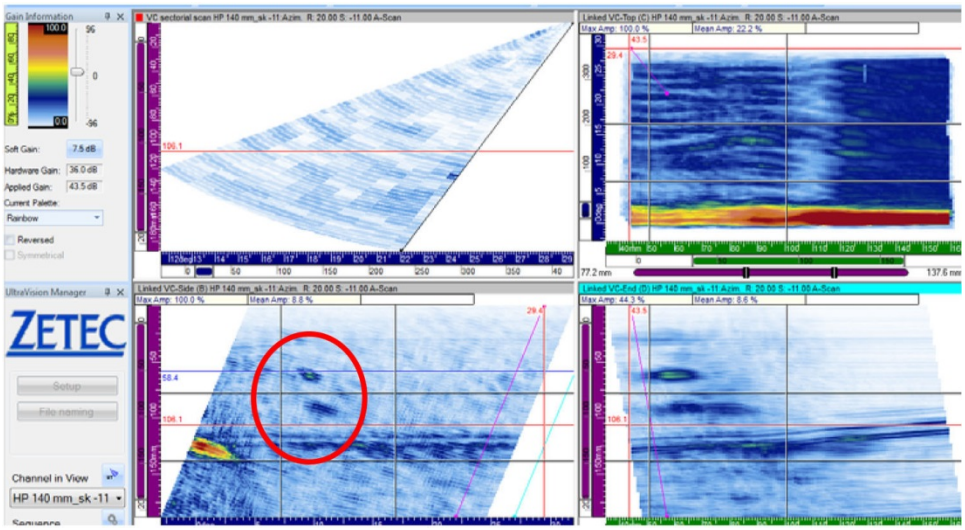

Figure C.19. CCW, Skew 11, File 250 to −3 (mm). Possible circumferential flaw 3 artifact at 10 degrees is visible and circled in red.

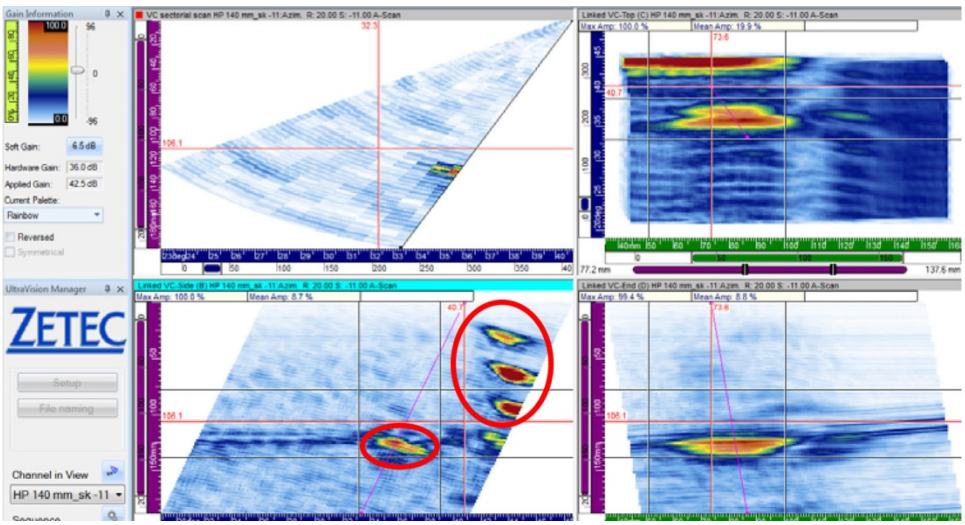

Figure C.20. CCW, Skew 11, File 400 to 200 (mm). Axial flaw 1 (left) and three side-drilled holes (right) are visible and circled in red.

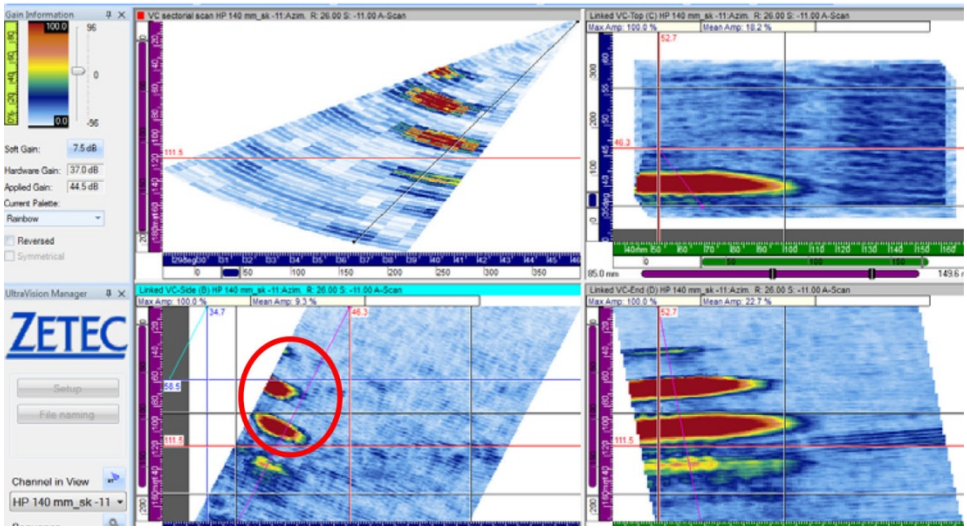

Figure C.21. CCW, Skew 11, File 550 to 350 (mm). The three side-drilled holes are visible and circled in red.

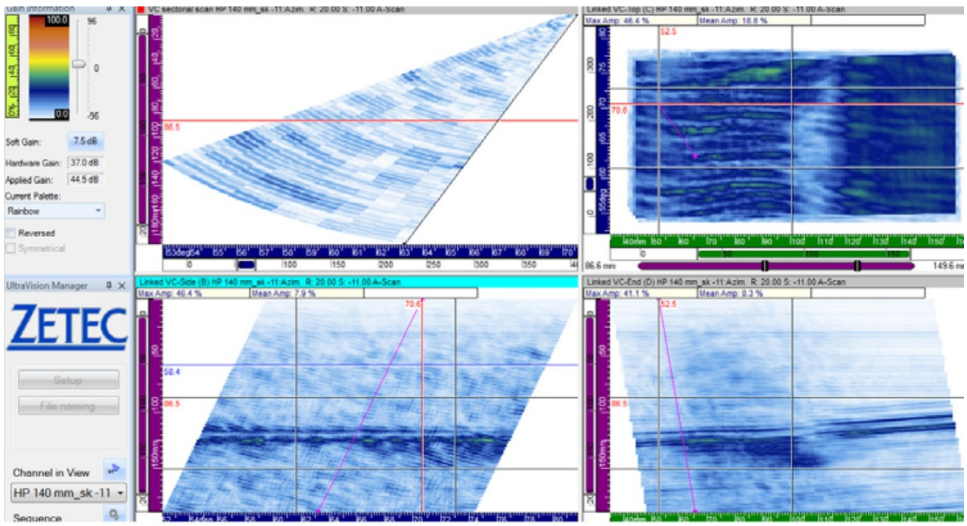

Figure C.22. CCW, Skew 11, File 700 to 500 (mm)

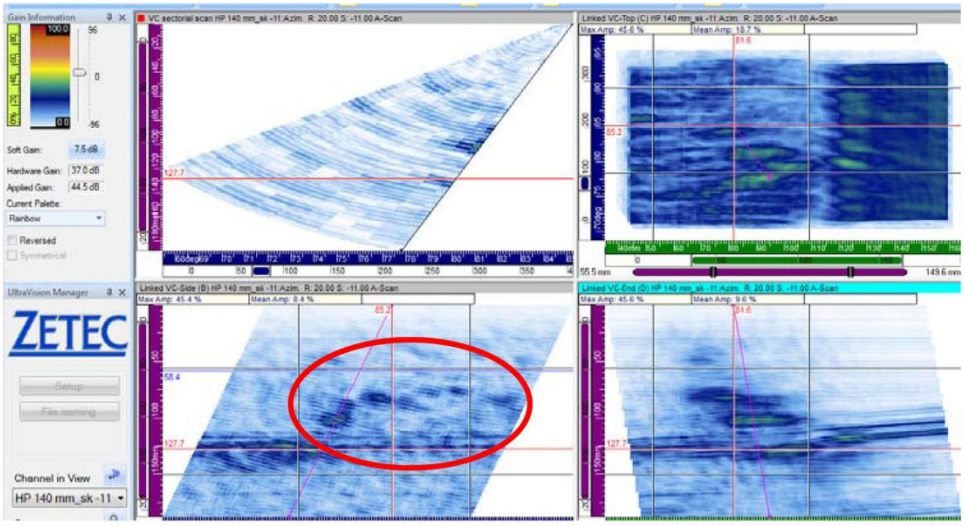

Figure C.23. CCW, Skew 11, File 850 to 650 (mm). Possible implantation artifact from circumferential flaw 2 is visible and circled in red.

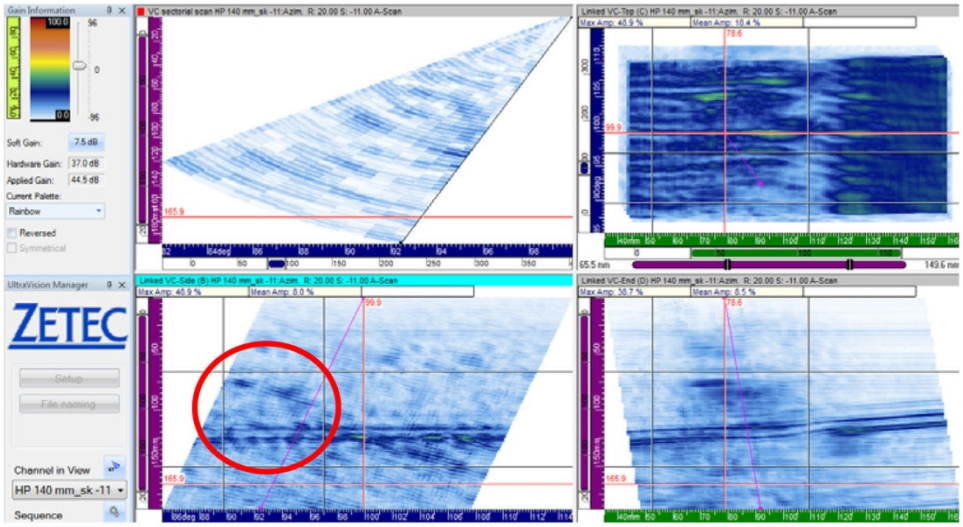

Figure C.24. CCW, Skew 11, File 1000 to 800 (mm). Possible implantation artifact from circumferential flaw 2 is visible and circled in red.

C.2 DM-10

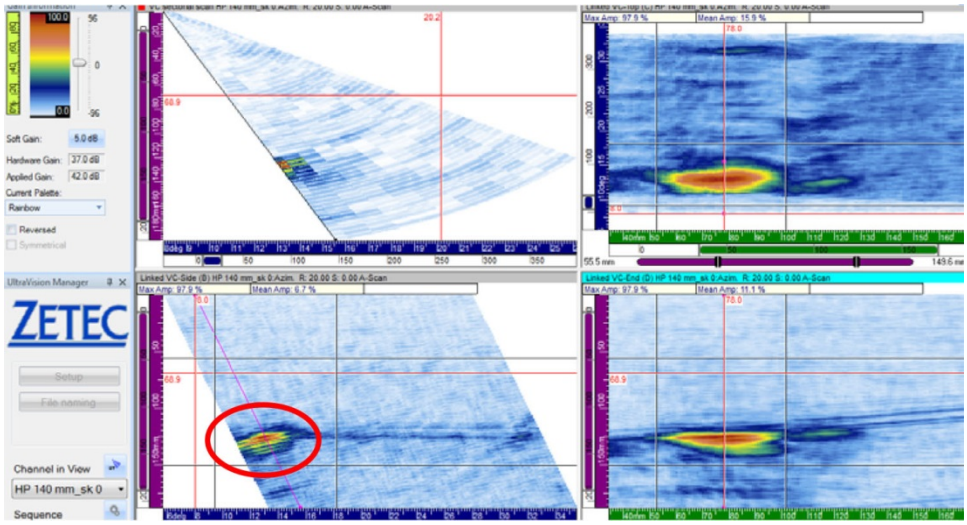

Figure C.25. CW, Skew 0, File 90 to 290 (mm). Axial flaw 3 is visible and circled in red.

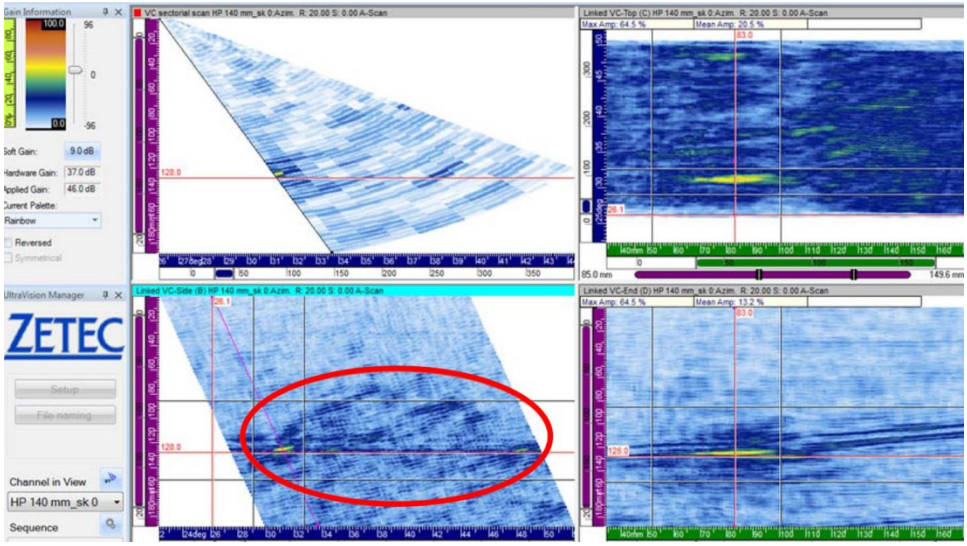

Figure C.26. CW, Skew 0, File 240 to 440 (mm). Possible implantation artifact from circumferential flaw 1 is visible and circled in red.

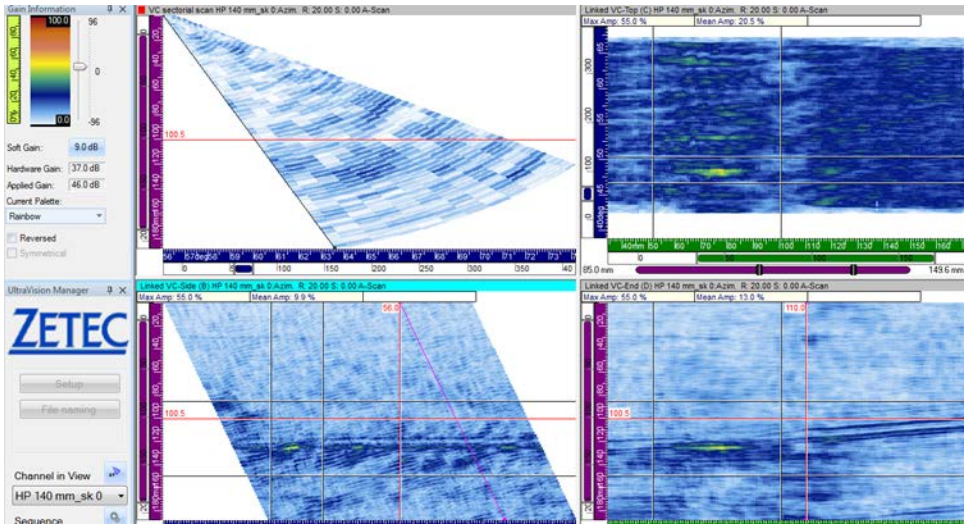

Figure C.27. CW, Skew 0, File 390 to 590 (mm)

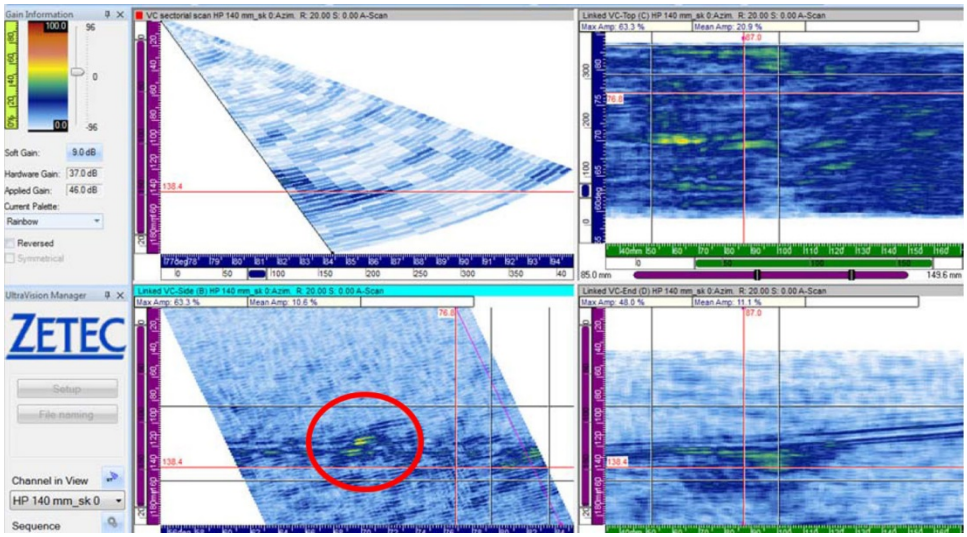

Figure C.28. CW, Skew 0, File 540 to 740 (mm). Possible flaw implantation artifact from circumferential flaw 4 is visible and circled in red.

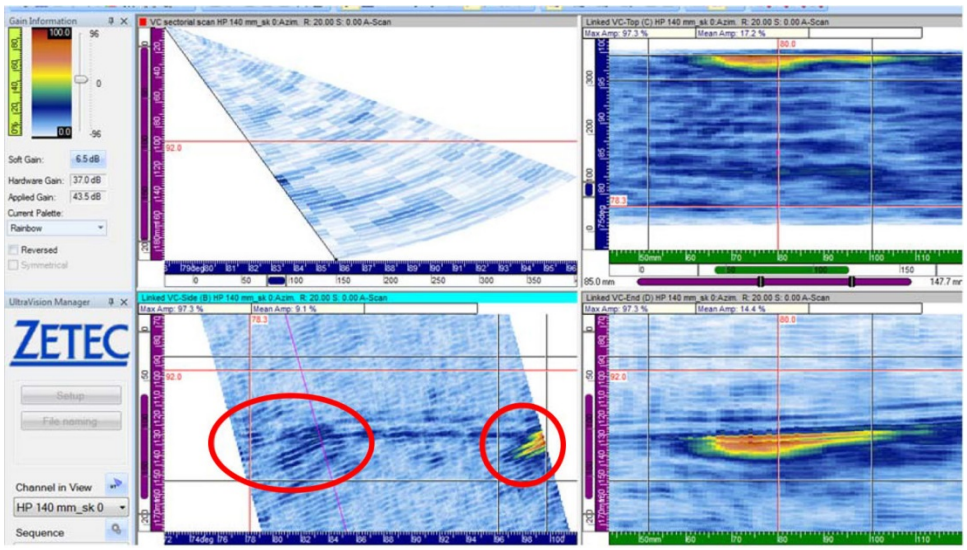

Figure C.29. CW, Skew 0, File 690 to 890 (mm). Circumferential flaw 4 implantation artifact (left) and axial flaw 2 (right) are visible and circled in red.

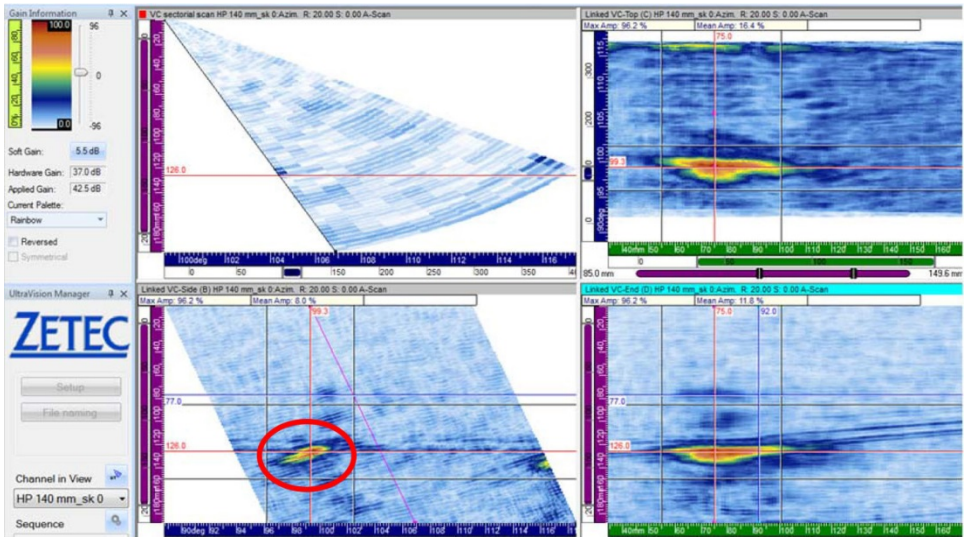

Figure C.30. CW, Skew 0, File 840 to 1040 (mm). Axial flaw 2 is visible and circled in red.

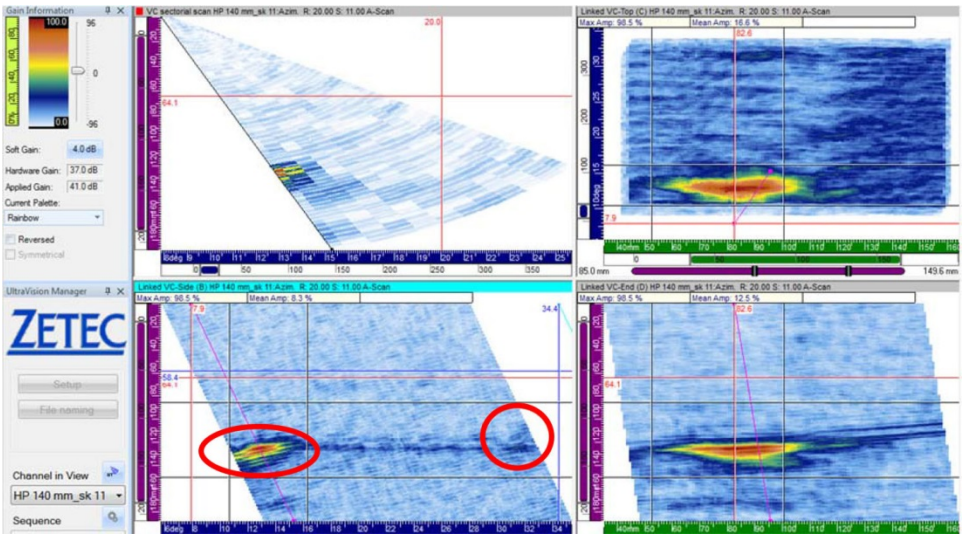

Figure C.31. CW, Skew 11, File 90 to 290 (mm). Axial flaw 3 (left) and possible implantation artifact from circumferential flaw 1 (right) are visible and circled in red.

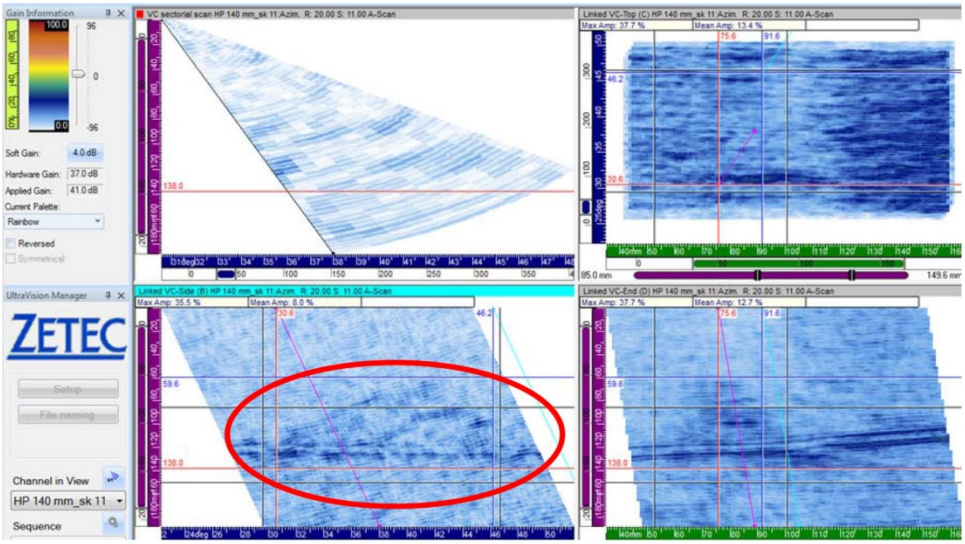

Figure C.32. CW, Skew 11, File 240 to 440 (mm). Possible implantation artifact from circumferential flaw 1 is visible and circled in red.

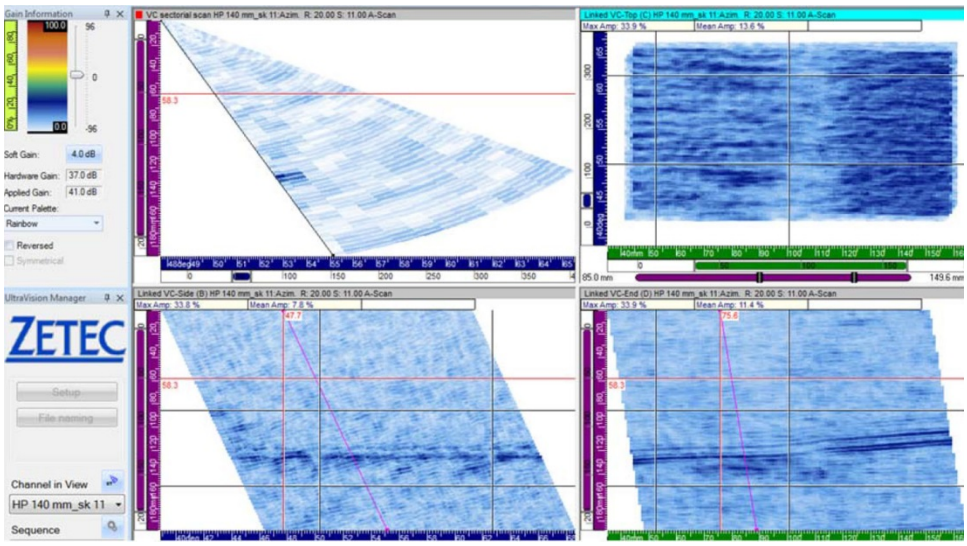

Figure C.33. CW, Skew 11, File 390 to 590 (mm)

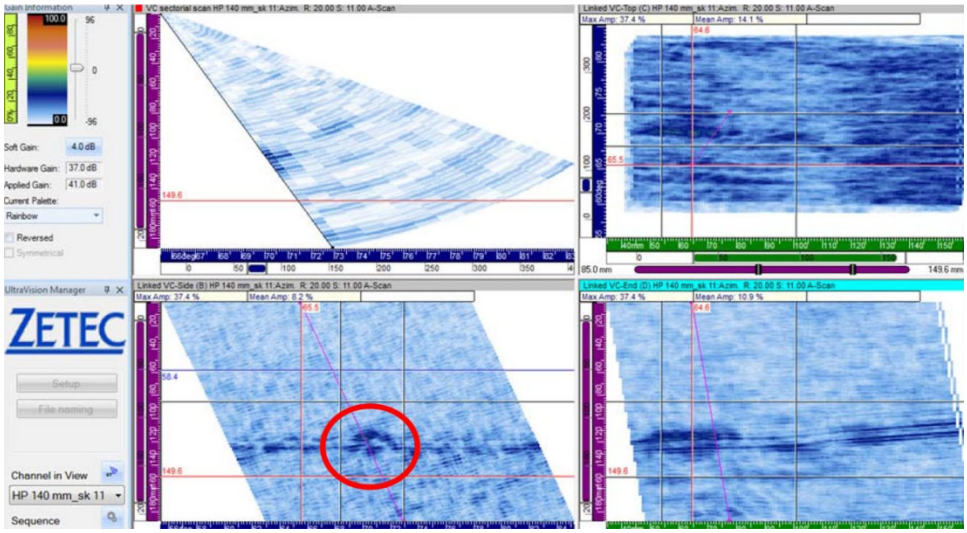

Figure C.34. CW, Skew 11, File 540 to 740 (mm). Possible implantation artifact from circumferential flaw 4 is visible and circled in red.

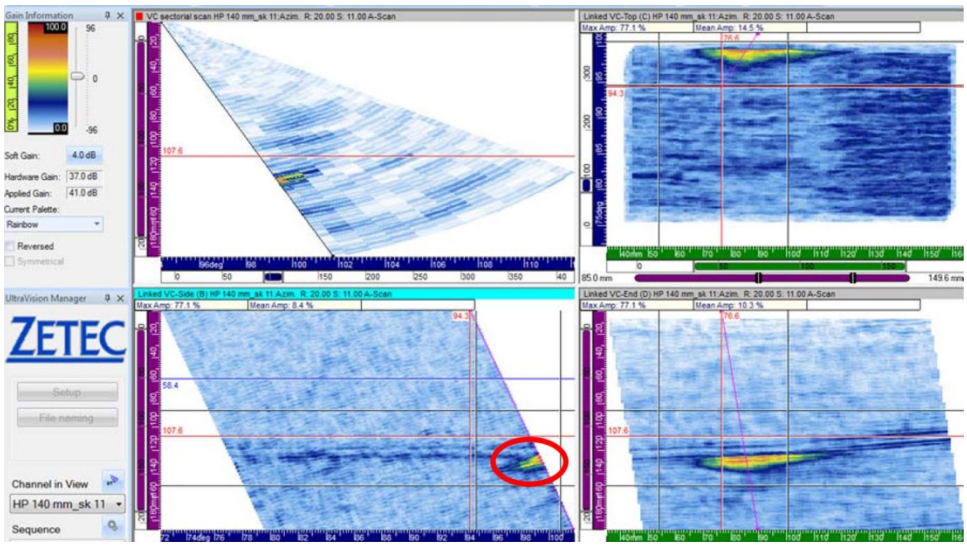

Figure C.35. CW, Skew 11, File 690 to 890 (mm). Axial flaw 2 is on the edge of the scanned aperture and circled in red.

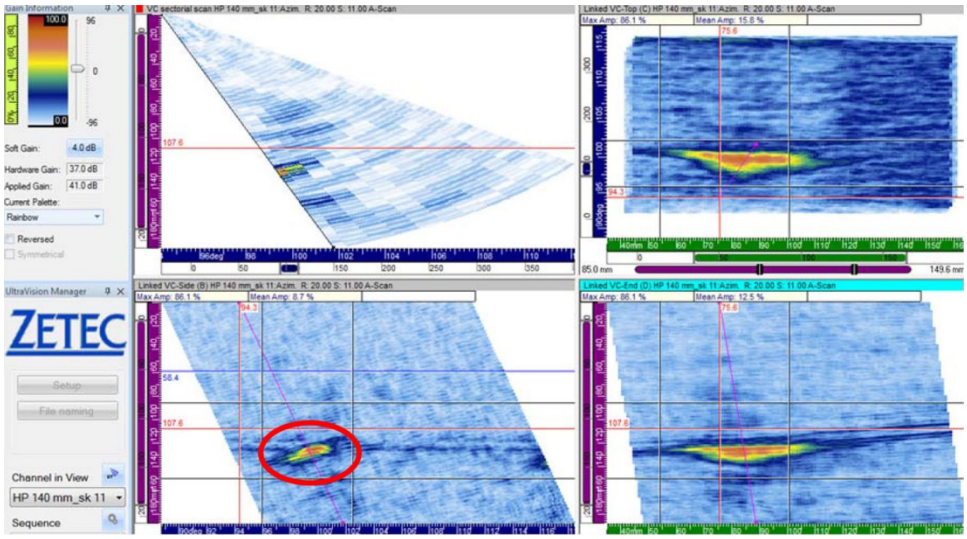

Figure C.36. CW, Skew 11, File 840 to 1040 (mm). Axial flaw 2 is visible and circled in red.

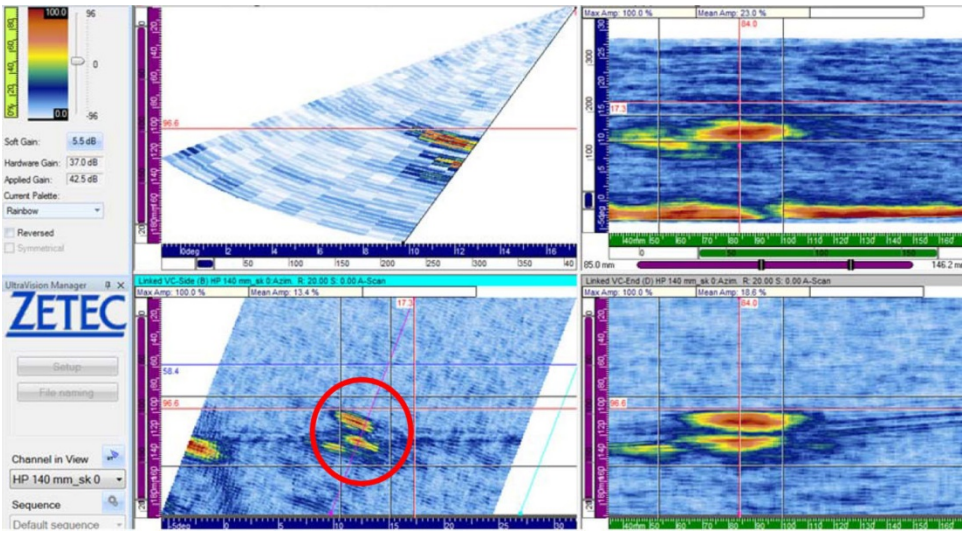

Figure C.37. CCW, Skew 0, File 250 to −20 (mm). Axial flaw 3 is visible and circled in red.

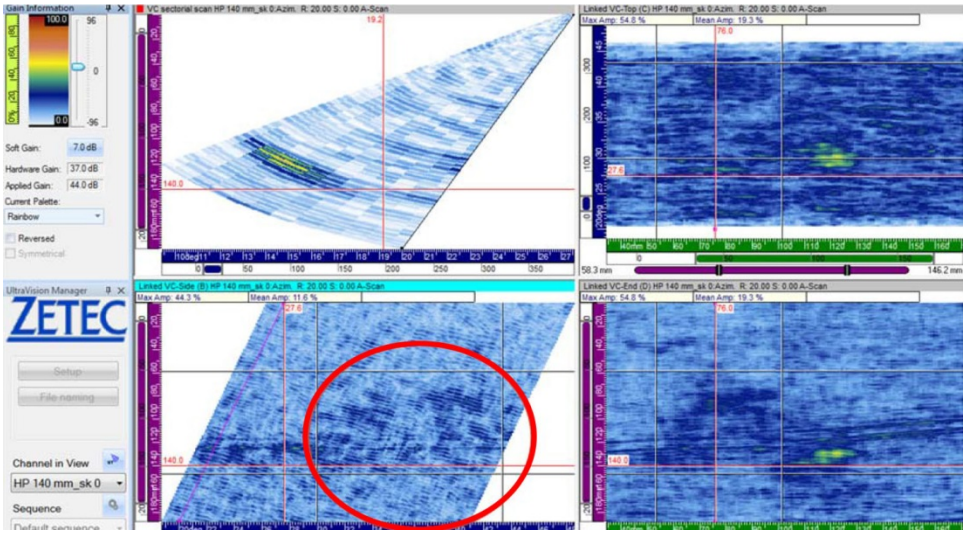

Figure C.38. CCW, Skew 0, File 400 to 200 (mm). Possible implantation artifacts from circumferential flaw 1 are visible and circled in red.

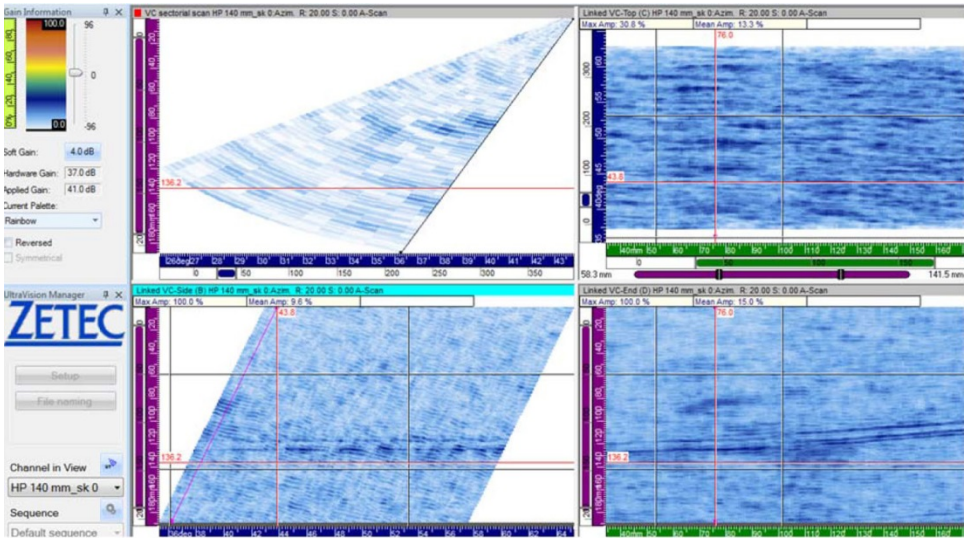

Figure C.39. CCW, Skew 0, File 550 to 350 (mm)

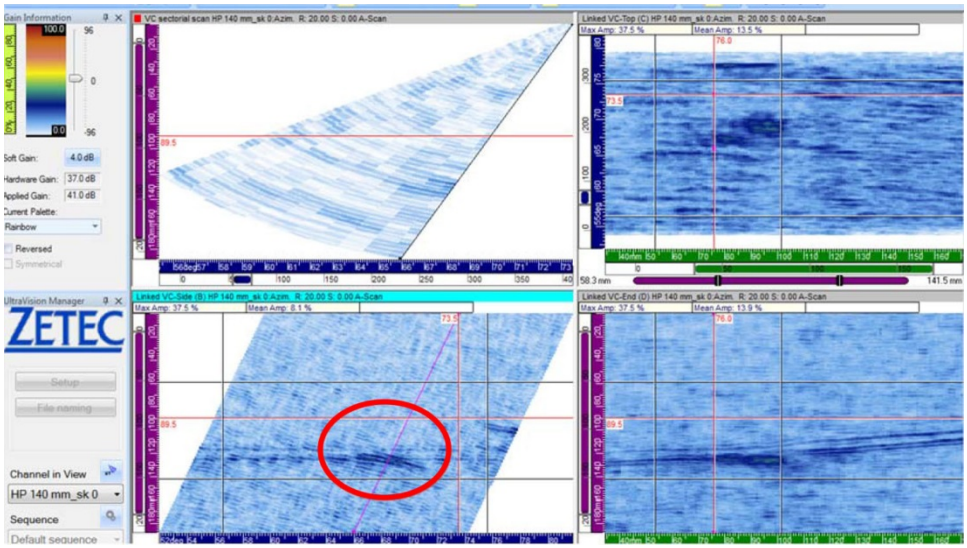

Figure C.40. CCW, Skew 0, File 700 to 500 (mm). A possible implantation artifact from circumferential flaw 4 is visible and circled in red.

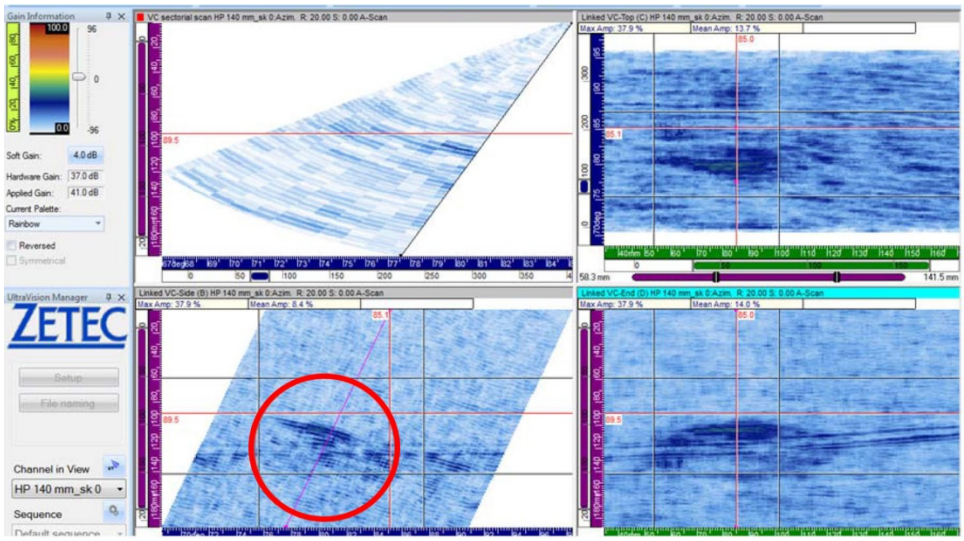

Figure C.41. CCW, Skew 0, File 850 to 650 (mm). Possible artifact from circumferential flaw 4 is visible and circled in red.

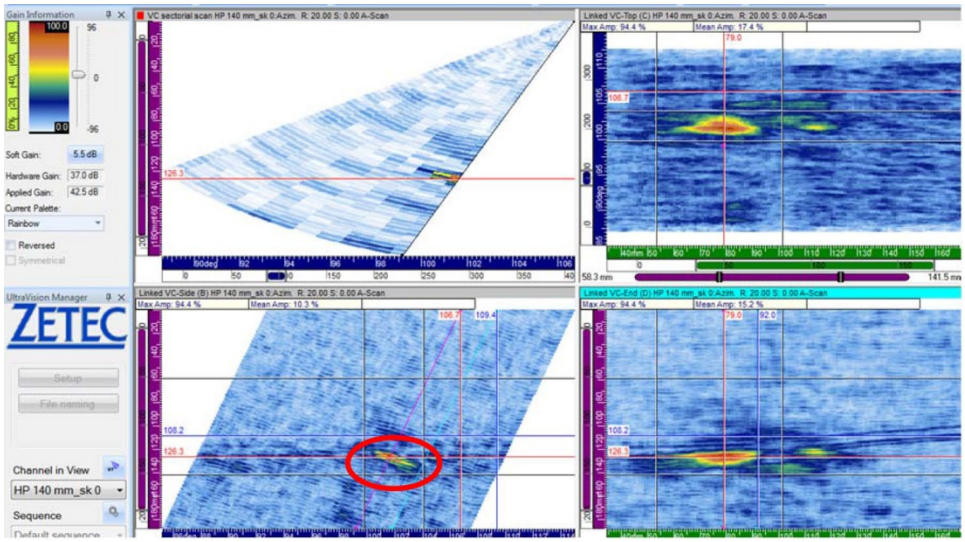

Figure C.42. CCW, Skew 0, File 1000 to 800 (mm). Axial flaw 2 is visible and circled in red.

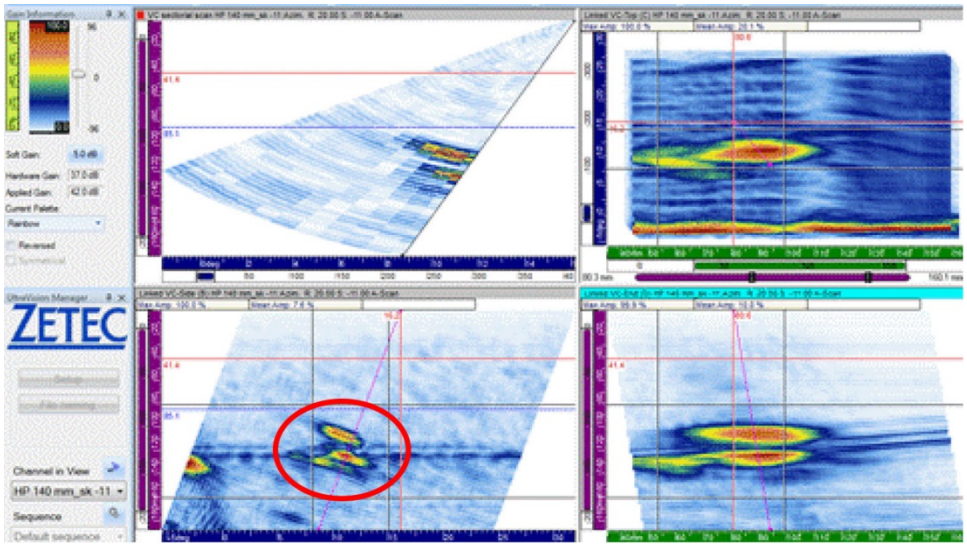

Figure C.43. CCW, Skew 11, File 250 to −20 (mm). Axial flaw 3 is visible and circled in red.

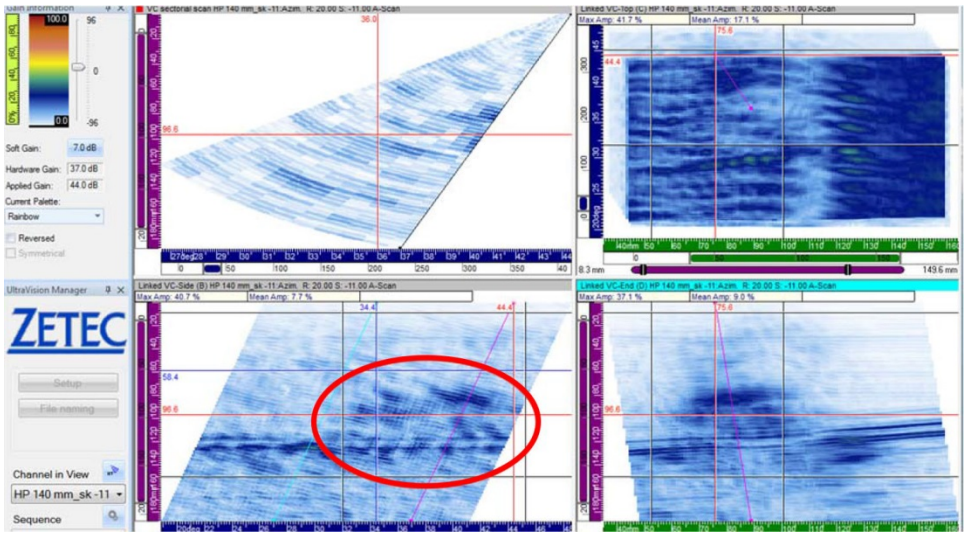

Figure C.44. CCW, Skew 11, File 400 to 200 (mm). Possible implantation artifacts from circumferential flaw 1 are visible and circled in red.

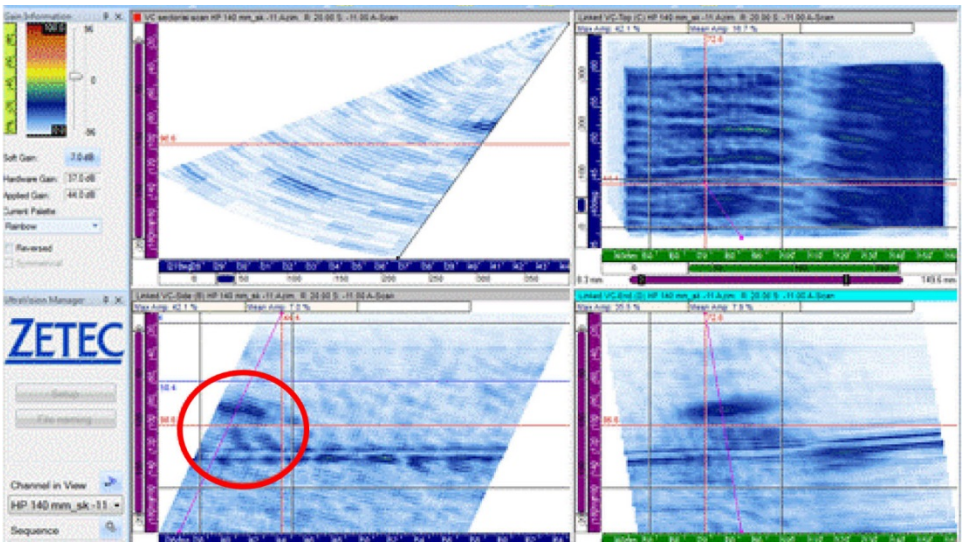

Figure C.45. CCW, Skew 11, File 550 to 350 (mm). Possible implantation artifacts from circumferential flaw 1 are visible and circled in red.

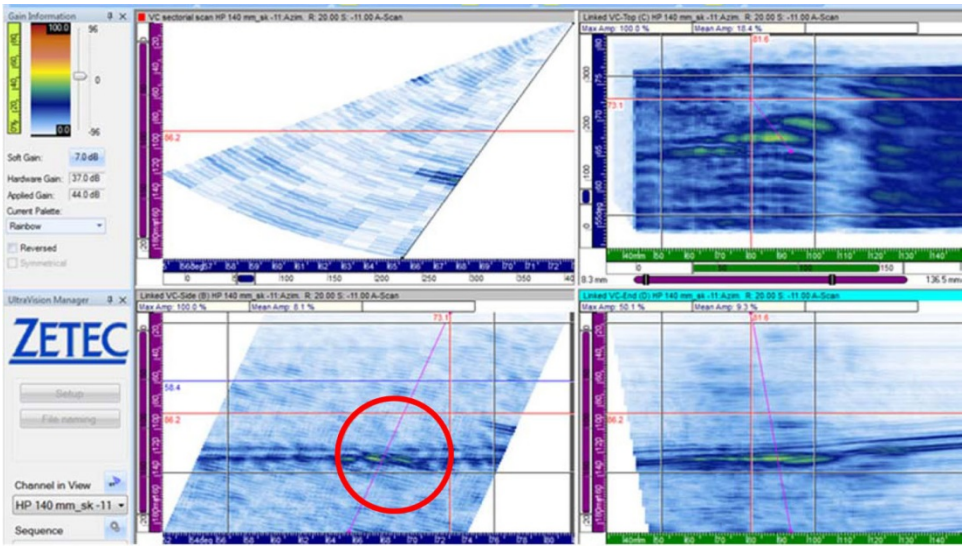

Figure C.46. CCW, Skew 11, File 700 to 500 (mm). A possible implantation artifact from circumferential flaw 4 is visible and circled in red.

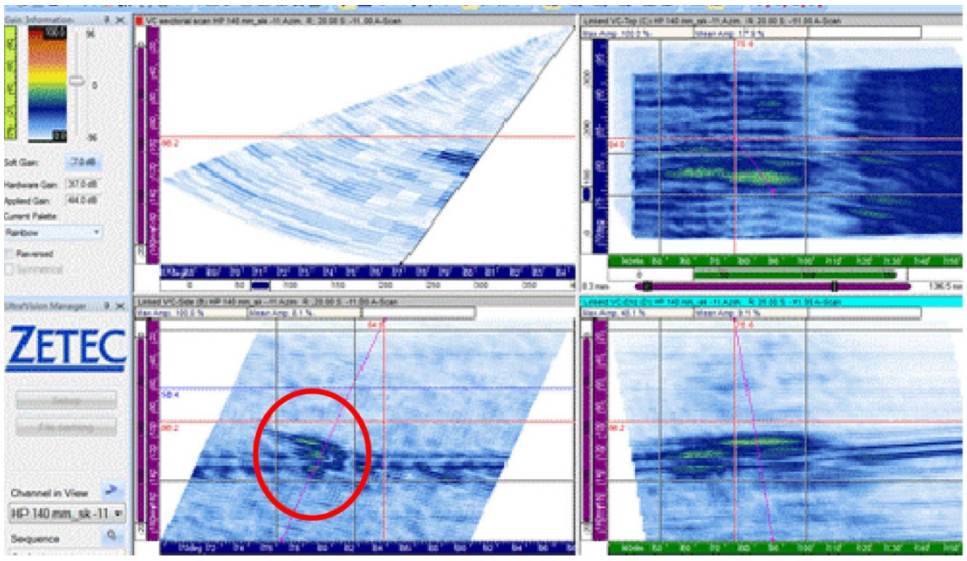

Figure C.47. CCW, Skew 11, File 850 to 650 (mm). Possible implantation artifact from circumferential flaw 4 is visible and circled in red.

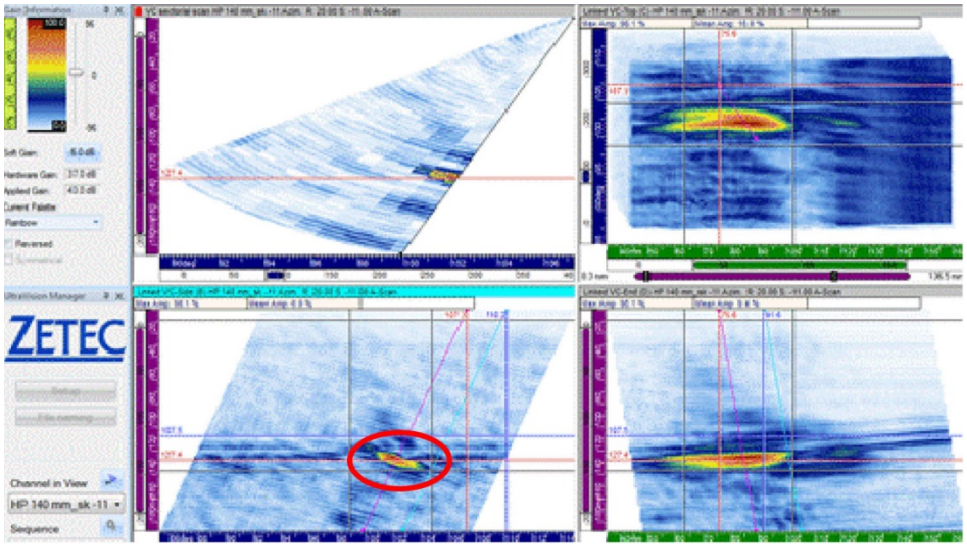

Figure C.48. CCW, Skew 11, File 1000 to 800 (mm). Axial flaw 2 is visible and circled in red.

C.3 Circumferential Flaws, 0-Degree Skew Angle

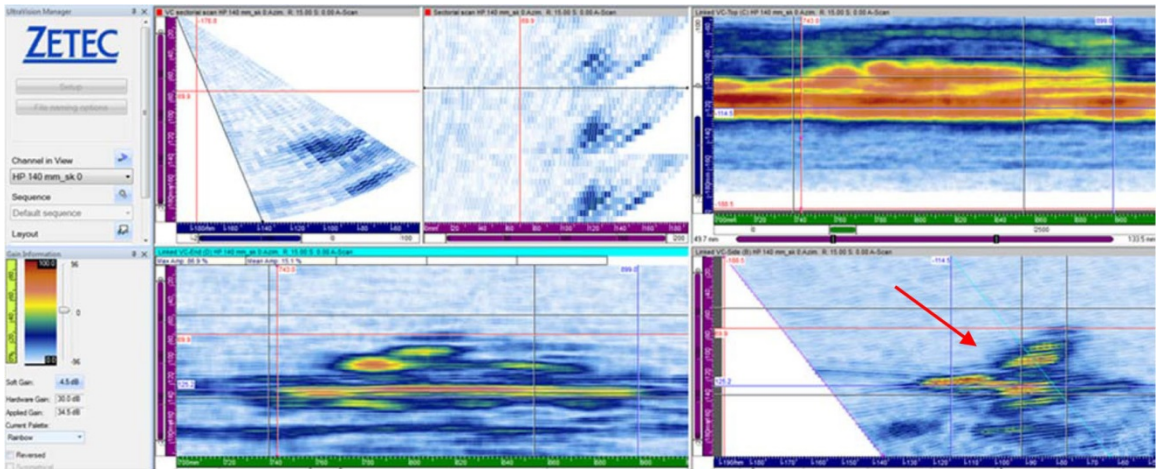

Figure C.49. DM-05 Flaw 2, Noted by Red Arrow

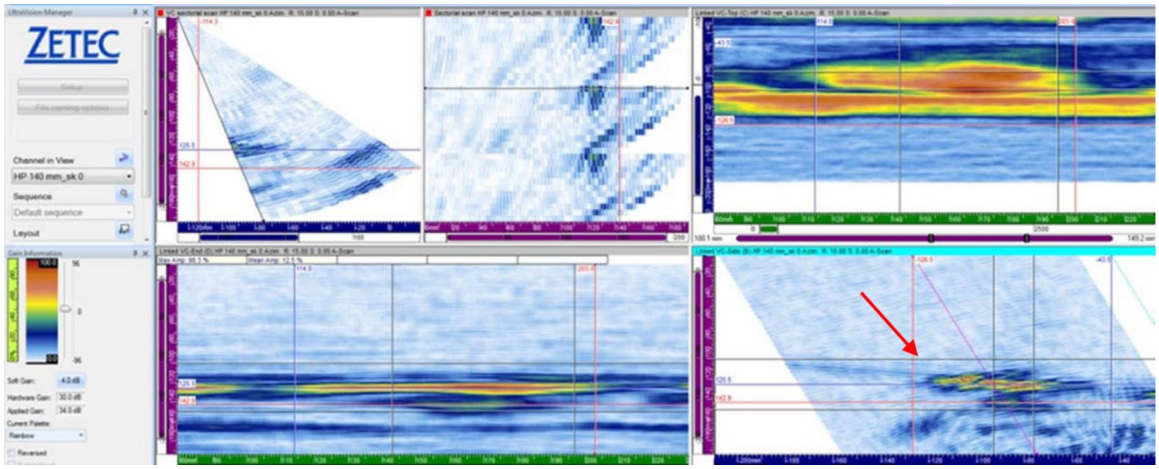

Figure C.50. DM-05 Flaw 3, Noted by Red Arrow

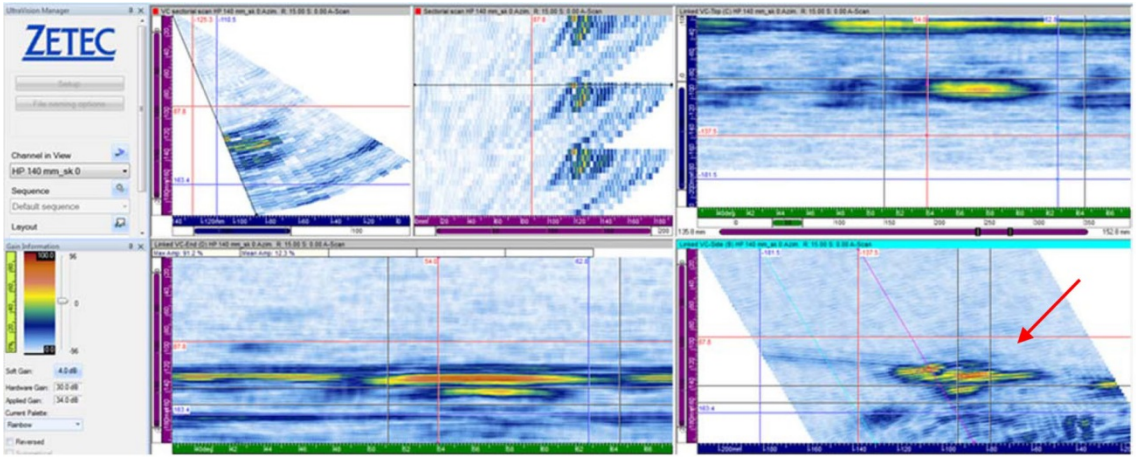

Figure C.51. DM-05 Flaw 4, Noted by Red Arrow

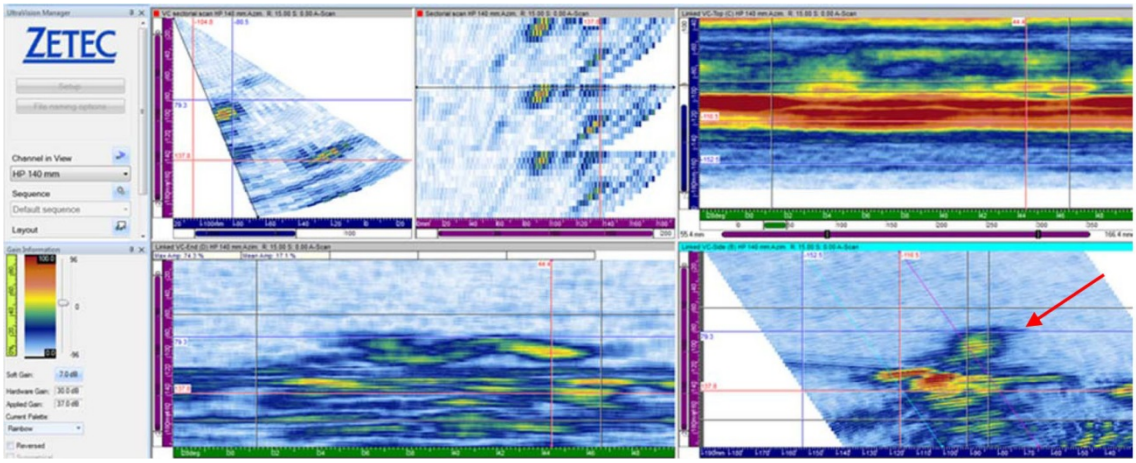

Figure C.52. DM-10 Flaw 1, Noted by Red Arrow

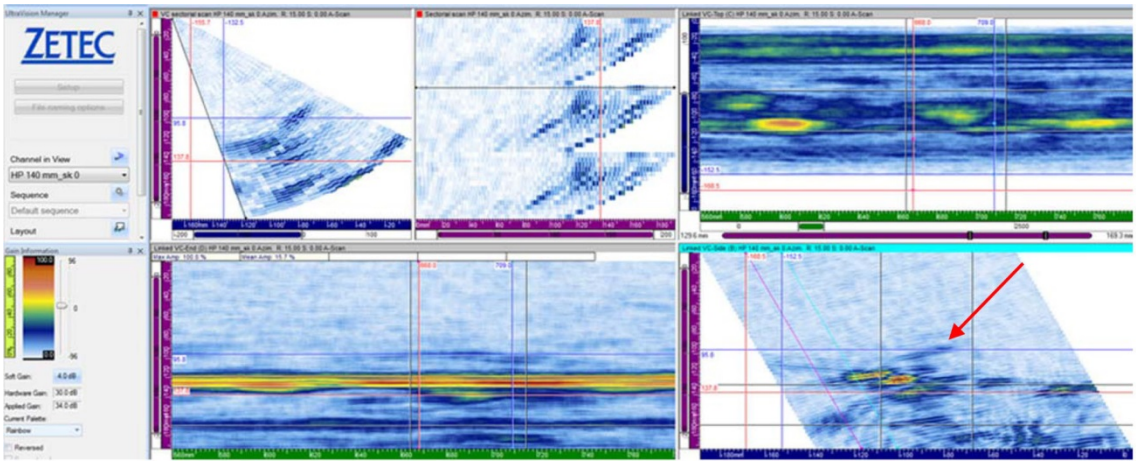

Figure C.53. DM-10 Flaw 4, Noted by Red Arrow

Appendix D

1.0-MHz PA Data Images, Half-Path Focus

Appendix D

1.0-MHz PA Data Images, Half-Path Focus

D.1 DM-05

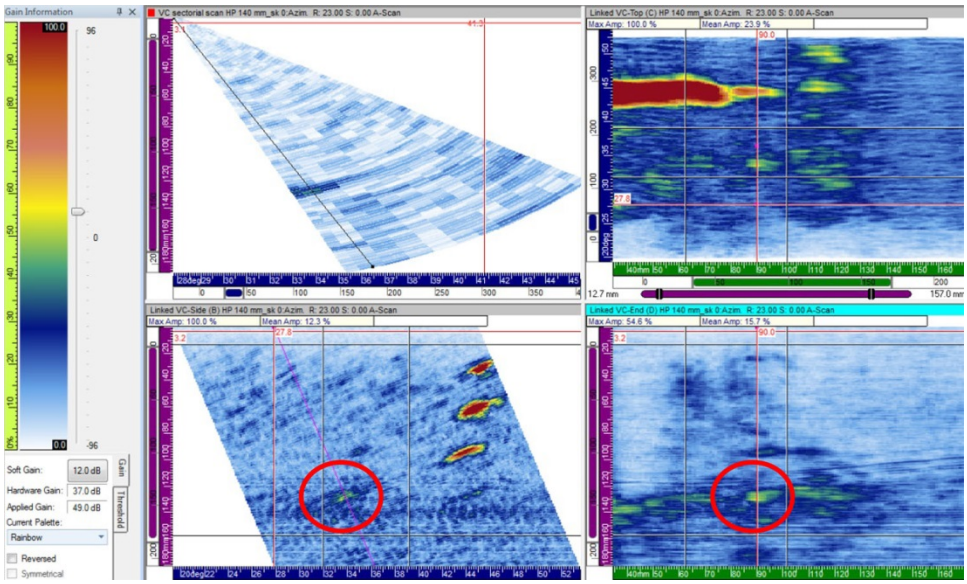

Figure D.1. CW, Skew 0, Axial Flaw 1, Circled in Red

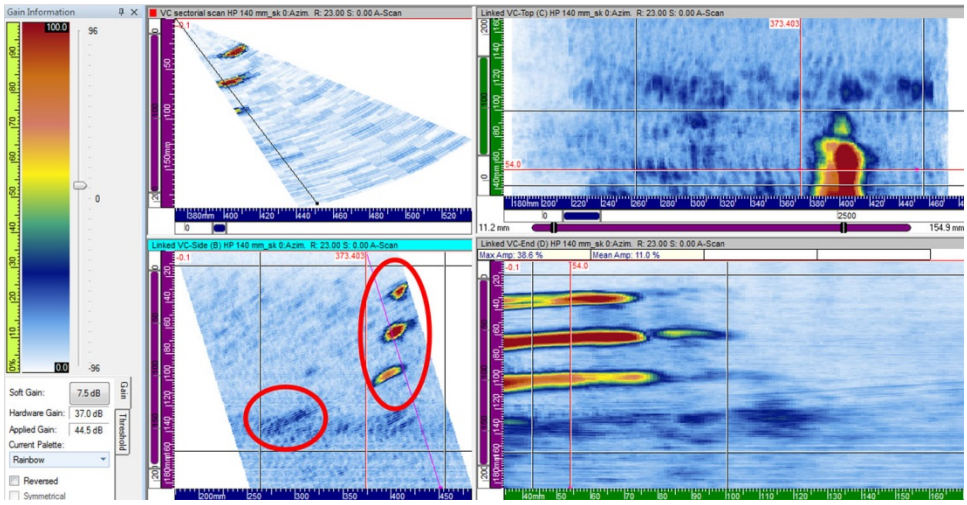

Figure D.2. CW, Skew 0 (reduced gain). Axial flaw 1 (left) and three side-drilled holes (right) are visible and circled in red.

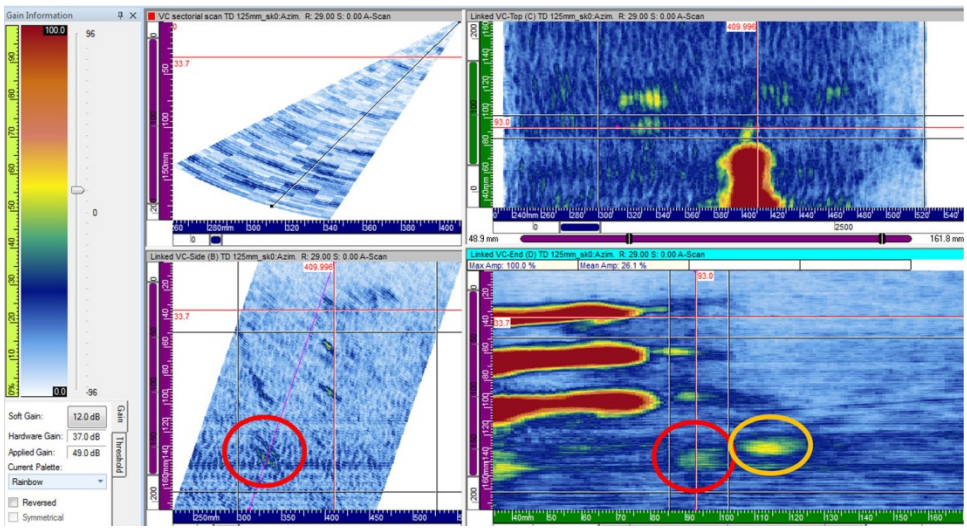

Figure D.3. CCW, Skew 0, Axial Flaw 1, Circled in Red. An artifact extending into the safe end is circled in orange.

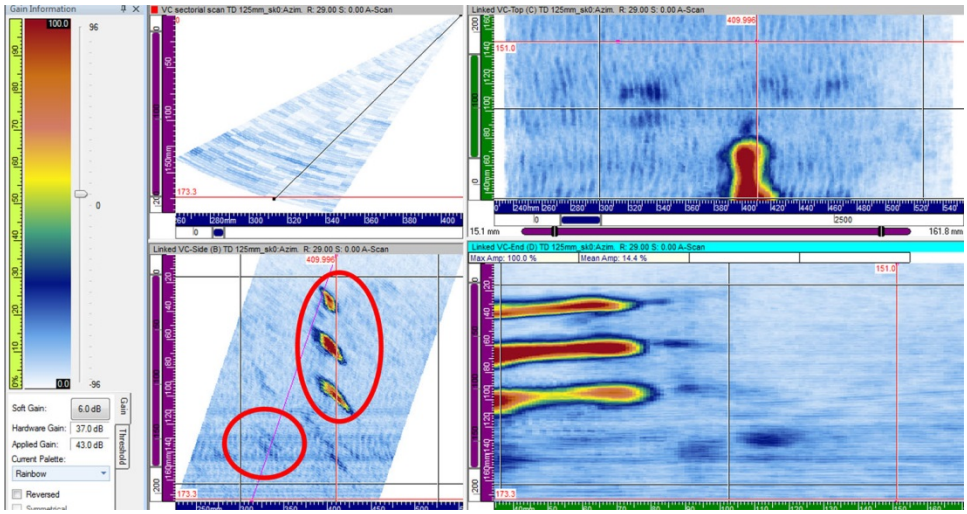

Figure D.4. CCW, Skew 0, Reduced Gain. Axial flaw 1 (left) and three side-drilled holes (right) are visible and circled in red.

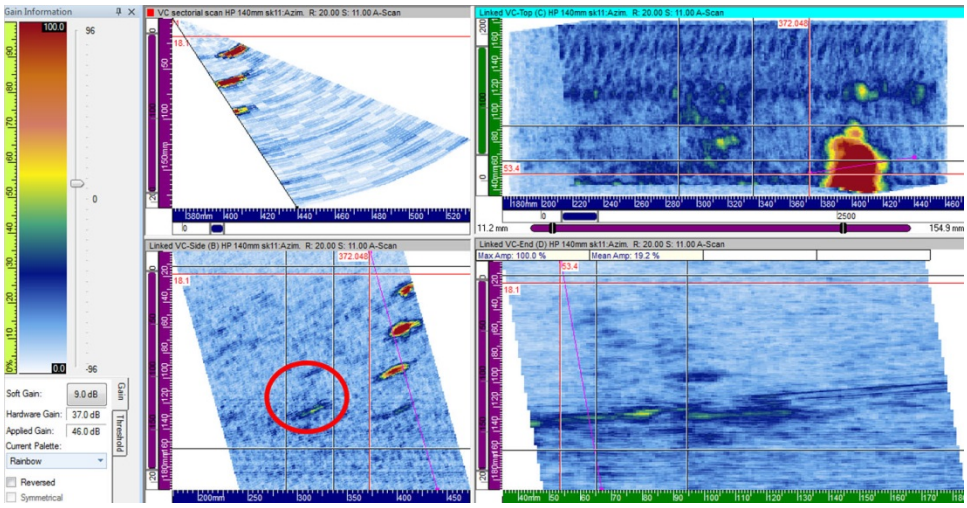

Figure D.5. CW, Skew 11, Axial Flaw 1, Circled in Red

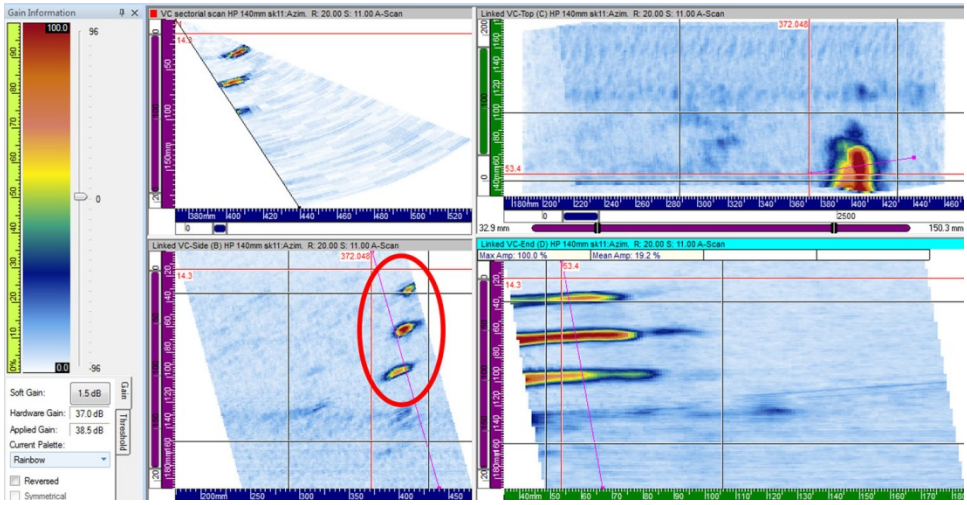

Figure D.6. CW, Skew 11, Reduced Gain. Three side-drilled holes are visible and circled in red.

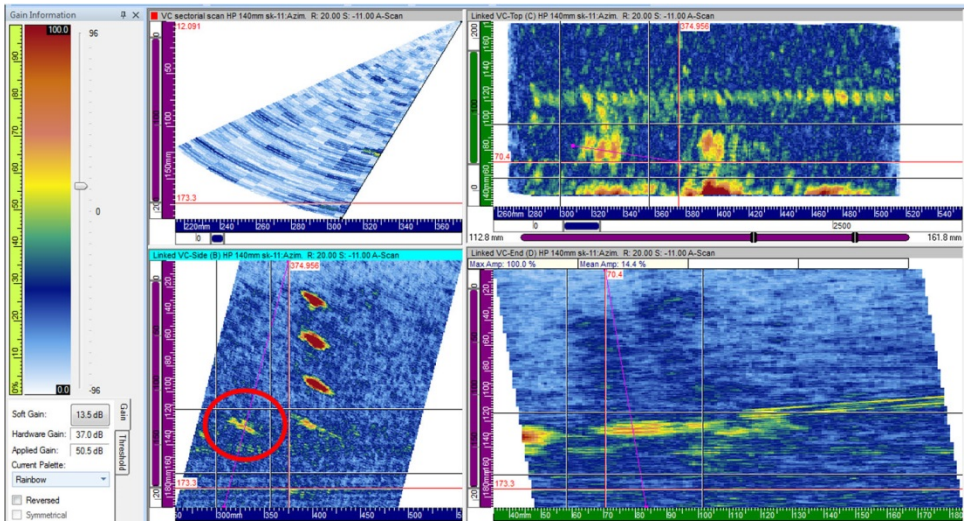

Figure D.7. CCW, Skew 11, Axial Flaw 1, Circled in Red

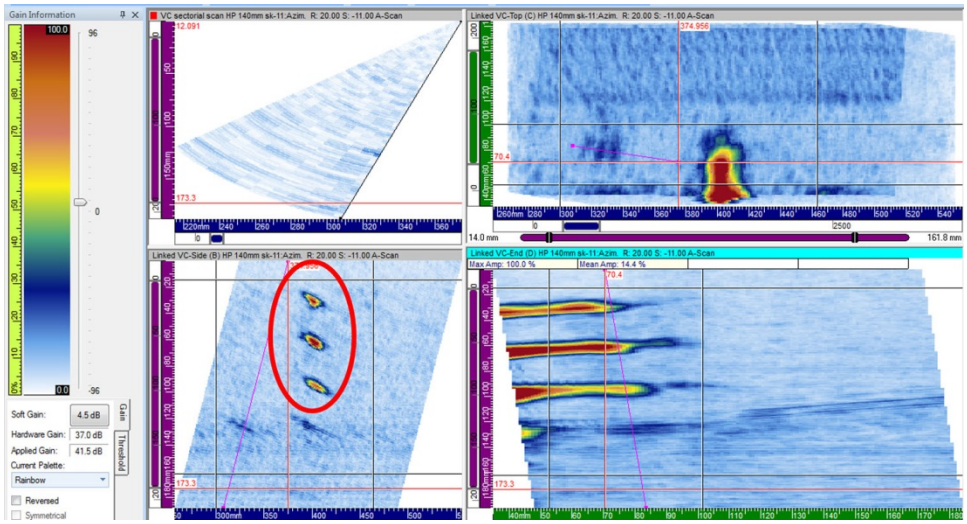

Figure D.8. CCW, Skew 11, Reduced Gain. Three side-drilled holes are visible and circled in red.

D.2 DM-10

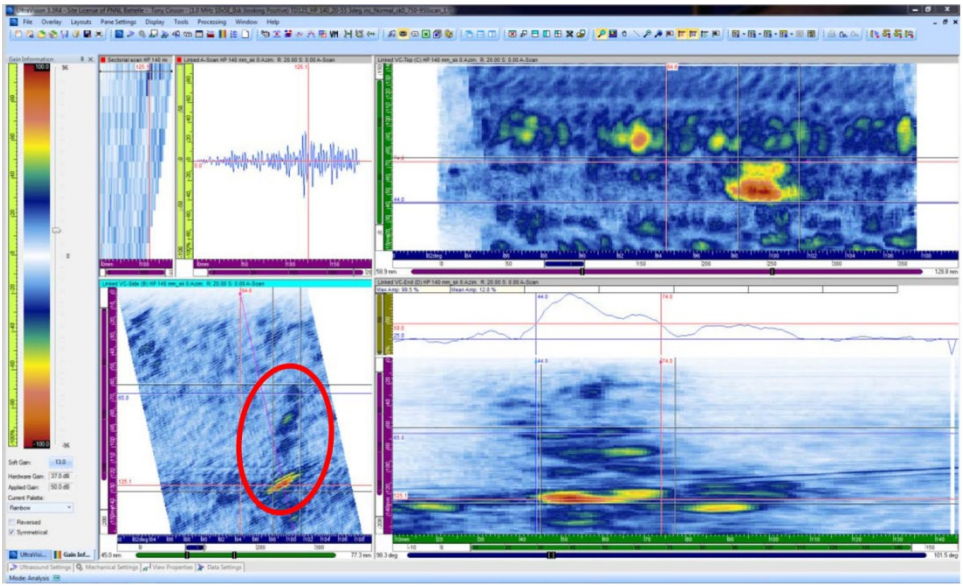

Figure D.9. CW, Skew 0, Axial Flaw 2, Circled in Red

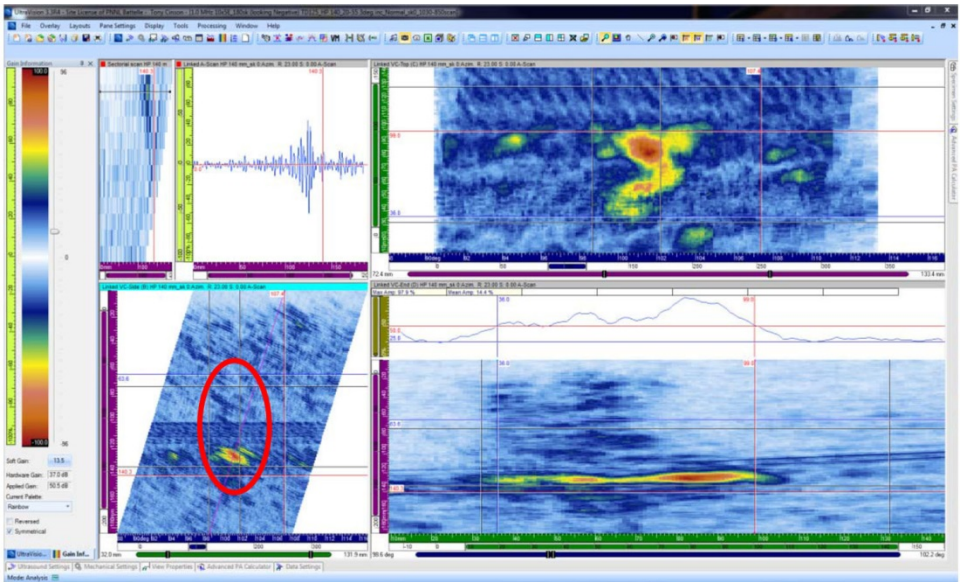

Figure D.10. CCW, Skew 0, Axial Flaw 2, Circled in Red

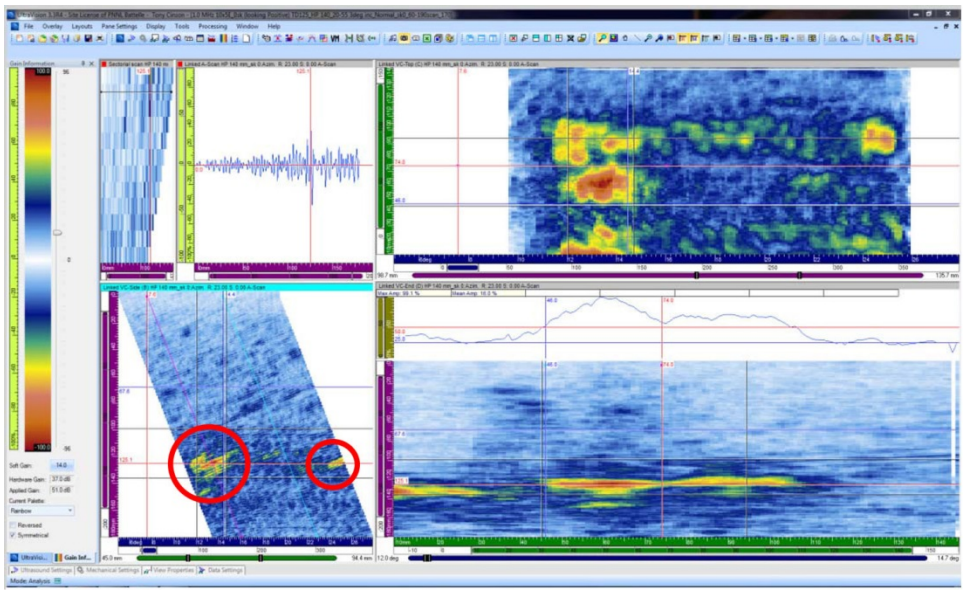

Figure D.11. CW, Skew 0. Axial Flaw 3 (left) and artifact (right) are visible and circled in red.

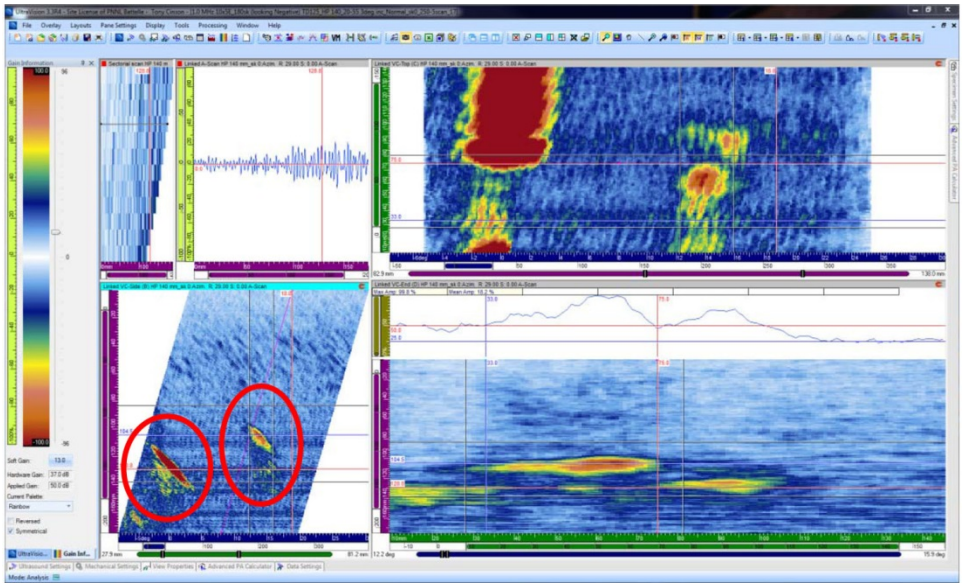

Figure D.12. CCW, Skew 0. Axial Flaw 3 and artifact (right), and end-of-specimen (left) are visible and circled in red.

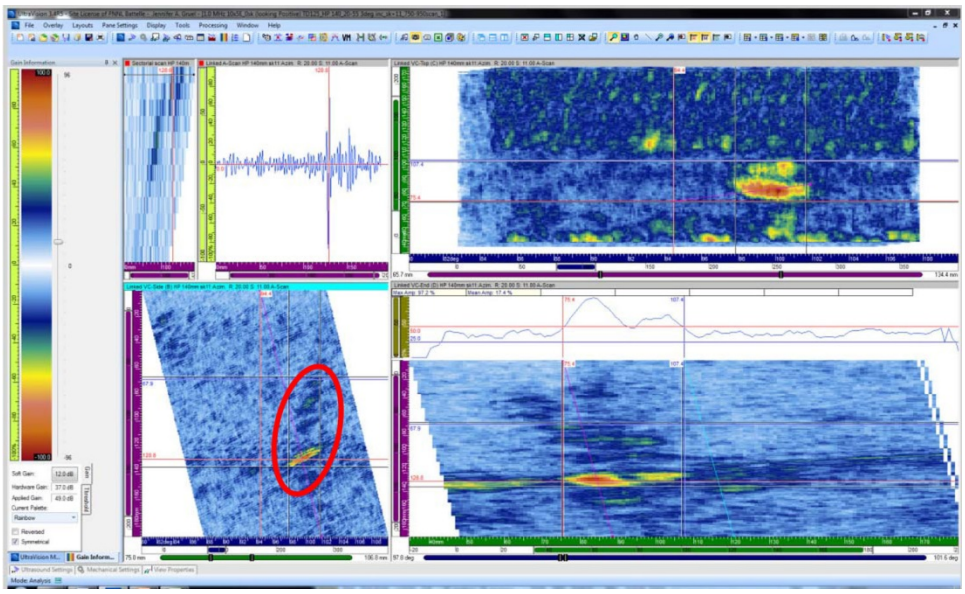

Figure D.13. CW, Skew 11, Axial Flaw 2, Circled in Red

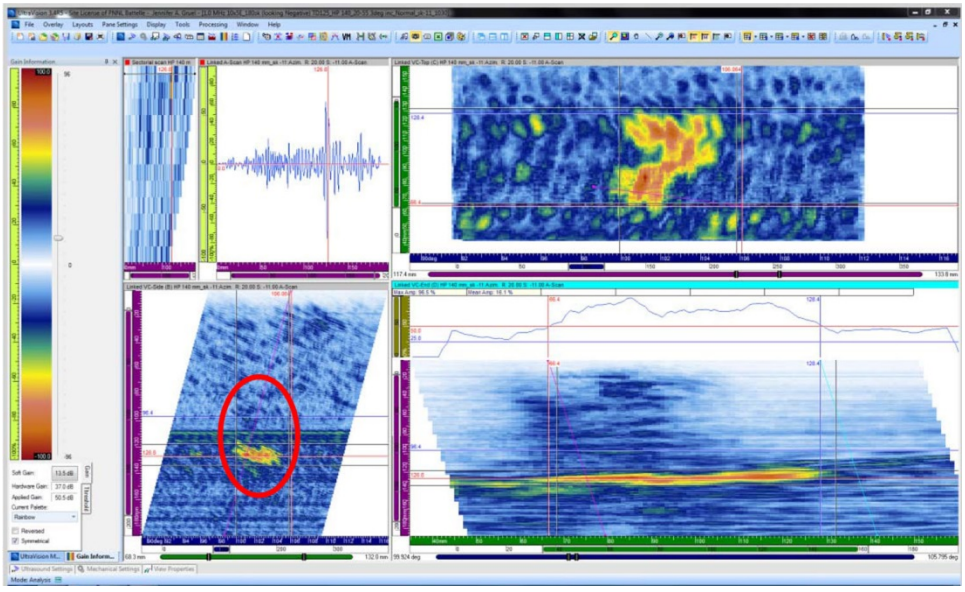

Figure D.14. CCW, Skew 11, Axial Flaw 2, Circled in Red

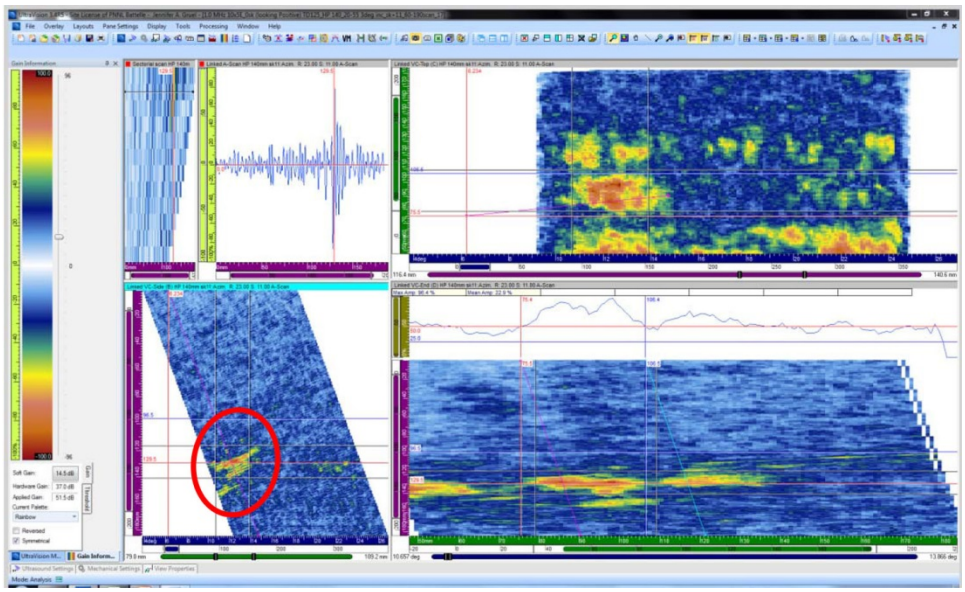

Figure D.15. CW, Skew 11, Axial Flaw 3, Circled in Red

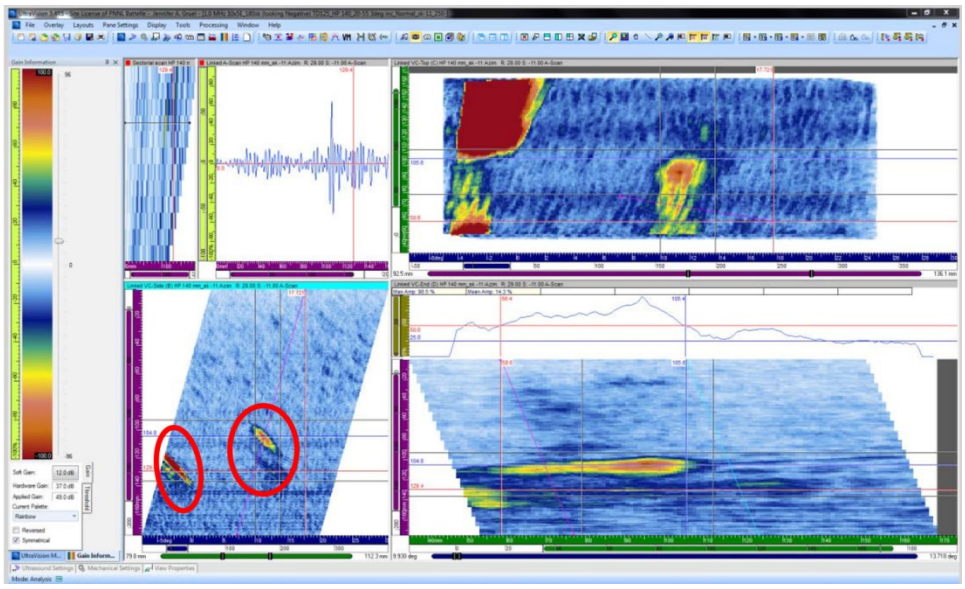

Figure D.16. CCW, Skew 11. Axial flaw 3 (right) and end-of-specimen (left) are visible and circled in red.

D.3 Circumferential Flaws, 0-Degree Skew Angle

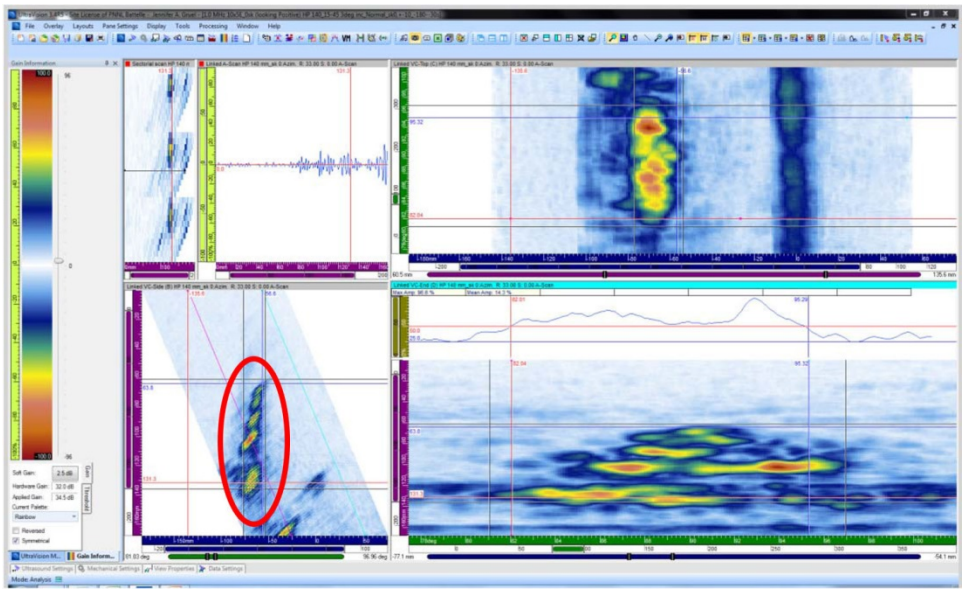

Figure D.17. DM-05 Flaw 2 Circled in Red

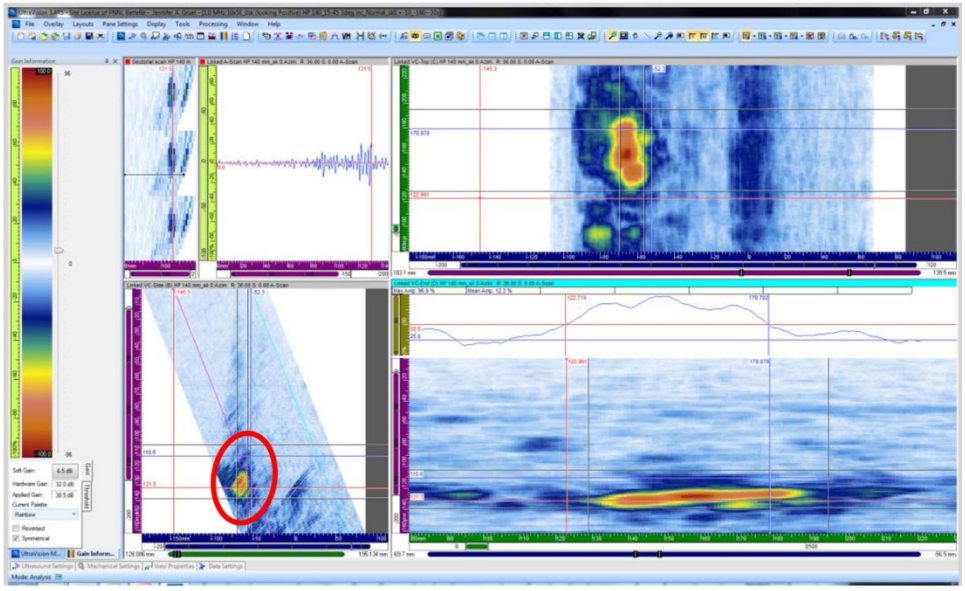

Figure D.18. DM-05 Flaw 3 Circled in Red

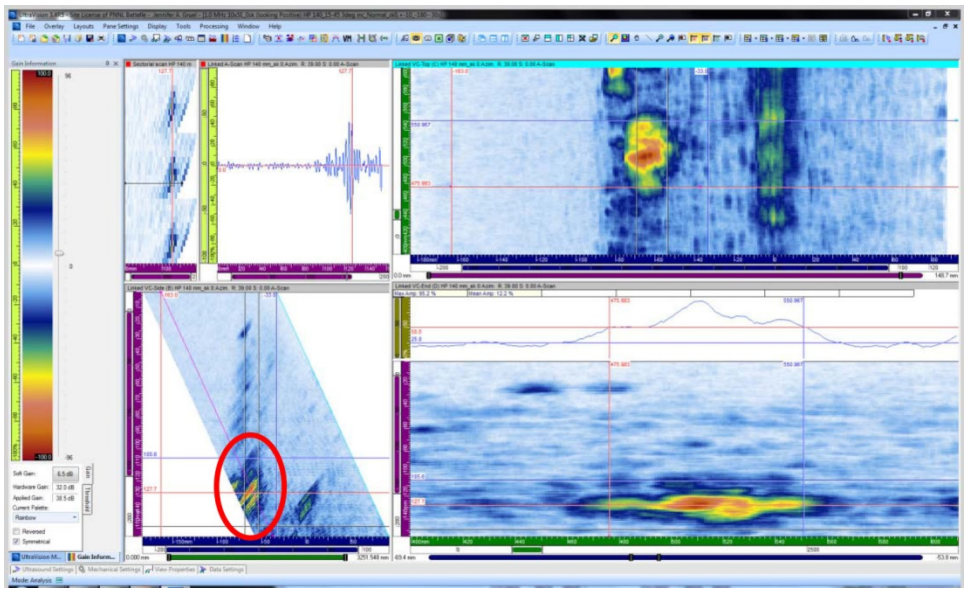

Figure D.19. DM-05 Flaw 4 Circled in Red

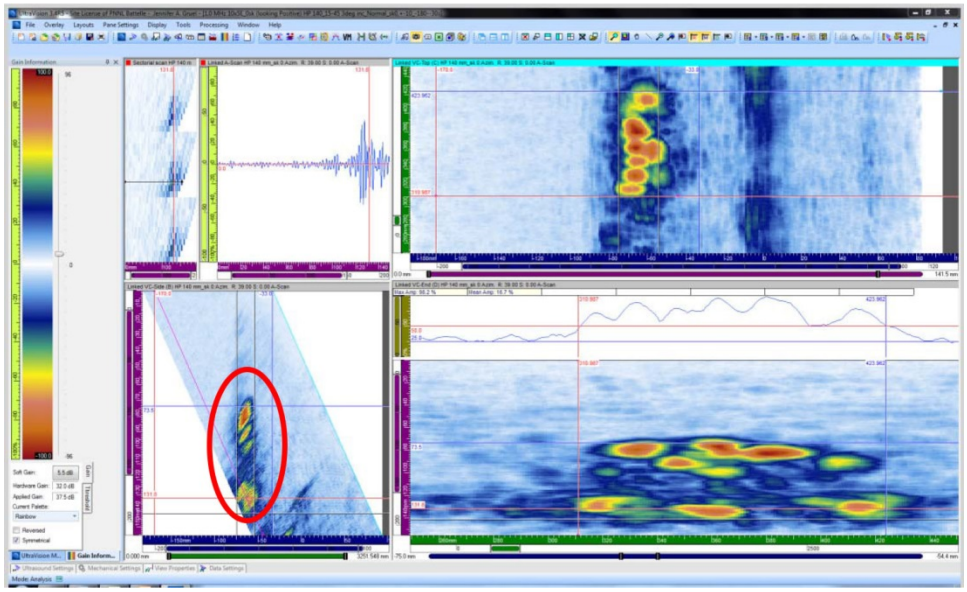

Figure D.20. DM-10 Flaw 1 Circled in Red

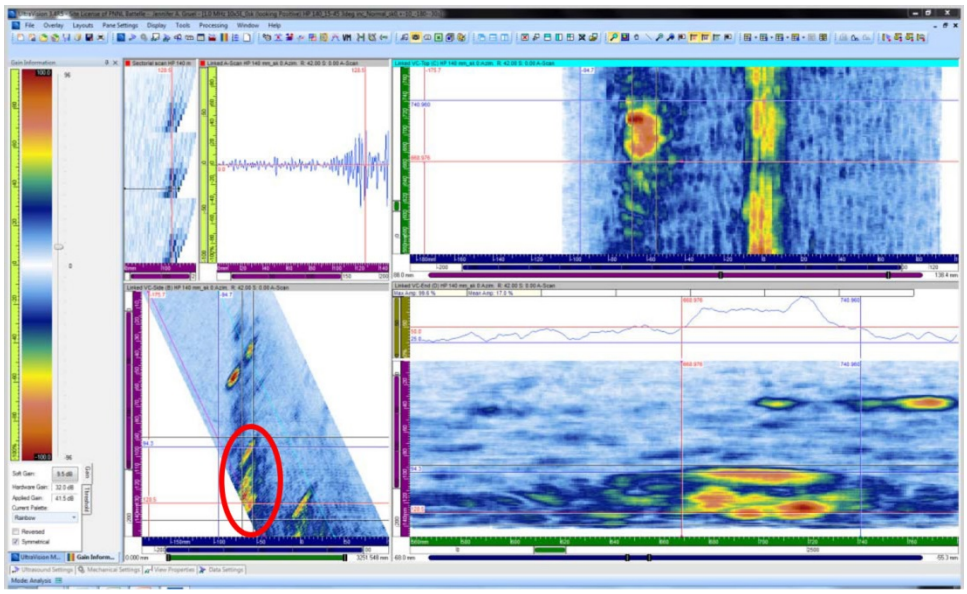

Figure D.21. DM-10 Flaw 4 Circled in Red

Appendix E

2.0-MHz PA Data Images, Half-Path Focus

Appendix E

2.0-MHz PA Data Images, Half-Path Focus

E.1 DM-05

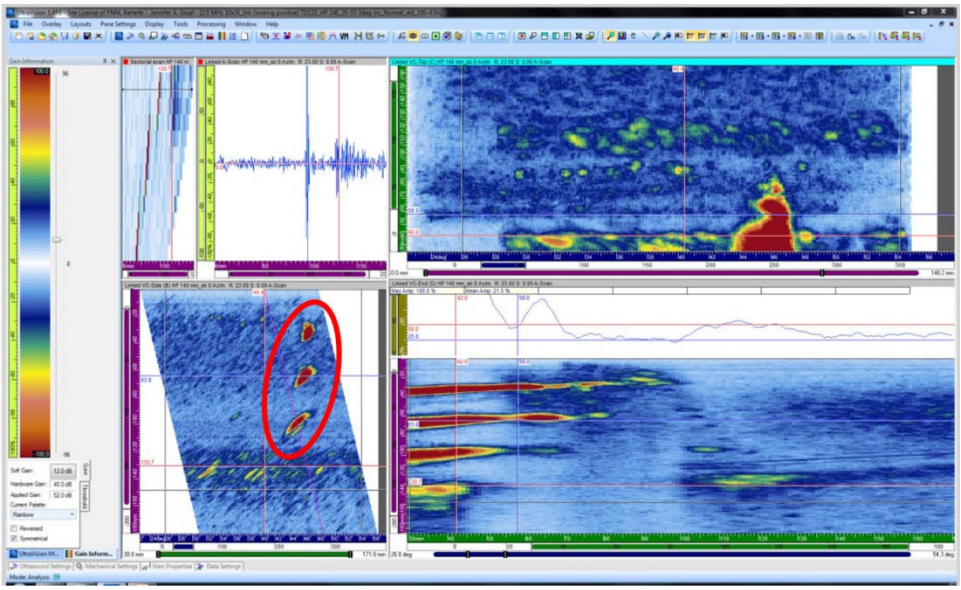

Figure E.1. CW, Skew 0, Axial Flaw 1 Region. Flaw not detected. Three side-drilled holes are visible and circled in red.

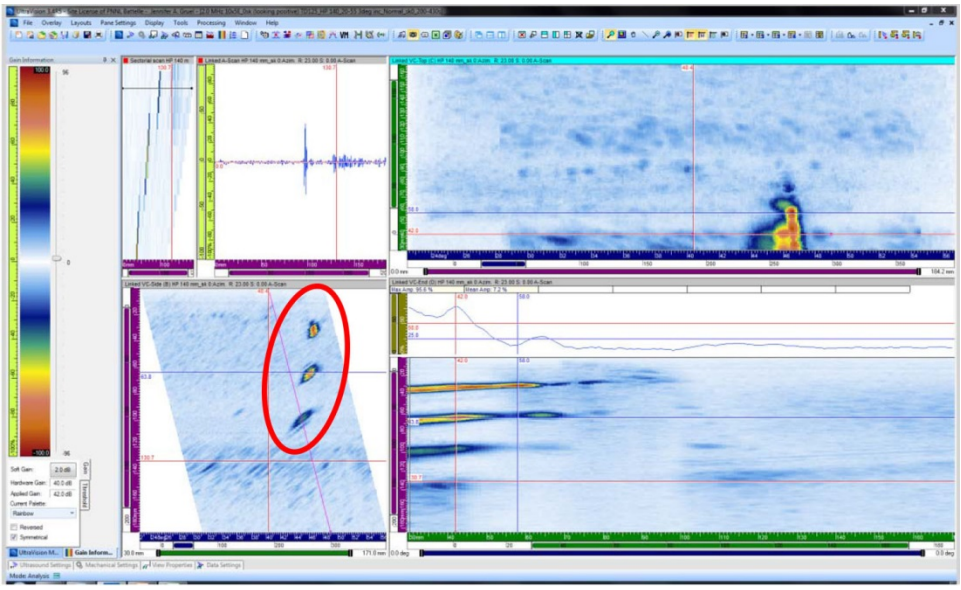

Figure E.2. CW, Skew 0, Reduced Gain. Three side-drilled holes are visible and circled in red.

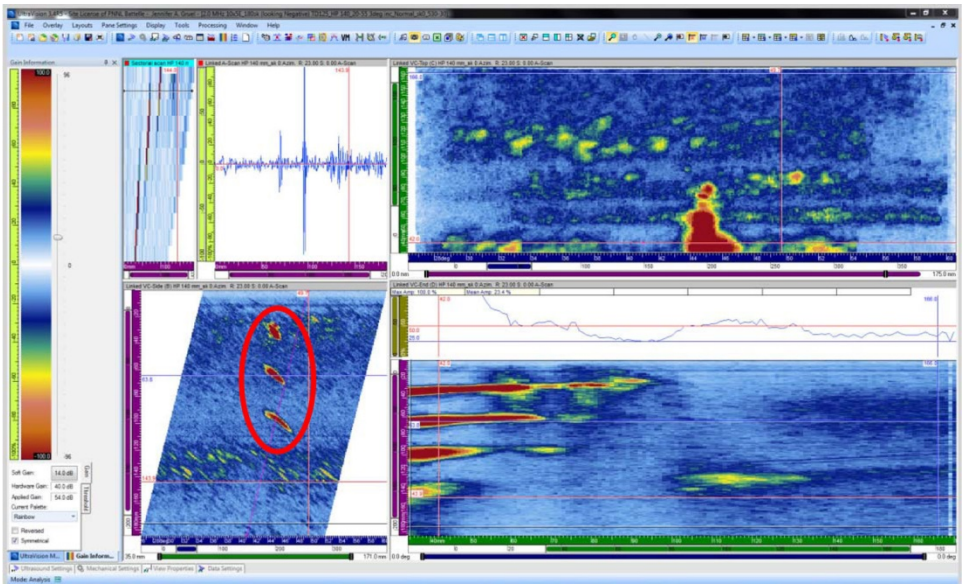

Figure E.3. CCW, Skew 0, Axial Flaw 1 Region. Flaw not detected. Three side-drilled holes are visible and circled in red.

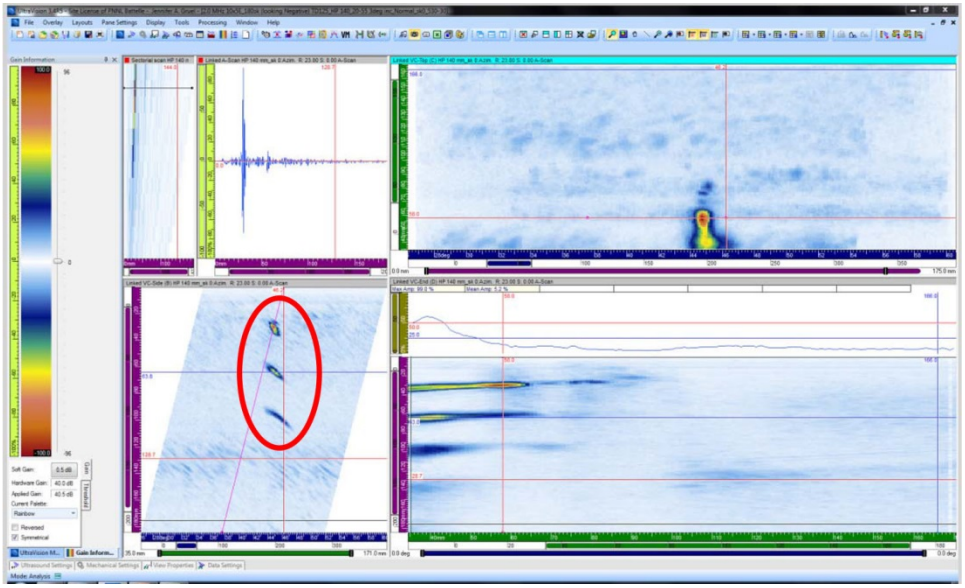

Figure E.4. CCW, Skew 0, Reduced Gain. Three side-drilled holes are visible and circled in red.

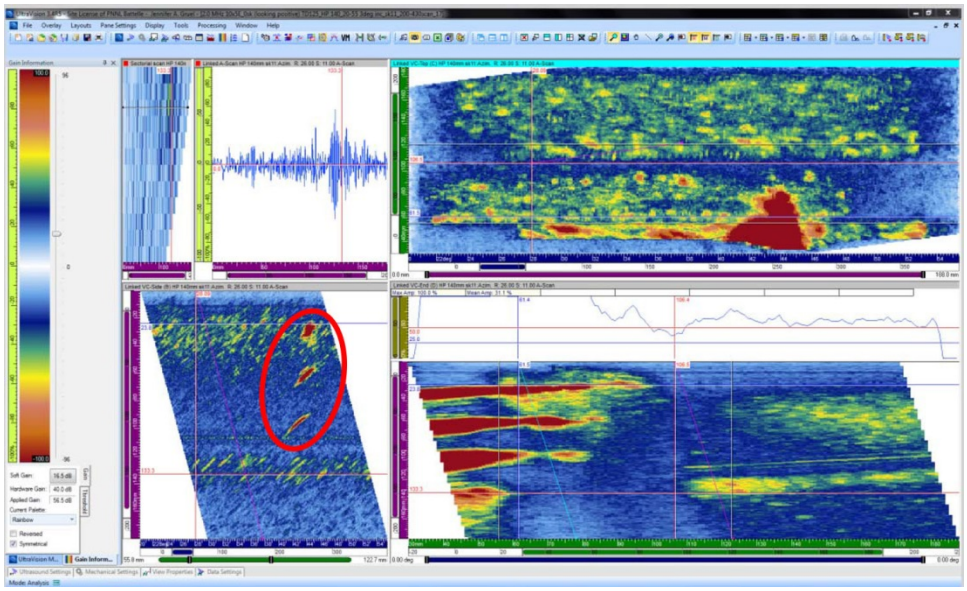

Figure E.5. CW, Skew 11, Axial Flaw 1 Region. Flaw not detected. Three side-drilled holes are visible and circled in red.

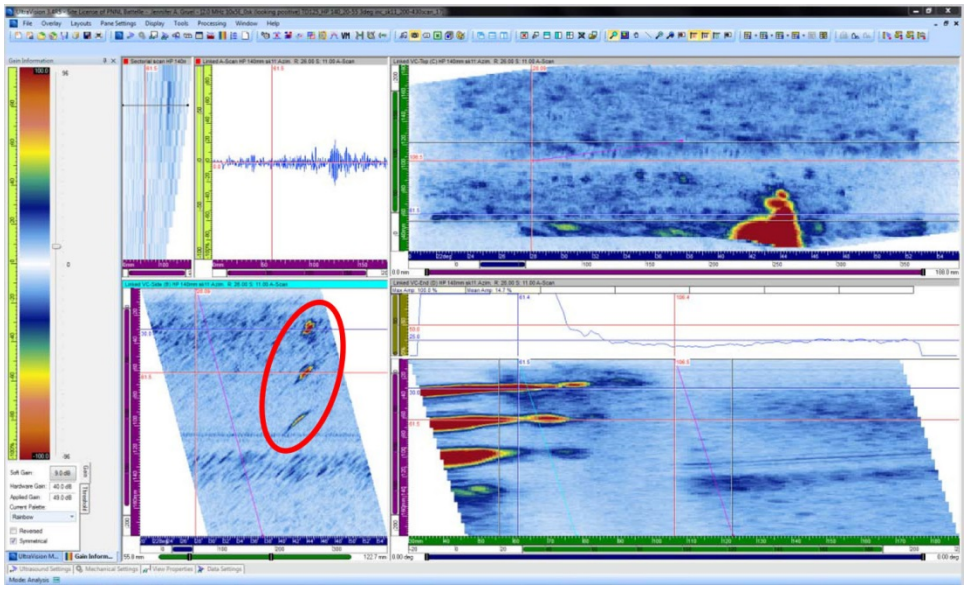

Figure E.6. CW, Skew 11, Reduced Gain. Three side-drilled holes are visible and circled in red.

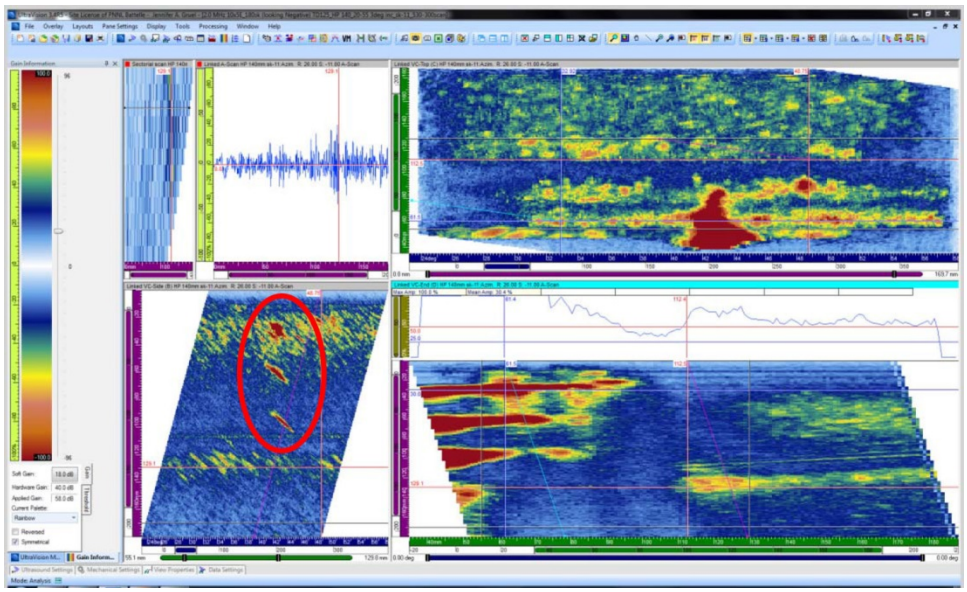

Figure E.7. CCW, Skew 11, Axial Flaw 1 Region. Flaw not detected. Three side-drilled holes are visible and circled in red.

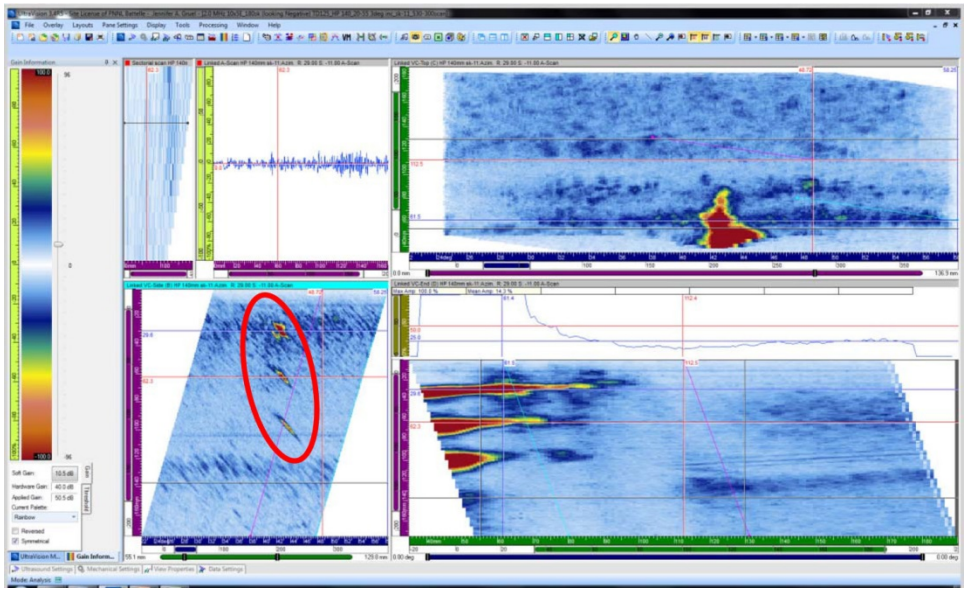

Figure E.8. CCW, Skew 11, Reduced Gain. Three side-drilled holes are visible and circled in red.

E.2 DM-10

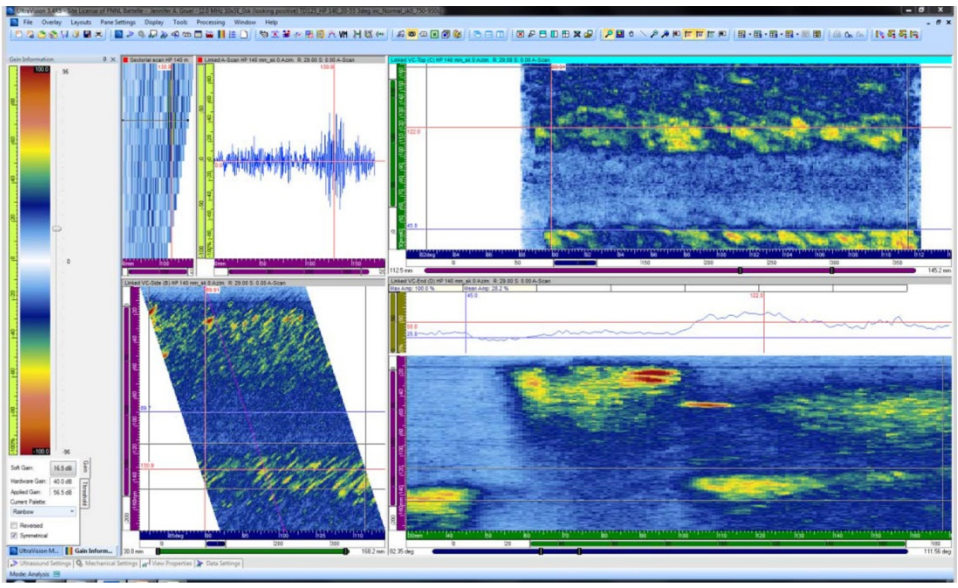

Figure E.9. CW, Skew 0, Axial Flaw 2 Region. Flaw not detected.

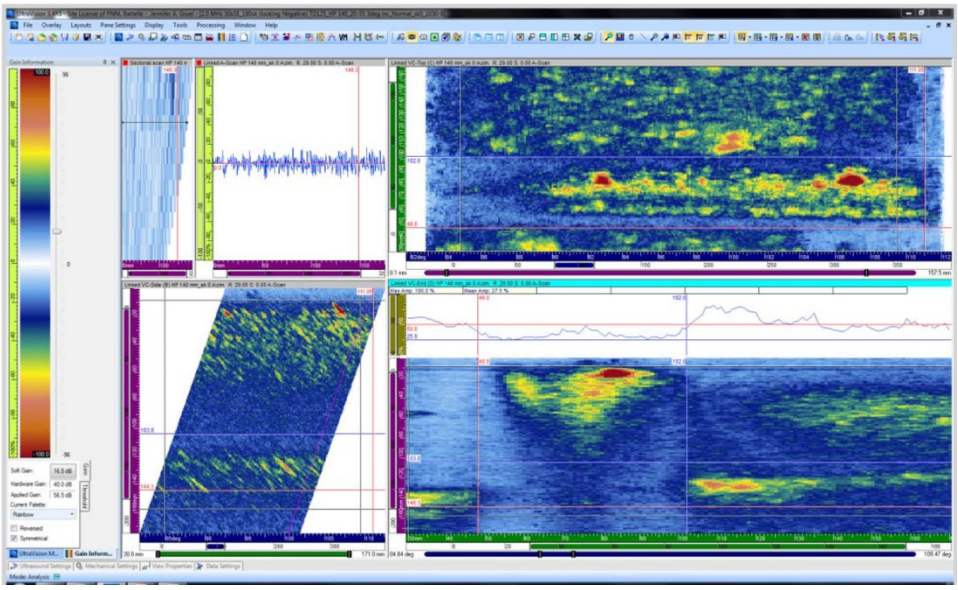

Figure E.10. CCW, Skew 0, Axial Flaw 2 Region. Flaw not detected.

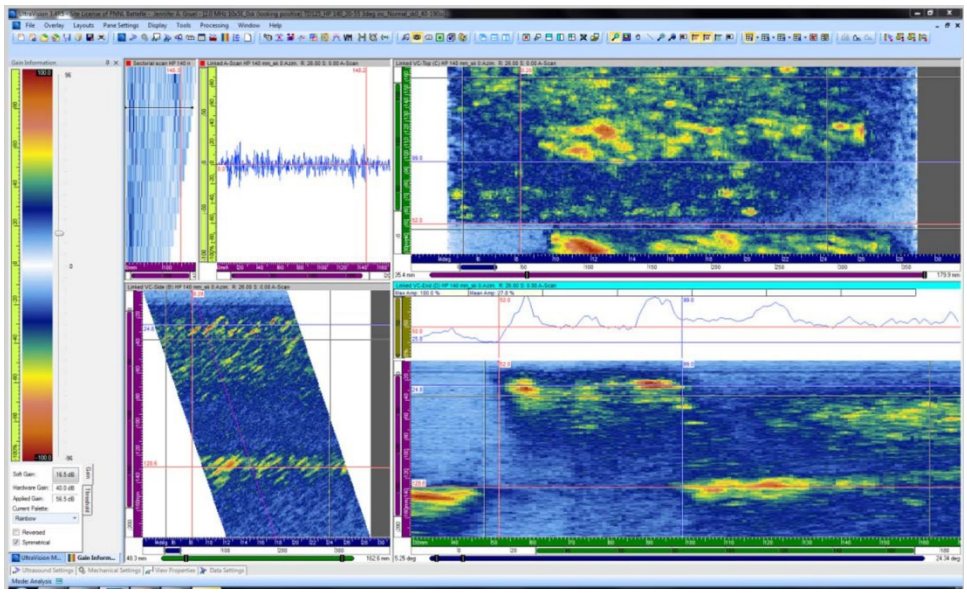

Figure E.11. CW, Skew 0, Axial Flaw 3 Region. Flaw not detected.

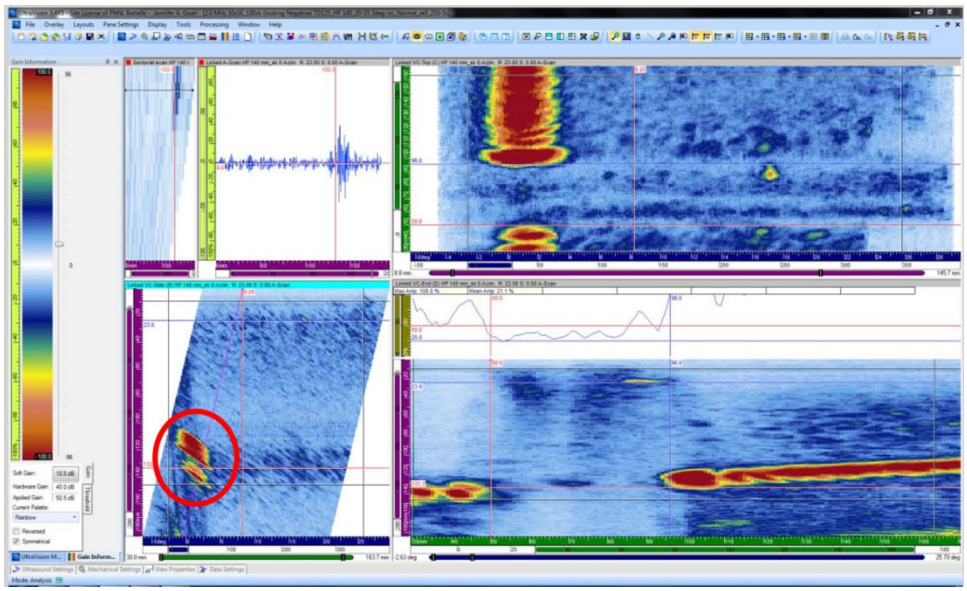

Figure E.12. CCW, Skew 0, Axial Flaw 3 Region. Flaw not detected; end-of-specimen is visible and circled in red.

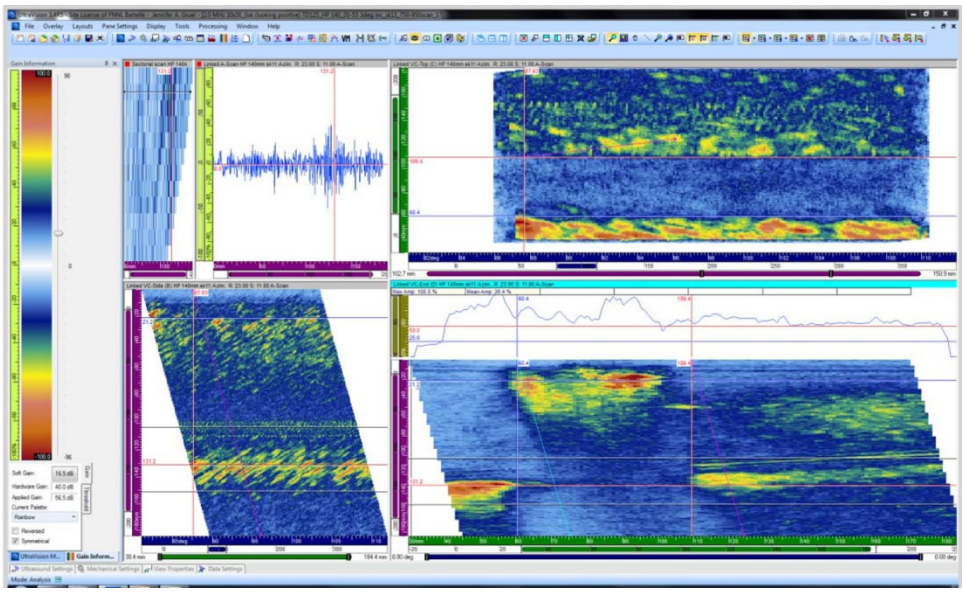

Figure E.13. CW, Skew 11, Axial Flaw 2 Region. Flaw not detected.

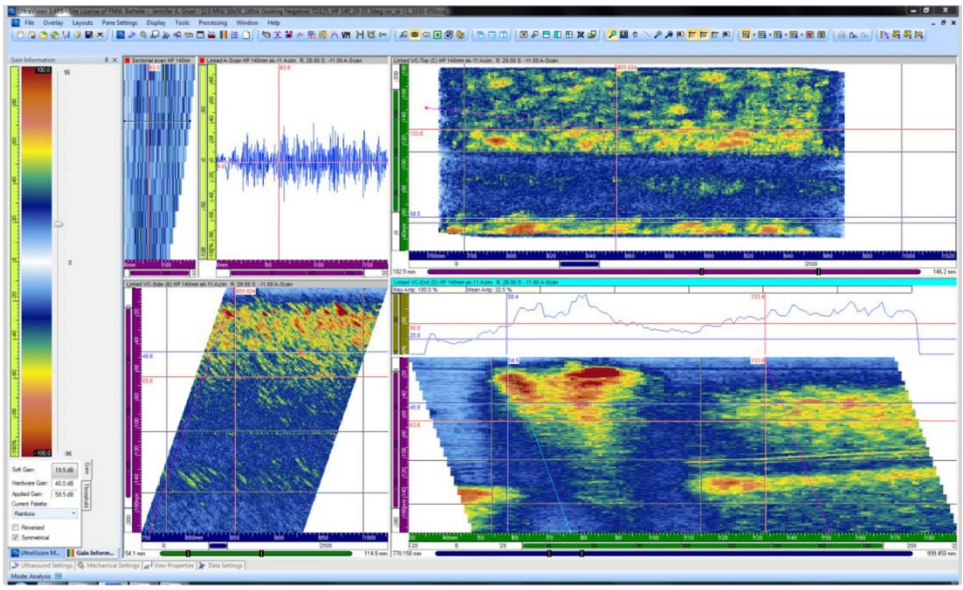

Figure E.14. CCW, Skew 11, Axial Flaw 2 Region. Flaw not detected.

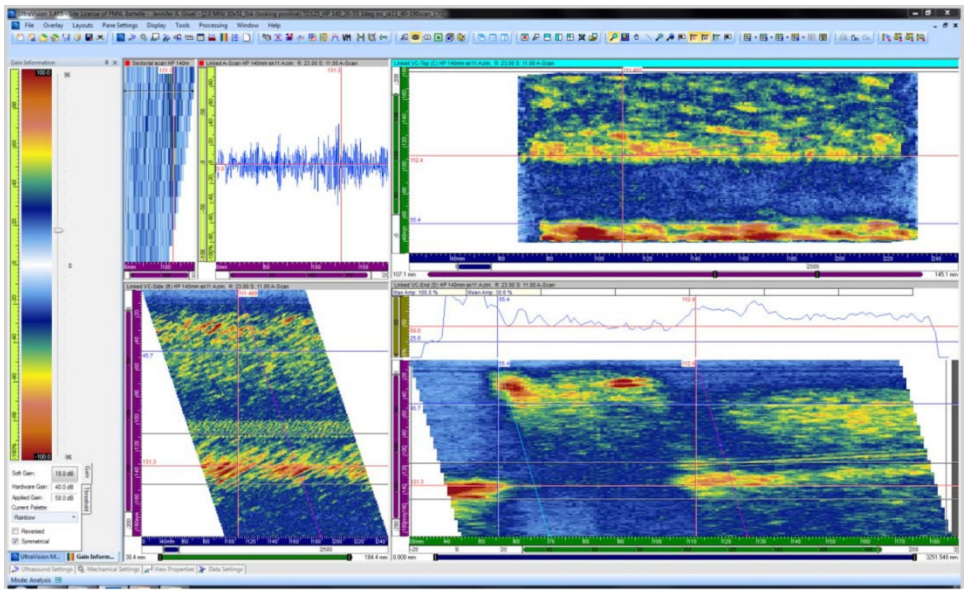

Figure E.15. CW, Skew 11, Axial Flaw 3 Region. Flaw not detected.

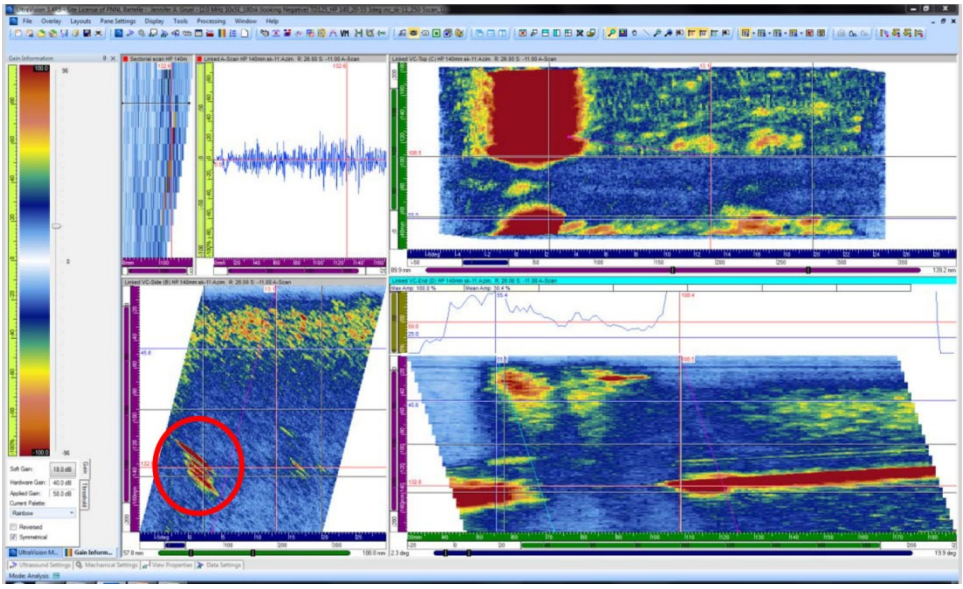

Figure E.16. CCW, Skew 11, Axial Flaw 3 Region. Flaw not detected; end-of-specimen is visible and circled in red.

E.3 Circumferential Flaws, 0-Degree Skew Angle

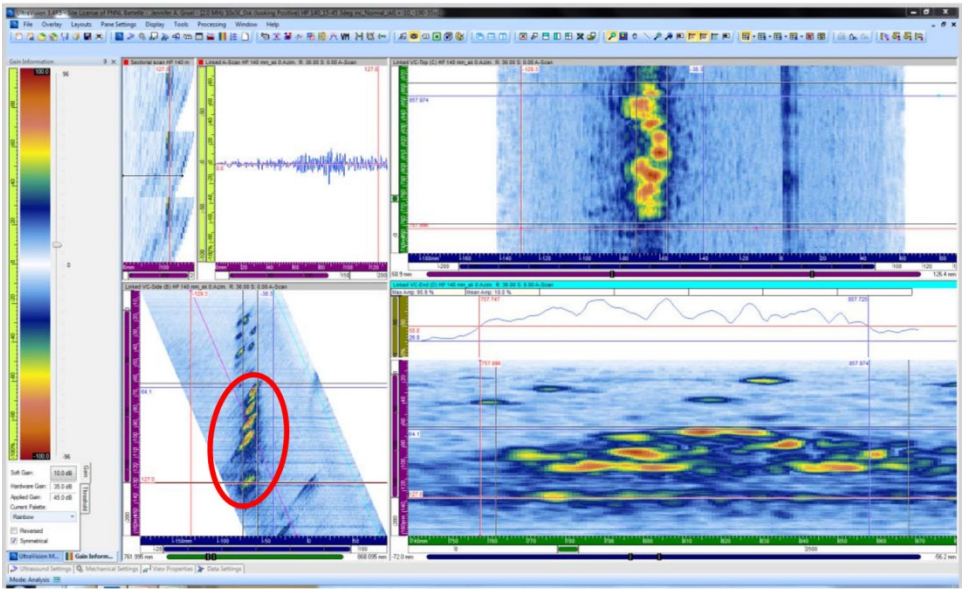

Figure E.17. DM-05 Flaw 2 Circled in Red

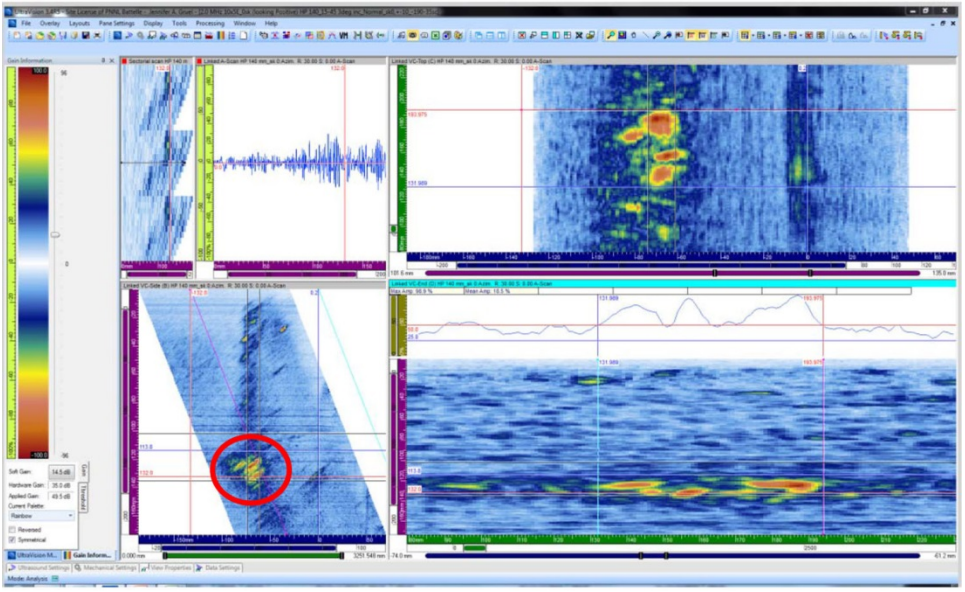

Figure E.18. DM-05 Flaw 3 Circled in Red

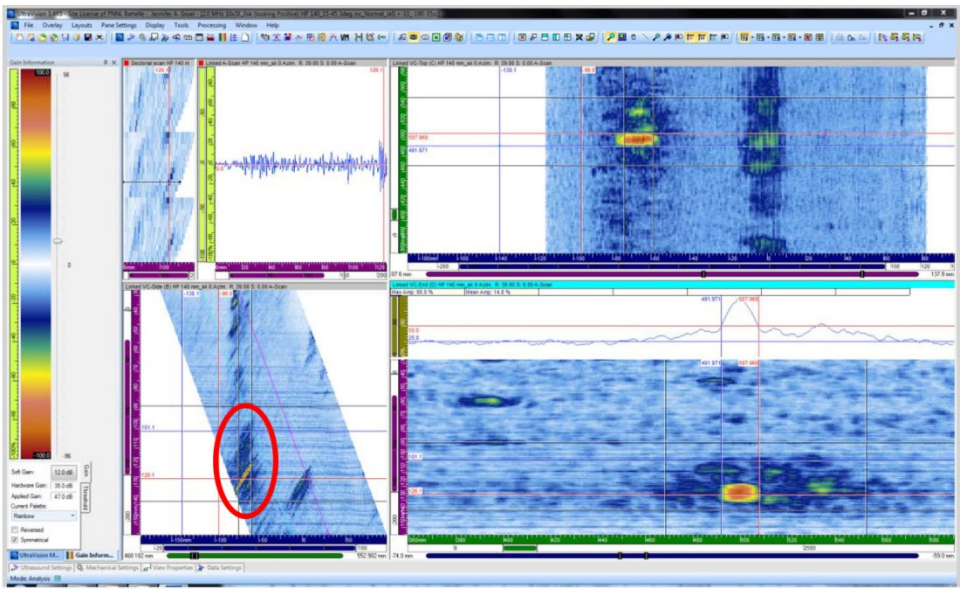

Figure E.19. DM-05 Flaw 4 Circled in Red

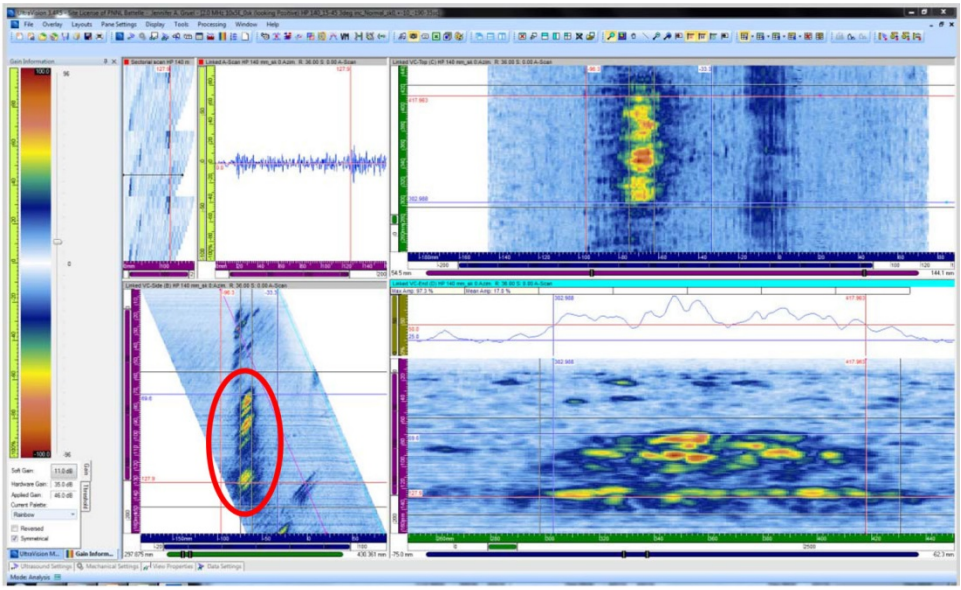

Figure E.20. DM-10 Flaw 1 Circled in Red

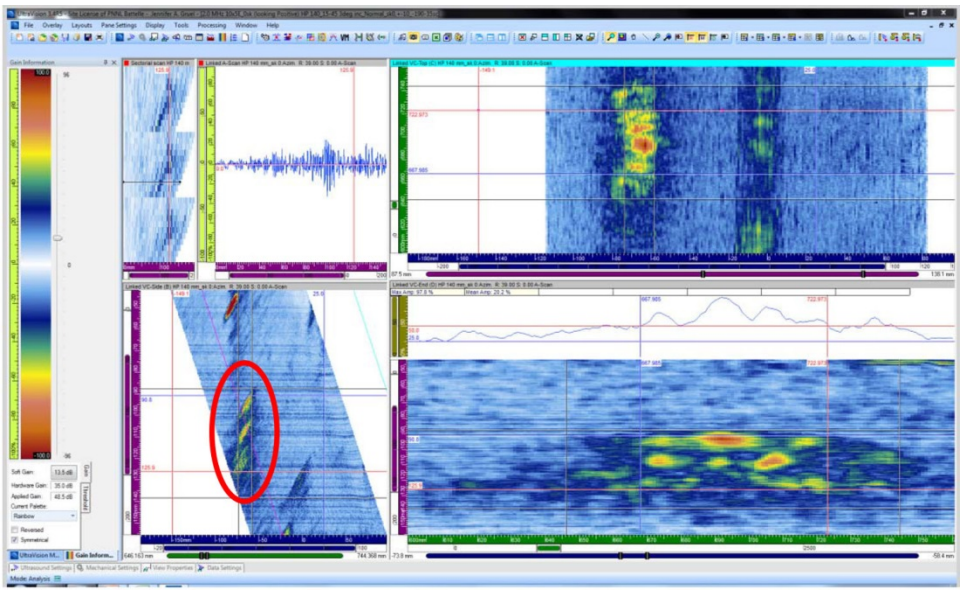

Figure E.21. DM-10 Flaw 4 Circled in Red

Appendix F

Ultrasonic Detection of Flaw Implantation Artifacts

Appendix F

Ultrasonic Detection of Flaw Implantation Artifacts

Professionally constructed mock-up welded components are commonly used to represent actual field components in operation at nuclear reactor power plants. The function of mock-up components is threefold. Mock-up components can serve as research specimens for evaluation of new inspection equipment and procedures, training and testing blocks for personnel training/evaluation in relation to performance demonstration initiative (PDI), or as in the case of North Anna—a site-specific mock-up replicating a real component critical to the operation of North Anna Nuclear Power Plant. The replica components are typically fabricated from similar piping and nozzle materials as their field counterparts and are welded together following the same nuclear grade welding specifications for matched authenticity.

Although constructed to match field components, the mock-up welds lack one critical attribute—representative flaws. Flaws, more specifically cracks, are commonly implanted into a welded mock-up component after construction of the weld is complete. The flaw implantation vendor employs a unique and proprietary process where heating/cooling under tension is used to initiate a thermal fatigue crack (TFC) in a coupon. The number of cycles is controlled to obtain the desired crack depth and "roughness." After taking exact physical measurements, the flaw implant is seal welded in place to establish final location and size. The remaining weld groove is then filled using a standard welding procedure. The disadvantage is that the coupon is surrounded by weld metal that may potentially introduce additional UT reflectors, and in the event that the weld cannot be precisely located, the excavation "remnants" can be detected with ultrasonic inspections.

Unfortunately, the invasive nature of some implantation processes may result in the generation of unwanted ultrasonically detectable implantation artifacts in the mock-up, if improperly executed. If the artifacts from the implantation process are volumetric in nature, they likely will not only interfere with detection and/or characterization of the intended implanted crack, but also negatively impact the detection/characterization of neighboring cracks. For example, if a planar crack is implanted in a circumferential orientation and the specimen is subsequently ultrasonically inspected in a circumferential scan configuration, for detection/characterization of axially oriented flaws, the implanted circumferential flaw should present the equivalent of a knife's edge to the ultrasonic beam and thus go undetected. However, if any volumetric artifacts from the implantation of the circumferential crack are present, then likely they will be detected by the circumferential scan and adversely affect the inspection. Additionally, if personnel are being qualified in a "blind" test using specimens with implantation artifacts, these artifacts could be a detriment to the very nature of the test. These artifacts essentially provide a "clue" to the examiner that an area needs to be examined more closely because of the knowledge that something has been implanted in this area.

The objective study herein describes the evaluation of two dissimilar metal weld (DMW) components complete with circumferentially-oriented coupon implanted TFCs as well as hot iso-static press electric discharge machining (HIP'ed EDM) notches in the weld region. The EDM process does not require implantation; thus, flaws of this nature should present no detectable volumetric attributes. The components were circumferentially scanned (for detection of axially orientated flaws) with the previously

described 2x(10×5) element 1.0-MHz phased-array probe. This probe was also used to scan the North Anna site-specific mock-up specimens DM-05 and DM-10.

F.1 Mock-up Components Evaluated

F.1.1 DMW Specimen 8C–032

Specimen 8C-032 consists of a SA508 nozzle welded to a 316 stainless steel (SS) safe end welded to an A312 TP304L pipe. The individual sections were sent to FlawTech where four circumferentially oriented TFCs were implanted in the nozzle butter material (Inconel 82/182) as the nozzle was welded to the safe end. This DMW mock-up specimen is 347.4 mm (13.68 in.) in diameter at the flaw position, and is approximately 249.5 mm (9.82 in.) in length, with approximately 37.1-mm (1.46-in.) wall thickness at the flaw location within the DMW. Photographs of the mock-up are provided in Figure F.1.

The four TFCs were inserted via a coupon-implant technique and were all constructed as circumferentially oriented flaws. A side-view illustration of the four flaws depicting flaw position relative to the DMW geometry and flaw depth is provided in Figure F.2.

A full-circumferential view of all flaw positions and extents on specimen 8C-032 is shown in Figure F.3. This pipe end-view depicts the circumferential extent (length) of the implanted ID surface-connected cracks, relative to the radial position along the pipe circumference.

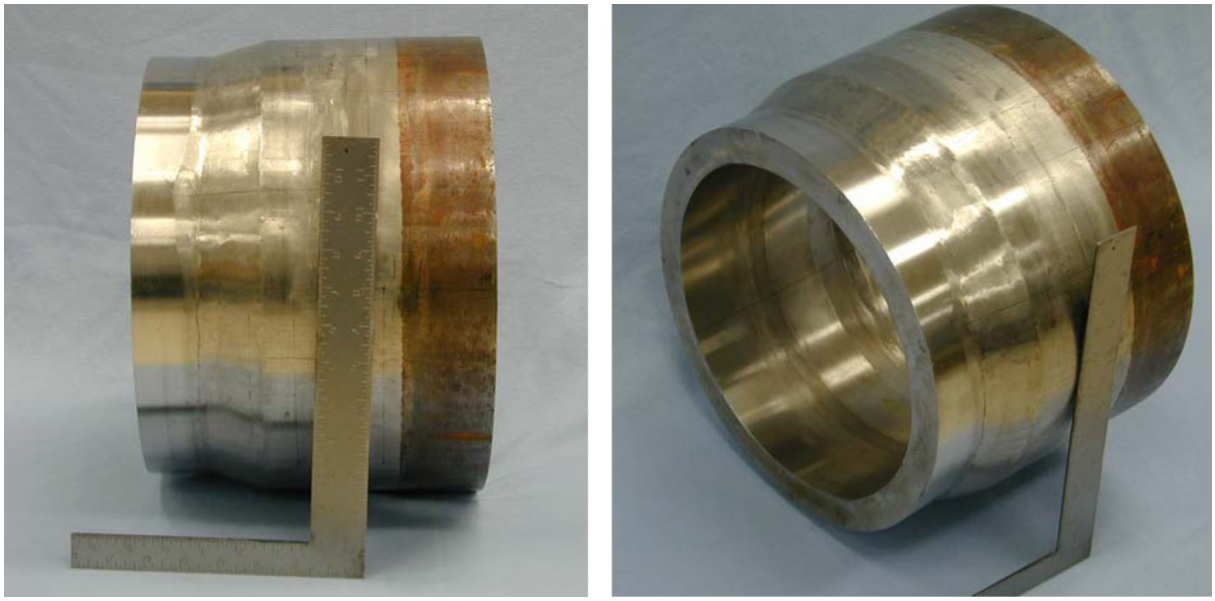

Figure F.1. Photographs of the DMW Mock-up Specimen 8C-032

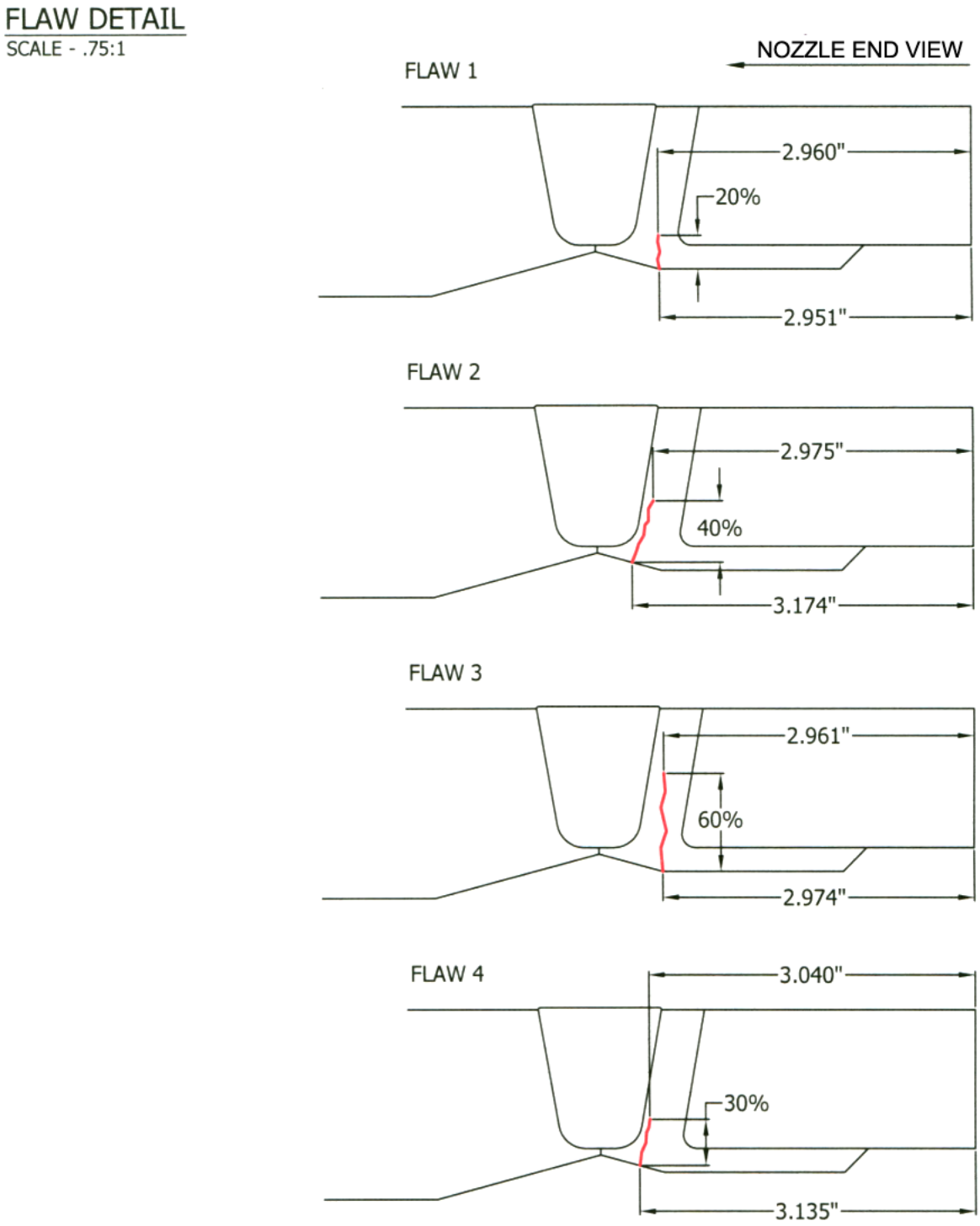

Figure F.2. Side View Illustration of All Four Thermal Fatigue Cracks Implanted into DMW Mock-Up Specimen 8C-032

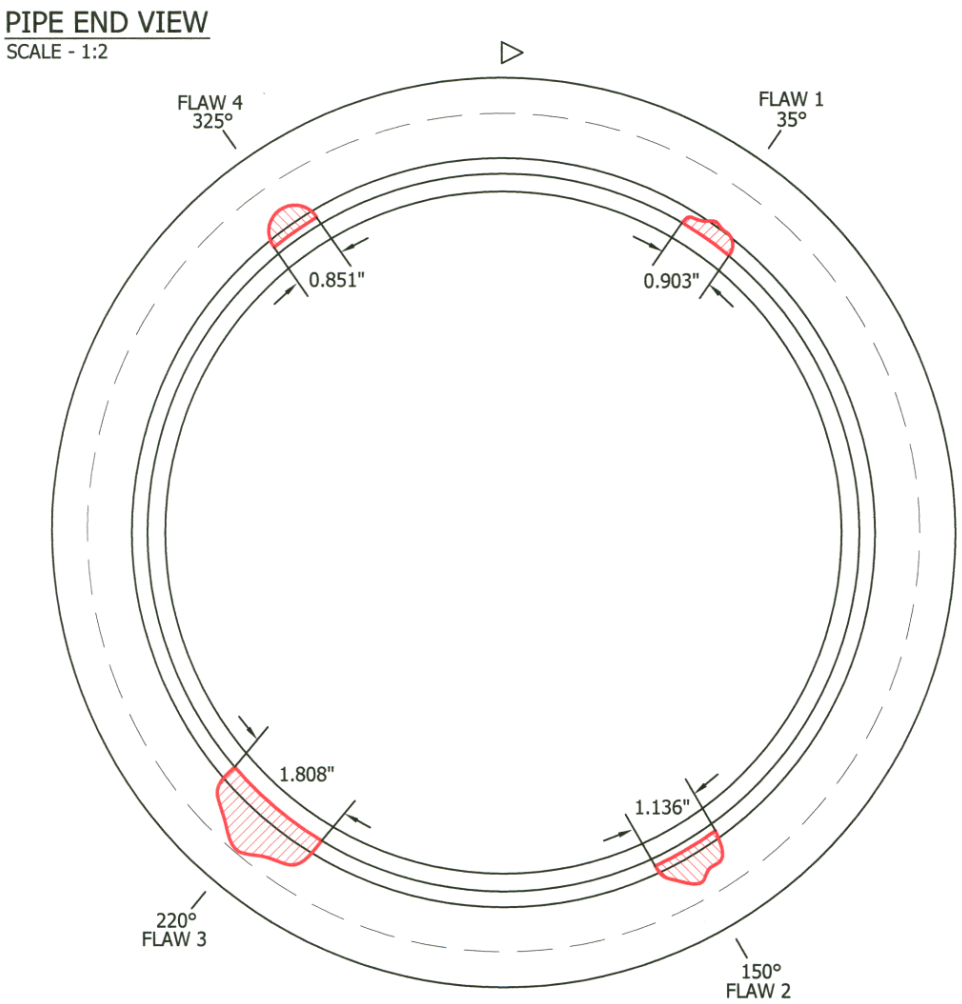

Figure F.3. End View Illustration of All Four Thermal Fatigue Cracks Implanted into DMW Mock-Up Specimen 8C-032

F.1.2 DMW Specimen 8C-036

Specimen 8C-036 is a nozzle-to-stainless steel safe end-to-pipe DMW configuration. It contains four TFCs and four HIP'ed EDM notches. Two of the EDM notches are axially oriented while the other six flaws are circumferential in orientation. The individual sections were sent to FlawTech where the DMW specimen mock-up was buttered and welded, and subsequently all six circumferential cracks were implanted in the Inconel 82/182 butter material while the two axial cracks spanned the butter and weld zones. This DMW mock-up specimen is 348.2 mm (13.71 in.) in diameter at the flaw position, and is approximately 241.0 mm (9.49 in.) in length, with approximately 37.8-mm (1.49-in.) wall thickness at the flaw location within the DMW. Photographs of the mock-up are provided in Figure F.4.

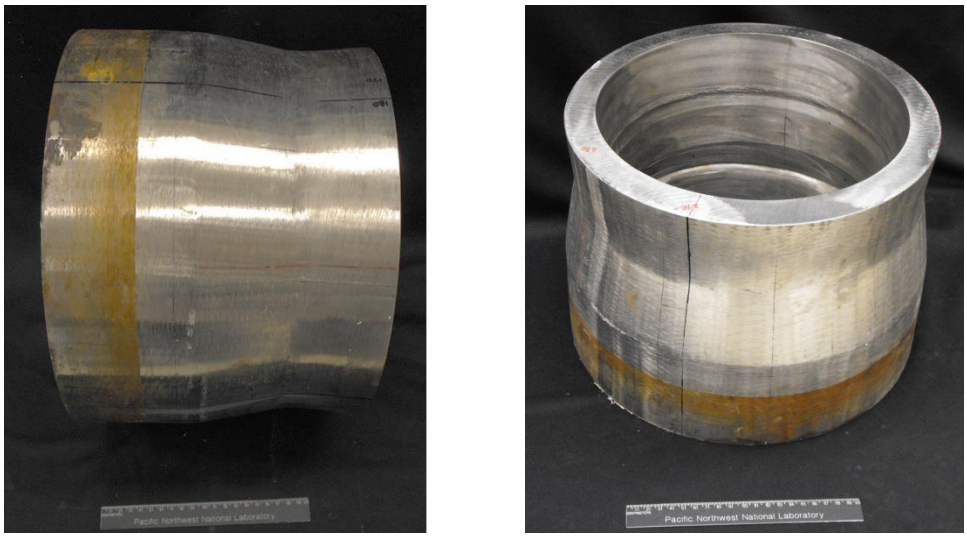

Figure F.4. Photographs of DMW Mock-up Specimen 8C-036

A side-view illustration of the four flaws depicting flaw position relative to the DMW geometry and flaw depth is provided in Figure F.5, while side views of the two circumferentially HIP'ed EDM notches and two axially HIP'ed EDM notches are provided in Figures F.6 and F.7, respectively.

Figure F.8 shows a full circumferential view of all flaw positions and extents on specimen 8C-036. This pipe end-view depicts the circumferential extent (length) of the implanted ID surface-connected cracks, relative to the radial position along the pipe circumference.

A summary of true-state flaw position, location, orientation, length, and depth (flaw height) for both DMW mock-up specimens is provided in Table F.1.

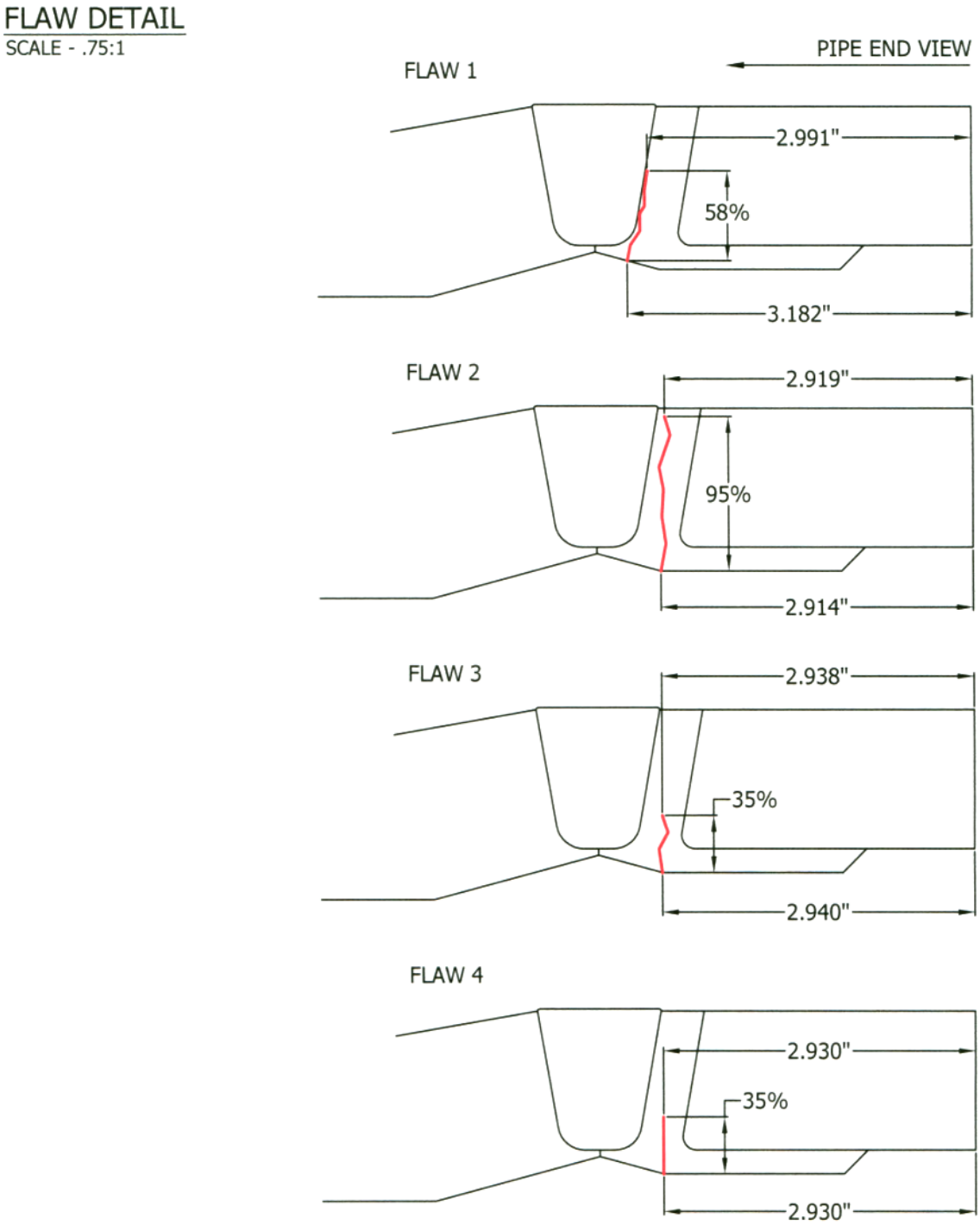

Figure F.5. Side-View Illustration of All Four Thermal Fatigue Cracks Implanted into DMW Mock-up Specimen 8C-036

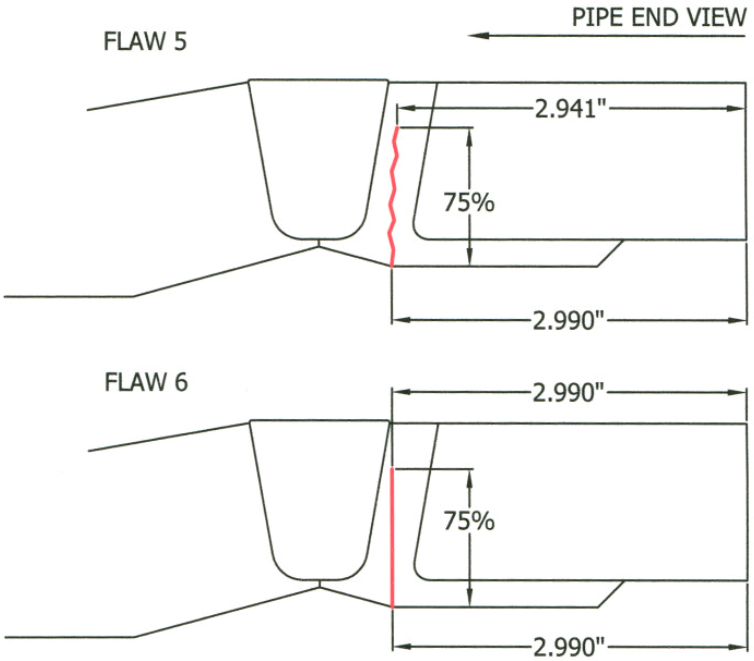

Figure F.6. Side-View Illustration of the Two Circumferentially HIP'ed EDM Notches Implanted into DMW Mock-up Specimen 8C-036

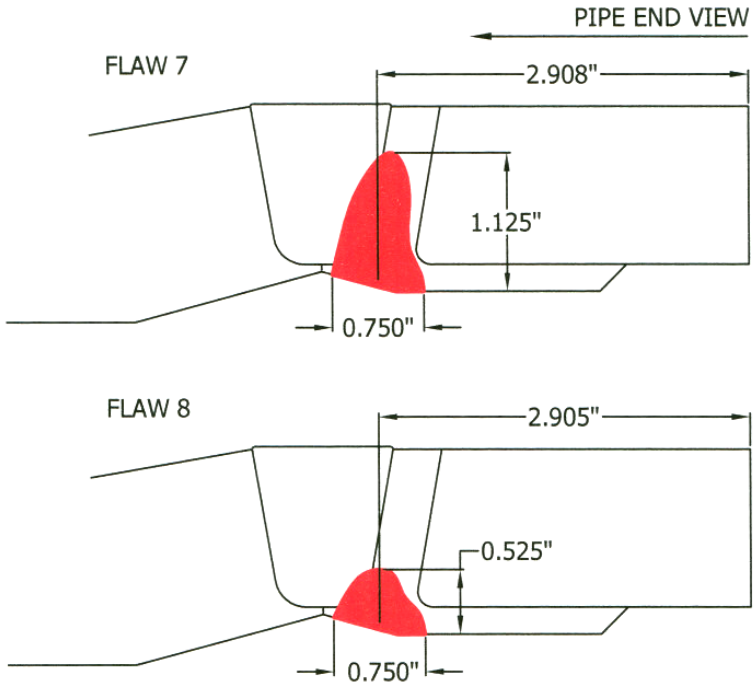

Figure F.7. Side-View Illustration of the Two Axially HIP'ed EDM Notches Implanted into DMW Mock-up Specimen 8C-036

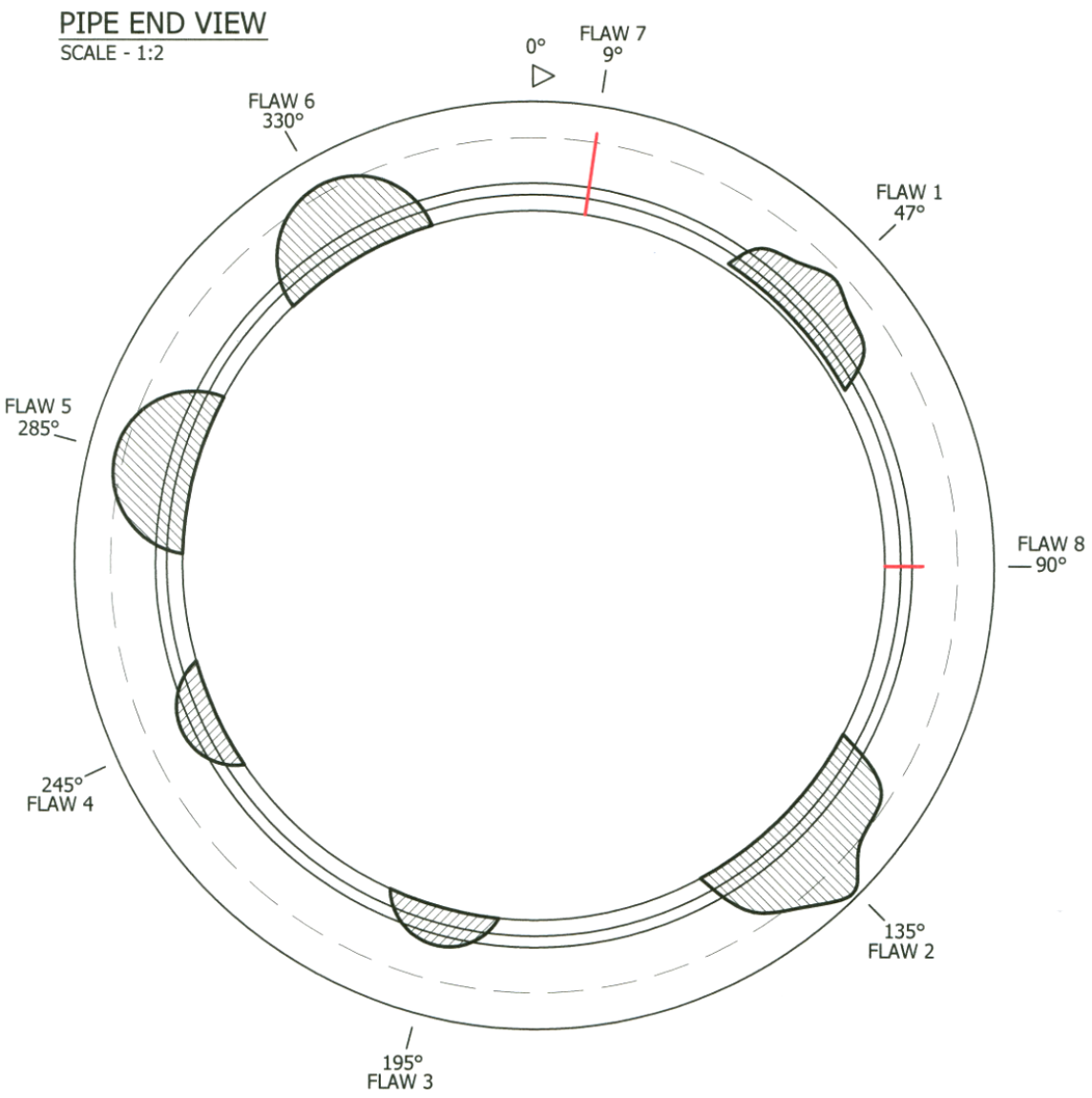

Figure F.8. End-View Illustration of All Eight TFCs and HIP'ed EDM Cracks Implanted into DMW Mock-up Specimen 8C-036

Table F.1. Summary Table Depicting True-State Dimensions and Locations of All Flaws in Both DMW Mock-Up Specimens Examined in This Study

Flaw	Type	Length (mm/in)	Depth (mm/in)	Depth (%)	Tilt (deg)	Orientation
8C-032						
1	TFC	22.9 (0.903)	7.7 (0.302)	20	0	Circ.
2	TFC	28.9 (1.136)	14.4 (0.568)	40	19	Circ.
3	TFC	45.9 (1.808)	23.0 (0.904)	60	0	Circ.
4	TFC	21.6 (0.851)	10.8 (0.427)	30	13	Circ.
8C-036						
1	TFC	63.1 (2.483)	21.1 (0.830)	58	30	Circ.
2	TFC	72.4 (2.852)	36.2 (1.427)	95	0	Circ.
3	TFC	40.1 (1.579)	13.4 (0.528)	35	0	Circ.
4	HIP'ed EDM	40.0 (1.575)	13.3 (0.525)	35	0	Circ.
5	TFC	57.4 (2.260)	28.8 (1.132)	75	0	Circ.
6	HIP'ed EDM	57.2 (2.250)	28.6 (1.125)	75	0	Circ.
7	HIP'ed EDM	19.1 (0.750)	28.6 (1.125)	74.7	0	Axial
8	HIP'ed EDM	19.1 (0.750)	13.3 (0.525)	50	0	Axial

F.2 Ultrasonic Phased-Array Data and Analysis

The DMW mock-up components were scanned with a transmit-receive longitudinal (TRL) 1-MHz phased-array probe. The array consists of two 1.0-MHz PA transducers mounted side-by-side on a Rexolite wedge configuration with cork being used as an acoustic damping material, essentially separating the two halves of the wedge for improved acoustic isolation to reduce any cross-talk effects. Both transmit and receive probes were identical in design with 10×5 element configuration. See Section 6.0 of the TLR for additional probe information. The Rexolite wedge was machined to have a matching OD contour to that of the DMW mock-ups, and the probe and wedge were configured for circumferential scanning—detection of axially orientated flaws.

Complete circumferential raster scans were conducted on each DMW component over the entire weld and butter region including an approximate 25 mm (1 in.) of base material on either side of the weld, where applicable. Raster scan resolution was 0.5 mm (0.02 in.) by 1.0 mm (0.04 in.) in the scan and index axes, respectively, for all scans. Data were acquired in quarter circumferential sections of each component with scan overlap to ensure designated features (flaws) were appropriately positioned within the scan bounds.

Data were analyzed for detection of circumferential flaws and any implantation artifacts associated with the insertion of the ten flaws into the DMW components. Ideally, a circumferential scanning technique should not be sensitive to the detection of circumferentially oriented flaws as only a minimal flaw face is presented to the ultrasonic beam. However, if improperly implanted, the circumferential flaws may have volumetric artifacts that are detectable in the circumferential scan configuration and negatively impact the detection of axially oriented flaws. Software sensitivity settings (applied gain) were globally established for both DMW components based on the overall detection of axially orientated

flaws #7 and #8 located in the weld/butter region of component 8C-036. Without a calibrated response setting, the post software sensitivity (gain) can be increased such that the amplification of noise could be misconstrued as a coherent response and falsely be classified as an artifact response.

F.2.1 Phased Array Data Acquired on the 8C-036 Component

Circumferential scan quadrant #1 of 8C-036 extended from approximately −10 degrees to 100 degrees in length from the reference ‘0’ position and contained both axially oriented flaws (for reference, flaw numbers 7 and 8). Figure F.9 shows the PA-UT data for quadrant #1 at an inspection angle of 32 degrees (43-degree impingement angle). The selected angle resulted with the largest response from both flaws and established the applied gain setting to be 36.5 dB for subsequent analyses. Flaws #7 and #8 were easily detected (indicated by the black arrows) at the true-state locations of 9 and 90 degrees circumferentially in the scan axis and adjacent to the weld (in the weld/butter region) in the top and side views. Signal-to-noise ratio (SNR) values for flaw #7 and #8 were 21.7 and 23.0 dB, respectively. Note: The data layout format will remain consistent for the remainder of the section.

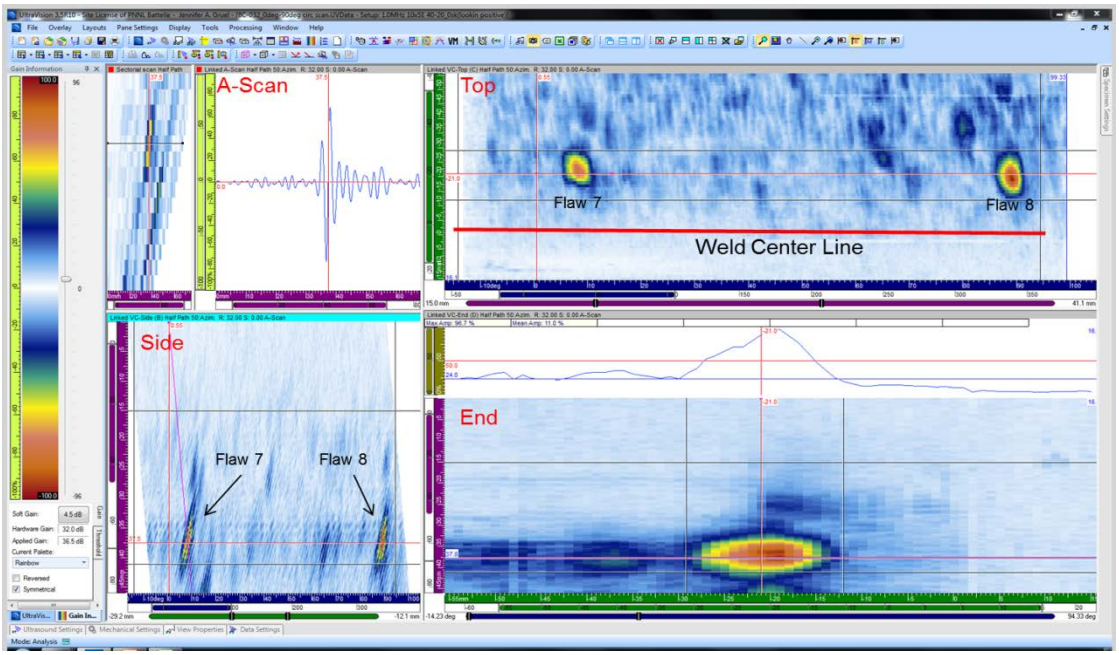

Figure F.9. 8C-036 Quadrant #1: Detection of Axially Orientated Flaws #7 and #8

In addition to the two axially orientated flaws, quadrant #1 contained the 58% through-wall circumferentially oriented flaw #1 between scan locations of 33.7 and 60.3 degrees circumferentially. The flaw #1 region of interested is boxed in red and shown in Figure F.10. At the same 32-degree inspection angle and applied gain settings, a mid-wall indication was identified and highlighted by the black arrows in the figure. Figure F.11 shows a mid-wall gate applied excluding ID responses, and sensitivity was increased displaying the through-wall extents of flaws #7 and #8 as well as the indication in the circumferential flaw region (boxed in red). Here it is shown that the indication is located closer to the weld center line and is detected with a SNR of 12.9 dB.

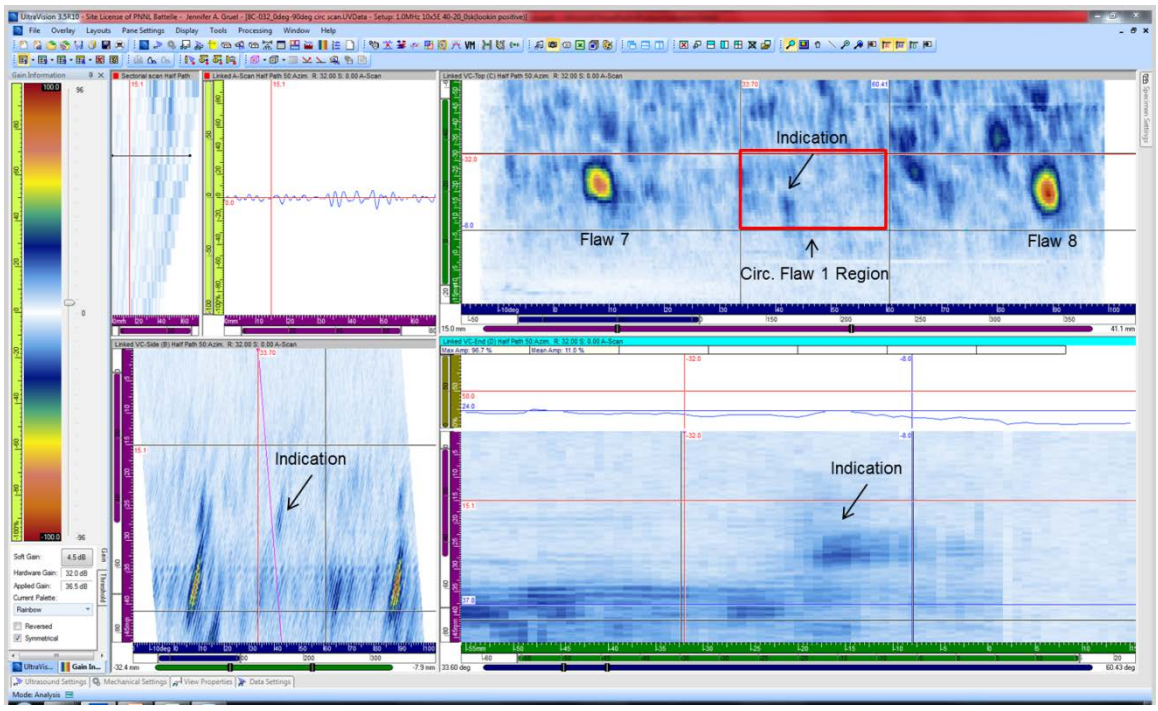

Figure F.10. 8C-036 Circumferential Flaw #1 Region Boxed in Red

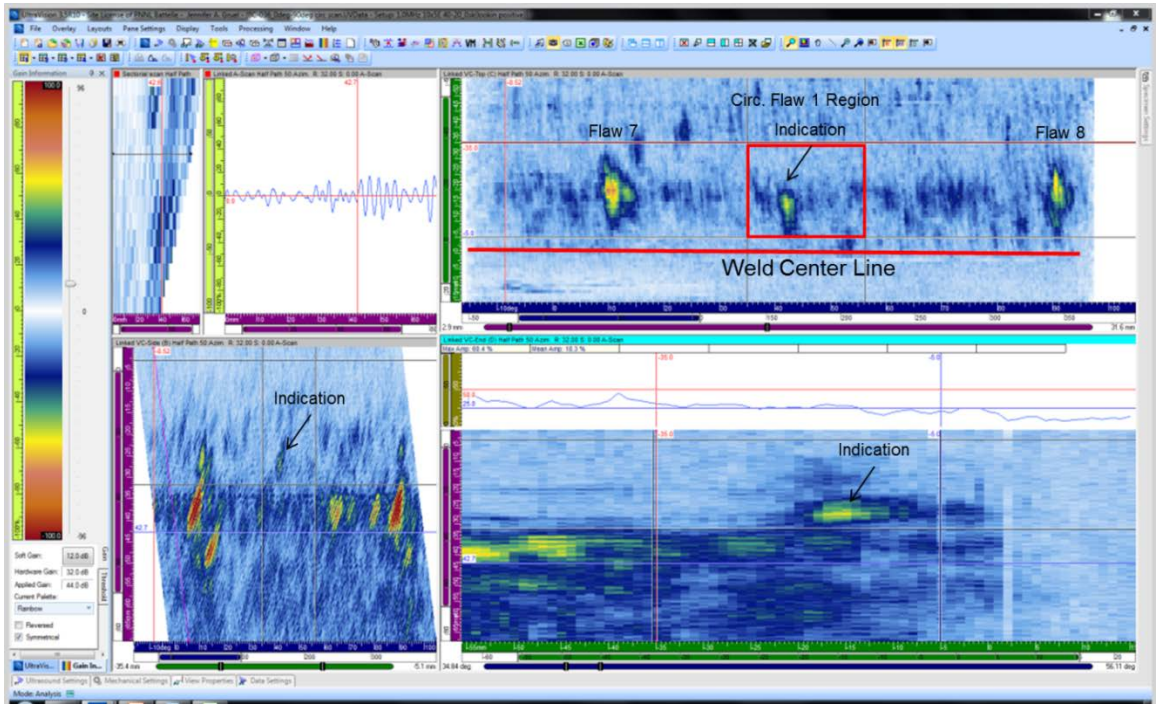

Figure F.11. 8C-036 Circumferential Flaw #1 Region Boxed in Red. Mid wall data gates are applied.

Subsequently, quadrants #2, #3, and #4 of the 8C-036 DMW component were analyzed. Figures F.12, F.13, and F.14 show data screenshots highlighting the circumferential flaw regions of interest boxed in red. In addition, the axial flaws are indicated where applicable. Quadrants #2, #3, and #4 did not show any discernable indications above background noise in the regions of circumferentially oriented flaws.

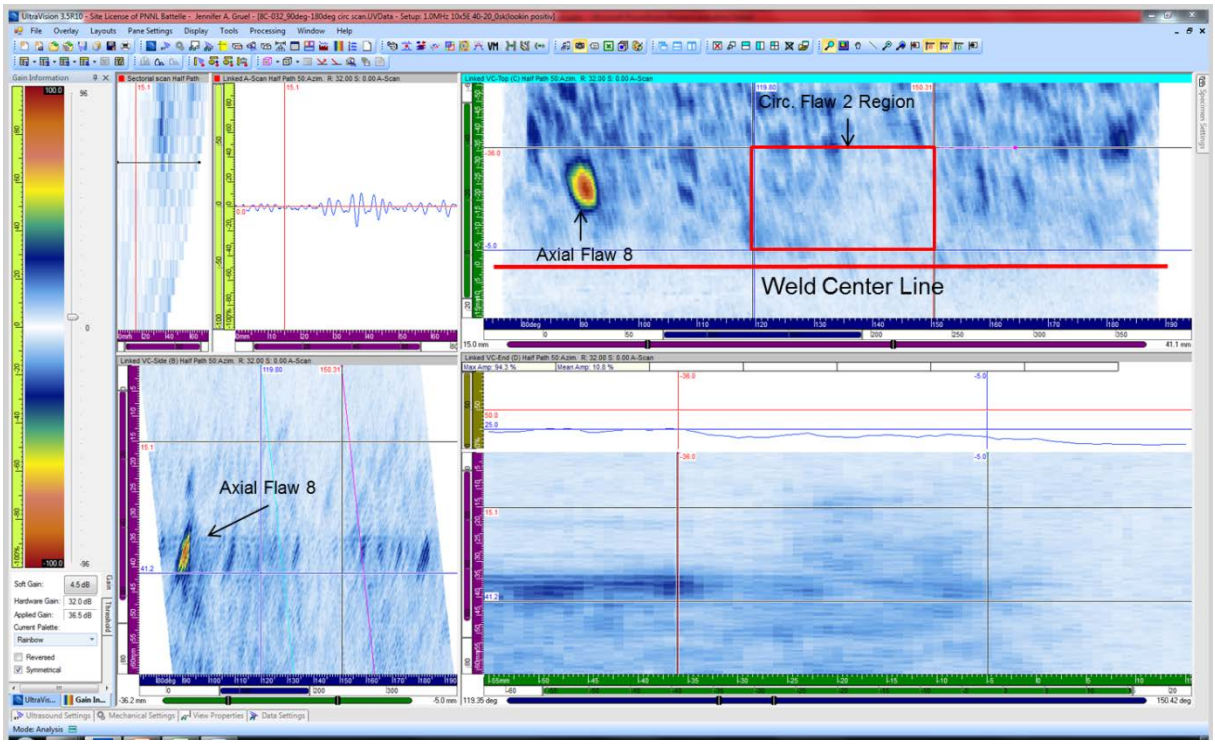

Figure F.12. 8C-036 Circumferential Flaw #2 Region Boxed in Red. No indications.

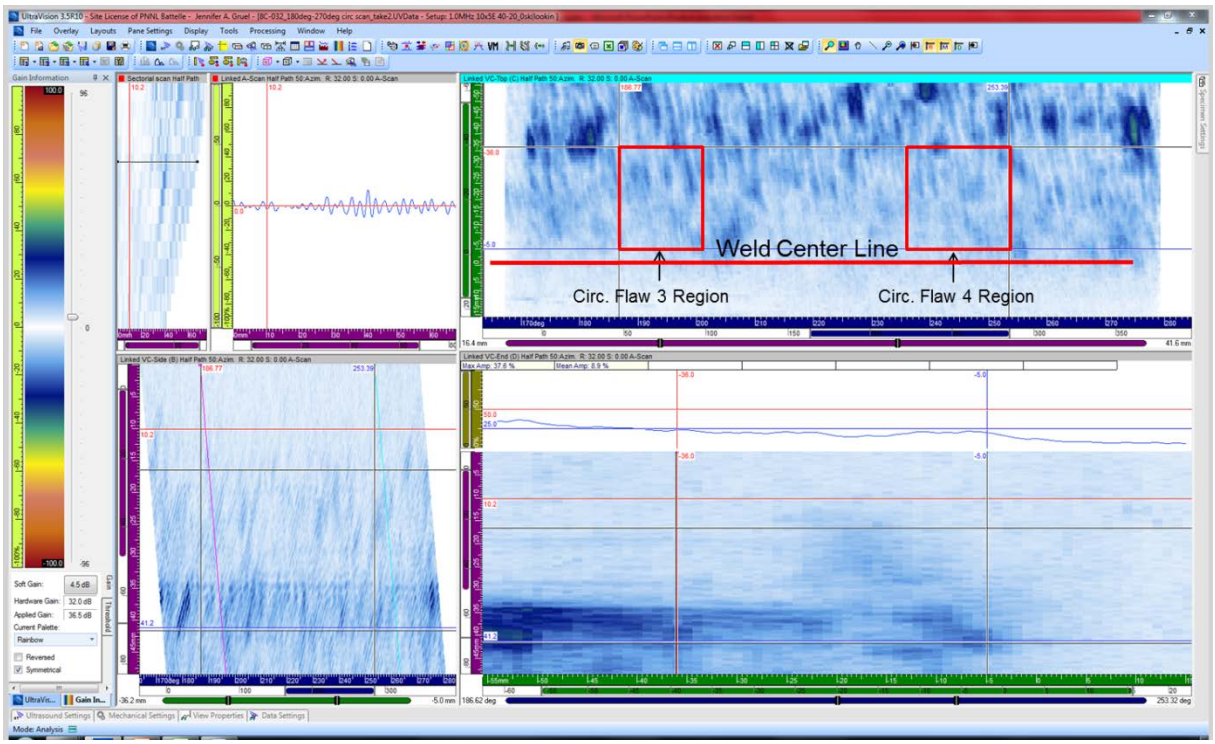

Figure F.13. 8C-036 Circumferential Flaw #3 and #4 Region Boxed in Red. No indications.

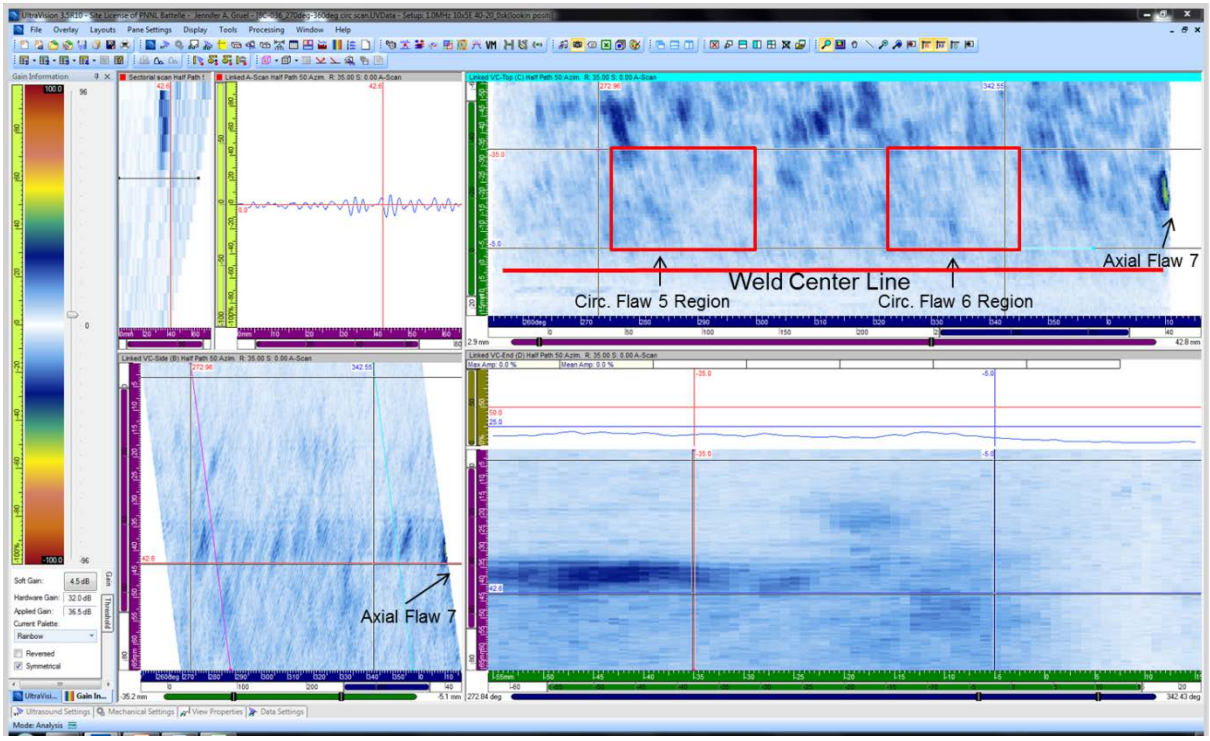

Figure F.14. 8C-036 Circumferential Flaw #5 and #6 Region Boxed in Red. No indications.

F.2.2 Phased Array Data Acquired on the 8C-032 Component

Circumferential scans were also performed on the 8C-032 DMW component in quadrant fashion with reference to the '0' position stamped on the specimen. The 8C-032 component only contains implanted circumferential flaws. For calibration purposes, a sensitivity setting of 36.5 dB at a 32-degree inspection angle was applied to all 8C-032 data—as established from the axial flaw responses #7 and #8 in the 8C-036 component. The red boxed region in Figure F.15 illustrates the circumferential flaw #1 region in quadrant #1 that extends from 30.2 to 39.8 degrees circumferentially. No indications above background noise are detected in this region.

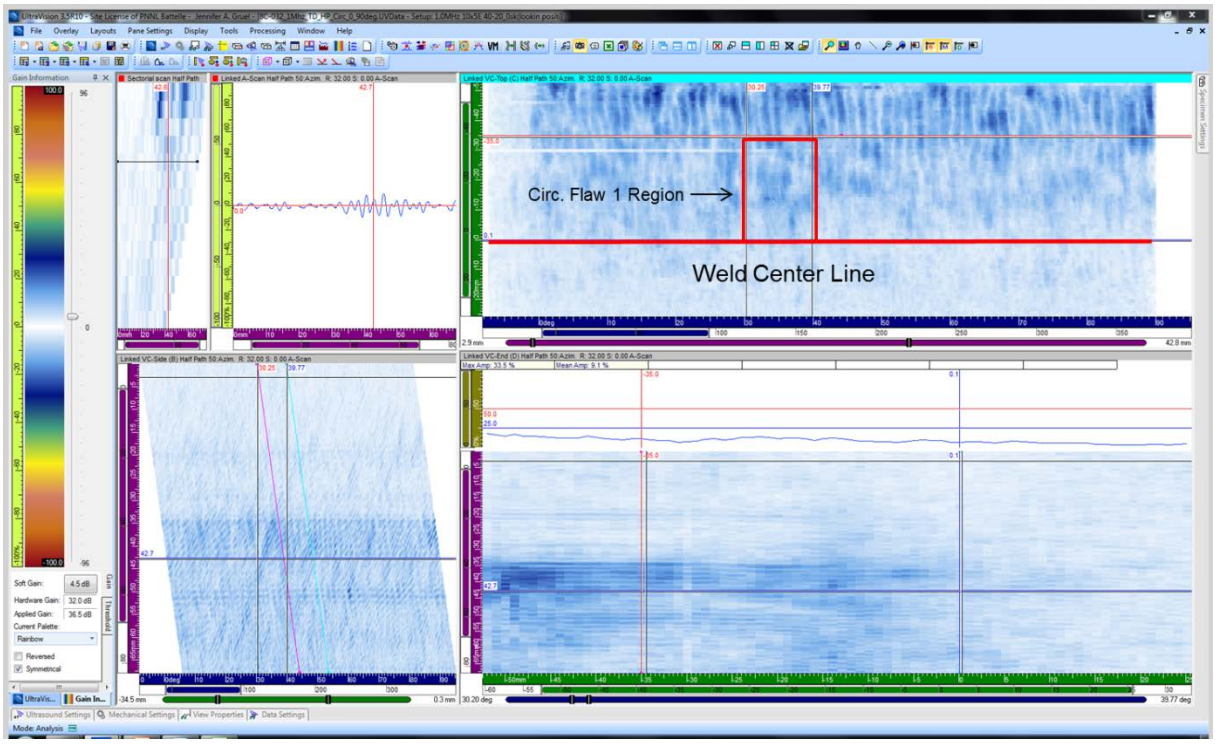

Figure F.15. 8C-032 Circumferential Flaw #1 Region Boxed in Red. No indications.

The quadrant #2 scan of the 8C-032 specimen contains circumferential flaw #2 between 144 and 156 degrees circumferentially. An indication above background noise levels was detected in the mid-wall region of circumferential flaw #2. The mid-wall gated view of the data is shown in Figure F.16 with increased sensitivity. The indication was detected with a SNR of 9.5 dB.

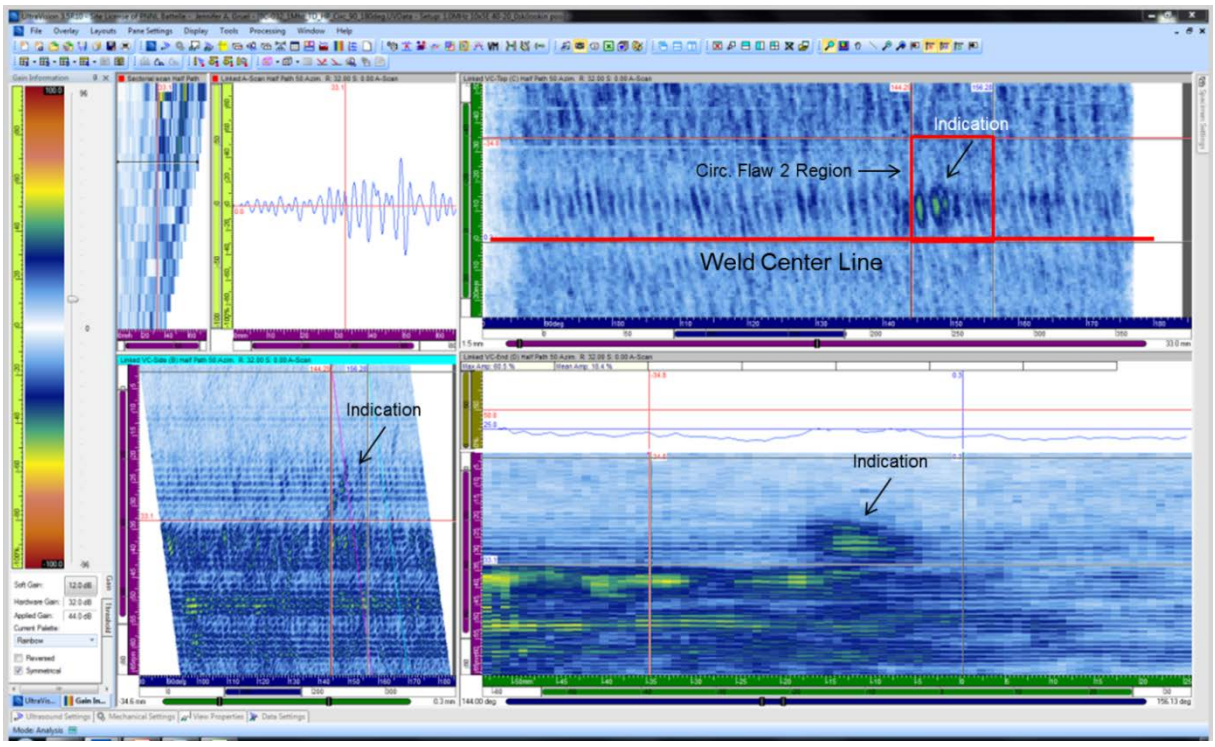

Figure F.16. 8C-032 Circumferential Flaw #2 Region Boxed in Red. Mid-wall data gates are applied.

Quadrants #3 and #4 of 8C-032 containing circumferential flaws #3 and #4, respectively, were also fully evaluated for detection of indications in the flawed regions. Figures F.17 and F.18 show data from each quadrant with the circumferential flaw regions boxed in red. Neither quadrant had indications above noise levels.

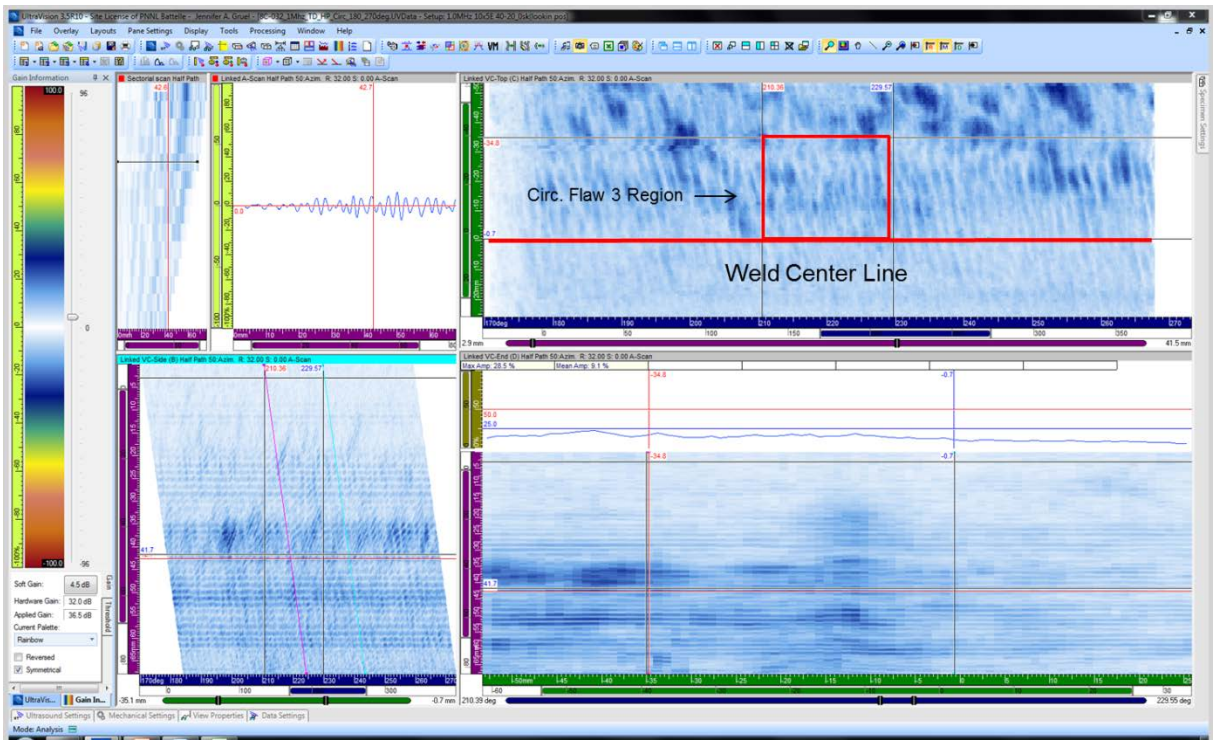

Figure F.17. 8C-032 Circumferential Flaw #3 Region Boxed in Red. No indications.

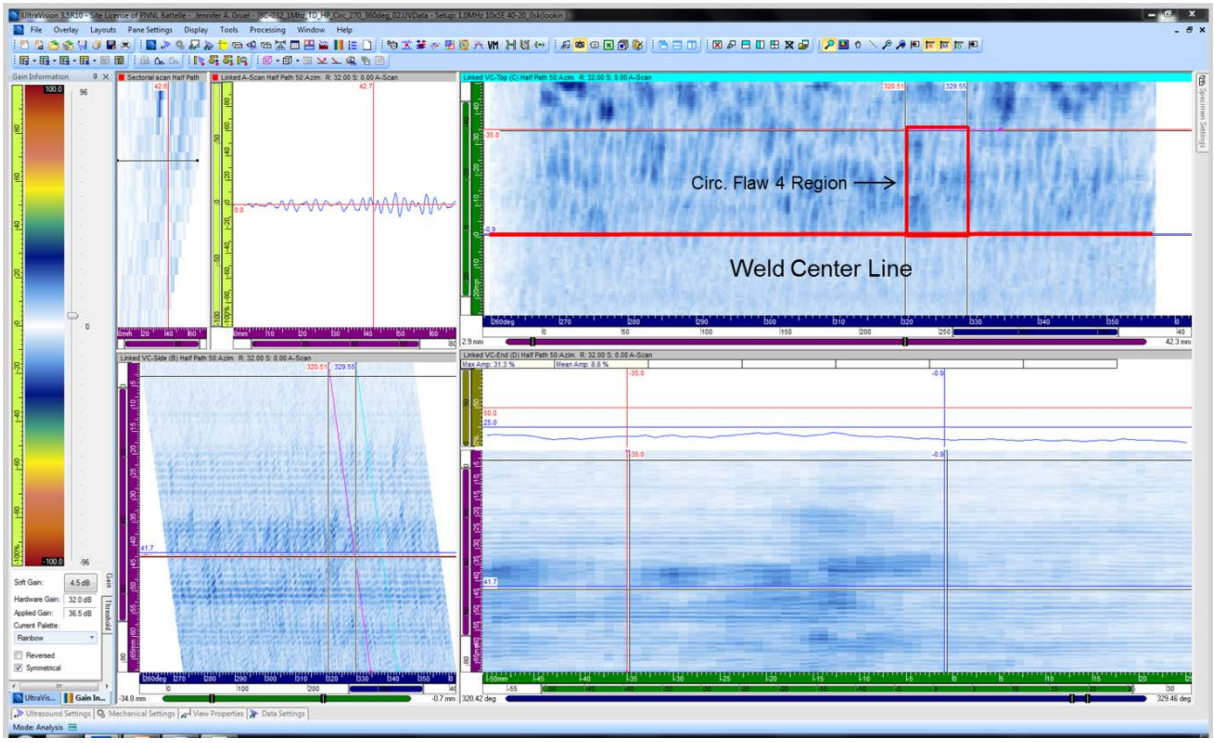

Figure F.18. 8C-032 Circumferential Flaw #4 Region Boxed in Red. No indications.

F.3 Circumferential Flaw/Implantation Artifact Detection Summary

Circumferential scans (for detection of axial flaws) using a 1-MHz phased-array TRL probe were performed on two DMW components. The components contained a combined total of ten circumferentially oriented flaws and two axially oriented flaws. Using the axial flaws for sensitivity calibration, the data were evaluated for the detection of circumferentially oriented flaws or any associated implantation artifacts. Undesired detection of artifacts and/or circumferential flaws in the circumferential scan configuration can negatively impact detection of axial flaws or increase the false call rate of axial flaws in the mockup specimen.

Considering the ten opportunities for detection of circumferential-flaw–related indications, only two regions of circumferential flaw locations presented indications above background noise from each DMW component. Circumferential flaw #1 region in 8C-036 contained an implanted TFC that was 58% through-wall and extended 26.6 degrees in the circumferential axis. This flaw also was specified to have a 30-degree tilt away from the weld with respect to radial. The detectable mid-wall indication from this flaw region had a SNR of 12.9 dB. The second indication was found in the circumferential flaw #2 region of 8C-032. Similarly, this was a 40% through-wall implanted TFC with a radial tilt of 19 degrees. This flaw was detected in the mid-wall region with a SNR of 9.5 dB.

Eight out of ten regions containing circumferential flaws did not have indications above background noise when evaluated at 1 MHz in the circumferential scanning configuration for the detection of axial flaws. The two examples where mid-wall indications were found contained circumferential flaws with a radial tilt greater than 15 degrees. The tilt of the flaw in this configuration presented more than a nominal knife's edge (as seen in the other eight circumferential flaws) to the ultrasonic beam, thus reflecting enough energy from the flaw face for detection above background noise (> 6 dB SNR). As the degree of tilt increased, the detection SNR value also increased as illustrated by the 30-degree tilted flaw having a 12.9 dB SNR, whereas the 19-degree tilted flaw was detected at 9.5 dB. The radially oriented or less than 15 degrees of tilt, circumferentially oriented flaws were without detectable artifacts in the regions of interest. Circumferential flaw implantation artifacts were not detected in either of the DMW components; rather, flaws with radial tilt were detected from scan configurations designed for detection of axial flaws.

Pacific Northwest
NATIONAL LABORATORY

Proudly Operated by Battelle *Since 1965*

U.S. DEPARTMENT OF
ENERGY

902 Battelle Boulevard
P.O. Box 999
Richland, WA 99352
1-888-375-PNNL (7665)
www.pnnl.gov